German-Korean Symposium 2004 on Power Electronics and Electrical Drives

2004 한독 전력전자 및 전기구동장치 공동 세미나

27.-29. June 2004
Aachen, Germany

SIEMENS

DELTA Energy Systems

Deutsche Forschungsgemeinschaft DFG

LUST ANTRIEBSTECHNIK

WELCOME TO GERMAN-KOREAN SYMPOSIUM 2004 AT AACHEN

Based on the Agreement between the German science foundation Deutsche Forschungsgemeinschaft (DFG) and the Korean Science Foundation (KOSEF), joint seminars on Power Electronics and Electrical Drives have been held several times. At these events, results of research were presented, new ideas were exchanged and many contacts and visits were initialized between participating institutes.

In the past, these bilateral symposiums were organized each time in Korea where the German attendants experienced great hospitality. Therefore, it is with great pleasure that the German organizers can welcome their Korean colleagues at a symposium in Germany now.

The City of Aachen not only features an interesting old town looking back to an old and famous history, but also will be host to the 35th IEEE Power Electronics Specialists Conference, PESC'04, in the week prior to the German-Korean Symposium. Therefore, the attendance of the Joint Symposium can be combined with participation at one of the greatest conferences in our field of interest.

Realization of the Joint Symposium would not have been possible without support of many organizations. First of all, the organizers thank DFG and KOSEF for financing traveling and living expenses of our scientific event. We also want to thank our industrial sponsors - Delta Energy Systems (Germany) GmbH, Lust Antriebstechnik GmbH and Siemens AG (Automation & Drives) - who made it possible to show a little bit of our country and culture to our Korean guests. Last but not least, we would like to thank RWTH-Aachen University for providing the facilities for the scientific seminar. In particular, we like to thank the staff members of the Institute for Power Electronics and Electrical Drives (ISEA) who, already burdened by organizing PESC'04, also managed to support us as our local organizing committee.

We hope that our Korean guests enjoy their stay at Aachen and in Germany. In name of all organizers, we wish you an effective symposium with many interesting discussions, which will stimulate future research and deepen contacts and exchanges between Korean and German colleagues.

Horst Grotstollen
University of Paderborn
General and Technical Chair

Rik De Doncker,Stephan Buller
RWTH-Aachen University
Local Organizers

Byung-Moon Han
Myonji University
Technical Chair and Korean Liaison

CONTENTS

Participants of Joint Symposium

Organizers

Horst Grotstollen
University of Paderborn
General and Technical Chair

Byung-Moon Han
Myonji University
Technical Chair

Rik De Doncker
RWTH-Aachen University
Organizer

Stephan Buller
RWTH-Aachen UniversityLocal
Local Organizer

German Speakers

Prof. Dr. Andreas Binder

Institut für Elektrische Energiewandlung
Technische Universität Darmstadt
Landgraf-Georg-Straße 4
D-64283 Darmstadt
Tel.: +49-6151 / 16-2167
Fax: +49-6151 / 16-6033
E-Mail: abinder@ew.tu-darmstadt.de

Prof. Dr.-Ing. Joachim Böcker

University of Paderborn
Faculty EIM-E
Power Electronics and Electrical Drives
D-33095 Paderborn, Germany
Tel. +49-5251/60-2209
Fax: +49-5251/60-3443
E-Mail: boecker@lea.upb.de

Dr.-Ing Juergen Buettner

Technical University of Ilmenau
Department Power Electronics and Control
PO BOX 100565
D - 98684 Ilmenau, Germany
Phone: [++49] 3677 69-2850
Fax: [++49] 3677 69-1469
Mail: juergen.buettner@tu-ilmenau.de

Prof. Dr. ir. Rik W. De Doncker

Institute for Power Electronics and Electrical Drives
Aachen University
Jaegerstrasse 17-19, D-52066, Aachen Germany
Tel.: +49 (0)241 80-96920
Fax: +49 (0)241 80-92203
E-Mail: dedoncker@rwth-aachen.de

Univ.-Prof. Dr.-Ing. Dieter Gerling

Universität der Bundeswehr München
Institut für Elektrische Antriebstechnik
Werner-Heisenberg-Weg 39
D-85577 Neubiberg
Tel: +49-89 / 6004-3708
Fax: +49-89 / 6004-3718
E-Mail: Dieter.Gerling@unibw-muenchen.de

Prof. Dr.-Ing. Horst Grotstollen

University of Paderborn
Faculty EIM-E
Power Electronics and Electrical Drives
D-33095 Paderborn, Germany
Tel. +49-5251/60-2206
Fax: +49-5251/60-3443
E-Mail: grotstollen@lea.upb.de

Prof. Dr.-Ing. Wilfried Hofmann

TU Chemnitz
Lehrstuhl Elektrische Maschinen und Antriebe
Reichenhainer Str. 70
D-09126 Chemnitz
Tel.: +49-371 / 531-3323
Fax: +49-371 / 531-3324
E-Mail: Wilfried.Hofmann@e-technik.tu-chemnitz.de

Prof. Dr.-Ing. Ralph Kennel

Electrical Machines and Drives
Wuppertal University,
D – 42097 Wuppertal, Germany
Tel: +49(0)202/439 1950
Fax: +49(0)202/439 1824
E-Mail: kennel@ieee.org

Prof. Dr.-Ing. R. Marquardt

Power Electronics and Control
University of Bundeswehr
D-85577 Munich/Germany
Tel.: +49-89/6004-2213 (Secretary)
Tel.: +49-89/6004-3939
Fax: +49-89/6004-3944 (Secretary)
E-Mail: rainer.marquardt@UniBw-muenchen.de

Prof. Dr.-Ing. Peter Mutschler

Technische Universität Darmstadt
FB 18, Institut für Stromrichtertechnik
und Antriebsregelung
Landgraf-Georg-Str. 4
D-64283 Darmstadt
Tel.: +49-6151 / 162-166
E-Mail: pmu@srt.tu-darmstadt.de

Prof. Dr.-Ing. J.M. Pacas

Universität Siegen
Institut für Leistungselektronik
und elektrische Antriebe
Hölderlinstr. 3
D-57068 Siegen
Tel.: +49-271 / 740-4671
Fax: +49-271 / 740-2777
E-Mail: pacas@uni-siegen.de

Prof. Dr.-Ing. Frank Palis

Otto-von-Guericke-Universität Magdeburg,
Institut für Elektrische Energiesysteme
Universitätsplatz 2
D-39106 Magdeburg
Tel.: +49-391 / 6718596
Fax: +49-391 / 6712481
E-Mail: Frank.Palis@e-technik.uni-magdeburg.de

Prof. Dr.-Ing. Dr.-Ing. h.c. D. Schröder

Lehrstuhl für Elektrische Antriebssysteme
TU München
Arcisstraße 21
D-80333 München, Germany
Tel.: +49-89 / 2892 8358
Fax: +49-89 / 2892 8336
E-Mail: dierk.schroeder@ei.tum.de

Prof. Dr.-Ing. Andreas Steimel

Ruhr-Universität Bochum
Lehrstuhl für Erzeugung und
Anwendung elektrischer Energie
D-44780 Bochum
Tel.: +49-234 / 32-23890
Fax: +49-234 / 32-14597
E-Mail: Steimel@eaee.ruhr-uni-bochum.de

Korean Speakers

Prof. Jin-Woo Ahn

Affiliation Kyungsung University
Phone: +82-51-620-4773
FAX: +82-51-624-5980
E-mail: jwahn@ks.ac.kr
Address 110-1 Daeyon-Dong Nam-Ku,
Busan 608-736 KOREA

Seung T. Baek

Affiliation Myongji University
Phone: 82-31-338-6563
FAX: 82-31-321-0271
e-mail: inverter@mju.ac.kr
Address Dept. of Electrical Engineering
Myongji University
38-2 Nam-dong, Yongin
Kyunggi-do 449-728, Korea

Prof. , Ph.D. Sewan Choi,

Affiliation Seoul National University of Technology
Phone: +82-11-768-6303
FAX: +82-2-972-2866
E-mail: schoi@snut.ac.kr
Address Dept. of Control and Instrumentation Eng.
Seoul National University of Technology
172 Kongneung-Dong, Nowon-Ku
Seoul 139-743, Korea

Prof. Ph.D. Byung-Moon Han,

Affiliation Myongji University
Phone: +82-31-330-6366
FAX: +82-31-321-0271
E-mail : erichan@mju.ac.kr
Address Dept. of Electrical Engineering
Myongji University
38-2 Nam-dong, Yongin
Kyunggi-do 449-728, Korea

Prof. Ph.D. Hyosung Kim,

Affiliation Cheonan Technical College, Korea
Phone: +82-41-550-0286
FAX: +82-41-563-3689
E-mail: hyoskim@cntc.ac.kr
Address 275 Budae, Cheonan, Chungnam
330-717 Korea

Prof. Dr.-Ing. Kee-Hwan Kim,

Affiliation Semyung University
Phone: +82-43-649 1312
FAX: +82-43-644 2111
E-mail: khkim@semyung.ac.kr
Address San 21-1, Sinwoldong, Jecheon, Chungbuk
390-711 Korea

Professor, Ph.D. Min-Huei Kim,

Affiliation: Yeungnam College of Science & Technology
Phone +82+53+650-9263
Fax +82+53+624-4736
E-mail mhkim@ync.ac.kr
Address: 1737 Daemyeung 7dong, Namgu,
Taegu Metropolitan City
705-703, Republic of Korea

Prof., Ph.D. Yoon-Ho Kim,

Affiliation Chung-Ang University
Phone: +82-2-820-5290
FAX: +82-2-812-1407
E-mail: yhkim@cau.ac.kr
Address School of Electrical and Electronics Engineering
Chung-Ang University
221 HukSeok-Dong, DongJak-Gu
Seoul, Korea 156-756

Prof. Dr.-Ing. Jongsun Ko

Affiliation : University of Dankook
Phone: +82-2-799-1185
FAX: +82-2-798-6132
E-mail: jsko@dku.edu
Address Devision of EEC, Dankook University,
San 8 Hannam-Dong, Yongsan-ku
Seoul, Korea

Associate Prof. Dong-Choon Lee

Affiliation: Yeungnam University
(School of Electrical Eng. and Computer Science)
Phone: +82-53-810-2582
FAX: +82-53-813-8230
E-mail: dclee@yu.ac.kr
Address: 214-1, Daedong, Kyongsan, Kyongbuk
712-749, Korea

Prof. Gun-Woo Moon

Affiliation KAIST
Phone: +82-42-869-3475
FAX: +82-42-861-3475
E-mail: gwmoon@ee.kaist.ac.kr
Address: 373-1, Kusong-dong, Yusong-gu
Taejeon, 305-701, KOREA

Prof. Ph.D Kwanghee Nam

Affiliation : POSTECH University
Phone : +82-54-279-2218
FAX : +82-54-279-5673
E-mail : kwnam@postech.ac.kr
Address : Hyoja San-31,
Pohang, 790-784 Republic of Korea

German-Korean Symposium 2004
on Power Electronics and Electrical Drives

June 27 - 29, 2004, Aachen, Germany

June 26,2004	**Arrival of Korean participants**
June 27, 2004	**Sightseeing City of Aachen and Trip to Eifel**

Scientific Program

June 28, 2004	Great Conference Room, Main Building of RWTH Aachen**,** Templergraben 55
8:30 - 9:00	**Welcome and opening by President of RWTH Aachen**
9:00 - 9:25	**Electrical Drives in Automobiles - An Overview** Dieter Gerling, Universität der Bundeswehr München
9:25 - 9:50	**Performance of SRM for LSEV Drive** Jin-Woo Ahn, Kyungsung University
9:50 - 10:15	**Hybrid Cars - Design, Optimization and Control** Dierk Schroeder, University of Munich
10:15	Coffee break
10:45 - 11:10	**Torque Control of Switched Reluctance Drives** Rik W. De Doncker, Aachen University
11:10 - 11:35	**An Optimal Efficiency Control of Reluctance Synchronous Motor Using Neural Network with Direct Torque Control** Min-Huei Kim, Yeungnam College of Science and Technology
11:35 - 12:00	**Technology of High-Speed Drives** Andreas Binder, University of Darmstadt
12:00 - 12:25	**A MTPA Control Scheme for an IPM Synchronous Motor Considering Magnet Flux Variations Caused by Temperature** Kwanghee Nam, Postech University
12:25	Lunch
14:00 - 14:25	**Advanced Hysteresis Control of Brushless DC Motors** Joachim Böcker, University of Paderborn
14:25 - 14:50	**Experimental Precision Position Control of PMSM using Disturbance Observer with System Parameter Compensator** Jongsun Ko, Dankook University
14:50 - 15:15	**Highly Dynamic Stator-flux-oriented Control of Traction Induction Machines without Speed Sensors** Andreas Steimel, Ruhr-Universität Bochum
15:15	Coffee break
15:45 - 16:10	**A 5 kW SOFC - low voltage battery hybrid fuel cell power conditioning system** Sewan Choi, Seoul National University of Technology
16:10 - 16:35	**Impedance Control of flexible Structures** Frank Palis, Otto-von-Guericke-Universität Magdeburg

16:35 - 17:00	**New Configuration of Unified Power Flow Controller Based on H-Bridge Inverter Modules** Byung-Moon Han, Myongji University
20:00	Dinner at Restaurant KONAK
June 29, 2004	Great Conference Room, Main Building of RWTH Aachen**,** Templergraben 55
9:00 - 9:25	**New High Efficiency Converter without Output Inductor** Gun-Woo Moon, Kaist University
9:25 - 9:50	**Multi-Phase Converter System as a testing generator for medium power applications** Dr. Juergen Buettner, Technical University of Ilmenau
9:50 - 10:15	**Analysis of DC link ripple current in three-phase ad/dc/ac PWM converters** Dong-Choon Lee, Yeungnam University
10:15	Coffee break
10:45 - 11:10	**Ballast Design with Integrated Circuits** J. Mario Pacas, University of Siegen
11:10 - 11:35	**Improved Adaptive Predictive Filter for Generating Reference Signal in Active Power Filters** Seung T. Baek, Myongji University
11:35 - 12:00	**"Sensorless" Control of 4-Quadrant-Rectifiers for Voltage Source Inverters (VSI)** Ralph Kennel, University of Wuppertal
12:00 - 12:25	**A Novel Control Method for the Compensation Voltages in Dynamic Voltage Restorers** Hyosung Kim, Cheonan Technical College
12:25	Lunch
14:00 - 14:25	**New Concept for High Voltage Modular Mulilevel Converter** Rainer Marquardt, Universität der Bundeswehr München
14:25 - 14:50	**Analysis of Power Quality for a Fuel-Cell System based on Multilevel Converter** Yoon-Ho Kim, Chung-Ang University
14:50 - 15:15	**Investigation of Practicable Bidirectional IGBT Switches for Using in Matrix Converters** Wilfried Hofmann, University of Chemnitz
15:15	Coffee break
15:45 - 16:10	**A Modular IGBT Converter System for High Frequency Induction Heating Applications** Peter Mutschler, University of Darmstadt
16:10 - 16:35	**Development of Heater Using Induction Heating Based on a High-Frequency Resonant Inverter** Kee-Hwan Kim, Semyung University
16:35 - 17:00	**Supply and Control of Piezoelectric Systems** Horst Grotstollen, University of Paderborn
17:25	Closure of symposium
20:00	Dinner at Pizzeria la Finestra
June 30, 2004	**Departure of participants**

Electrical Drives in Automobiles – An Overview

Prof. Dr.-Ing. Dieter Gerling
Universität der Bundeswehr München
D-85577 Neubiberg, Germany
Email: Dieter. Gerling@unibw-muenchen.de

Abstract— **Since the very beginning of building passenger cars electrical drives are known in automobiles. Today, more than 120 electrical drives can be found running in a modern passenger car of the luxury class. It is expected that this number will even increase in future.**

This paper will analyze the current status of electrical drives in the automotive industry, and upcoming trends will be described. In addition, some exemplary future applications will be shown to illustrate the challenges and perspectives of this part of the electrical drives industry.

I. INTRODUCTION

Since the very beginning of the automotive business, electrical drives are known being a part of the car. The electrical traction drive, which was in use hundred years ago, was soon substituted by internal combustion engines, mainly because of the poor storage possibilities of the electrical energy (a fact where pure electric vehicles suffer from even today).

A next step was the introduction of some "fundamental" electrical drives like starter, generator, wiper, blower and fuel pump. These electrical drives were realized with brushed DC-motors, and even today these functions are mainly served by conventional DC-motors [1].

Some decades ago, electrical drives started to become one major growing field inside the car. The applications can be clustered into the following sections:

- Comfort (e.g. window lift, mirror and seat adjustment, sun roof).
- Safety (e.g. ABS-motor).
- Drivetrain (e.g. fuel pump, engine cooling fan, electronic throttle plate).
- Traction (e.g. hybrid or fuel cell cars).

In any case, electrical drives have to be adapted carefully to the regarded system to generate an optimum solution. Most often this results in a drive concept which is superior to existing mechanical or hydraulic solutions.

II. CURRENT STATUS

Today, in a modern passenger car of the luxury class, one can find more than 120 electrical drives. Many of these drives are conventional DC-motors (e.g. window lift, seat adjustment, fuel pump, wiper, engine cooling fan, etc.). The main reasons why (for the time being) DC-motors are dominating the electrical drive technology in cars are:

- Costs (simplicity of the motor, existing production facilities).
- Quality (simplicity of the motor, experience over decades in the automotive industry).
- Time to market (new applications can be served by modifying existing ones).
- Functionality is achievable.

Today, the automobile industry is in a phase where more and more electrical drives are used. The main driving forces to the ever increasing number of electrical drives inside a car are:

- The customer desire for safety, comfort and driving pleasure forces the car manufacturer to introduce more and more complex functions, many of them require electrical motors or actuators.
- Legislation due to ever decreasing pollution limits forces the engineers to ever complex drivetrain designs, resulting in more and more electrical components (many of them being drives and actuators).
- Because of the competition between the car manufacturers more functions are introduced for differentiation reasons. In addition the extreme pressure on costs forces the suppliers to realize new solutions.

III. FUTURE TRENDS

A. Future Trends in Drive Technology

In the past, drive technology itself has been stimulated by:

- Power electronics (availability and cost reduction of devices made new drive concepts affordable).
- Microelectronics (ever complex control algorithms can be realized).

- Mathematical modeling (better analytical and numerical models result in better drive designs).
- Materials (new materials like NdFeB magnets or soft magnetic compounds open new possibilities).

These stimulations will further be present, with much influence even on electrical drives in the automotive industry: Drives including electronics (e.g. BLDC-drives instead of conventional DC-motors) will become more feasible.

Today it is estimated that the number of brushless electrical drives in the automotive industry will increase from about 5 million pcs. per year in the year 2000 to about 60 to 70 million pcs. per year (world market) at the end of this decade. Only partly, this new brushless drives substitute existing DC-motors, mainly new functions or existing mechanical functions are realized electrically. Because of the future increased usage of brushless drives, power electronics and microelectronics will become more and more important in addition to motor technology. This future development becomes obvious if the market of mechatronics in passenger cars is analyzed, see the following figure.

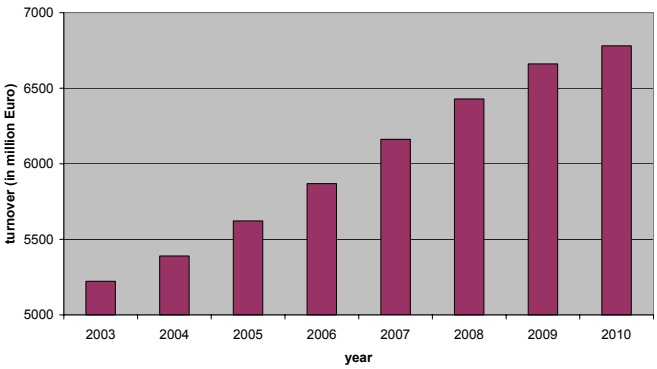

Fig. 1. European market of mechatronics in passenger cars [2].

B. *Economical Trends in the Automotive Industry*

The following figure 2 (based on an evaluation published by "Roland Berger & Partner" consultants) shows that the value-added contained in a today's automobile mainly is produced by the suppliers rather than by the car manufacturers itself. The percentage realized by the suppliers will even increase in future, up to about three quarters at the end of this decade.

For the percentage of the development the same trend is visible, and in the year 2010 the same amount of development will be done by the car manufacturers and the suppliers.

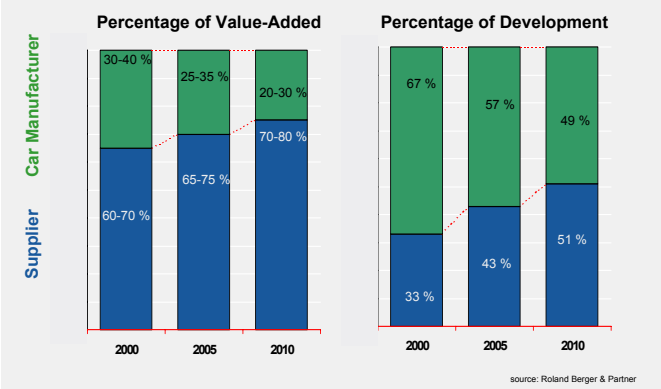

Fig. 2. Percentage of value-added and development of car manufacturer and supplier.

C. *Technical Trends in the Automotive Industry*

The most important technical trend in the automotive industry is that more and more mechanics and hydraulics will be substituted by "mechatronics". Some examples are the electrical throttle plate (avoiding the well-known bowden-cable) and the electrical steering assistance (substituting the belt-driven hydraulic pump). The main challenges are, to realize these functions at least with the same quality level like before and to guarantee low costs.

Miniaturization and integration (like in many sections of the industry) will speed up in future even in the automobile industry. Realizing a small volume with sufficient cooling while guaranteeing low costs are the main working areas.

The ever increasing number of intelligent subsystems requires safe and low-cost communication (hardware and software): the diagnosis of each subsystem will become being a standard.

The belt-less combustion engine is another trend for future passenger cars. With electrically driven auxiliary systems (like water pump and A/C compressor) the power can be easily adopted to the time-dependent required value and is no longer determined by the speed of the combustion engine. Thus fuel economy can be increased and emissions reduced.

If the 42V power net will come for passenger cars, this will have an additional impact. There are some applications, which are only feasible with a higher voltage level than the today's 12V, e.g. the electrical A/C-compressor. In addition, some conventional DC-motors will suffer from the higher inter-bar voltage, resulting in new possible applications for brushless drives.

High-temperature electronics will become more and more a decisive success factor. Because of miniaturization and integration and because of the ever increasing ambient temperature under the hood, there is a very strong necessity to realize electronic systems that can operate at temperatures of 120°C and even above.

IV. EXEMPLARY FUTURE APPLICATIONS

A. *Steer-by-Wire*

Electrical steering systems can be divided in:

- Force assisting systems (like electric power steering).
- Active steering systems, the most advanced of these is the steer-by-wire.

In future, the steering column will be avoided by realizing a steer-by-wire design, with dramatic consequences for the safety concept: The electronics as well as the electromechanics has to be realized redundantly (see figure 3). Beside avoiding space limitations under the hood, further advantages of such systems are:

- Enhanced stabilization of the car by introducing an additional steering angle (see figure 4).
- Variable (e.g. speed-dependent) transmission of the steering angle.
- Suppression of unwanted reactions.
- Improved dynamic steering.
- Reduction of fuel consumption (if the hydraulic pump will be substituted by an electrically driven pump).

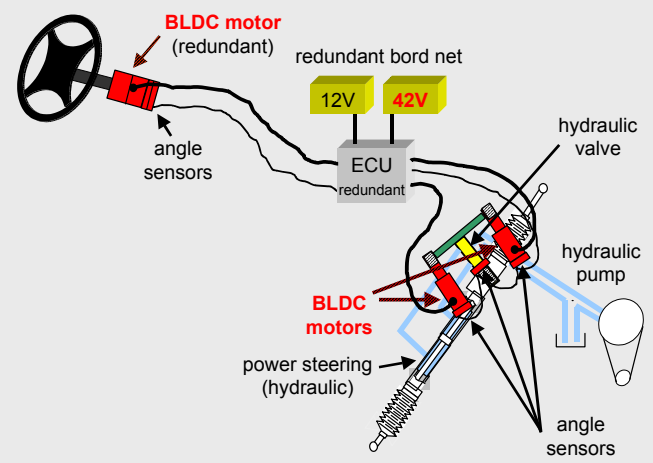

Fig. 3. Concept of a steer-by-wire system.

Braking the wheels of an automobile on a non-homogeneous surface means that different braking forces are acting on the wheels, resulting in a yaw torque for the car (see figure 4). In modern passenger cars, this yaw torque can be eliminated or at least reduced by the ESP-system (i.e. generating different braking forces on each wheel in such a way that the car still moves in the desired direction). A weakness of this system is, that only forces in the driving direction of the car can be generated. If it is possible to introduce an additional steering angle, then we can generate lateral forces, that means forces perpendicular to the driving direction of the car. With this additional degree of freedom the ESP-functionality can be enhanced to more critical driving situations.

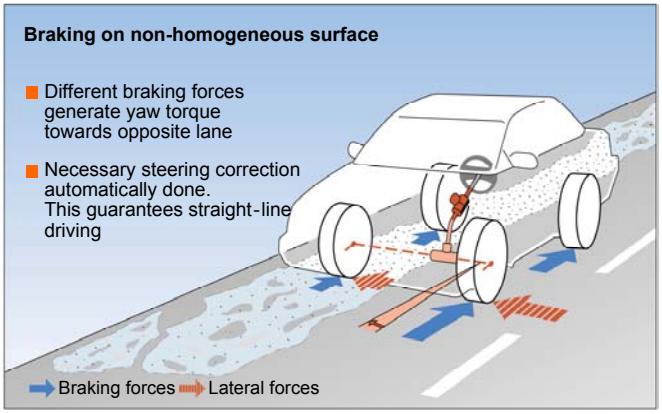

Fig. 4. Braking on non-homogeneous surface.

B. *Electronic Throttle Plate*

Using an electronic throttle plate, the conventional bowden cable will be substituted by electrical transmission of information and an electrical actuator for positioning the throttle plate, see figure 5 for the concept and figure 6 for an exemplary realization.

The main advantages of such an electrical actuator for this application are:

- In addition to the regulation of the power of the combustion engine, it is possible to integrate different functions like idle air control, cruise control and anti-slip-control.
- The emissions can be reduced, because the position of the throttle plate is calculated by the control unit and it is no longer directly determined by the driver. The control unit takes the driver's wish (e.g. for acceleration) as one input signal for the calculation of an optimized position.
- In the same way, improved fuel economy can be realized.
- The installation effort is reduced, because no mechanical bowden cable, but only electrical cables have to be considered to be distributed under the hood.
- Because of the integration of different functions and the reduced installation effort, there could be even an economical advantage on system level (most probably not on component level).
- Last, but not least, the driving comfort can be increased by far. E.g. in situations, where the mechanical throttle plate is opened or closed too far by the driver, this can be eliminated or damped by the control unit when an electronic throttle plate is used.

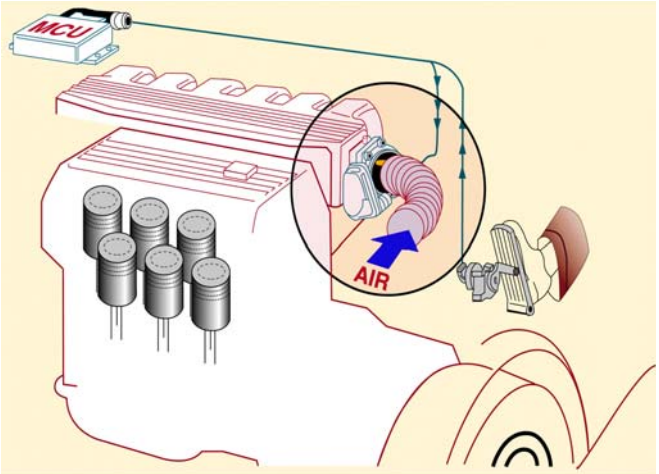

Fig. 5. Concept of the electronic throttle plate.

Fig. 6. Realization of an electronic throttle plate (Siemens VDO).

C. *Startergenerator*

The ever increasing demand for electrical energy forces the automobile industry to introduce a new generator system, because the well-known belt-driven claw-pole generator has its power limit at about 3kW. One solution can be to mount the generator directly onto the crankshaft between the combustion engine and the gear box. If this electrical machine is then additionally used for starting the combustion engine, we have the so-called "startergenerator".

The design of such a startergenerator is quite complex, because this electrical machine has to be optimized for two completely different operating conditions:

- Starting operation (low speed, high torque, short-time operation).
- Generating mode (high speed, high power, continuous operation).

The great advantage of such a startergenerator is that it can be used for fuel economy improvement:

- If moderate braking power is required to slow down the car, this can be realized by regenerative braking via the startergenerator, and the power can be stored in the battery (for higher braking power the realistic size of electrical machine, power electronics and storage capacity make regenerative braking not feasible).
- In driving situations, where the power of the combustion engine is not required (e.g. rolling with idle speed towards a red traffic light or stopping at a red traffic light), the combustion engine can be switched off. Just at that moment, where the power is required, the startergenerator can start the engine without any time-lag.

Investigations exist, where a fuel economy improvement (based on regenerative braking and start-stop-operation) better than 15% for typical driving cycles are published. This is of course a strong motivation to introduce such a new system.

D. *Further Applications*

Today, there is a strong tendency to ever more electrical drives in a passenger car: Water pump, input/output valve actuation, A/C compressor, turbo-compressor, etc. Some of these drives need a higher voltage level than the today's 12V as a prerequisite, because of the high input power (otherwise the currents become too high so that they cannot be handled). The 42V power net could be a solution. Despite the high effort being made by the automotive industry to come to a common definition of this 42V power net, at the time being it is very uncertain, if and when this power net will be introduced. The main reason for this uncertainty is, that the introduction of a new voltage level rises extremely high costs and at the moment nobody (customer, car manufacturer or supplier) is willing or able to pay these additional expenses.

V. CONCLUSION

Coming from the historical evolution of electrical drives inside a passenger car the current status of electrical drives in the automotive industry has been presented.

Stimulated by the general trends in drive technology (availability of new power electronic devices and microelectronics, improved mathematical modeling and new or better materials), the number of electrical drives inside a car increased by far in the last years and will further increase.

The main driving forces for these new applications are: The customer desire for safety, comfort and driving pleasure, the legislation due to ever decreasing pollution limits and the competition between the car manufacturers (new functions are introduced for differentiation reasons).

An economical trend in the automobile industry is that more and more value-added and development is realized by the suppliers rather than by the car manufacturers.

The main technical trends are: Substitution of mechanics and hydraulics by mechatronics, miniaturization and integration, diagnosis (intelligent subsystems), the realization of a belt-less combustion engine, and operation at an ever increasing ambient temperature (resulting in a strong demand for high-temperature electronics). In different applications, some of these trends are mutually dependent.

Looking into some exemplary applications (steer-by-wire and electronic throttle plate), the above mentioned technical trends are demonstrated. It has been shown that microelectronics, power electronics and motor technology have to be adapted carefully to the system to generate an optimum solution.

The technical trends in the automobile industry together with the stimulations being present in drive technology in general will make it happen, that ever complex functions and applications can be realized electrically. Therefore, the market potential of mechatronics in passenger cars is enormous, please refer to figure 1.

REFERENCES

[1] D. Gerling, "Challenges and Perspectives of Electrical Drives in the Automotive Industry", 9th European Conference on Power Electronics and Applications (EPE), 2001, Graz, Austria, CD-ROM proceedings

[2] Frost & Sullivan Report B237 (02/04), published in Automobil Industrie 3/2004 (in German)

Performances of SRM for LSEV Drive

Jin-Woo Ahn
Kyungsung Univ.
Busan, Korea
jwahn@ks.ac.kr

Dong-Hee Lee
Otis-LG,
Changwon, Korea
dhlee@hanmail.net

Abstract – This paper presents an application of SR drive for LSEV(Low Speed Electric Vehicle) which is used for golf and leisure. Two types of 5[HP] SRM and its drive system are designed and tested. In order to have energy saving and effective braking during deceleration, a multi-level inverter is proposed. This is to have a high efficiency drive during braking. For the precise switching angle control, a new type of analog encoder is proposed. A current control is adopted for a soft starting and an angle control in a high speed range for efficiency. Drive characteristics and performances are shown with test results.

Keywords - Switched Reluctance Motor, Traction drive, Multi-level inverter, Analog encoder, Angle control, Current control

1. Introduction

Nowadays, exhaust control is more consolidating all over the world because of serious air and environmental pollution. Strenuous efforts have been made for a long time. For these reasons, some motor companies developed HEV(hybrid electric vehicle) which has mechanical engine and motor drive with battery. And an EV which use only battery and motor drive is being also widely developed. Actually, the pure EV has higher energy efficiency than engine or HEV and an advantage for reduction of air pollution. Although The EV system has a high cost of battery and lack of charging infra, various EVs are being developed for leisure and medical care.

Because of reliability and mechanical strength, brushless type motors such as induction and permanent AC motors are much considered as EV traction. Recently SRM(switched reluctance motor) is being investigated for EV application due to a mechanical strength and cost advantages.[1] The SRM is a simple, low-cost, and robust structure suitable for variable-speed and traction applications.[2]. In addition, the SRM has high power-to-weight and torque-to-weight ratio and a wide speed range and excellent starting characteristics. Therefore it is fitted for traction drives such as electric car which is frequently stopped and started.

In this paper, The SRM drive system is studied for LSEV used for leisure and golf. First, in the restricted space and dimensions, design of the motor is implemented to satisfy the requirements. From a CAD and a FEM analysis of efficiency and output characteristics according to the rotor and stator structure, detailed design parameters are determined.

In order to have an effective regeneration at deceleration and braking, a novel multi-level inverter is introduced. The proposed multi-level inverter is suitable to excite and demagnetize a phase rapidly. And, a single-pulse exciting method is introduced to prevent the decrease of efficiency and torque at the light load.

In addition, a new low-cost analog encoder for precise switching angle control suitable for this drive is presented, in which the switch on-off angle is controlled with a simple circuit. In the proposed switching technique, the resolution of switch on-off angle, different from the general methods, is not affected by the sampling period of a microprocessor and the speed of a motor; hence, the on-off switching angle control can be always carried out at any desired positions.

2. Configurations of LSEV and Specifications

Fig. 1 shows the configuration of LSEV concerned in this paper. This configuration is simpler than that HEV because engine control system is not required. The main power source is battery which is controlled by a BMS(battery management system) and battery charger, and regenerative energy is returned back to a battery during braking and deceleration.

It has rear drive system which has a 10 : 1 gear box to transfer the driving power from the motor to wheel shaft. The maximum speed is 40[km/h] at street mode and 20[km/h] at golf mode.

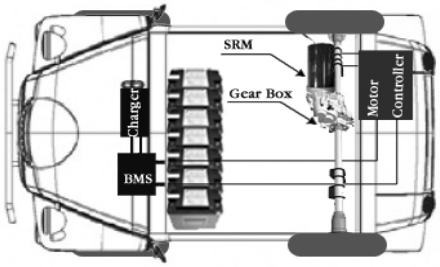

Fig. 1 Configuration of LSEV system

The required maximum speed of the motor can be easily obtained from the maximum speed as follow.

$$\omega_{rm\_\max} = \frac{LSEV\ Speed \cdot \eta \cdot 1000}{2\pi \cdot D \cdot 60} \qquad (1)$$

where, LSEV Speed : required maximum speed [km/h], η : gear ratio, D : diameter of wheel[m]

In this application, the motor speed to satisfy the drive speed is about 3600[rpm]. Table 1 shows the specifications of the motor for LSEV.

Table 1. The specification of SRM for LSEV

Output power	3.5[kw] continuous, 9[kw] 2minutes
Voltage	72[V] (50 ~ 90[V])
Torque	10[Nm] at 4000rpm, 22[Nm] at 2000rpm
Weight	16[kg] below
Size	180[mm] × 190[mm] below
Insulation	H grade
Cooling	Air cooling
Efficiency	80% over

The size and weight of the motor drive system are restricted by vehicle space and the supply voltage is determined by the battery.

3. Design of Motor for LSEV

3.1 Basic principle

The SRM is a doubly salient, singly excited machine and the developed torque is produced by the reluctance variations. The torque is proportional to the square of switching mmf current and the gradient of phase inductance according to rotor angular position as shown in (2).

$$T(\theta,i)=\frac{\partial W(\theta,i)}{\partial\theta}=\frac{1}{2}\frac{\partial L(\theta,i)}{\partial\theta}i^2 \qquad (2)$$

where i denotes a phase current and $L(\theta)$ is a nonlinear inductance profile as a function of angular rotor position.

The instantaneous voltage equation depends on nonlinear winding impedance and phase current as follow.

$$V(\theta)=R\cdot i(\theta)+L(\theta)\frac{di(\theta)}{d\theta}+i(\theta)\frac{dL(\theta)}{d\theta} \qquad (3)$$

where the first in the right terms is resistance voltage drop, the second is reactance voltage drop, and the last is the back speed *e.m.f* which can be converted to mechanical energy. In the instantaneous voltage equation, a phase current for torque production depends on a winding impedance, a speed e.m.f., a switching-on/off angle and an applied voltage. The first and second factors depend on the motor and operating speed. The third and last factors can be adjustable in the controller with proper control algorithm. Therefore, The design parameters of the motor are determined with the restricted supplied voltage and rated speed in the actual application. And the advance angle and applied voltage could be controlled appropriately to have a stable and high efficiency drive.

3.2 Comparisons of Design Results

Although there are some advantages of SRM, the actual application is much restricted because of acoustic noise and mechanical vibration. The design specifications have some requirements such as torque and speed, and restricted term such as supply voltage and dimensions. The design process of SRM is different from that of conventional DC and AC motors. Because SRM uses reluctance torque and the characteristics are differ greatly according to the selection of stator and rotor poles.

The general combinations of stator and rotor pole arrays are 6/4, 8/6, 12/8 and 16/12. However 8/6 and 16/12 SRM are not preferred for LSEV application because of the complexity of four-phase inverter and cost. In this paper, the characteristics of 6/4 and 12/8 SRM are compared and tested.

Fig. 2 and 3 show the FEM analysis and comparison of 6/4 and 12/8 SRM according to stator and rotor pole arc, stroke angle(ε_0), and yoke ratio. The analysis results show that the torque and efficiency of 6/4 SRM are higher than that of 12/8 SRM.

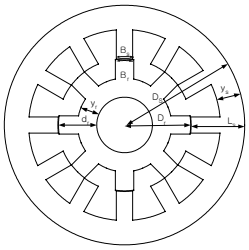

(a) Motor notations

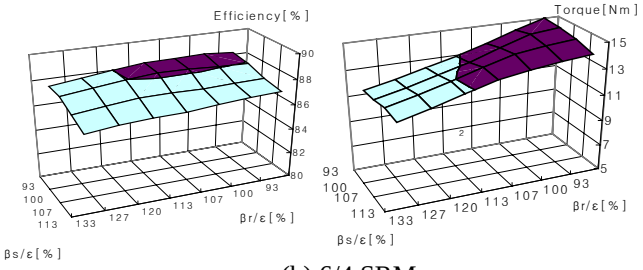

(b) 6/4 SRM

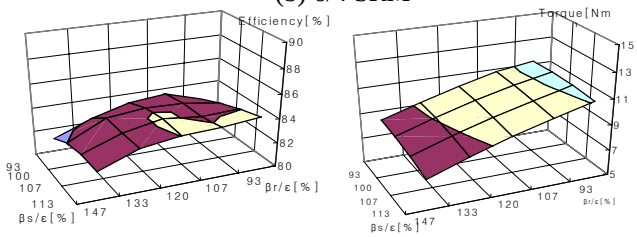

(c) 12/8 SRM

Fig. 2 Performance comparisons of FEM analysis according to rotor and stator pole arc

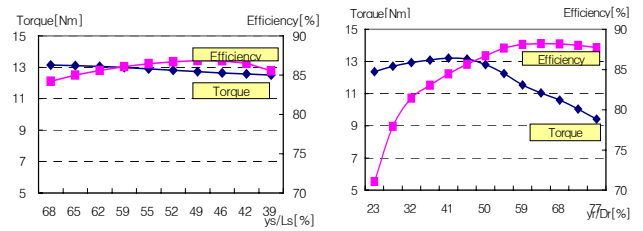

(a) Torque and efficiency of 6/4 SRM

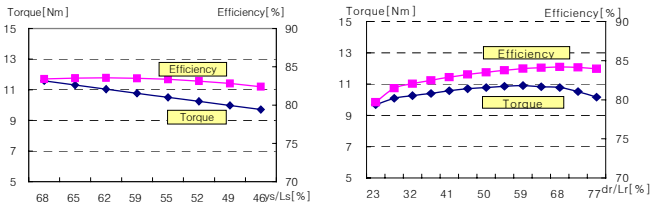

(b)Torque and of 12/8 SRM

Fig. 3 Performance analysis according to rotor and stator yoke

Fig. 4 shows the simulation result of acoustic noise of 6/4 and 12/8 SRM. The acoustic noise of 12/8 SRM is lower than 6/4 SRM because torque ripple and rebounding force of 6/4 SRM is higher than that of 12/8 SRM at the switching off instant.

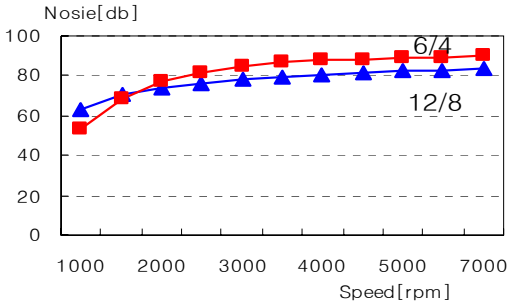

Fig. 4 Simulation result of acoustic noise

From the analysis, the final dimensions are determined with the satisfied conditions of requirements. Table 2 and Fig. 5 show the detailed design parameters which are from the analysis of characteristics according to the parameter variations.

Table 2. Design parameters of the prototype SRM

Motor	6/4	12/8	Motor	6/4	12/8
Ns	6	12	Nr	4	8
Stator pole arc [deg]	34	14	Rotor pole arc [deg]	36	16
Dia. Stator[mm]	138	138	Dia. Rotor[mm]	76	76
Stator yoke[mm]	14	16	Rotor yoke[mm]	9	11
Airgap[mm]	0.25	0.25	Stack length[mm]	100	100
Turn per phase[mm]	11	20	Dia.Conducor[mm]	1.9	1.7

Performances of 12/8 SRM are better than those of 6/4 SRM in the view of torque ripple and acoustic noise. However, 6/4 SRM are better in view of torque and efficiency characteristics.

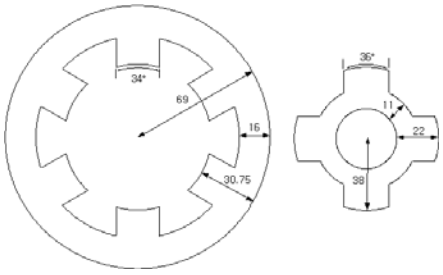

(a) 6/4 SRM

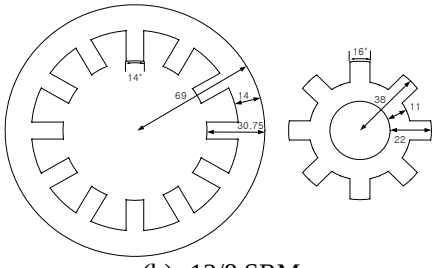

(b) 12/8 SRM

Fig. 5 Cross sectional dimensions of prototype SRM

Fig. 6 shows the photograph of prototype 6/4 and 12/8 SRM. In order to verify the effectiveness of the proposed SRM system in LSEV application, the prototype 6/4 and 12/8 SRM with analog encoder and multi-level inverter is tested.

Fig. 6 Prototype 6/4 and 12/8 SRM

For the switching angle control, 2-channel, 10bit D/A converter and TMS320F241 DSP controller are used. The calculated switching-on angle as a digital data is out to the a channel of D/A converter as an analog data, then the switching-off angle is out to the other channel of D/A converter.

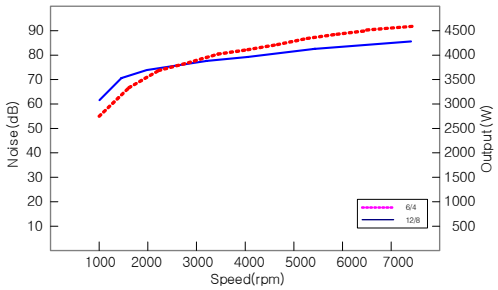

Fig. 7 Acoustic noise measurement of prototype SRM

Fig 7 shows the measured acoustic noise comparison of prototype SRM. As shown in Fig. 7, experimental result shows that higher acoustic noise in 6/4 SRM than in 12/8 SRM.

Fig. 8 shows measured efficiency of prototype SRM according to speed and exciting angle. From the FEM analysis, the efficiency of 6/4 SRM is higher than that of 12/8 SRM.

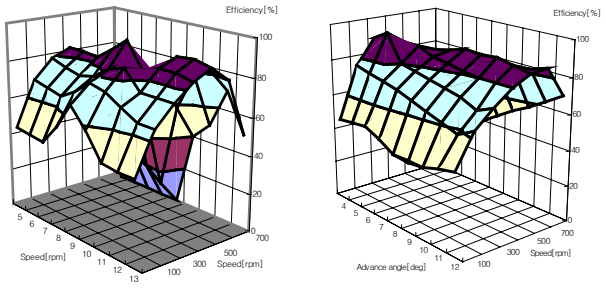

(a) 6/4 SRM (b)12/8 SRM

Fig. 8 Comparison of efficiency according to speed and exciting angle

4. The Multi-level Inverter

4.1 Excitation Control

For the proper application of SRM to a LSEV, a high performance and a stable inverter system is required. The

classic inverter is very simple and effective but the control of the regenerative mode is not easy. The regeneration is essential in the EV application because of energy efficiency and dynamic braking in deceleration operation.

In this paper, a multi-level inverter topology is proposed to magnetize and demagnetize quickly in the motoring and regenerative mode with flat-topped current. Fig. 9 shows the proposed excitation voltage level in the motoring and regenerative mode. The high C-Dump voltage is used to build-up current quickly and to extinguish current fast when the switch-off occurs and also to build-up generating current quickly.

When SRM is operated in single-pulse mode in regenerative mode, it is difficult to develop the rated output. A discontinuous PWM mode is used to improve regenerative power.

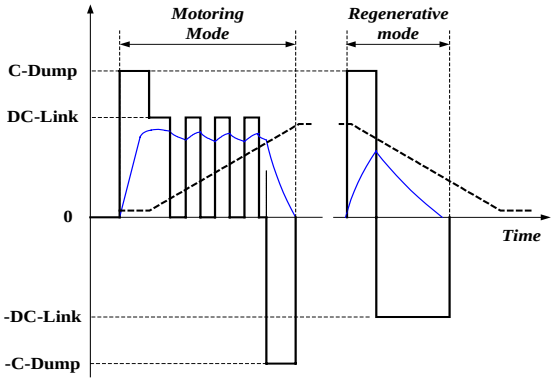

Fig. 9 5-level excitation voltage control

In order to satisfy these conditions, a circuit is proposed as shown Fig. 10, which is able to impress a high voltage for building-up current and a source voltage for motoring and regenerative operating.

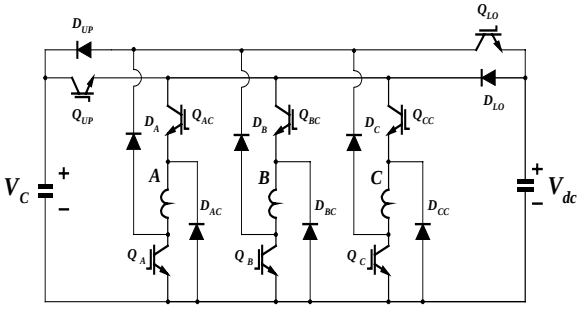

Fig. 10 The proposed 5-level inverter

The operations can be separated into four modes and the circuit of each mode is shown in Fig. 11.

(a) *Mode 1* :

When $Q_{UP,}$ Q_{AC}, Q_A is switched on, the capacitor voltage is impressed on phase winding. The high C-dump voltage which is charged in the capacitor, is used effectively to quickly build up phase current in motoring mode without excessive advanced angle for proper flat-topped current.

(b) *Mode 2* :

When Q_{AC}, Q_A is switched on, the D.C. link voltage is impressed on phase winding. When the phase current is PWM controlled, the higher C-dump voltage is not good for smooth current control. This mode is proper for current control method.

(c) *Mode 3* :

When Q_A is switched on, a commutation circuit is consisted by diode D_A such that zero voltage is impressed on phase winding. This mode is proper for current control method.

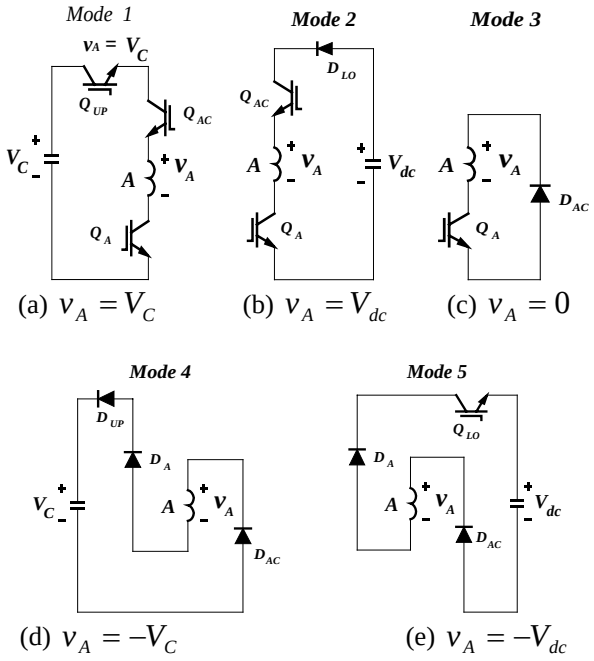

Fig. 11 Operation modes of the proposed 5-level inverter

(d) *Mode 4* :

When switch is turned off completely, the circuit is consisted by diode $D_{UP,}$ D_A, D_{AC} such that the opposite polarity of capacitor voltage is impressed on phase winding. The high negative C-dump voltage is effective to extinguish current fast when the switch-off action.

(e) *Mode 5* :

When Q_{LO} is switched on, the negative sign of the source voltage is impressed on phase winding. And the recovery energy is transfer to the side of the source.

The operation of this circuit is able to be selected by switch Q_{LO} from source and C-Dump voltage and in the regenerative region, though the regenerative is lasted for a long time, the recovery energy is transferred to the source without chopper. This is different from a conventional method of a C-Dump circuit.

In the proposed control method, the fast response has the same characteristic as the delta modulation method and it can operate as a constant switching frequency.

4.2 Switching Topology of Multi-level Inverter

With the proposed multi-level inverter, an additional freewheeling mode is added to achieve a near unity energy conversion ratio which is very effective under the light load. The stored energy of a motor is not recovered to the source but transferred as mechanical power that is generated by phase current and back-emf. If the increasing period of inductance is

sufficiently large compared with the additional mode, the stored field energy in inductance can be entirely converted into mechanical energy; then the energy conversion ratio approaches to unity.

Fig. 12 shows a graphical analysis of the field energy conversion process of the conventional method and the proposed switching method with a multi-level inverter.

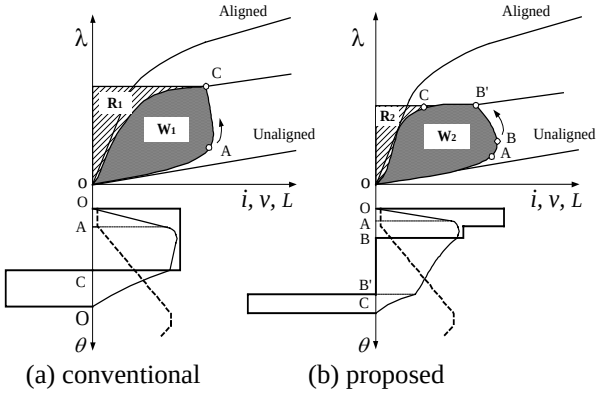

(a) conventional (b) proposed

Fig. 12 Energy conversion process

Under an unaligned position, during the current build-up period both methods show an equivalent path for energy conversion between ***O*** and ***A***. But during other modes because of an additional wheeling period, it forms path ***B'C*** resulting in a considerable increase to the energy conversion ratio. While in the case of the conventional, the path follows ***AC***. In path ***B'C***, the stored energy in the field is transferred as a mechanical output. And the total flux linkage maintains a near constant form, because the decrease of the current can be compensated for the increase of the inductance. The path ***CO*** shows a demagnetizing mode. The proposed wheeling mode converts the field energy into the mechanical one without returning to the source. An additional wheeling mode can enlarge the field energy region converted to a mechanical output; therefore, a reactive power will be decreased.

Fig. 13 shows the experimental waveform of phase current and flow through the energy recovery capacitor in multi-level inverter.

It was tested on steady-state under the command speed 4000[rpm] at rated load. From the experimental results, magnetizing, wheeling and demagnetizing periods appear at approximately 7 10°, 20° and 5°, respectively. As shown the experimental result, to obtain a fast demagnetizing, high excitation voltage is applied, and the recovered capacitor voltage is used to settle current rapidly. Its displacement is proportional to the recovered energy.

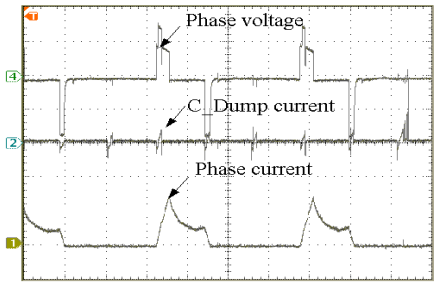

Fig. 13 Voltage and current waveforms of proposed inverter

Fig. 14 shows the capacitor voltage, phase voltage and current in regenerative mode.

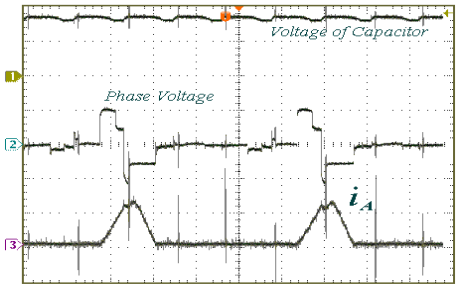

Fig. 14 Voltage and phase current in regenerative mode

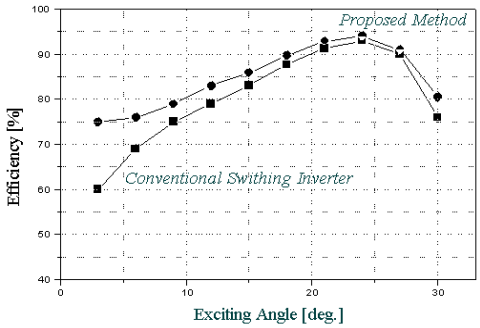

Fig. 15 Comparison of efficiency according to the switching method

Fig. 15 shows the efficiency comparison of conventional and the proposed switching method in case of 6/4 SRM. When the excitation angle is small, considerable efficiency improvement is possible. The proposed wheeling mode is effective under a light load shown as Fig. 15.

With the increase of exciting angle, the proposed method has almost same efficiency as that of the conventional because the wheeling period is small.

5. Analog Encoder for precise angle control

5.1 Conventional Encoder

In general, an optical encoder which has a digital pulse signal is much used in motor control systems because of its high performance, easy treatment of data and programming of controller. The information of rotor position and speed is obtained in a control period by the digitalized encoder such as incremental and optical encoder.

However, general optical encoders, such as incremental and absolute type are not suitable for SRM systems because of cost and harsh operating environments such as mechanical vibration and high speed. These days, high resolution serial absolute encoders are being considered to industrial applications. But, the cost is much higher and the maximum operating speed is limited to 8000[rpm] generally.

For these reasons, a simple disk plate encoder with optical sensor is used in SRM system shown as Fig. 16.

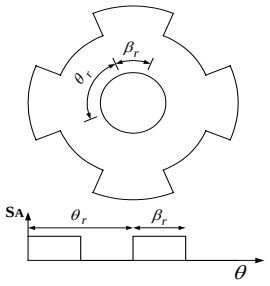

Fig. 16 A simple optical encoder disk and sensor signal

The structure of the optical encoder is very simple and low cost but the high resolution switching angle control is very difficult. The switching-on and off angle are to be calculated from all of the rising and falling edges of the optical encoder signals. The accuracy of calculated switching angle depends on microprocessor and rotor speeds. In this case, a simple PWM method is adopted for torque control and high frequency switching increases switching losses.

5.2 Proposed Analog Encoder

In order to control an accurate switching angle, a high resolution encoder and a proper control method are essential. This paper proposes a new type of encoder for switching angle control. The proposed encoder is simple but high resolution switching control is possible.

Fig. 17 shows the proposed analog encoder for 6/4 and 12/8 SRM respectively. The output signal of a proposed encoder is an analog signal that is proportional to a gray gradation of the plate while is digital signal in conventional encoder such as incremental and optical encoder. The gray gradation of the disk plate is set for the linear analog signal of photo transistor. The output of the photo-transistor is a triangular wave, which is the function of the position angle; therefore, the rotor position of the SRM can be obtained by the output voltage of the photo-transistor.

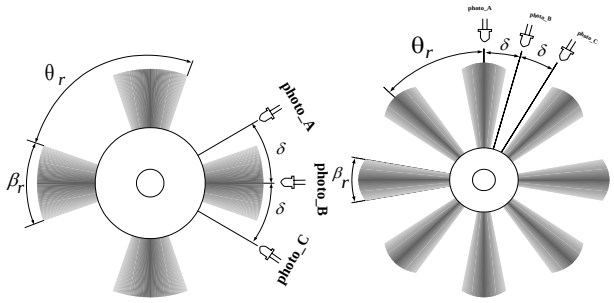

(a) 6/4 SRM (b) 12/8 SRM

Fig. 17 Disk plate of the proposed analog encoder

The interval between gradated pattern is determined by the number of rotor poles N_r as follows.

$$\theta_r = \frac{2\pi}{N_r} \text{ [rad]} \qquad (4)$$

And the minimum angle of a gradation is determined by the continuous torque production as follow.

$$\beta_r \geq 2\frac{2\pi}{N_s N_r} \text{ [rad]} \qquad (5)$$

where, N_s and N_r denote the number of stator and rotor poles, respectively. In Fig. 17, sensor interval δ denotes the phase intervals of SRM. Therefore, δ is 15° in 8/6 and 12/8 and 30° in 6/4 SRM.

Fig. 18 shows the output signal of the proposed encoder according to the inductance profile. The dip point θ_o of the output signal is the center point of the maximum dwell angle β_r of the proposed encoder. The advance angle θ_a and delay angle θ_d are determined by the excitation voltage, rated current and motor parameters. In the motoring mode, the switching-on angle is set on the negative slope of output signal between θ_a and θ_o. Similarly, a switching-off angle can be set on the positive slope of the output signal between θ_o and θ_d. The end of the negative and positive slopes of the encoder signal has step shape for limitation of excitation interval in the maximum dwell angle β_r.

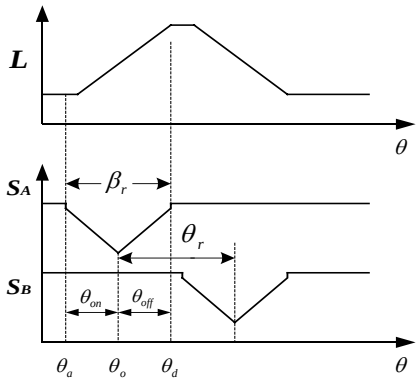

Fig. 18 Inductance profile and encoder signal

With the proposed simple encoder, very accurate switching angle control can be obtained without any high performance microprocessor.

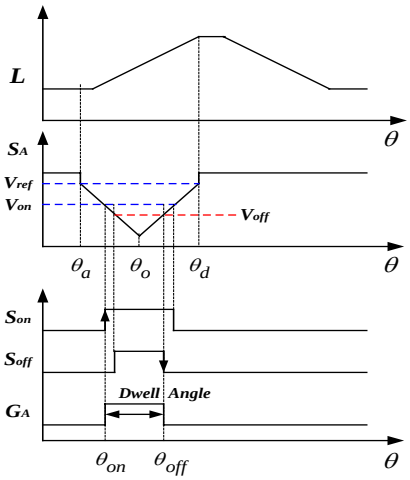

Fig. 19 Switching angle control of a phase

5.3 Switching Angle Control Topology

Fig. 19 shows the principles of switching angle control topology with the proposed analog encoder. According to the motor speed and load condition, proper switching-on angle θ_{on} and switching-off angle θ_{off} can be controlled independently by the command signal V_{on} and V_{off}, respectively. The advance

angle θ_{on} is set at the cross point of the negative slope of the sensor signal, and the switching-on command signal V_{on} as follow.

$$\theta_{on} = \left(1 - \frac{V_{on}}{V_{ref}}\right)(\theta_o - \theta_a) + \theta_a \tag{6}$$

The maximum switching-on angle is in the minimum inductance region, so fast building-up of current is possible at the rated load. And the minimum switching-on angle is in the increasing region of inductance, so smooth building-up of current is possible at a light load with a smooth torque production.

Similarly, the delay angle θ_{off} is set at the cross point of positive slope of the signal and switching-off command signal V_{off}.

$$\theta_{off} = \frac{V_{off}}{V_{ref}}(\theta_d - \theta_o) + \theta_o \tag{7}$$

And the dwell angle is the interval of switching-on and off angle.

$$\theta_{dwell} = \theta_{off} - \theta_{on} \tag{8}$$

Fig. 20 shows the sensor signal, switching-on reference, switching signal and phase current. The waveform of phase current is determined by the sensor signal and switching command at 1750[rpm].

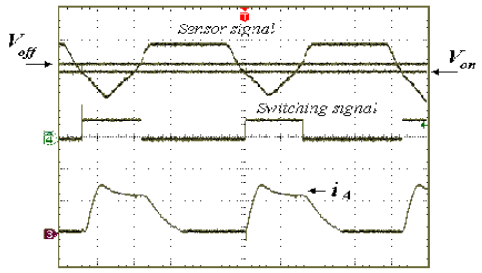

Fig. 20 Encoder, switching signal and phase current

Fig. 21 shows the switching angle adjusting and phase current according to load variation in the proposed encoder and control system at 2000[rpm]. Switching angle is increased by the changing of the switching-on reference. With a sudden load variation, the switching angle can be controlled properly, so a smooth torque production is possible. The experimental results show the effectiveness of the proposed encoder and control method.

6. Conclusions

This SRM drive system for LSEV application is designed with a new analog encoder and multi-level inverter. In the design process of prototype SRM, the parameters are determined from CAD and FEM analysis results according to rotor and stator factors.

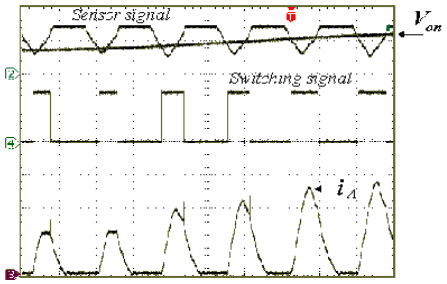

Fig. 21 Encoder signal and current with increasing of load

The motor is designed to have a high efficiency and low noise characteristics. Two types of prototype motor are designed and tested. A 12/8 motor is good in view of low noise, while 6/4 motor is good for power and efficiency point.

For the switching angle control, a low cost and simple structure but high performance analog encoder with proper control method suitable for the practical and stable drive is proposed. The proposed encoder uses a simple structure of optical encoder and analog gradation for high resolution of rotor position. The switching-on and off angle control can be easily implemented by a separated command signals of switching-on and switching-off.

In addition, a five-level inverter is used to be able to build-up and extinguish phase current quickly. A high level of demagnetizing voltage is used to prevent a divergence of phase current during the regenerative mode. Also, current level control is unsuitable. The peak current controller is proposed to be able to improve the transient response and keep the switching frequency constant. The regenerated energy is used effectively because the motoring interval is minimized and the regenerative interval is increased relative to the motoring interval.

From the experimental results, the effectiveness of the proposed system with a proper control method is verified.

REFERENCES

[1] R. B. Inderka, M. Menne, R. DeDoncker,"Contol of Switched Reluctance Drive for Electric Vehicle Applications", IEEE Trans. Power Electronics, vol. 49, no. 1, pp. 48-53, 2002.

[2] P. J. Lawrenson, J.M. Stephenson and P. T. Blenkinsop et al, "Variable-speed Switched Reluctance Motors", IEE Proc. B, vol.127, no.4, 1980, pp.253-265.

[3] J. W. Ahn et al, "Novel Encoder for SRM Drive with High Resolution Angle Control", Proceedings of IEEE/ISIE 2001, pp. 1781-1785, 2001.

[4] J. W. Ahn et al, "High Energy Conversion Strategy of SRM with Single-pulse Switching", Proceedings of IEEE/ISIE 2002, pp. 695-700, 2002.

[5] C. Wu and C. Pollock, "Analysis and Reduction of Vibration and Acoustic Noise in the Switched Reluctance Drive", IEEE Trans. Industrial Applications, vol. 31, no. 1, pp. 91-98, 1995

Hybrid Cars - Design, Optimization and Control

Dierk Schröder
Institute of Electrical Drive Systems
Technical University of Munich
Arcisstr. 21, D-80333 Munich, Germany
Phone +49 89 289 - 28357, Fax +49 89 289 - 28336
E-Mail: dierk.schroeder@ei.tum.de

Abstract— **The paper presents new methods for the optimization of powertrain control at a parallel hybrid vehicle. An offline optimization was developed for fundamental research and allows to find the optimum time behaviour of control and the minimum possible fuel consumption. The paper will discuss computed results and compare them to a normal passenger car. To approach the results at realtime control, a new method for online optimization was found. The optimization derives the control from a special online objective which considers the driveline's efficiency as well as the problem of latching electrical energy. The online method can be applied both for simulation and for the control of the vehicle and considers the emission aspect. The emission aspect of the hybrid vehicle was studied by a direct comparison of the behaviour of diesel engines at hybrid "pulse" operation versus conventional operation in a reference vehicle. For the simulation of a TDI system, a mean value model for the engine, a heat transfer model for the exhaust system and a model for the reaction kinetics in the catalyst were developed. For the actually integrated TD engine, the study was realized by measurements at a test stand.**

I. THE HYBRID POWERTRAIN

A. The TUM's Autark Hybrid Vehicle

The Autark Hybrid is a parallel hybrid electric vehicle with a continuously variable trans-mission gear. The construction of this vehicle is organized in a special research project, SFB 365. A conventional passenger car, an Opel Astra Caravan, is used as substructure. The structure of the new powertrain with combustion engine (CE), the parallel electric motor (EM) and the continuously variable transmission gear (CVT) is depicted in Figure 1.

The integrated combustion engine is a conventional 1.7 l turbo diesel (TD) with a maximum power of 55 kW. The electrical drive consists of a high speed induction motor with a converter. It is connected by a 3:1 gear transmission to the input shaft of the CVT. For electrical power storage, a NiMH traction battery is implemented with a nominal voltage of 120V and a capacity of 52 Ah. The large capacity was supplied for electrical propulsion in urban areas, but would not be necessary for optimal hybrid operation. The continuously variable transmission is an i^2-gear: by an internal set of clutches, the transmission unit can be used twice to realize an extremely wide range of gear ratios. At the synchronous switching point between range 1 (start up) and range 2 (overdrive) of the i^2-gear, it is possible to transmit the torque by integrated cogwheels to improve the transmission efficiency [11].

B. The fundamental problem of hybrid operation

For zero emission driving in urban areas or when driving at a low level of speed, the vehicle can be propelled electrically while the CE is disconnected from the powertrain by the engine clutch. Also, the vehicle can be braked electrically to recover a high percentage of kinetic energy. At medium speed and power request, the powertrain is run at "hybrid operation", and both the CE and the EM are enabled. The CVT gear is used to constantly hold the combustion engine's speed on low level, ideally below 2000 rpm. As shown in Figure 2, the electric motor can increase the CE's load by shifting the point of operation towards the area of good specific fuel consumption. In this case, the EM would operate as a generator and charge the traction battery. The EM's torque in Fig. 2 would be negative. The energy is stored for electrical propulsion in later periods and for the supply of the electrical load circuits. The traction battery is charged either at regenerative braking or when power is transmitted from the CE to the EM. Since the battery's state of charge is managed by the operation of CE and EM to be self-sufficient, the vehicle is called "Autark Hybrid".

As known from optimization results, the threshold from electric to hybrid operation amounts up to 8 kW of demanded driving power and depends on many factors, e.g. the battery's state of charge, the vehicle's speed, the CE's state of operation and the different efficiency behaviour of the powertrain's components. The amount of electrical load increase would depend on the same factors.

On the one hand, a significant load increase of the CE's torque enables an operation near the point of best efficiency. But therefore, a large amount of electrical power would be generated and had to be stored in the traction battery. To avoid an overloading of the battery, the CE would have to operate only for short term periods, and the vehicle would be propelled electrically at the rest of time. On the other hand, the losses of latching electrical power can be reduced by longer terms of the CE operation with less load increase, but also less efficiency. In principle, the optimization of fuel consumption leads to a trade off between the CE's efficiency and the losses of electrical power storage. Besides the constant data, it is influenced by time dependent factors like the battery's SOC or the CE's state of operation.

At high speed, typically above 70 km/h, it is preferable to use only the CE for propulsion. To smooth peaks of high torque request, the EM can support the CE by short term

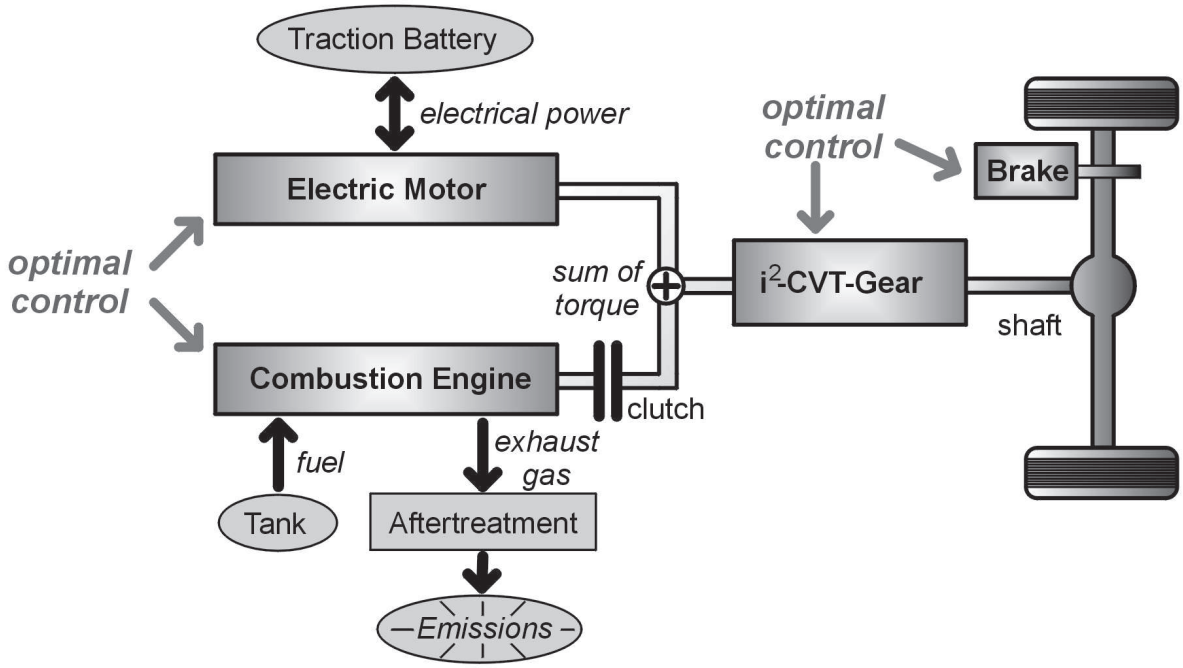

Fig. 1. Structure of the TUM's Autark Hybrid Vehicle

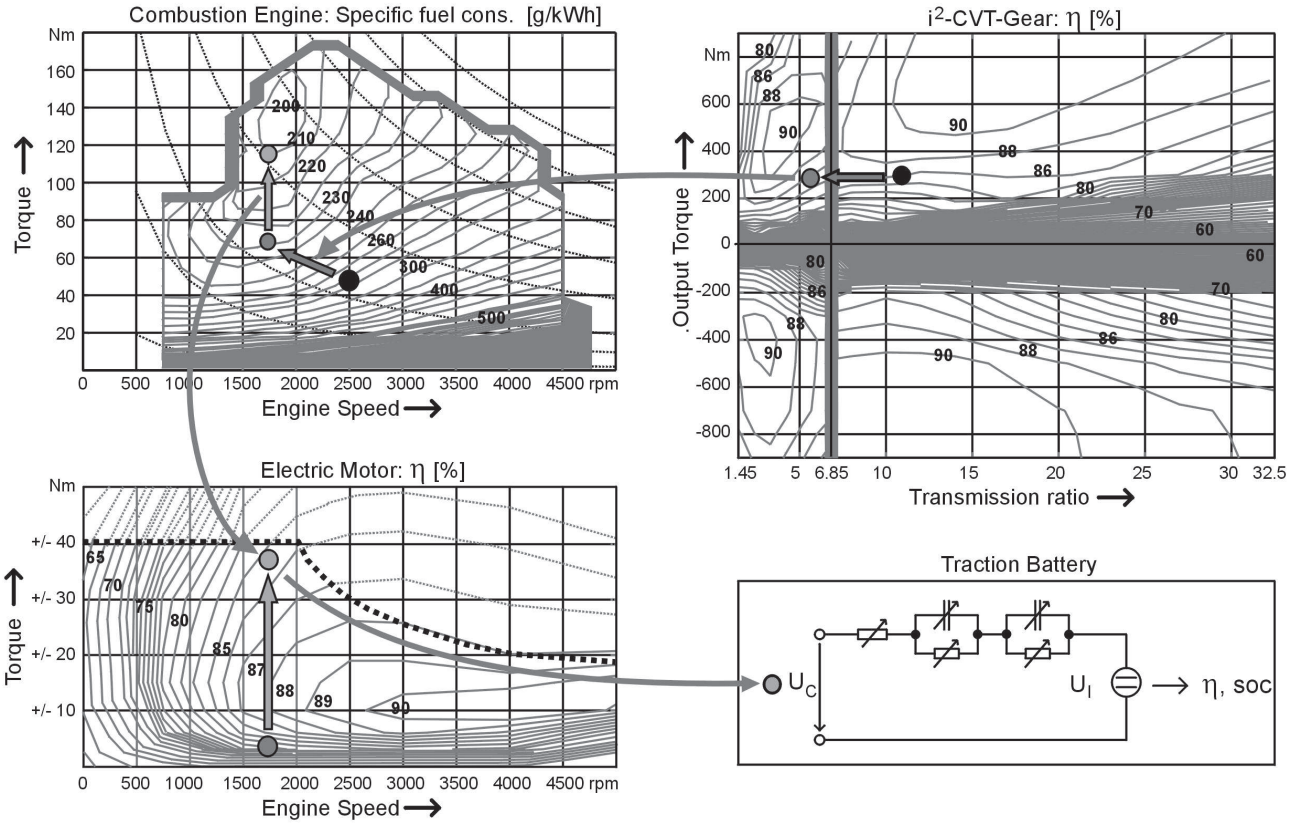

Fig. 2. Electrical load increase and low engine speed at hybrid operation

boosting. Even here, the CVT's overdrive range allows to hold the engine speed on a low level.

II. Optimization of powertrain control

A. The offline optimization method

For the fundamental study of optimal design and control of the powertrain, the target was set to directly calculate the optimal time behaviour of the powertrain's control using optimal control theory. Therefore, an offline method with a dynamic optimization tool for the solution of optimal control problems named DIRCOL [10], [12] was utilized. The control vector of the powertrain could be calculated directly in dependency on the driveline's physical behaviour and a given driving cycle. The features of the driveline and its components as well as the system's constraints and conditions were adapted automatically by the optimization process. For the use of optimal control theory, a problem formulation in state space had to be found. The most important equations and variables are listed below. The efficiencies η and the specific fuel consumption be_{CE} are given by maps which depend again on the state variables. The driving cycle is given by time dependent curves for the wheel's angular velocity ω_2 and its derivation. A more detailed description of the optimization method and first results can be found in [6] and [7].

The hybrid's model is formulated by state equations for the component's time behaviour and an equation constraint for the dynamics of the driveline including flywheel effects of the CVT. In addition, constraints for the operation range limits of the CVT, the CE and the EM, switching conditions (e.g. if the CE's clutch is open or closed) and bounds of the variables are specified. The most important boundary condition of the system is the condition of an equalized state of charge of the traction battery: the given value for initial time has to be met again at the final time of the cycle. After the optimization, the curve of the control vector was set as input of a Simulink forward simulation model to analyze the power train's behaviour. From the analysis of the results, the following basic information about hybrid operation was obtained:

- The minimum possible fuel consumption at an exactly equalized state of charge
- The shape of optimal control and the system's behaviour [5]
- The influences of different component ratings on efficiency and control
- The flat minimum, caused by the trade off between load increase and storage losses [6]

B. Results from the offline optimization

The offline optimization was applied to compute results for the optimal powertrain behaviour of the Autark Hybrid with different combustion engine types and varied sizes of the electric motor. In Figure 3, the results for hybrid control at the the New European Driving Cycle (NEDC) are depicted. The combustion engine was the original TD diesel motor. The limits of the EM were fixed to its rated power of 8 kW and a maximum torque of 40 Nm. At the low speed part of the cycle (4x ECE-Citycycle), this rating of the electrical engine is sufficient for regenerative braking. At the high speed part, which is also known as Extra Urban Driving Cycle (EUDC), a power up to 20 kW would be necessary for electric braking. Because of the EM's limit, a fourth control variable for an addtitional mechanical brake was implemented in the model to support the EM.

The dimension of a dynamic optimization problem depends on the duration of the given time period and is restricted by a maximum number of discretization points. For this reason, the whole cycle had to be subdivided into sections which were optimized separately. The results for control were put together for the forward simulation of the whole cycle. As it can be seen from the first plot of Figure 3, the simulated velocity exactly meets the curve of the original driving cycle. In the second plot, the time behaviour of the engine torques T_{CE} and T_{EM} are depicted. The CE is run in "pulse operation". The engine operates only at periods, when high propulsion torque is demanded at acceleration or high speed. In this case, the EM's torque is negative (except for the period of high speed) to increase the CE's point of operation. At periods of low driving resistances, the torque of the CE reaches zero level, and the vehicle is propelled electrically. In this case, the CE is disabled and the clutch is opened. The behaviour of the brake is indicated by the dotted curve, but is not scaled. The maximum value at the end of the cycle would reach 450 Nm at the shaft.

The third plot shows the behaviour of the gear ratio i_{CVT} and the engine speed N_1. When the CE operates, the engine speed is held on low levels, and the CE operation accords to the considerations indicated in Figure 2. At the beginning of some braking periods, when the vehicle is decelerated to a lower level of velocity, high gradients of gear ratio and engine speed occur: the flywheel effects of the CVT are utilized to brake and to latch energy for a short time. The dotted line in this plot indicates the synchronous point at a gear ratio of 6.85. It is reached mainly at electrical propulsion. At the standstill periods, the CVT reaches its maximum gear ratio of 32.5 to provide maximum torque for the next startup.

C. The online optimization method

The basic condition for an online optimization control is the implementation into the vehicle's main controller. As depicted in Fig. 4, the desired engine power P_{Eng} is determined by the interpretation of the driver's request and is given to the optimization and to the main driveline controller. Dependent on this power, the optimization has to find the optimum values for the engine speed $N_{Eng,opt}$ and the CE's torque $T_{CE,opt}$. The torque of the electric motor T_{EM} is given implicitly by the static balance of power at the CVT-gear's input shaft. Because the controller has to compensate the CVT's dynamics, mainly the flywheel effects, it will adjust a value which can differ from the static balance. A prediction of the dynamic part of the torque is hardly possible. In contrast to the offline optimization

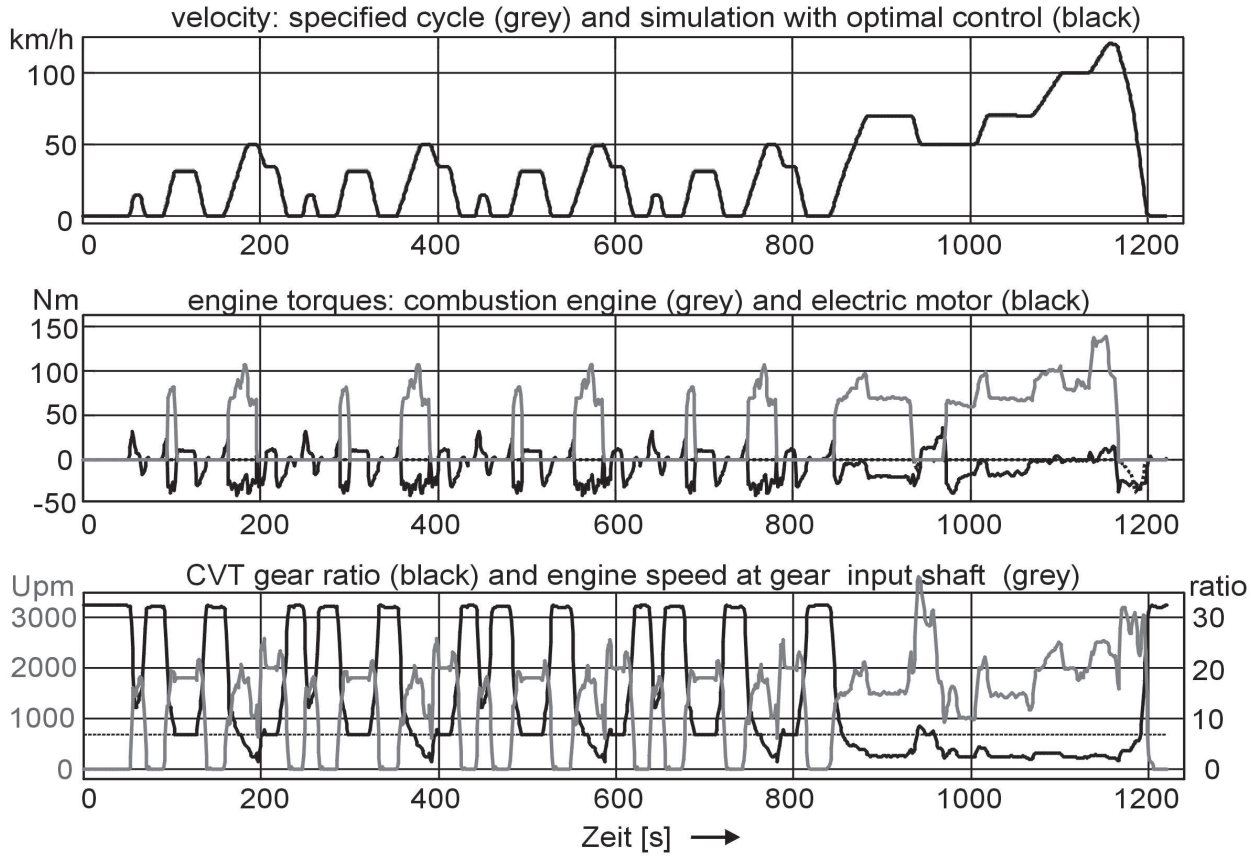

Fig. 3. Optimal control of the Autark Hybrid with TD engine at the NEDC-cycle

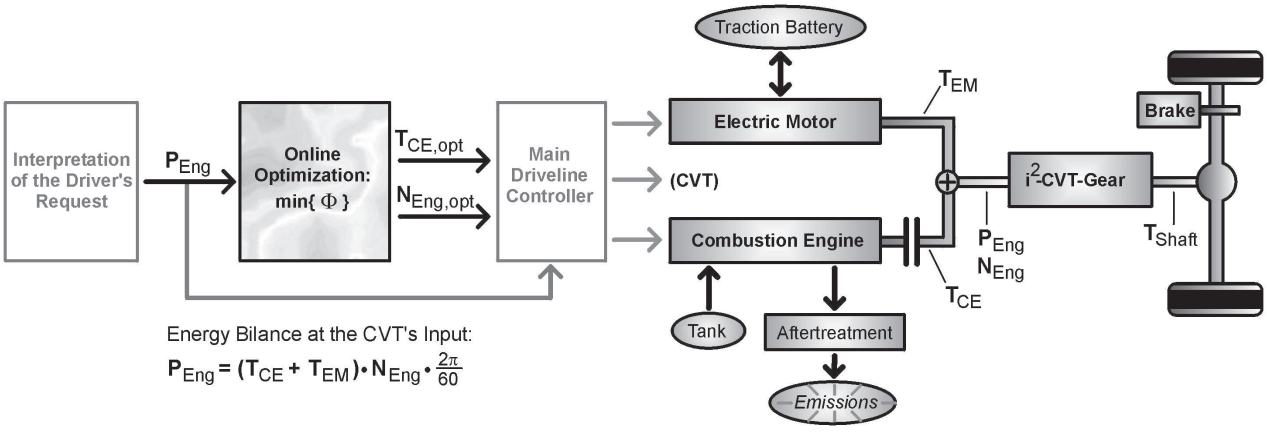

Fig. 4. Structure of the controller system

method, where the whole shape of the vehicle's velocity was preknown and given by a driving cycle, an online optimization would only dispose of the information of the actual system's state and the desired engine power. So a new approach had to be found, which relates only to the actual state at the particular sample time interval and which solves the fundamental problem of a parallel hybrid's powertrain control: it has to find the points of time to enable or to disable the combustion engine, the split of torque for the two engines and also the engine speed, which can be varied over a wide range by the CVT. Former approaches, which exclusively consider the optimization of the CE's efficiency, did not match the problem of latching electrical energy at the traction battery.

As it was shown in section 1, the load increase of the CE is associated with the storage of electrical power and for this reason with electrical conversion losses in the dimension of the CE's fuel saving. From the analysis of the offline optimization's results it was known, that this trade off problem leads to different modes of hybrid engine operation: short periods of CE-operation with high

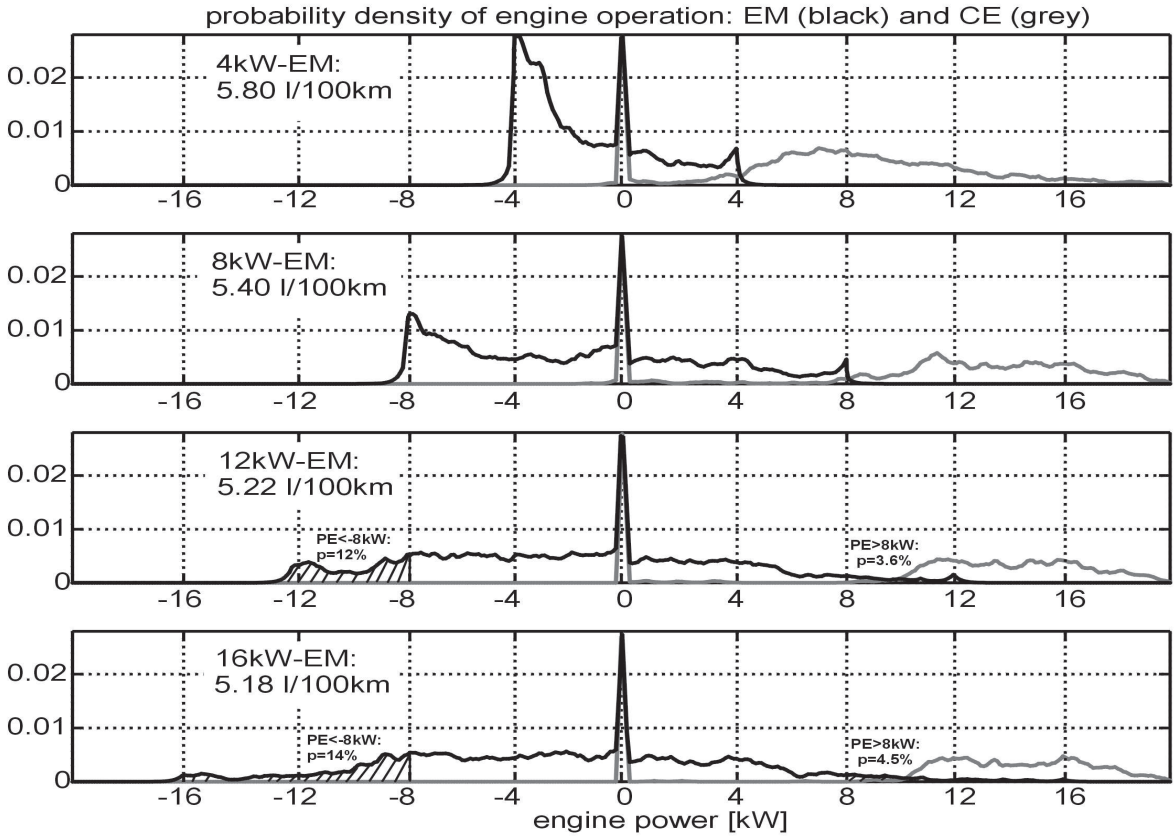

Fig. 5. Probability density of engine operation at the FTP72-cycle, TD engine

load increase or long periods of CE-operation with less load increase. Furthermore, the control of the traction battery's state of charge (SOC) significantly influences on the powertrain's operation, which represents an additional problem. The approach for the online optimization bases on a new objective which minimizes the whole driveline's power losses in depenency on the system's actual state. The power loss is corrected by the weighted change of energy of the traction battery P_{Batt}. The weighting depends on a fixed value and on the battery's SOC. Besides the thermal power loss of the combustion engine $P_{Diss,CE}$ the expression $\alpha \cdot P_{Batt}$ repesents to most important influence on the objective. The conditions and constraints of the system are included by the non-physical "power" K_{Cond}. It contains a hysteresis for enabling/disabling the combustion engine by $K_{CE-Status}$, the limits of the system with $K_{Sys-limits}$ and additional conditions for the consideration of the exhaust emissions by K_{Emis}. A more detailed description can be found in [1].

D. Comparison of the optimization methods

For a simulation test, the vehicle's controller structure in the Matlab/Simulink model of the Autark Hybrid has been adapted to meet the offline method's results as good as possible with the online optimization. The driver's request was computed by a speed controller to meet the specified driving cycle. An additional brake controller allowed the recovery of maximum kinetic energy, dependent on the limits of the electric motor. The online optimization was realized by a S-function with the optimization algorithm and the function of the objective. The online optimization avoided larger drifts of the SOC very effectively, even at a test when the consumption of the electrical loaded power circuits was varied. Even so, the condition of an exactly equalized SOC (offline optimization) had to be met by adapting the parameter α_0. The fuel consumption of the reference vehicle - an identical Opel Astra Caravan with conventional driveline - is compared to the Hybrid Vehicle, simulated with different control methods. (The ECE- and NEDC-cycle was simulated with an EM of 8 kW, the FTP with an EM of 16 kW) The online optimization would save between 0.2 and 0.4 l/100km more than a conventional operation strategy and would reach a value near 0.1 l/100km above the absolute (offline computed) minimum. The shape of the control vectors is very similar to the offline computed results.

The most significant fuel saving can be realized at city traffic, see the results for the ECE-Citycycle. The saving at the NEDC and the FTP72 cycle are more moderate: the simulation model emulates the actual state of an experimental vehicle and the data were set carefully. Further saving potentials are given by the advancement of some components, e.g. by the optimization of the battery's weight or the consumption of the CVT's hydraulic power supply pump. For this comparison, the actual used TD engine was supposed. The influence of the combustion engine will be

discussed later.

E. Results from the online optimization

Because the behaviour of the simulation model with online optimization rather corresponds to real driving conditions and because it is much easier to handle, it was used for the computation of a new, consistent row of simulation runs with different sizes of the electric motor and different types of combustion engines. The percental savings are referenced to the fuel consumption of the original Opel Astra Caravan.

With the TD-engine, the fuel saving potential would reach up to 15% at the NEDC and 12% at the FTP72-cycle. The saving at the FTP is less because this cycle contains faster speed-up and slow-downs. The optimum rated power of the electric motor was found at 12 kW (NEDC) and 16 kW (FTP). In this case, the rated value corresponds to the absolute power limit; overload operation was not supposed.

The peak at the origin represents the standstill periods. A small power limit would lead to a significant constraint of the control which can be seen at the peaks of the EM's density (black curve). In particular the electric braking is constricted. Futhermore, the density of the combustion engine is located at low power values which means partial load operation with disadvantageous efficiency. In combination, this leads to the higher values of fuel consumption. Above the 12 kW-limit this effects are less noticeable, and the combustion engine's operation mainly starts above 10 kW. The partial load operation can be avoided by a higher threshold from electrical to hybrid propulsion and by more electrical load increase. The rated power of the Autark Hybrid's EM actually amounts 8 kW.

With a TDI-engine, the fuel consumption would reach significantly lower values because of the better efficiency of direct injection engines. In contrast to the TD, the engine emissions of NO_x would be significantly increased (nearly doubled) in comparison to the reference vehicle (with TDI in this case). The reasons will be discussed in the following section. To avoid this problem, it was tested to consider the emission values within the online optimization's objective. If an increase of fuel consumption can be taken, it is possible to reduce the NO_x production by 40% resp. 45%.

Finally, a gasoline (SI, spark ignition) engine was supposed for the simulation. As it can be seen, the possible fuel saving potential would be less distinctive. At gasoline engines, the area of best efficiency would be reached at lower levels of torque, in this case at 90 Nm in contrast to 130 Nm (TD) and 145 Nm (TDI). So even the reference vehicle can reach good consumption values by an economical shifting of the gear, and additionally, the electrical load increase at the hybrid would be less advantageous. In combination, this leads to less relative fuel saving.

REFERENCES

[1] KLEIMAIER, A., SCHRÖDER, D.: *An Approach for the Online Optimized Control of a Hybrid Powertrain.* 7th Int. Workshop on Advanced Motion Control, Maribor, Slov., July 2002.

[2] KLEIMAIER, A., SCHRÖDER, D.: *Optimal Rating of the Electric Drive in a Hybrid Vehicle.* 2nd Int. Conference on Integrated Power Systems, Bremen, Germany, June 2002.

[3] KLEIMAIER, A., SCHRÖDER, D.: *The Autark Hybrid Vehicle - Optimal Engine Operation.* 18th International Electric Vehicle Symposium, Berlin, Germ., Oct. 2001.

[4] HÖHN, B.-R., GUTTENBERG, P.: *Experiences of the Autark Hybrid Drive Line on Test Rig.* 18th International Electric Vehicle Symposium (EVS 18), Berlin, Oct. 2001.

[5] KLEIMAIER, A., SCHRÖDER, D.: *Optimized Design and Control of a Hybrid Vehicle with CVT.* 1st IFAC Conference on Mechatronic Systems, Darmstadt, Germany, Sept. 2000.

[6] KLEIMAIER, A., SCHRÖDER, D.: *Design and Control of a Hybrid Vehicle by Optimal Control Theory.* 4th International Power Electronics Conference, Tokyo, Japan, April 2000.

[7] KLEIMAIER, A., SCHRÖDER, D.: *Optimization Strategy for Design and Control of a Hybrid Vehicle.* 6th Intern. Workshop on Advanced Motion Control, Nagoya, Japan, Mar. 2000.

[8] SEILER, J.: *Betriebsstrategien für Hybridfahrzeuge mit Verbrennungsmotoren unter Berücksichtigung von Kraftstoffverbauch und Schadstoffemissionen während der Warmlaufphase.* Dissertation, Lehrstuhl für Elektrische Antriebssysteme, TU München, 2000.

[9] STAMATELOS, A. M. ET AL: *Computergestützter Entwurf von Abgasnachbehandlungskonzepten, Teil 2: Dieselmotoren.* MTZ 60, pp 195-204, Mar. 1999.

[10] ZOELCH, U.: *Ein Beitrag zu optimaler Auslegung und Betrieb von Hybridfahrzeugen.* Dissertation, Lehrstuhl für Elektrische Antriebssysteme, TU München 1998.

[11] HÖHN, B.-R., PFLAUM, H., PINNEKAMP, B., FÖRSTER, W.: *A Wide Ratio Range CVT for the Autark Hybrid Transmission.* ISATA, Aachen 1994, pp. 613-620.

[12] VON STRYK, O.: *Numerische Lösung optimaler Steuerungsprobleme: Diskretisierung, Parameteroptimierung und Berechnung der adjungierten Variablen.* Dissertation, Lehrstuhl für höhere Mathematik und numerische Mathematik der TU München, 1994.

driving Cycle	reference vehicle	simulation of the Autark Hybrid Vehicle		
	normal driver	operation strategy	online optimization	offline optimization
ECE-City	7.13 l/100km (base)	5.12 l/100km -28.2%	4.89 l/100km -31.4%	4.77 l/100km -33.1%
NEDC	6.02 l/100km (base)	5.49 l/100km -8.8%	5.19 l/100km -13.8%	5.09 l/100km -15.4%
FTP72[1]	5.89 l/100km (base)	5.61 l/100km -4.8%	5.18 l/100km -12.1%	–

[1] FTP72: Electric motor of 16 kW at the hybrid; 8 kW at the NEDC and the ECE-City

TABLE I

COMPARISON OF THE FUEL CONSUMTION FOR DIFFERENT CONTROL METHODS (TD–ENGINE)

combustion engine	reference / hybrid, electric motor	consumtion at 100 km and saving potential	
		NEDC	FTP
TD 55 kW 170 Nm 240 g/kWh	reference vehicle	6.02 l base	5.89 l base
	Hybrid, 4 kW-EM	5.50 l 8.3%	5.80 l 1.5%
	Hybrid, 8 kW-EM	5.19 l 13.8%	5.40 l 8.3%
	Hybrid, 12 kW-EM	5.12 l 14.9%	5.22 l 11.5%
	Hybrid, 16 kW-EM	5.12 l 14.9%	5.18 l 11.9%
TD 55 kW 180 Nm 200 g/kWh	reference vehicle	5.27 l base	5.01 l base
	Hyb, 8 kW, NO_x-Red[1]	4.63 l 12.1%	4.81 l 4.0%
	Hybrid, 8 kW-EM	4.42 l 16.1%	4.71 l 6.0%
	Hybrid, 16 kW-EM	4.42 l 16.1%	4.48 l 10.6%
SI 55 kW 120 Nm 250 g/kWh	reference vehicle	5.85 l base	5.73 l base
	Hybrid, 8 kW-EM	5.43 l 7.2%	5.65 l 1.4%
	Hybrid, 16 kW-EM	5.34 l 8.7%	5.39 l 5.9%

[1] NO_x-Red: Reduction of the NO_x-engine emissions: 45% at the NEDC and 40% at the FTP-cycle

TABLE II

BENCHMARK DATA FROM THE SIMULATION RUNS WITH THE ONLINE OPTIMIZATION

Instantaneous Torque Controller for Switched Reluctance Vehicle Propulsion Drives

N. H. Fuengwarodsakul R.W.A.A. De Doncker
Institute for Power Electronics and Electrical Drives
Aachen University, Aachen, Germany
Email: fu@isea.rwth-aachen.de

***Abstract*—Among those electrical drives, a drive concept with switched reluctance machine appears to be a promising solution for traction applications due to its numerous advantages such as robust structure, simple construction, low maintenance requirement etc. However, up to now, the utilization of switched reluctance drives in traction applications is still limited in comparison to the other types of electrical drives, because the current technology of switched reluctance drive controllers is not able to offer satisfying control quality and the performance of the same standard obtained from rotating field machines with field oriented control. In order to allow switched reluctance machine to come up with the other electrical drive concepts, a new control concept to improve the control quality and drive performance is required.**

This paper presents a switched reluctance machine torque controller for vehicle propulsion applications based on a novel control strategy called Direct Instantaneous Torque Control (DITC). Using DITC, the direct controllability of instantaneous torque is achieved, which leads to torque ripple minimization and good control accuracy. Control quality and drive performance are, therefore, significantly improved in comparison to the torque controller using classical hysteresis current control. DITC means that the torque is directly applied as control variable instead of phase currents. The actual instantaneous torque is calculated by an observer based on the machine characteristic. The torque command and the actual instantaneous torque are compared by a hysteresis torque controller, which generates the corresponding switching signals to deliver the desired torque. Furthermore, this paper describes and discusses the detailed functionality of DITC by using simulation and experimental results. An additional control scheme for maintaining the control linearity at high speeds is proposed at the end of this paper.

I. INTRODUCTION

Since the very beginning of electrical drives for electric vehicle applications, the advantages and disadvantages of the different drive systems with induction, permanent magnet, transversal flux, switched reluctance, and other machines have been discussed. However, each system has its individual characteristics and therefore special advantages in comparison to the other existing solutions. The choice of the appropriate drive system for a concrete application depends on the goal that has to be reached with the drive system if not with the whole vehicle design. As a result, there is nothing like a best electrical machine in general.

Up to now, the switched reluctance machine has not reached the position within the electrical traction drives that would be expected despite its evident advantages. Perhaps one reason can be found in the number of sold units of electrical traction drives which is still marginal. As a result, the lower machine costs of a switched reluctance machine cannot compensate the higher costs of the power converter for switched reluctance machines which is not state-of-the-art as a converter for rotating field machines. Nevertheless, the switched reluctance machine has the most simple and robust rotor of all machine types known. Just a stack of laminations without windings, a squirrel cage or even permanent magnets, the rotor of a switched reluctance machine can withstand the highest temperatures. Furthermore, the stator with its single winding per tooth can be manufactured much cheaper than a distributed winding of a rotating field machine.

There are further advantages of switched reluctance machine drives that make an application more simple. With permanent magnet machines, a problem with induced voltages at idle mode exists. This becomes extreme at high speeds and a high current component which compensates these high induced voltages is necessary. Indeed, it is the active field weakening that lowers the high efficiency of a permanent magnet machine in high speed operating areas. These problems do not occur in switched reluctance machines.

Nevertheless, the switched reluctance machine also has disadvantages in comparison to the other machine types. These can be reduced by means of modern control technology. State-of-the-art is a hysteresis current control in combination with switched reluctance drives (Figure 1). The

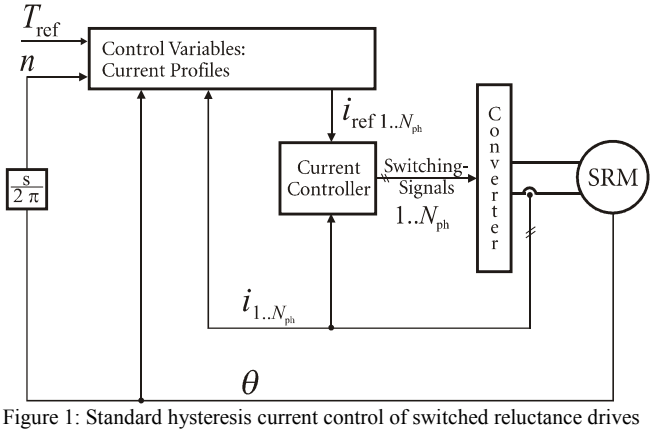

Figure 1: Standard hysteresis current control of switched reluctance drives

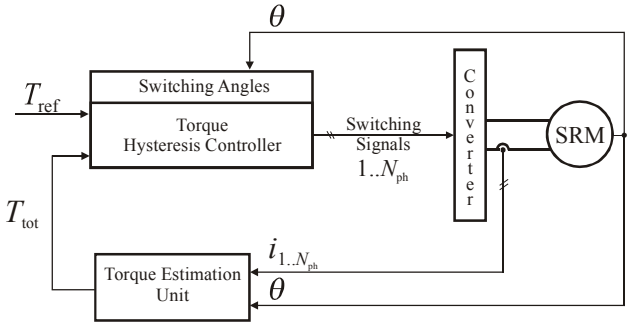

Figure 2: Direct Instantaneous Torque Control (DITC) for switched reluctance.

control variables turn-on and turn-off angle and the reference current are precalculated offline in dependence on the stationary operating point defined by commanded torque, actual speed and dc-link voltage. In the end, this kind of control is an open-loop torque control. Indeed, the control deviation and the torque ripple does not reach a quality that is known from rotating field machines with field oriented control. The torque ripple that results from the commutation from one phase to the other can be minimized by means of current profiling. But also these profiles are precalculated off-line for stationary operating points. Moreover, the profiles take a big amount of memory within the microcontroller system.

The basic idea to cope with the problem of torque ripple and an unsatisfying control quality of the torque sounds very simple. Not the current has to be controlled but the torque itself. A new control strategy called Direct Instantaneous Torque Control (DITC) has been developed [1][3]. It leads to a smooth torque and a good control accuracy that is especially important for advanced drive control such as active damping of drivetrain oscillations [4].

The heart of DITC is the torque estimation unit (Figure 2). With the phase currents and the rotor angle, the instantaneous torque is calculated and then a hysteresis controller regulates this quantity to the reference torque. The control variables turn-on and turn-off angle still have to be precalculated. However, the accuracy requirements of these values are not as high as with current control. Obviously, the reference current as the third control variable is eliminated.

II. DITC

A. *Functionality of DITC*

The basic requirement for DITC is the on-line availability of the total instantaneous machine torque. The instantaneous torque of switched reluctance machines cannot be determined by simple analytical equations as in dc machines or rotating field machines. Due to the nonlinear machine characteristics and block-wise excitation of SR-technology, the instantaneous torque can only be estimated by means of stored machine characteristics [2]. For torque estimation, these characteristics represent torque as a function of phase current and rotor position or as a function of phase current and phase flux linkage. The estimation of flux linkage is always difficult at low speeds due to the integration of a low average phase voltage for a long excitation period. Therefore, for the project presented in this paper, the instantaneous torque is estimated using phase current and rotor position.

The control strategy of DITC comprises a digital torque hysteresis-controller, which generates the switching signals for all activated machine phases. In single-phase conduction, the hysteresis controller regulates the estimated torque of one phase. During phase commutations, the phase torque of two adjacent phases is controlled indirectly by controlling the total torque with a multiple-level comparator. To obtain satisfactory torque commutation, a special switching strategy is implemented in the controller. If the machine operates in two-phase conduction (i.e. phase commutation), the magnetized outgoing phase switches into the zero-voltage state. If the incoming phase cannot yet produce the required torque within an inner hysteresis band, the outgoing zero-voltage phase changes back to switching state. In this way, total torque can be regulated.

The performance of the hysteresis controller is demonstrated by a simulation result shown in Figure 3. Aside from the presentation of the total instantaneous torque ripple (top), the phase voltage (middle) and the torque produced by each phase (bottom) are depicted.

At T1 the commutation process starts by turning on the subsequent machine phase. The phase which was previously activated changes into the zero-voltage state. A few microseconds later, the total torque drops below the lowest switching threshold (see top graph in Figure 3). This means that the incoming phase cannot provide sufficient torque and the outgoing phase must be connected to the positive dc-link voltage again. By doing so, the total torque can be controlled within the outer hysteresis bands. As can be seen, the outgoing phase is required to take action twice to maintain total torque within the outer hysteresis band. Once the incoming phase is able to regulate the total torque, the outgoing phase dwells in the zero-voltage state. At T2, the total torque rises above the highest switching threshold. To avoid demagnetization of the incoming phase, the outgoing

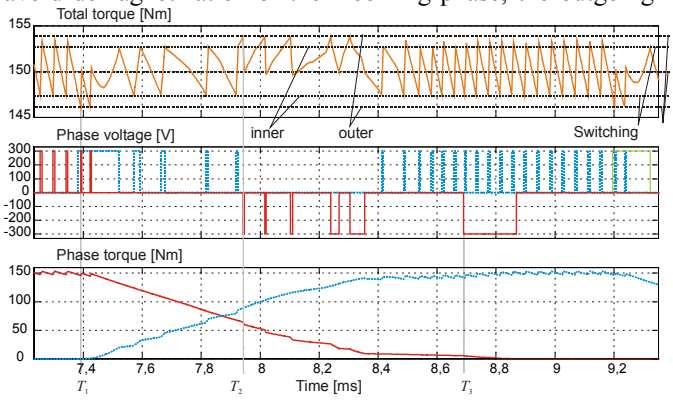

Figure 3: The functionality of DITC

phase, which is in zero-voltage state, is demagnetized with negative voltage. Finally, this phase is completely demagnetized at T3, i.e. the end of the conduction period is reached. After T3, the controller acts as a normal hysteresis controller using the inner hysteresis bands to switch the incoming phase.

B. Advantages of DITC

Since the advantages of DITC are very fundamental, they are summarized in this section once again.

- Smooth torque quality
- Direct compensation of the inherent torque ripple during phase commutation
- Good steady state torque control accuracy in the lower speed range
- Simplification of sets of control variables
- Reduction of control variables tuning

C. Simulation Results

Figure 4 shows impressively the improvement in steady-state control of switched reluctance drives which can be reached by using DITC in comparison to classical current hysteresis control.

From Figure 4 (left), it is evident that, despite smooth current control, the instantaneous electromagnetic torque fluctuates significantly above and below the commanded

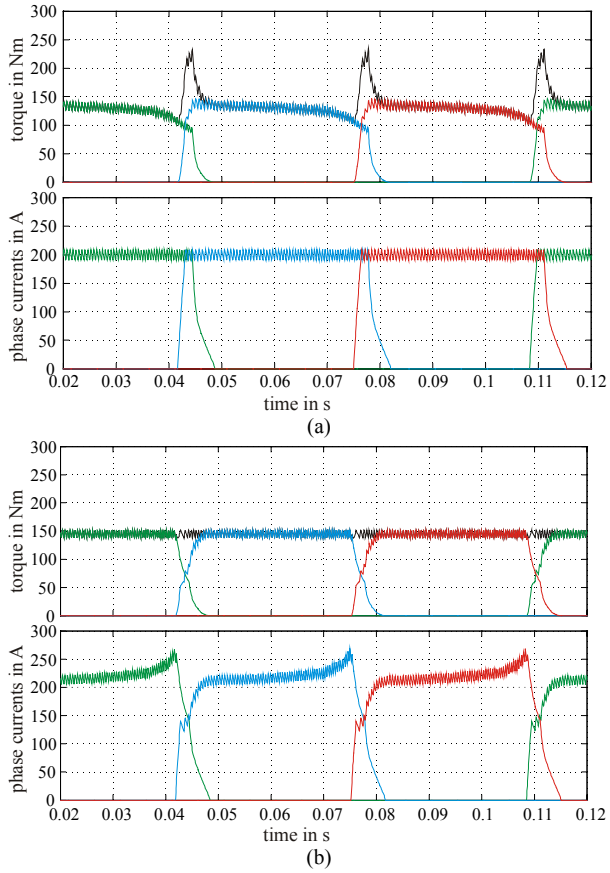

Figure 4: Simulated torque (top) and phase current (bottom) of a current controlled SRM (a) and DITC (b)

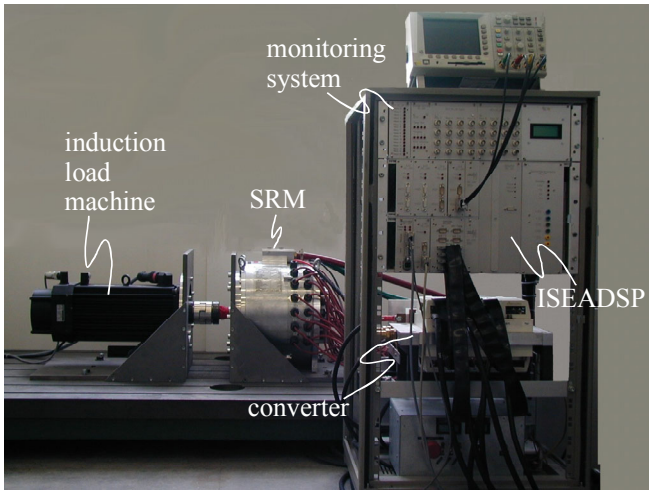

Figure 5: Switched reluctance drive on the test bench

value (150 Nm) during phase commutations when using a common open-loop torque controller containing an inner current control loop. As it is shown in Figure 4 (right), DITC regulates the total instantaneous torque within a small hysteresis band for the identical average operating point, as in the left simulation. For verification of these results, DITC was implemented in a switched reluctance prototype drive system.

D. Experimental Results

A complete test-bench arrangement was built up to verify the performance of a DITC switched reluctance machine drive. The test drive is a 16/12-pole switched reluctance starter-alternator application. The drive is designed and developed for the 42 V Powernet and has to supply a continuous power of 6 kW in generator operation. Figure 5 illustrates the test bench with load machine, switched reluctance machine, converter, and control unit. A digital signal processor platform ISEADSP is utilized in the control unit. Using this ISEADSP platform, rapid prototyping and implementation of various control strategies of switched reluctance drives are possible [6]. In addition to DITC, the normal hysteresis current control was implemented on this platform in order to compare and demonstrate the improved performance by DITC.

Figure 6 illustrates the experimental results of DITC and the normal hysteresis current control. The experiments were carried out at identical operating points. In Figure 6a, the switched reluctance drive is operated with DITC at a speed of 200 rpm. The torque command is set to 35 Nm. As can be seen from Figure 6a, the instantaneous torque is always regulated in the hysteresis band even during phase commutation. This shows a significant improvement of the drive performance, since the inherent torque ripple is completely eliminated by DITC. Furthermore, the developed torque is determined solely by one control parameter, i.e., the torque command. It is verified not only by the simulations but also by the experiments that DITC can deliver the desired torque independently from the switching

angles in a wide operating range. Hence, the control accuracy of DITC is better than a control strategy with off-line precalculated control parameters, since the control accuracy does not depend on the accuracy of those parameters, i.e. turn-on and turn-off angle.

Figure 6b shows the experimental results with a hysteresis current control. In contrast to DITC, this control is characterized by the enormous torque ripple during phase commutation. This kind of controller can only regulate the average torque and this leads to a low dynamic performance at low speeds. In order to achieve the desired average torque, the corresponding control parameters, i.e. reference current, turn-on and turn-off angle have to be determined by either online or offline calculations based on the given criterion, e.g. torque ripple or efficiency. As a consequence, the torque control accuracy depends on the accuracy of three control parameters and this increases the possibility of torque deviation from the torque command. As a conclusion, DITC offers a high performance and a good control accuracy. The instantaneous torque is smoothly regulated and always follows the torque command. Therefore, the drive performance with DITC is significantly improved in comparison to other conventional switched reluctance controllers.

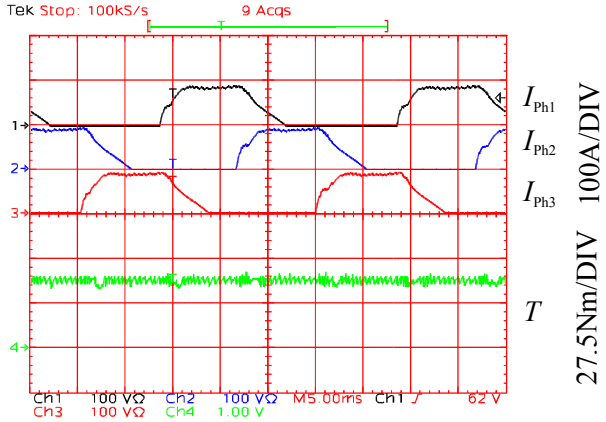

a) DITC at n= 200 rpm, V_{dc}= 36 V, θ_{On}=20° elec., θ_{Off} =160° elec., T= 35 Nm

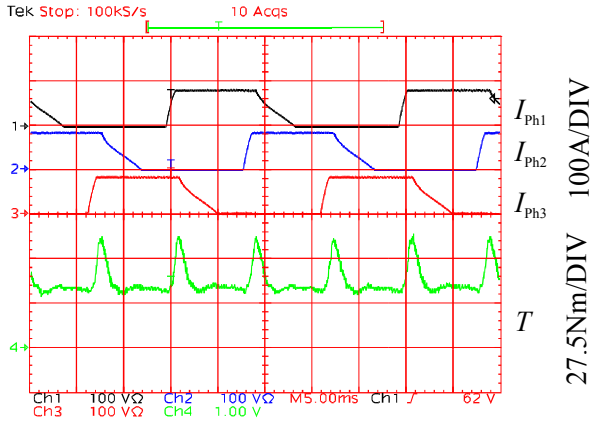

b) Hysteresis current control at n= 200 rpm, V_{dc}= 36 V, θ_{On}=20° elec., θ_{Off} =160° elec., T= 35 Nm

Figure 6: Experimental comparison of DITC and hysteresis current control

III. DITC AT HIGH SPEED

As in other electrical machines, the back emf of SR-machines increases proportionally to speed. In high speed operating regions, this back emf becomes significant in comparison to the dc-link voltage and leads to a reduction of current and torque slope respectively. Due to the reduced torque slope, the total torque cannot be continuously regulated within the hysteresis band all the time because the produced instantaneous torque increases and decreases with a too low slope to follow the controller command. This results in a rise of torque ripple and loss of good control accuracy, because the average torque begins to drop and deviate from the torque command, as shown in Figure 7.

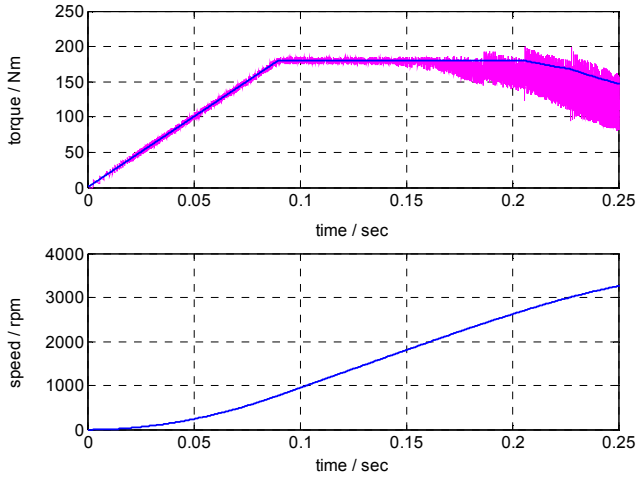

Figure 7: Loss of control accuracy at high speeds

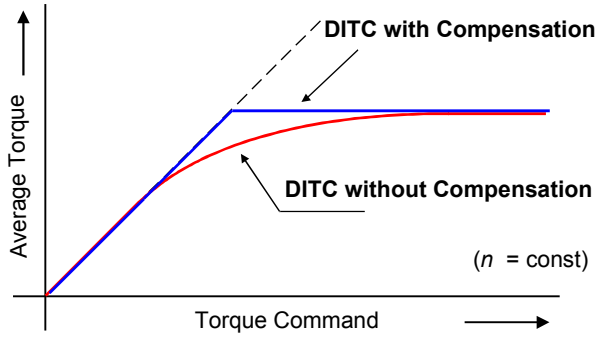

a) Transfer function of torque command and developed average torque at high speed

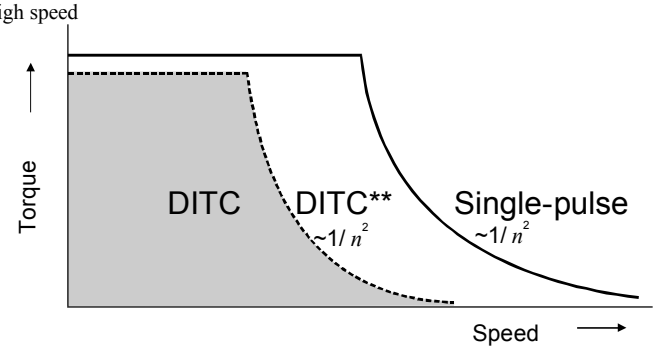

b) Operating regions by constant turn-on and turn-off angles

Figure 8: Operating Regions

Therefore, an additional control function is required to compensate the drop of average torque, so that a good control accuracy and linearity can be achieved up to the limit of the single-pulse operation, as shown in Figure 8a. Figure 8b shows the whole operating range of a switched reluctance drive with DITC. The operating region, in which the additional compensation should be active, is illustrated in Figure 8b as DITC**. On the other hand, in the region, which is indicated with DITC, i.e. the low speed range, the instantaneous torque can be continuously regulated within the hysteresis band without any additional control function.

Figure 9 illustrates an additional control function for compensating the drop of average torque at high speed. This function is additionally integrated in the basis control without any change of the main structure of DITC. The torque command provided to the torque hysteresis controller is defined by Tref**. In the low speed range, Tref** is set equal to Tref*, which is given from the higher level controller or the user. The torque compensation is not necessary at this low speed range and, therefore, is automatically deactivated (Tcom = 0), because the controller can still regulate the instantaneous torque in the hysteresis band.

In the high speed range, in which the average torque begins to drop below the torque command, the torque compensation is activated in order to compensate this torque drop. This torque compensation is implemented by a digital integrator, which integrates the difference between the estimated average torque and the torque command and provides Tcom as output signal. Tcom will increase until the average torque reaches the desired torque. The dynamics of the compensation can be adjusted by varying the integrator gain.

The further discussion is in which conditions the torque compensation should be activated and deactivated. Since a sudden transition of control strategies may lead to an undesired drive behavior or uncontrollability of the drive, criterion for smooth transition of this torque compensation have to be determined to avoid the problem of hard transition. From a study using the simulation model, the proper criterion, which can be applied for all operating ranges, were found as follows:

- compensation activated, if |Tref*-Tavr| > k|Tref*| in steady state
- compensation deactivated and reset, if the sign of Tcom or Tref* change

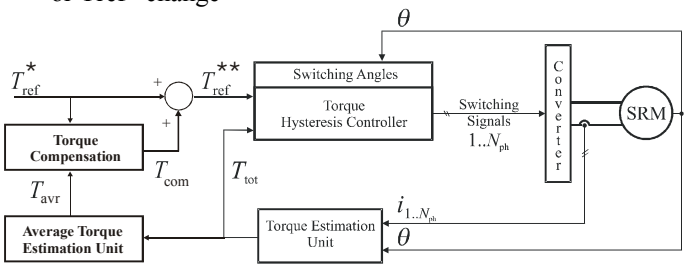

Figure 9: DITC with compensation at high speeds

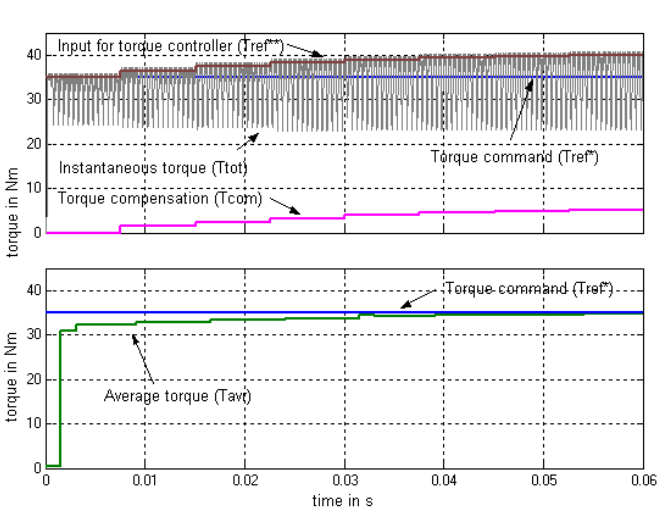

Figure 10: Simulation result of the torque compensation

The compensation is activated, when the average torque Tavr deviates from the torque command Tref* more than the threshold value k|Tref*| in steady state. The typical value of the threshold factor k lies between 1%-5%. After the compensation is activated, the compensation value Tcom is increased stepwise by the digital integrator (or decreased by negative torque command) until the average torque Tavr reaches the command value.

For deactivating the compensation, two criteria are applied. The first criterion is that the compensation is turned off if the compensation value Tcom changes it sign. As Tcom crosses zero value, it means that the average torque is approximately equal to the torque command. And then the compensation is not necessary any more and should be deactivated.

The second criterion is the sudden sign change of the torque command (Tref*). With the sign change of torque command, the sign of compensation torque Tcom will be changed later as the actual torque follows the torque command. The compensation could be also automatically deactivated by the first criterion. However, the transient process can be accelerated by resetting the compensation torque Tcom at once as the sign change of torque command is detected.

Figure 10 presents the simulated result of this torque compensation function. The drive is operated at 3500 rpm with the torque command of 35 Nm. At this operating point, the average torque drops from the torque command by 10% (3 Nm), which can be seen at the beginning of the measurement. After that, Tref*-Tavr is greater than the threshold value (2 %Tref* in this simulation) in steady state , therefore, the compensation is activated. The torque compensation is increased stepwise by the digital integrator until the average torque reaches the desired torque command. The settling time and dynamic of the torque compensation can be optimized by adjusting the integrator gain. In this simulation, the gain is adjusted so that the drive

delivers no average torque overshoot in order to avoid torque oscillations. Furthermore, this simulation result demonstrates a smooth transition from the normal DITC to the operation with torque compensation resulting in a good control stability.

The implementation and experiments of this additional control function for DITC at high speeds are being carried out. More details and experimental results will be presented in the future work.

IV. CONCLUSION

The instantaneous torque controller of switched reluctance vehicle propulsion drives was introduced. Using a new control strategy called Direct Instantaneous Torque Control (DITC), an improved drive performance is achieved in comparison to a conventional switched reluctance torque control. The controller with DITC possesses the direct controllability of the instantaneous torque by means of the hysteresis torque controller resulting in smooth torque and a good accuracy. By using the machine characteristics the instantaneous torque is estimated. Since torque is directly applied as a control command, the control variable set is substantially simplified due to the elimination of the precalculated current command. Moreover, the controller can operate with a large tolerance of precalculated control variables, i.e. turn-on and turn-off angle, without reducing control accuracy. In high speed ranges, the instantaneous torque cannot be regulated within the desired hysteresis all the time due to the high back-emf. Hence, an additional control scheme was proposed to maintain the control accuracy and the torque output linearity over the entire operating range.

It can be concluded that the proposed instantaneous torque controller offers evident improvements of the control quality and drive performance. Using this instantaneous torque controller, the switched reluctance drive becomes more competitive in vehicle propulsion applications compared to the conventional rotating field machines.

REFERENCES

[1] Inderka, R.B.; De Doncker R.W. DITC Direct Instantaneous Torque Control of Switched Reluctance Drives. 37th Annual Meeting of the IEEE Industrial Application Society IEEE-IAS, 2002.

[2] Inderka, R.B.; Krehenbrink, M.; De Doncker, R. W. On-line Estimation of Instantaneous Torque of Switched Reluctance Machines. International Symposium on Industrial Electronics IEEE-ISIE, 2000.

[3] Inderka, R.B. Direkte Drehmomentregelung Geschalteter Reluktanzantriebe. Dissertation, RWTH-Aachen University, 2002.

[4] Menne M.; Bitsche O. Comparison of Drivetrain-Oscillation Damping-Algorithms for Electric Vehicles, Electric Vehicle Symposium EVS-18, 2001.

[5] Mir S.; Elbuluk M.; Husain I. Torque Ripple Minimization in Switched Reluctance Motors Using Adaptive Fuzzy Control. Annual Meeting of the Industrial Application Society IEEE-IAS, 1997.

[6] Fuengwarodsakul, N. H.; Radermacher, H.; De Doncker, R.W. Rapid Prototyping Tools for Switched Reluctance Drive Controls in Traction Applications, 5th International Conference on Power Electronics and Drive Systems PEDS, 2003.

[7] Schramm D.S.; William B.W.; Green T.C. Torque Ripple Reduction of Switched Reluctance Motors by Phase Current Optimal Profiling. Power Electronics Specialists Conference IEEE-PESC, 1992.

[8] Rahman K.M.; Schulz S.E.. High Performance Fully Digital Switched Reluctance Motor Controller for Vehicle Propulsion. IEEE Transaction IAS Vol.38 No.4 July/Aug, 2002.

[9] Miller T.J.E. Electronic Control of Switched Reluctance Machines, Oxford, UK, Newnes, 2001.

An Optimal Efficiency Control of Reluctance Synchronous Motor Using Neural Network with Direct Torque Control

Min-Huei Kim, Nam-Hun Kim

Dept. of Automatic Electrical Engineering,
Yeungnam College of Science & Technology, Republic of Korea
Email: mhkim@ync.ac.kr

***Abstract*—This paper presents an implementation of efficiency optimization of reluctance synchronous motor (RSM) using a neural network with a direct torque control. The equipment circuit in RSM which consider with iron losses is theoretically analyzed and the optimal current ration between torque current and exiting current analytically derived. For RSM, torque dynamics can be maintained even with controlling the flux level because a torque is directly proportional to the stator current unlike induction motor. In order to drive RSM at maximum efficiency and good dynamics response, the neural network is used and to achieve complex control algorithms, the TMS320F2812 board is employed as control drivers. The experimental results are presented to validate the applicability of the proposed method. The developed control system show high efficiency and good dynamic response features with 1.0 [kW] RSM having 2.57 ratio of d/q.**

Index Terms—Direct Torque Control, Neural Network, Reluctance Synchronous Motor, TMS320F2812, Optimal Efficiency.

I. INTRODUCTION

The need to save energy has drawn the industrial attention to the losses and efficiency of motors. The main efforts for higher efficiency are focused on improvement of materials and optimization of design strategies. However, efficiency can also be improved by intervening in the operational principle of motors. Several simple and effective control methods have been proposed in order to minimize the losses, to improve dynamic response[1],[2].

Also recently, neural network(NN) and direct torque control(DTC) have much attention in control application. The application of NN and DTC to induction and synchronous motor drive are developed in many researches. Because the former has capability of mapping non-linear relation between inputs and out signals, the latter has simple and good dynamic response.

In general, the DTC method divided into constant flux method and variable flux method. The constant flux method, have been commonly used, is always kept constant as exciting current component whenever a load is light or heavy.

At lighting loads, maximum efficiency will be achieved with a reduced exciting current component, compared with the constant flux method. Consequently, there is an optimum exciting current component which gives a specified torque and speed with maximum efficiency[3].

The reluctance synchronous motor(RSM) have gained an increasing popularity in a variety of industrial application. Especially, RSM have recently attracted as a viable alternative to induction, synchronous and switched reluctance machines in medium-performance drive applications. This has been made possible by limiting some traditional RSM drawbacks, such as poor power factor and low-torque density, related to the limited saliency ratio obtainable using conventional rotor design. The RSM has certain advantages over other types of ac machines. Compared to other type ac machines, since the RSM has a mechanically simple and robust structure, it is capable of high-speed operation and for use in high temperature environments. In addition, the absence of rotor Joule losses and of iron rotor losses in the case of sinusoidally distributed mmf., results in better exploitation of the stator structures and colder rotor, which is preferable in certain application. Furthermore, these motors require little maintenance. These advantages make the RSM very attractive for wide variety of applications from low to high speed and also in high dynamic performance drives[4]-[10].

In this paper, efficiency optimized current angle condition in RSM which minimizes the copper and the iron loss is derived based on the equivalent circuit model of the machine. From this mathematical analysis, we get a simulation data and the NN used in this paper are trained off-line to map the optimal flux reference. In order to achieve neural network and DTC algorithm, TMS320F2812 DSP board is used. In the proposed algorithm allows the electromagnetic losses in variable speed/torque drives to be reduced while keeping good dynamic responses. Experimental results are presented to validate the proposed algorithm.

II. RELUCTANCE SYNCHRONOUS MOTOR

A Structure of Reluctance Synchronous Motor

RSM has stator winding similar to those of a three-phase induction motor and a rotor designed with appreciably different values of the reluctance on the direct and quadrature axes. This RSM has the advantages of both the induction motor and the synchronous motor[11]. The electromagnetic torque production of RSM depend on ratios of L_d and L_q inductance(saliency ratio). Early, d-axes and q-axes inductance ratios of RSM could not exceed much more than 2:1 resulting in a larger frame size than an equivalent induction motor. However, development of power electronics enabled variable speed drive and also improvement of design technique allowed higher saliency ratio. Indeed, ratios L_d / L_q (8~20) have been reported. There are many different saliency ratio versus rotor type. In this paper, rotor of flux barrier type was used to cost and mass production[4],[11].

The vector diagram in synchronously rotating reference frame is illustrated in Fig.1. The RSM can be starting asynchronously, and be operating synchronously at steady state from rest by proper inverter control. Hence, elimination of both the field winding and damper winding equation forms the basis for the d-q equation for a RSM. The equations are (1)-(5)[3],[4],[7],[12],[13].

$$\begin{bmatrix} V_{ds} \\ V_{qs} \end{bmatrix} = \begin{bmatrix} R_s & 0 \\ 0 & R_s \end{bmatrix} \begin{bmatrix} I_{ds} \\ I_{qs} \end{bmatrix} + \begin{bmatrix} -w_r & 0 \\ 0 & w_r \end{bmatrix} \begin{bmatrix} \Phi_{qs} \\ \Phi_{ds} \end{bmatrix} + \frac{d}{dt} \begin{bmatrix} \Phi_{ds} \\ \Phi_{qs} \end{bmatrix} \tag{1}$$

$$\frac{dw_r}{dt} = \frac{1}{J}(T_e - T_L - Bw_r) \tag{2}$$

$$\begin{aligned} T_e &= \left(\frac{3}{2}\right)\left(\frac{P}{2}\right)\left(\Phi_{ds} I_{qs} - \Phi_{qs} I_{ds}\right) \\ &= \left(\frac{3}{2}\right)\left(\frac{P}{2}\right) L_d \left(1 - \frac{L_q}{L_d}\right) I_{ds} I_{qs} \\ &= \left(\frac{3}{2}\right)\left(\frac{P}{2}\right)\left(L_d - L_q\right) I_s \frac{\sin(2e)}{2} \\ &= \left(\frac{3}{2}\right)\left(\frac{P}{2}\right)\frac{\left(L_d - L_q\right)}{L_d L_q} \Phi_x^2 \sin(2d) \end{aligned} \tag{3}$$

$$\begin{bmatrix} \Phi_{ds} \\ \Phi_{qs} \end{bmatrix} = \begin{bmatrix} L_{ls} + L_{md} & 0 \\ 0 & L_{ls} + L_{md} \end{bmatrix} \begin{bmatrix} I_{ds} \\ I_{qs} \end{bmatrix} = \begin{bmatrix} L_d I_{ds} \\ L_q I_{qs} \end{bmatrix} \tag{4}$$

$$|\Phi_s| = \sqrt{\Phi_{ds}^2 + \Phi_{qs}^2} \tag{5}$$

Where L_{md}, L_{mq} and L_{ls} are, respectively, the direct axis and quadrature axis magnetizing inductances and the leakage inductance. The qauantity R_s is the stator resistance per phase and w_r is the speed of the rotor.

From (3), we know that the electromagnetic torque can be expressed in terms of the stator current amplitude and current angle e. It is mean that torque control dynamics can be maintained with adjusting the flux to optimizing the efficiency. This is because the flux linkage in RSM is dirctly proportional to the stator currents since the rotor circuit is opened[1]-[4].

The equations are simply compared induction machines because the field winding is nonexistent and rotor cage is normally omitted, which predicts that the control scheme of RSM can be simpler than ones of synchronous or induction machines.

The inductances are nonlinear function of rotor position and current due to the magnetic saturation have to be compensated. In order to measure nonlinear inductance, we measure inductance versus stator current and rotor position angle. Fig.2 shows measured inductance versus position and current. Fig. 3 shows measured L_d and L_q versus stator current.

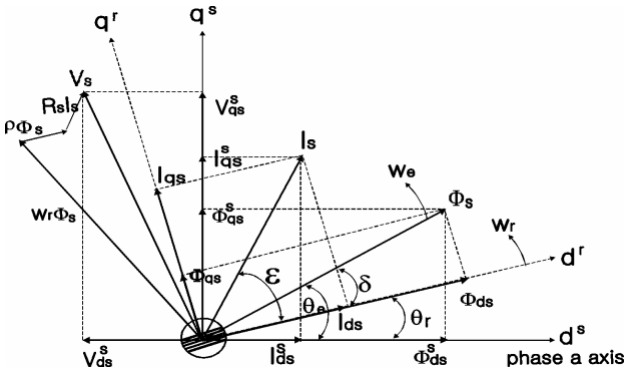

Fig. 1. Vector Diagram of RSM

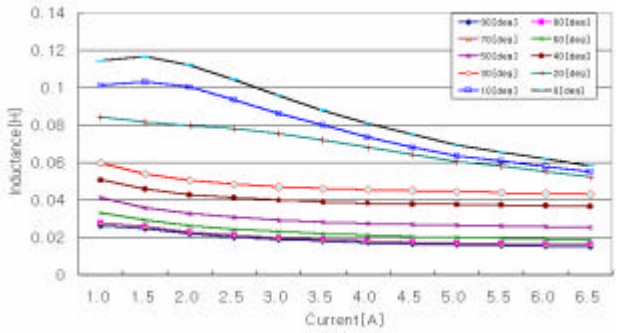

Fig. 2. Measured inductance versus position angle

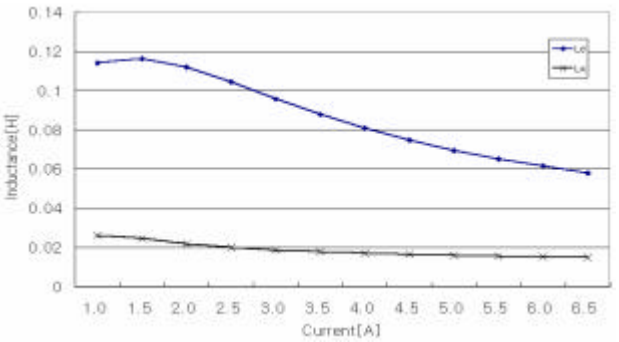

Fig. 3. The Measured Ld and Lq versus stator current

III. OPTIMAL EFFICIENCY CONTROL

A. *Mathematical analysis*

Fig. 4 shows d and q-axis equivalent circuit of RSM in synchronously rotating reference frame. The resistance R_s is occurred copper loss. The resistance R_m which accounts for core loss is connected in parallel with the magnetizing branch and induced speed voltage. The current components which are directly responsible for torque and flux production are I_{do}, I_{qo}. These currents differ form the terminal current I_{ds}, I_{qs} because of the existence of core loss branch. From Fig. 4, the d-q voltage equation in synchronously rotating reference frame for RSM are (6) and (7).

$$\begin{aligned} V_{ds} &= R_s I_{ds} + \frac{d}{dt} L_d I_{do} - w_r L_q I_{qo} \\ V_{qs} &= R_s I_{qs} + \frac{d}{dt} L_q I_{qo} + w_r L_d I_{do} \end{aligned} \tag{6}$$

$$\begin{aligned} I_{do} &= I_{ds} - I_{dm} \\ &= I_{ds} - \frac{1}{R_m}\left(\frac{d}{dt}(L_d I_{do}) - w_e L_q I_{qo}\right) \\ I_{qo} &= I_{qs} - I_{qm} \\ &= I_{qs} - \frac{1}{R_m}\left(\frac{d}{dt}(L_q I_{qo}) + w_e L_d I_{do}\right) \end{aligned} \tag{7}$$

where, L_d, L_q are direct axis inductance and quadrature axis inductance respectively. Equation (8) is electromagnetic torque cosidered core loss as

$$T_e = (3/2)(P/2)(L_d - L_q) I_{do} I_{qo} \tag{8}$$

Where, P is the number of poles.

As mentioned previously, the efficiency of variable speed drive is one of the most important factor. It is possible to compute the copper and the iron losses as the function of I_{do}, I_{qo} as (9), (10).

Copper loss :

$$\begin{aligned} P_{co} &= \frac{3}{2} R_s (I_{ds}^2 + I_{qs}^2) \\ &= \frac{3}{2} R_s \left\{ (I_{do} - \frac{w_e L_q I_{qo}}{R_m})^2 + (I_{qo} + \frac{w_e L_d I_{do}}{R_m})^2 \right\} \end{aligned} \tag{9}$$

Iron loss :

$$\begin{aligned} P_{ir} &= \frac{3}{2} R_m (I_{dm}^2 + I_{qm}^2) \\ &= \frac{3}{2} R_m \left\{ (\frac{w_e L_q I_{qo}}{R_m})^2 + (\frac{w_e L_d I_{do}}{R_m})^2 \right\} \end{aligned} \tag{10}$$

The losses are concentrated in the stator and those in the rotor which are mainly due to the flux ripple are assumed to be negligible. The efficiency is optimized by minimizing the total losses of copper and iron losses. Let the ration of d- and q-axis current be $z = I_{qo} / I_{do}$, the optimal ratio minimizing the total losses can be found under given speed and load condition as (11). In the calculation of (11), the generated torque must be constant for the given operation point as (12).

$$\partial P_{total} / \partial z = 0 \tag{11}$$

$$I_{do} I_{qo} = \text{constant} \tag{12}$$

By solving (11) and (12), optimal ration of torque producing current $z_{optimal}$ can be found as (13)

$$z_{optimal} = \sqrt{\frac{R_s R_m^2 + (R_s + R_m)(w_e L_d)^2}{R_s R_m^2 + (R_s + R_m)(w_e L_q)^2}} \tag{13}$$

The reference flux are calculated from current angle(e)and current vector(I_s) as (14)

$$\left|\Phi_s^*\right| = I_s \sqrt{L_q^2 \sin^2 e + L_d^2 \cos^2 e} \tag{14}$$

Thus, for minimum loss, the $z_{optimal}$ is constant at a given speed and depends on only the motor parameters and motor speed. Therefore, the high efficiency RSM drive can be achieved with simple algorithm.

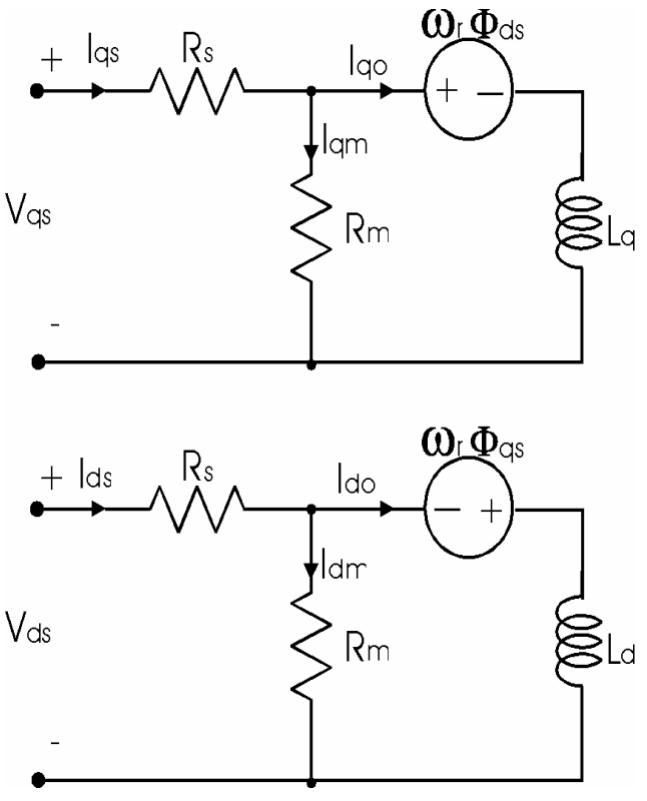

Fig. 4 Equivalent circuit of RSM with core loss

B. Neural Network

In this paper, the NN is utilized to map (14). Fig. 5 shows the configuration of NN used in the proposed algorithm. This NN consists of 2 input node(speed and stator current), 4 hidden layer and 1 output(flux reference). Nodes in the hidden layer and output layer have the sigmoid function. The back propagation(BP) rule to train the NN is used. The off-line training of the network is performed to updating the weights[2].

IV. DIRECT TORQUE CONTROL OF RSM

A DTC of RSM divided into constant flux method and variable flux method. A DTC algorithm is possible to control of directly the stator flux linkage and the electromagnetic torque by the selection of optimum inverter switching pattern. The selection is made to restrict the flux and torque errors within respective flux and torque hysteresis bands, to obtain fast torque response, low switching frequency, and low harmonic losses. So that DTC allow very fast torque response and flexible control of a RSM. The main advantage of the DTC are absence of coordinate transformations and voltage decoupling block, reduced number of controller and effect of motor parameter variation, actual flux-linkage vector position does not have to be determine, but only the sector where the flux linkage is located[3],[12],[13].

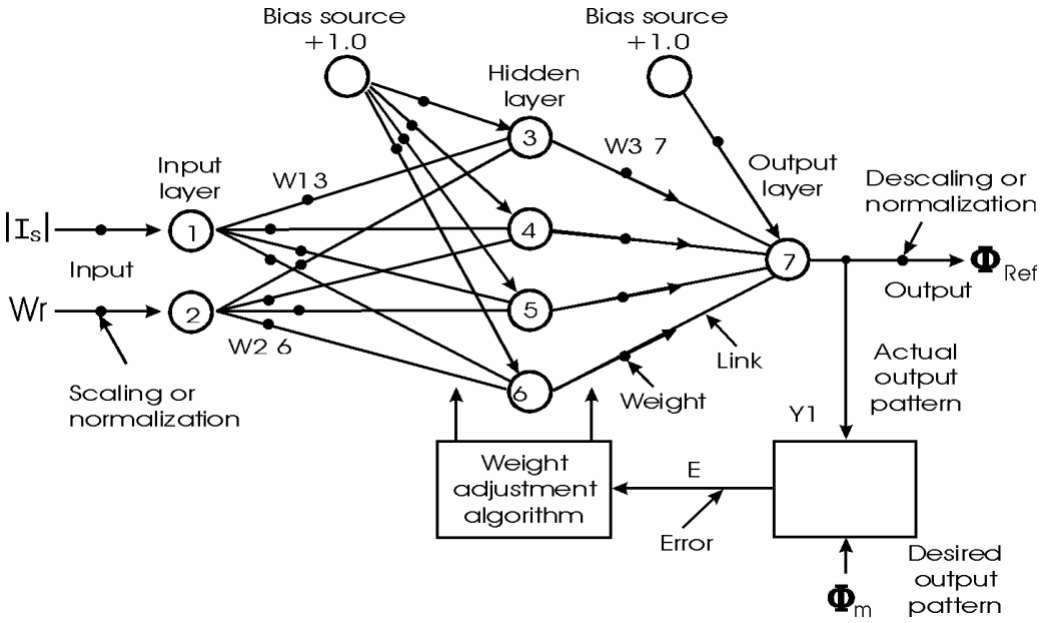

Fig. 5. Configuration of the neural network

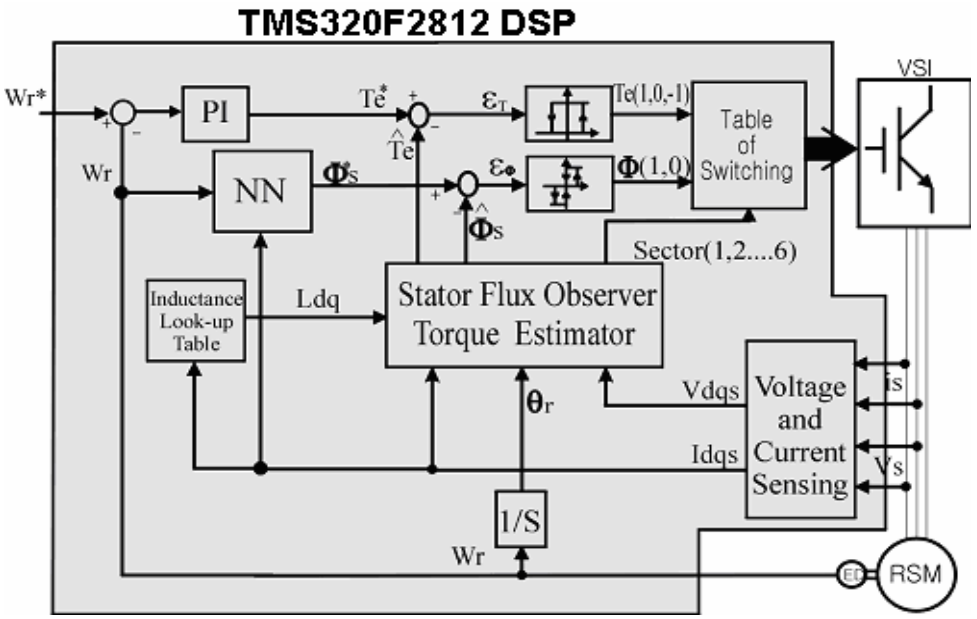

Fig. 6. System configuration

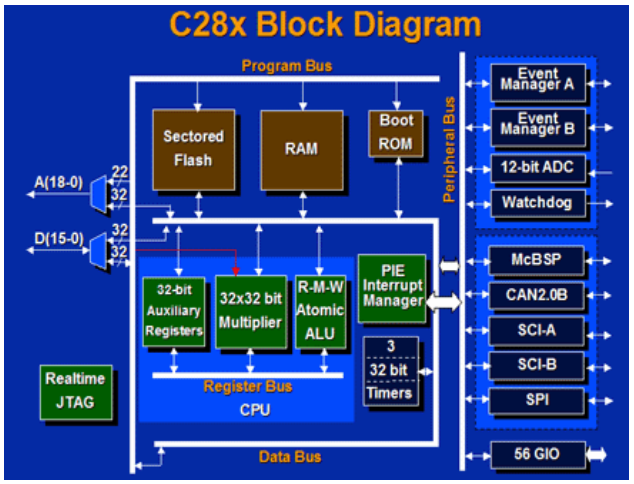

Fig. 7. Functional block diagram of TMS320F2812 DSP

Fig. 8. A Model of the Reluctance Synchronous Motor

TABLE I
APPLIED MOTOR PARAMETERS

Inertia moment	0.003	Rs	1.0[ohm]
Poles of stator	4	Rated torque	4.0[Nm]
Poles of rotor	4	Rated current	5.0[A]
Rated output	1.0[kW]	Lq	28[mH]
Rated rpm	2400[rpm]	Ld	72[mH]

V. SYSTEM CONFIGURATION

Fig.6 shows the applied system configuration. The control system consist of IGBT voltage source inverter(VSI), stator flux observer, two hysteresis controllers, a neural network, an optimal switching look-up table, and TMS320F2812 DSP controller by using fully integrated control software. In order to remunerate nonlinear inductance, be used compensated L_d and L_q value against d-axis and q-axis current

The reference flux is made to maintain current angle within optimum angle, to obtain optimal efficiency with neural network. Table 1 shows applied motor parameters.

A. TMS320F2812

The TMS320F2812 DSP is the newest member of the TMS320C2000 DSP platform. The TMS320F2812 is a very efficient C/C++ engine, hence it enable to use math algorithms and neural network algorithms using C language. The TMS320F2812 has 6.67ns' instruction cycle(150MIPS) and the 32 x 32-bit MAC. These high performance feature is removes the need for a second processor in many systems and enable the it to efficiently handle higher numerical resolution problems [14].

The TMS320F2812 DSP has hardware features such as 12bit ADC(80 ns, 16channel), PLL base clock module, 56 digital I/O, 3 external interrupt, 4 general purpose timer, 3 CPU timer(32 bit), 1.8V core, 3.3V I/O and 16 PWM.
Fig. 7 shows the functional block diagram of TMS320F2812 DSP.

VI. EXPERIMENTAL RESULTS

In this paper, an experimental study of the optimum-efficiency control of the RSM using neural network with direct torque control was carried out. In order to obtain optimum efficiency, optimum current angle was mathematically delivered. Fig. 8 shows photo of applied RSM with a flux barrier rotor type. Fig.9 show static efficiency versus torque characteristics of constant flux control and proposed control at various speed conditions. From the results, the improvements of efficiency for the proposed method are remarkable especially at light load condition.

Fig. 10 and 11 show dynamic characteristics of constants flux control and proposed control. In these figures, speed command is changed by 1000 to -1000[rpm]. Fig.10(a) represents characteristics of speed response at constant flux control, (b) waveform of stator flux linkage at constant flux control. Fig.11(a) shows characteristics of speed response at proposed control, (b) waveform of stator flux linkage at proposed control. In steady state, flux values of proposed control are maintained at low value compared constant flux control to minimize the machine losses.

Fig. 12 show dynamic characteristics of control algorithm which flux is proportional to torque and proposed control algorithms . In this figure, speed command isvaried to –1500 to 0 and 1500[rpm]. Fig.12(a) represents comparison of speed response. (b) represents the enlarged characteristics in transient state. As you can see, the proposed control algorithm, is used neural network, is good dynamic performance than control algorithm, is proportional to torque. (c) represent waveform of stator flux linkage under proposed method. (d) represent waveform of stator flux linkage under control method which flux is proportional to torque.

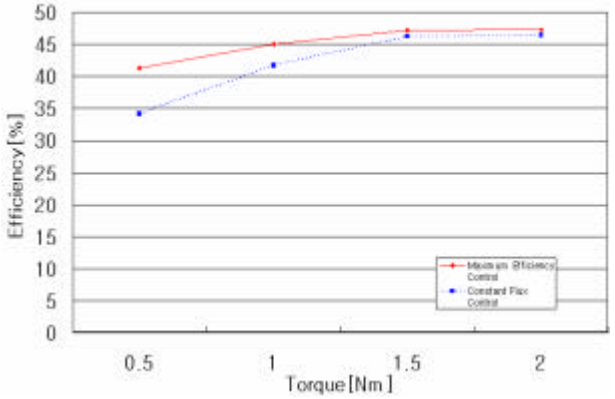

(a) Efficiency characteristics at 300[rpm]

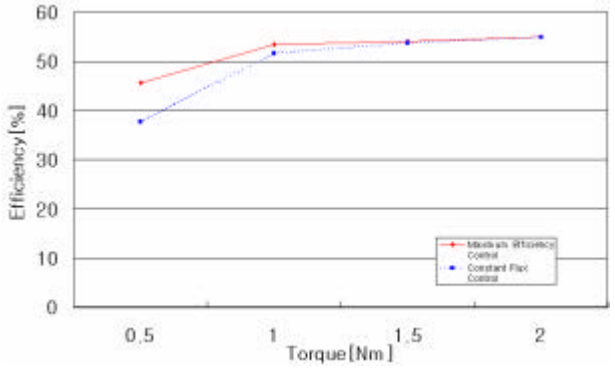

(b) Efficiency characteristics at 500[rpm]

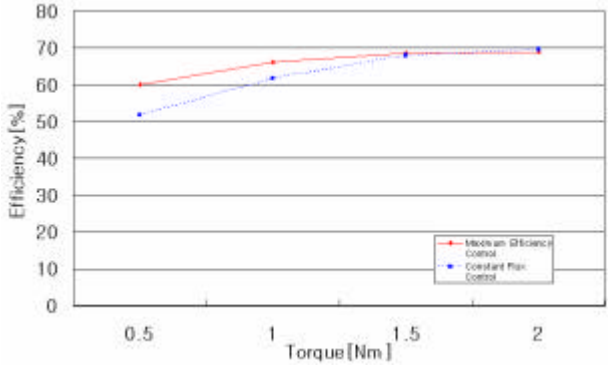

(c) Efficiency characteristics at 1000[rpm]

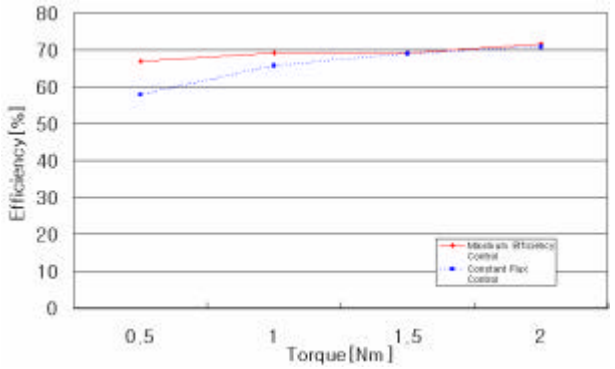

(d) Efficiency characteristics at 1500[rpm]

Fig. 9. Efficiency characteristics versus control method

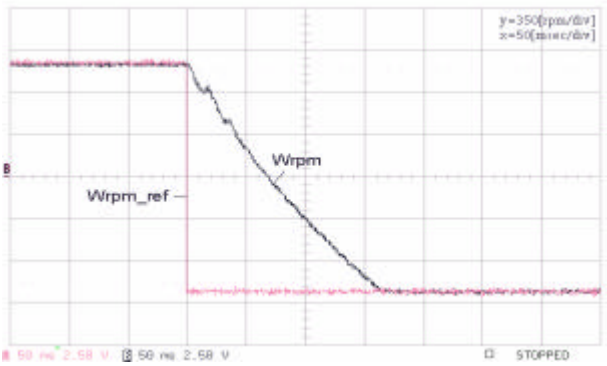

(a) Characteristics of speed response

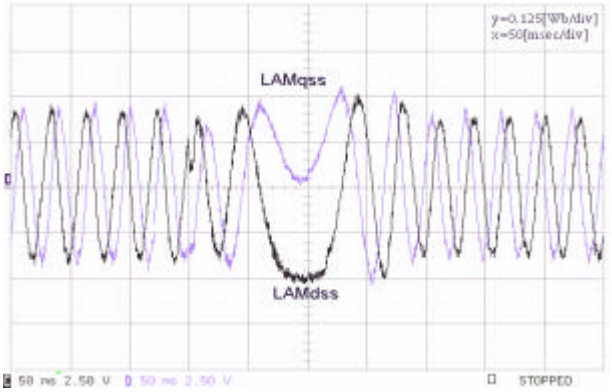

(b) Waveform of stator flux linkage

Fig. 10. Control characteristics of constant flux control

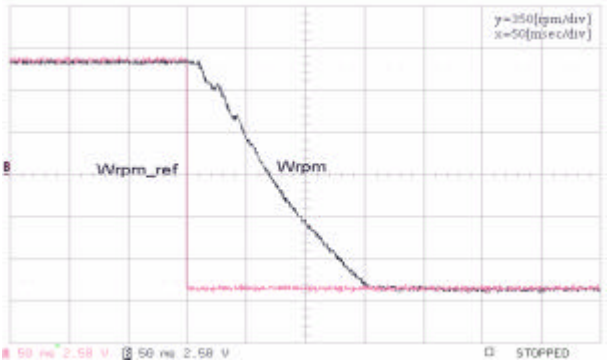

(a) Characteristics of speed response

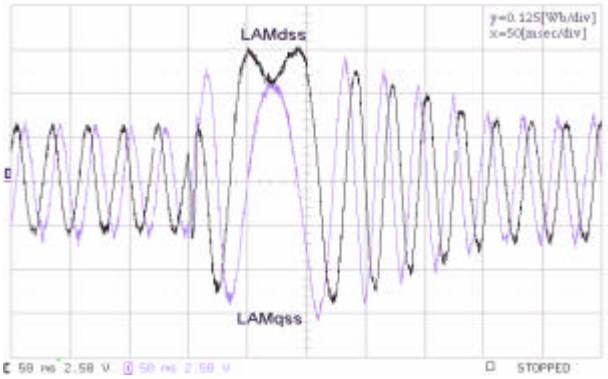

(b) Waveform of stator flux linkage

Fig. 11. Control characteristics of efficiency optimized control

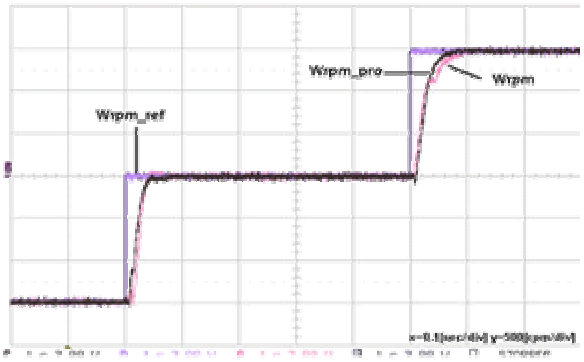

(a) Comparison of speed response

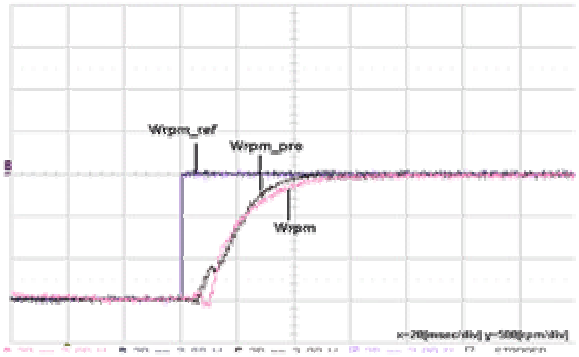

(b) Enlarged speed response in transient state

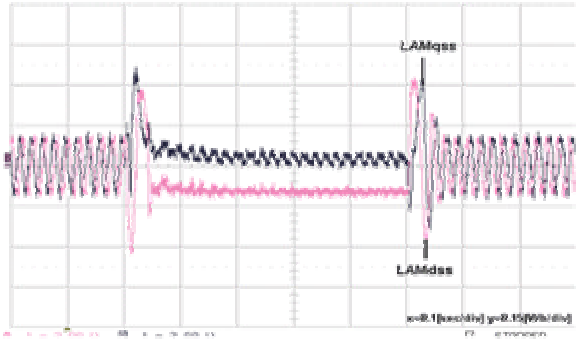

(c) Waveform of stator flux linkage under proposed method

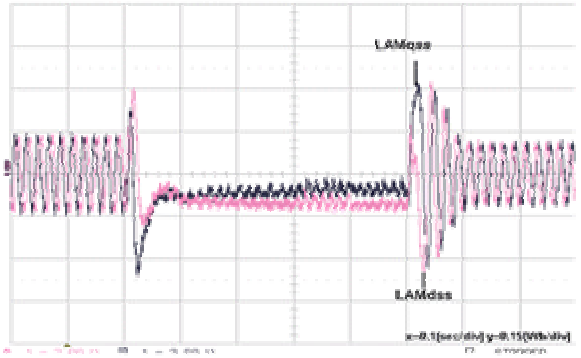

(d) Waveform of stator flux linkage under control method which flux is proportional to torque

Fig. 12. Control characteristics of efficiency optimized control

VII. CONCLUTIONS

For reluctance synchronous motor, torque dynamics can be maintained with controlling the flux level because the generated flux is directly proportional to t he stator current. So, in this paper, to obtain minimize the machine losses and good dynamic response, the stator flux command which is maintained optimum current angle is derived based on equivalent circuit model of the machine. And the NN is trained off-line to map the optimal flux reference. To validate the performance of proposed method carried out experiments with 1.0[kW] flux barrier reluctance synchronous motor. Experimental results shows that the proposed control algorithm allows machine losses in variable operating points to be reduced while keeping a good dynamic response.

REFERENCE

[1] Hyeoun-Dong Lee, Seog-Joo Kang, and Seung-Ki Sul, "Efficiency-Optimized Direct Torque Control of Synchronous Reluctance Motor using Feedback Linearization, " IEEE Trans. on IE, Vol. 46, No. 1, pp. 192-198, Feb. 1999.

[2] Seog-Joo Kang, and Seung-Ki Sul "Efficiency Optimized Vector Control of Synchronous Reluctance Motor." IAS '96., Vol. 1, pp. 117-121, 1996.

[3] Peter Vas, Sensorless Vector and Direct Torque Control, Oxford Press, 1998.

[4] T. Matsuo, and T. A. Lipo, "Field Oriented Control of Synchronous Reluctance Machine," in Proc. PESC.1993.

[5] Hyeoun-Dong Lee, Seog-Joo Kang, and Seung-Ki Sul, "Efficiency-Optimized Direct Torque Control of Synchronous Reluctance Motor using Feedback Linearization, " IEEE Trans. on IE, Vol. 46, No. 1, pp. 192-198, Feb. 1999.

[6] H. Murakami, Y. Honda, S. Morimoto, and Y. Takeda, "Performance Evaluation of Synchronous Reluctance Motor and the Order motors with the Same Distributed Winding and Stator Configuration," T.IEEE Japan, Vol. 120-D, No.8/9, pp. 1062-1074, 2000.

[7] A. Vagati, and T. A. Lipo, "Synchronous Reluctance Motors and Drives : A New Alternatives," IEEE Industry Application Society Annual Meeting Tutorial, 1994.

[8] R. E. Betz, R. Lagerquist, M. Jovanovic, and T. J.E. Miller, "Control of Synchronous Reluctance Machines," IEEE Transactions on Industry Applications, vol. 29, no. 6, November/December, pp. 1110 1121, 1993.

[9] Seog-Joo Kang, and Seung-Ki Sul "Efficiency Optimized Vector Control of Synchronous Reluctance Motor." IAS '96., Vol. 1, pp. 117-121, 1996.

[10] W. L. Soong, D. A. Staton, and T. J. E. Miller, "Validation of Lumped-Circuit and Finite-Element Modeling of Axially-Laminated Brushless Motors," IEEE Conference on Electrical Machines and Drives, pp. 85 90, 1993.

[11] Iron Boldea, Reluctance Synchronous Machines and Drives, Oxford Science, 1996.

[12] A. Kilthau, and J.M. Pacas, "Sensorless Control of the Synchronous Reluctance Machine", JPE, Vol. 2, No. 4, pp3 95-103, April, 2002.

[13] Min-Huei Kim, Nam-Hun Kim, Dong-Hee Kim, Shigeru Okuma, and James C. Hung, "A Position Sensorless Motion Control System of Reluctance Synchronous Motor with Direct Torque Control", ISIE 2002, pp.1148-1153, 2002.

[14] Hamid A. Toliyat, and Steven Campbell, DSP-Based Electromechanical Motion Control, CRC press, 2004.

High-Speed Drives with Permanent-Magnet Machines and Active Magnetic Bearings

A. Binder
Electrical Energy Conversion, TU Darmstadt
Landgraf-Georg-Str. 4, 64283 Darmstadt, Germany
++49-6151-16-2167 / fax -6033
Email: abinder@ew.tu-darmstadt.de

***Abstract*—Permanent magnet technology allowed – together with advances in glass and carbon fiber shell development – design of high-speed drives with surface mounted magnets. Use of double-layer pitched winding, leading to flux distribution with small field harmonics, and low loss sheets result in low additional losses at high speed and sine wave supply. Inverter supply needs filtering to keep additional losses low. Stator water-jacket cooling contributes to compact motor design. Compared with high-speed copper cage induction motors the PM synchronous machines are superior in power density, lower losses and winding temperature. Measured results on 24000/min, 30 kW, induction and PM machines with grease lubricated spindle bearings are presented along with magnetically levitated 40000/min, 40 kW PM prototype machines. Magnetic bearings allow raising of speed and offer additional functionality such as active imbalance compensation.**

I. INTRODUCTION

It is technically and economically profitable to use high speed applications with direct drives, because they do not need any gear units as additional mechanical components ! It is possible to use them in machine tools performing high speed cutting with an improved cut quality and reduced processing time. Typically, speed in range of 15000 to 80000/min is required for a cutting power of up to 100 kW.

Applications of high-speed drives in compressors lead to clearly reduced unit volume for both the compressor and the drive at a given volume rate of flow and back-pressure. Typically, the speed ranges from 40000 to 60000/min at a compressor power of typically 50 to 500 kW. No field weakening of electric machine is applicable, as compressor power rises with third power of speed. So surface mounted permanent magnet rotors are well applicable. High-speed trend is also existing for larger compressor motors. Due to their bigger rotor diameter, speed in the range of 8000 to 10000/min has to be counted already as "Hi-Speed" application with typical compressor power of 5 to 15 MW.

Micro gas turbines are considered in the trend today for applications in the distributed power system which is intensely discussed. The high speed turbines require a special Hi-Speed generator in order to spare any gear units.

Other examples for the applications of Hi-Speed drives are motor-generators for flywheel storage, starter-generators for airplane propulsion units or braking machines for test rigs e.g. for *Formula 1* internal combustion engines.

The gearless direct drives demand special Hi-Speed electrical machines. The design and behavior of these machines is discussed in this paper !

The advantages of the Hi-Speed drives are:

- *No gear units:* No cost for the units, no oil leakage and oil change respectively, operation with low rate of wear, no losses of gear units, low noise and higher overload capacity.
- *Small motors*: The high speed at a low torque makes a high power possible. The motor size is determined by the torque, therefore, in spite of the high power it is possible to use a small motor ("power from speed") which leads to a low weight construction.
- *Concept of integrated motor applicable:* The compact and volume-reduced construction allows the integration of the motor into the machine module. This is supported by the low amount of components (no gears), which reduce the total "parasitic mass" (less couplings). The integration of the drives stimulates new construction varieties in the machine manufacturing.
- *Improved dynamics:* Avoiding mechanical transmission elements (gears, couplings) leads to mechanically stiff drives, which can be controlled with a higher control quality ("dynamic" control).

II. MOTOR DESIGN RULES

DC-drives are less convenient for Hi-Speed applications due to the problems of brush contacts and commutator strength. But, there are various AC-motor concepts which are applicable in high-speed drives [7].

- **Induction Squirrel-Cage-Rotor Machines** [1]: They can be operated in the field-weakening range, where it is possible to limit the converter power for applications with constant power operation. No encoders are necessary for high speed. Highest stress due to the centrifugal forces are allowable when using special massive rotor without any cage.
- **Permanent-Magnet Synchronous Machine** [5]: Thanks to the excitation of the rotor fields "requiring no excitation current", it is possible to reduce the losses which is significant when considering that the Hi-Speed drives have high additional losses. In case of surface mounted magnets, glass fiber or carbon fiber bandages are necessary to fix the magnets. For rotors with buried magnets [8], the rotor plate itself fixes the magnets. The field-weakening operation for the rotors with buried magnets is easier to perform than with rotors with surface mounted magnets.
- **Homopolar Synchronous Machines**: This machine has a variable DC-excitation in the stator, therefore it

is easy to perform field-weakening. The unwound rotor is mechanically very rugged. However, the motor utilization is lower than other motor types in consequence of its principles.

- **Switched Reluctance Motors**: This motor type has also a rugged unwound rotor and good field-weakening performance. However, a special converter is necessary for its operation. The rotor is built using toothed-wheel principles. This requires measures to limit the friction and windage loss, which is generated by the pump effect at high speed.

Electromagnetic and geometric design parameters for high-speed motors are current load A, flux density B, current density J, rotor and average bearing diameter d and d_m, and the active rotor length l_{Fe}. Machine power

$$P \sim d^2 \cdot l_{Fe} \cdot A \cdot B \cdot n \qquad (1)$$

rises with the speed n. For low speed machines winding temperature rise $\Delta\vartheta$ is mainly determined by the current density and current load

$$\Delta\vartheta \sim A \cdot J \qquad (2)$$

and by the cooling system e.g. stator water jacket cooling and increased thermal conductivity from winding overhangs to cooled stator housing. In high speed machines the following losses, which rise with speed, are much more dominant in determining the winding heating, namely the iron losses,

$$P_{Fe} \sim B^2 \cdot n^x, \qquad x \approx 1.8 \qquad (3)$$

the friction and windage losses,

$$P_{fr+w} \sim d \cdot l_{Fe} \cdot n^y, \qquad y = 2 \ldots 3 \qquad (4)$$

and the additional stray load losses

$$P_{ad} \sim I^2 \cdot n^z, \qquad z = 1.5 \ldots 2 \quad . \qquad (5)$$

These losses must be kept within reasonable limits by keeping B low, by using windings with low space harmonic flux wave generation and by using inverter output filters to reduce current time harmonics. Further it is important to keep the tangential mechanical stress due to centrifugal force

$$\sigma \sim v_u^2 \qquad (6)$$

within allowable material values. Thus, the rotor circumference speed is a main parameter of "Hi-Speed"-operation

$$v_u = d \cdot \pi \cdot n \quad , \qquad (7)$$

which ranges between 100 m/s and 250 m/s at maximum speed operation. Over-speed test according to IEC 60034-1 demands 20% higher speed, at which the machine must be able to run for 2 minutes without any inelastic deformation. Mechanical stiffness of rotor correlates with natural bending frequency of the rotor, which depends on rotor dimensions.

$$f_e \sim \frac{d}{l_{Fe}^2} \qquad (8)$$

This requires a minimum rotor diameter in case of operation at $n < f_e$. The average bearing diameter d_m depends strongly on the rotor diameter. The corresponding bearing circumference speed

$$v_m = d_m \cdot \pi \cdot n \sim d_m \cdot n \qquad (9)$$

determines bearing life. For grease lubricated ball bearings limit is $d_m \cdot n \le 5 \cdot 10^5 \, mm/\min$. Special ball bearings such as spindle bearings with reduced ball mass or hybrid bearings with ceramic balls allow increased speed. Minimum oil lubrication instead of grease, which makes oil pump necessary, allows $d_m \cdot n \le 2.5 \cdot 10^6 \, mm/\min$. Instead of this, at very high speed, active magnetic bearings are also used.

III. COMPARISON OF INDUCTION VS. SYNCHRONOUS MACHINE

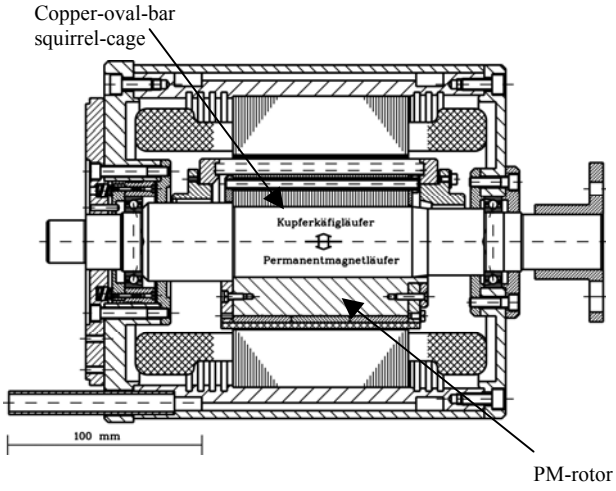

Fig. 1. 30 kW, 24000/min, 4 pole Hi-speed 3-phase AC machine: above: induction machine, below: synchronous PM rotor

For identical stator construction (Fig. 1) with water jacket cooling a 4 pole induction machine with copper oval bar squirrel cage and a synchronous machine with permanent magnet rotor with surface mounted Sm_2Co_{17} magnets, fixed by fiber glass sleeve, were compared by simulation and experiment considering their operation behavior. The rotors

(a)

(b)

Fig. 2. Four pole rotors of Fig.1: (a) PM-rotor with surface mounted magnets, before mounting of glass fiber sleeves, (b) Copper cage induction rotor: Oval bars and rings

(Fig. 2) used spindle bearings with grease lubricating and axial springs for axial pre-loading. Both motors were designed for 30 kW nominal power at 24000/min. The main rotor dimensions were identical: $d = l_{Fe} = 90$ mm. The power density as nominal power referred to the motor active volume equaled 25 kW/dm^3 [10].

Motor	Induction copper cage	Synchronous PM-Sm_2Co_{17}
$U_{s,LL}$ (line-to-line), I_s, cos φ	330 V, 72.8 A, 0.77	311 V, 62.2 A, 0.95
Speed, slip	23821/ min, 0.008	24000 / min, 0.0
Output power	29933 W	30157 W
$P_{Cu,s}$, $P_{Cu,r}$	537 W, 251 W	353 W, 0 W
P_{Fe}, P_R, P_{ad}	650 W, 480 W, 49 W	660 W, 440 W, 100 W
Cooling-water temperature	Inlet: 41.5°C Outlet: 47.5°C	Inlet: 44.4°C Outlet: 48.1°C
Cooling water rate of flow	3.25 l/min	3.25 l/min
Heating: Winding overhang / slot *)	84.5 K / 68.5 K	42 K / 36 K
Efficiency	93.7 %	95.1 %

*) Temperature rise over water-outlet temperature

Table 1: Comparison of steady-state measurements at thermal load runs at a sine wave supply 800 Hz for prototype induction and PM-synchronous motor

The measurement results of the thermal load runs - performed at the institute test bench (Fig.3) - show that the induction machine generates higher losses and heating for a sinusoidal power supply with 800 Hz at similar power level.

Note, that the chosen induction motor is already a machine type with low losses compared to other constructions for squirrel-cage motor in high-speed applications like aluminum die-cast rotors [11]. The lower losses and temperature rise of the PM synchronous machine recommends this type for further investigation.

IV. Measures For Current Smoothing

The current time harmonics due to the machine power supply by a converter have significant influence on the additional losses and heating of the Hi-Speed drives because of the low winding number and inductance as a consequence of the high speed. Therefore, the current harmonics with relatively high amplitudes generate in turn magnet fields that induce additional eddy-current losses [6]. Loss calculations and experiments (Fig. 3) were done for comparing different power supply modes. The PM synchronous motor was supplied at 800 Hz with power generated by

a) a sinusoidal voltage from synchronous generator,
b) a PWM-IGBT Voltage Source Inverter (VSI) at a switching frequency of 12 kHz,
c) a VSI with six-step modulation and variable DC link voltage 0...520 V.

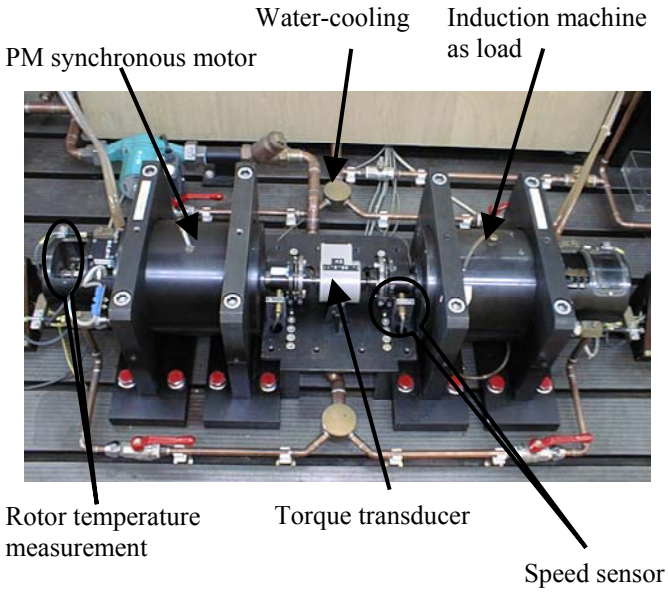

Fig. 3. Test bench for 24000/min, 30 kW, for thermal load run

Additionally, for the VSI supply according to b) a stator current smoothing [12] is implemented by
b1) an output choke and alternatively by
b2) a sine wave filter.

The losses and temperature rise in the stator windings and rotor magnets were measured. Rotor temperature signal transmission was implemented by thermo-couple wires via measurement slip rings for the on-line measurements. The VSI PWM supply experiment *without the current smoothing* resulted in a temperature of the magnets beyond 180°C, thus surpassing the limit of the glass-fiber epoxy resin matrix. This high temperature rise of more than 120 K made the cancellation of the heat run necessary. In the other experiments, the temperature rise of the magnets was always lower than 90 K and the heating of the windings lower than

60 K (Fig. 4).

Following "ranking of heating" shows the results of the experiments:

b1)	PWM with output choke	+
c)	block voltage	++
b2)	PWM with sinusoidal filter	+++
a)	sinusoidal converter	+++

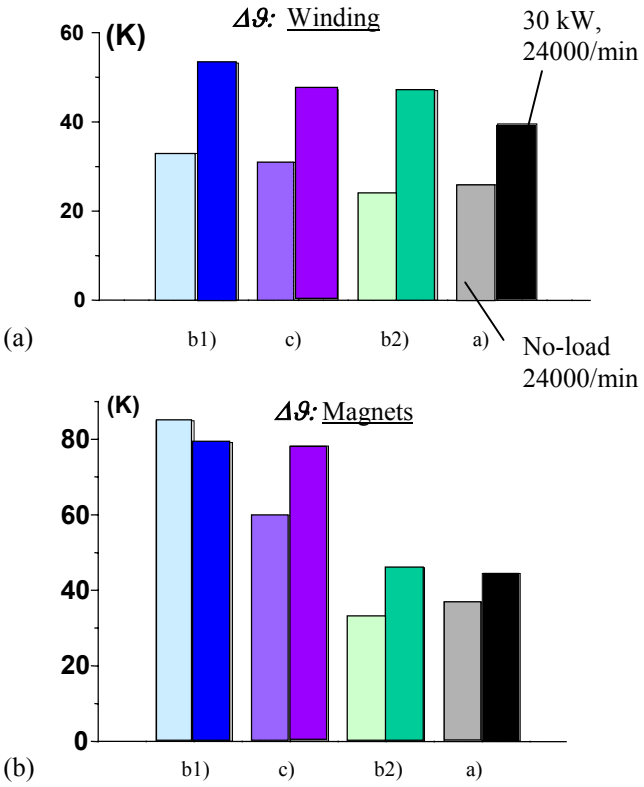

Fig. 4. Measured temperature in 30 kW, 24000/min PM synchronous machine: b1) PWM with output choke, c) six-step modulation, b2) PWM with sine wave filter, a) sinusoidal supply

Hence, for the Hi-Speed drive the six-step modulation is preferred instead of the PWM method. This is contrary to the established rules for common industry applications, where six-step modulation with lower fundamental frequency compared to the PWM method, generates higher losses in the electrical machines. The established method to use sine wave filter for the Hi-Speed induction drives is also well-suited for the PM synchronous technology. The filtering is very important in case of massive rotor yoke, which is often chosen to provide higher mechanical rotor stiffness. Experiments and numerical calculations showed that even the time harmonic magnet fields in case of the six-step modulation lead to high eddy current losses in the massive rotor yoke. This means that only the sine wave filter supply is a good solution in that case.

V. HIGH-SPEED DRIVES WITH ACTIVE MAGNETIC BEARING

With further increase of speed, the centrifugal impacts on the rolling elements in the bearings will be very high which makes the use of either hybrid bearings with minimum oil lubrication or active magnetic bearings necessary. A drive system (Fig. 5) for 40 kW, 40000/min with radial magnetic bearings was built and tested.

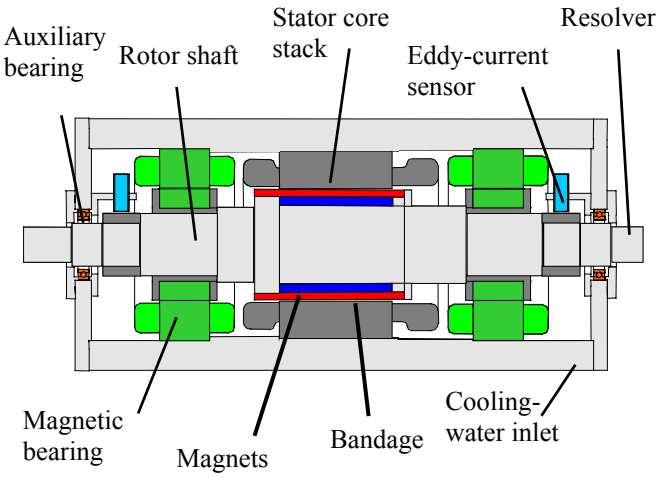

Fig. 5. Cross section of 40 kW, 40000/min, PM synchronous motor with radial active magnetic bearings

Bearing type	*Spindle bearing*	*Hybrid bearing, minimum oil lubrication* or *Magnetic bearing*
Power / Speed	30 kW / 24000/min	40 kW / 40000/min
$n \cdot d_m$	960 000 mm / min	2 500 000 mm / min
Circumference rotor speed	v_u = 113 m/s	v_u = 180 m/s
Bandage (sleeve)	Glass-fiber	Carbon-fiber
Over speed n_{ov}	28800 / min	48000 / min

Table 2: Comparison of bearing and rotor characteristic for the manufactured drives at n_N = 24000/min and 40000/min

Specifications of the radial magnetic bearings (Fig. 6) are:

1) $F_{Bearing}$ = 1200 N, 8 magnetic poles (x-and y-axis)
2) DC base excitation: N_0 = 45/pole, I_0 = 4 (6) A
3) Controllable excitation: N_1 = 18/pole, I_1 = 15 A
4) Bearing dimension: Laminated stator: d_a = 154 mm, d_i = 90 mm, l_{Fe} = 40 mm
5) Bearing air gap: δ_{Lager} = 0.4 mm,
6) Air gap of auxiliary bearing: δ_{aux} = 0.2 mm

The weight force of the rotor for each bearing is 100 N, this means 12 times higher force capability of the bearing which enables a high control dynamic during the disturbance of the rotor position. No axial bearing was used because of the small external force in axial direction. The axial guidance is provided by axial magnetic attraction of the motor rotor in the stator bore. The advantages and disadvantages of the drives with magnetic bearings are presented in detail in [2] and [3]. In any case, magnetic bearings have a high potential which makes it a technically very interesting solution. Furthermore, the use of permanent

magnet instead of use of DC base electric excitation makes it possible to build smaller bearings with lower losses at the same time. In particular applications e.g. the flywheel storage, the magnetic bearing is even indispensable.

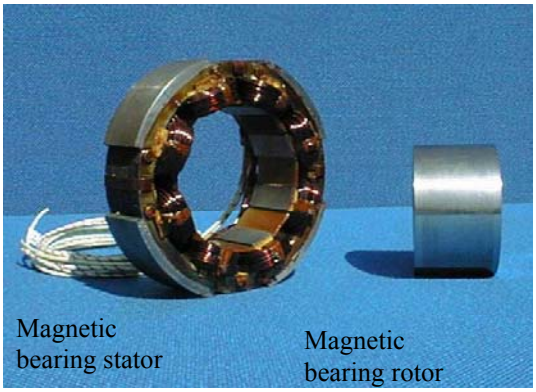

Fig. 6. Radial magnetic bearing for 1200 N, 40000/min

VI. Design of Bandages for Permanent-Magnet Rotors

The bandages are manufactured as sleeves from glass-fiber or carbon fiber which is imbedded into epoxy resin matrix. With this method, the pre-stressing and thus the pressing force on the surface-mounted magnets are well-defined. At very high circumference speed above 150 m/s, the glass fiber bandages are no longer able to fix the magnets. Here, the carbon fiber technology offers a solution with a maximum allowable tangential stress of carbon fiber in epoxy matrix of $\sigma_{t,lim} = 1100$ N/m^2 in the sleeve.

The rotor is manufactured in the way that the "sleeves" are either pressed on the rotor or the "cold" rotor is shrunk into the sleeve using the cold shrinking process with liquid nitrogen. The tangential mechanical stress in the sleeves is caused by different forces. Moreover, on rotors with pole gaps between the magnets (pole coverage ratio $\alpha_e < 1$) there exists an additional bending stress in the bandage.

Stress factors for the bandages are:

- *Temperature:* The shaft and magnets expand, but the bandage does not expand significantly, so with increasing temperature tangential bandage stress increases.
- *Centrifugal force*: It consumes a part of the bandage pre-stressing with higher speed.
- *Bandage pre-stressing:* Generated by the shrinking process, a positive residual pressure on magnets at n_{ov} is necessary for fixing the magnets, as gluing is not safe enough.
- *Influence of pole gaps:* Due to bending torque only a lower centrifugal force is admissible.
- *Magnet edges:* They cause a local notch effect on the bandage
- *Axial expansion*: Due to coupling of radial and axial expansion, additional stress may be induced by axial pressing of bandage.

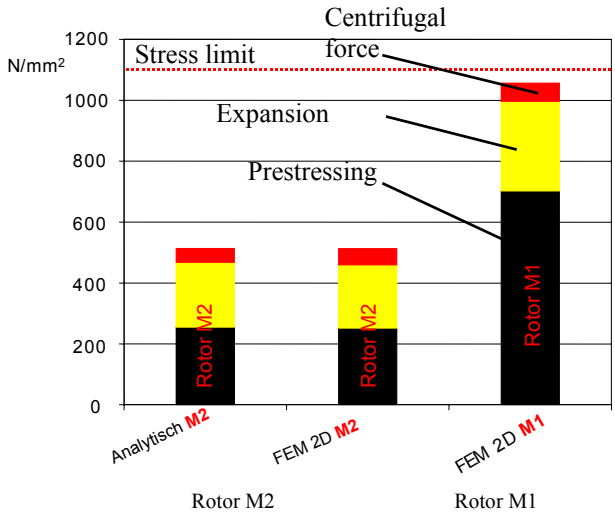

Fig. 7. Calculated *von Mises* equivalent stress in carbon fiber bandage at over-speed 48000/min, 150°C, with finite elements: right: rotor M1, left: rotor M2 – compared with analytical method

Two rotors M1 and M2 were manufactured for the drive system with 40000/min, 40 kW. Rotor M1 had pole gaps filled with resin, which lead to additional bending stress, so two-dimensional stress calculation was necessary, using Finite Element Package ANSYS, assuming bandage as orthothropical shell. As bandage and magnets were rather thick (Table 3), this rotor had increased mechanical stress (Fig. 7). Rotor M2 had no gaps, so cylindrical symmetry was given. Analytical and Finite Element calculation therefore yielded nearly same results of rather low bandage stress.

Rotor type	*M1* *"strong" magnets*	*M2* *"weak" magnets*
Outer diameter d_a	88.6 mm	83.6 mm
Bandage thickness h_b	5.7 mm	4.7 mm
Magnet height h_m	7 mm	4.5 mm
Pole coverage α_e	0.87	1.0
Air gap δ	0.7 mm	3.2 mm
Shrink rule ΔD	0.24 mm	0.13 mm
Mounting of the bandage	Axial pressing	Cold shrinking of the rotor

Table 3: Data of two different PM rotors M1 and M2 for magnetically levitated PM synchronous machine 40000/min, 40 kW

Both rotor magnets provide sufficient capability against continuous de-magnetization. Of course, rotor M2 with "weaker" magnets provides the lower capability. The calculations show that at an assumed temperature of $\vartheta_{rotor} = 150°C$ the total stress of the bandage as a sum of pre-stressing, thermal expansion and centrifugal force for M1 is two times higher than M2. Although rotor M1 also fulfilled stress limit, this rotor surprisingly crashed already at 35 000/min. Obviously, the real allowable stress in M1 was lower than 1100 N/mm^2, perhaps due to some defect of material, which would explain that bandage tore off already at 35000/min (Fig. 8). Rotor M2 was successfully tested up

to 40000/min.

a)

Burst length

Total active length

b)

Fig. 8. (a) Damaged rotor M1 after crash, (b) New rotor M2 with reduced stress

VII. CONTROL OF MAGNETIC BEARINGS

Uncontrolled magnetic bearings using attractive force on magnetized iron are unstable according to *Earnshaw* theorem. The function of the controlled magnetic bearings together with the elastic rotor is significant for the low flexural vibrations of high-speed drives. If the bending natural frequency is at least 40% beyond the maximum operation speed (as in our case), then the rotor may be regarded as rigid. However, the 1st and 2nd rigid body vibration mode of the rotor in the bearings must be taken into account. The installed active magnetic bearings are equipped with analogue PID-control and 50 kHz MOS-FET power stage. The rotor position was measured by eddy-current position sensors. In Fig. 9 experimental results for *x*- and *y*-position of drive-end radial magnetic bearing is shown a) for take-off and b) for impulse response at $I_0 = 4$ A base excitation current. At take-off the rotor hits in y-direction the auxiliary bearing at air-gap 0.2 mm, before being centered in rotation axis. A simulation program was set up to investigate different control methods for further dynamic improvement. So, simulating the controlled bearings and the levitated rigid rotor, following control methods were investigated [13]:

a) PID-control

b) State-space control with disturbance model

c) State-space control with integral part

Simulation result for conventional PID-control showed also hitting of auxiliary wining during take-off.

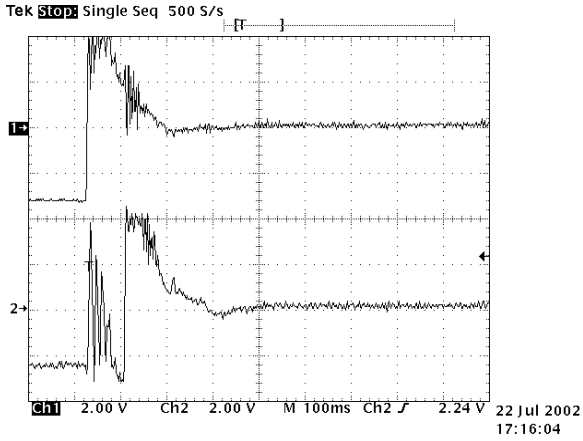

(a) Turn-on of the magnetic bearing (2V/Div., 100ms/Div.)

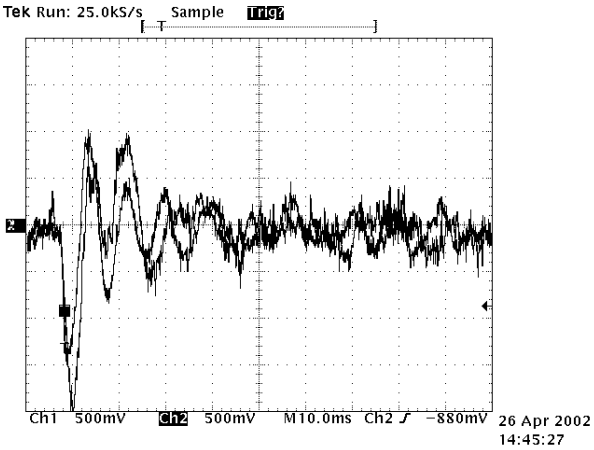

(b) Impulse response of a radial it with hammer at shaft end (500mV/Div., 10ms/Div.)

Fig. 9. Measurement of the shaft center point at $n = 0$ for *x*- and *y*-axis position with a position scale of $c_{x,y} = 20$V/mm: a) Take off, b) Impulse response

The methods b) and c) have higher control value due to better dynamic response, however they need a digital control system. The design of the control system for the state-space control may be refined, if the elastic rotor is simulated.

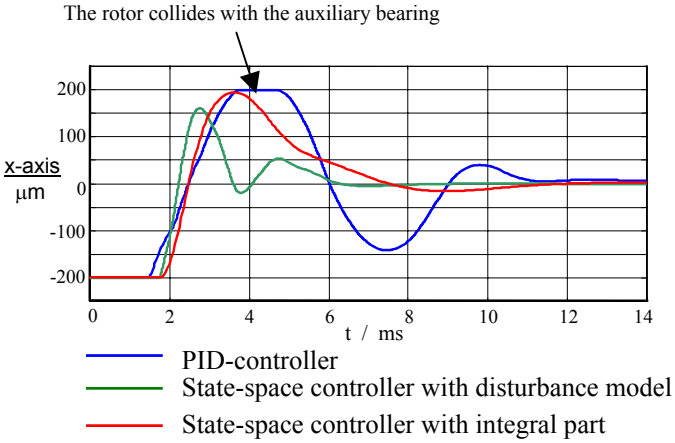

Fig. 10. Calculation of the vertical position $x(t)$ at $n = 0$ during the take off. Specified value: $x = 0$ at $t = 0$ and $n = 0$ and $I_0 = 2$ A.

VIII. Benefits of Magnetic bearings and Outlook

Interesting features of magnetic bearings are:

- Use of the bearings as position sensors by inductance measurement
- Frequency response measurement of the drive at the standstill in order to calibrate the control system model
- Active positioning of the rotor by the bearings (e.g. displaced grindings in machine tools)
- Active imbalance compensation (e.g. variable unbalance force) by the bearings

An option to the magnetic bearing control using DC-converters is the "bearingless" motor. There, the levitation function is performed by additional three-phase windings in the slots of the stator core stack. Two three-phase windings with different pole numbers (e.g. 2 and 4), the drive and levitation winding, generate both the torque and the radial levitation force. Hence, shortening of the drive and the use of a three-phase converter is possible.

IX. Conclusions

Hi-Speed drives with very good performance are available on the market. They provide a high innovation potential for many applications, offering the possibility of reducing the amount of mechanical components.

Development of high-speed drives needs special know-how, namely knowledge of the combination of magnetic, thermal, and mechanical inter-action, as well as knowledge in dynamics, control theory and applications of power electronics.

The advances in the magnetic bearing technology will broaden their utilization in many fields. The application of PM materials for the motors and for the base excitation of the magnetic bearings reduces the losses.

The digital control makes additional functions possible in addition to improved control behavior e.g. bearing and drive diagnostic.

"Bearingless" concepts lead to the use of only three-phase converters instead of DC choppers and allow axially shorter machines.

References

[1] Werth, L.: Betriebsverhalten und Wirkungsgrad von umrichtergespeisten Käfigläufermotoren für hohe Drehzahlen, Diss. TU Darmstadt, 1990, Shaker-Verlag

[2] Schweitzer, G.; Traxler, A.; Bleuler, H.: Magnetlager, Springer, Berlin, 1993

[3] Jungkunz, C.; Binder, A.: Entwurf und Bau des Prototypmagnetlagers SIMAB, 3. Zittauer Workshop Magnetlagertechnik, 11.-12. Sept.1997, p.21-31

[4] Klohr, M.; Binder, A.; Eichhorn, J.: Bemessung und Simulation eines magnetgelagerten Permanentmagnetantriebs (MAGPERM), 40 kW, 40000/min, 4. Workshop Magnetlagertechnik, Kassel, 30.9.-1.10.1999, 7 pages

[5] Greifenstein, E.: Entwurf, Konstruktion und experimentelle Untersuchungen von hochtourigen Drehstrommaschinen mit Käfigläufer und Permanentmagnetläufer, Diss. TU Darmstadt, 1999, Shaker-Verlag

[6] Binder, A.: Analytical Calculation of Eddy-Current Losses in Massive Rotor Parts of High-Speed Permanent Magnet Machines, Proceedings of the Symposion on Power Electronics and Electrical Drives (SPEEDAM), 13.-16. June 2000, Ischia, p. C2-1 ... C2-6

[7] Binder, A.: Comparison of Motor Types with Respect to System Integration, Proc. Conf. on Integrated Power Systems (CIPS), 20.-21. June 2000, Bremen, p. 151 - 160

[8] Schätzer, C.: Binder, A.; Müller, W.: Vector Optimization of a High-Speed Drive using Two-Dimensional Numerical Field Calculation, COMPEL Vol. 19, No.2, 2000, p. 646 – 650

[9] Lu, T.; Binder, A.; Pfeiffer, R.: Rotor losses in Permanent Magnet High-Speed Machines, Proceedings of the International Conference on Electrical Machines (ICEM), Aug. 2000, Helsinki, p. 608 - 612

[10] Schätzer, Ch.; Binder, A.: Design Optimization of a High-Speed Permanent Magnet Machine with the VEKOPT Algorithm, Proc. IEEE-IAS Annual Meeting, Rome, 8.-12. Oktober 2000, 6 pages

[11] Lu, T.; Binder, A.; Pfeiffer, R.: Wirkungsgradverbesserungen bei Hochdrehzahlantrieben, Proc. Fachkonferenz Elektrische Automatisierung SPS/IPC/Drives, 28.-30. Nov. 2000, Nürnberg, p. 522 - 530

[12] Lu, T.; Binder, A.: Experimental Investigation of the Additional Losses in Permanent Magnet High-Speed Machines under Inverter Operation, Proc. of the Spring Annual Conf. 2001, KIEE/EMECS, 19.-21.4.2001, Jeju, Korea, p.B-10...B-15

[13] Klohr, M.; Binder, A., Hinkelmann, Ch: State space control of a high speed rotor on active magentic bearings, 10th Int. Symp. On Electromagnetic Fields in Electrical Engineering ISEF 2001, p. 593-598, 20.-22.9.2001, Cracow, Poland

[14] Lu, T.; Binder, A.: Losses in inverter-fed permanent magnet high-speed machines, Proceedings of the Symposion on Power Electronics and Electrical Drives (SPEEDAM), 11.-14.June 2002, Ravello, Italy

[15] Klohr, M.; Binder, A.: Design of Carbon Fiber Bandages for High Speed Permanent Magnet Rotors, Proceedings of the Symposion on Power Electronics and Electrical Drives (SPEEDAM), 11.-14.June 2002, Ravello, Italy

[16] Lu, T.; Binder, A.: Analytical and experimental analysis of losses in inverter-fed permanent-magnet high-speed machines with surface-mounted magnets, Proceedings of the International Conference on Electrical Machines (ICEM), 25.-28. Aug. 2002, Bruges, Belgium

A MTPA Control Scheme for an IPM Synchronous Motor Considering Magnet Flux Variation Caused by Temperature

Gubae Kang*, Jaesang Lim, Kwanghee Nam,
Hyung-Bin Ihm* and Ho-Gi Kim*
Division of Electrical and Computer Engineering,
POSTECH University, Hyoja San-31, Pohang, 790-784
Republic of Korea. Tel:(82)54-279-2218, Fax:(82)54-279-5699,
E-mail:kwnam@postech.ac.kr.
*Electric Powertrain Development Team, Advanced R&D Center,
Hyundai Motor Company, Kyungki-Do, 445-706, Korea.

Abstract— **In a hybrid electric vehicle(HEV), an interior permanent magnet(Nd-Fe-B) synchronous motor is widely used. However, the flux density of the Nd-Fe-B magnet is sensitive to the temperature variation. Particulary, in a HEV, the heat coming from internal combustion engine causes high temperature rise of the motor. It degrades the flux density and output torque. In this paper, a maximum torque per ampere (MTPA) control scheme for IPM motor is proposed considering the temperature dependence of the magnet field. With the use of an empirical look-up table, saturation effect is also considered. The effectiveness of the proposed control method is demonstrated through MATLAB/Simulink simulation and experiment.**

I. Introduction

Interior permanent magnet (IPM) synchronous motors are widely used in hybrid electric vehicle (HEV) due to its positive features such as high efficiency, high power factor, and high power density[1]-[5]. Ferrites, ceramic magnets and Neodymium-Iron-Boron (Nd-Fe-B) material are well known material for IPM motor. Particulary, energy density of Ne-Fe-B is superior to the others, Nd-Fe-B magnets are usually adopted for an IPM motor in a HEV application[12]. Since the IPM motor is attached to the engine block, it is always under the influence of engine heat. However, the flux density of Nd-Fe-B magnets changes significantly as temperature changes. The flux variation causes the output torque change for the same current. This will affect the performance of IPM motor and eventually the performance of the HEV.

Normally IPM has different reluctance paths along d and q axes. Specifically, $L_q > L_d$, where L_d and L_q are d, q axis inductances, respectively. Therefore, IPM has a torque contribution from reluctance and d axis current can play a role of increasing the torque. The concept of Maximum Torque Per Ampere (MTPA) control has been emerged as a method of maximizing torque for a given magnitude of current vector[2]. Morimoto et al. modelled the saturation effects on L_d and L_q as linear functions of current magnitude [6]. Sebastian dealt with the temperature effects on the torque production and efficiency of the motor[7]. Park et al. applied MTPA control method to HEV with the use of learning capability of neural network[8].

In this paper, the magnet flux is expressed as a function of temperature. The proposed controller reads the magnet temperature periodically and reflects its dependence on the torque production. Further, MTPA rule is made as a look-up table. Experiments were performed with the real HEV IPM motor (12 pole, V_{DC} = 150V, 78Nm) in the different temperature environments.

II. Model of an IPM Synchronous Motor

The d-q axes inductances of IPM synchronous motors are susceptible to saturation due to high current excitation, and can be modelled by making L_d and L_q as function of the d-q axes currents, i_d and i_q. Further, the magnet flux density changes with temperature. Thus, we need to consider the effect of flux variation with temperature. The dynamics of an IPM synchronous motor in a synchronous reference frame are described as follows [11]:

$$v_d = R_s i_d + \Big(L_d + i_d \frac{\partial L_d}{\partial i_d}\Big)\frac{di_d}{dt} - \omega_r L_q i_q \quad (1)$$

$$v_q = R_s i_q + \Big(L_q + i_q \frac{\partial L_q}{\partial i_q}\Big)\frac{di_q}{dt} + \omega_r L_d i_d + \omega_r \Phi_m(t^\circ) \quad (2)$$

where v_d and v_q are the d- and q-axis stator input voltage, i_d and i_q are the d- and q-axis stator current, L_d and L_q are the d- and q-axis inductance, R_s is the stator resistance, ω_r denotes the electrical angular speed, and $\Phi_m(t^\circ)$ is the PM flux linkage at an arbitrary temperature t°. Note from (1) and (2) that $\partial L_d/\partial i_d$ and $\partial L_q/\partial i_q$ are introduced to reflect the core saturation effect.

The torque of the IPM motor is given by

$$T = \frac{3}{2}\frac{P}{2}\big[\Phi_m(t^\circ) i_q + (L_d - L_q) i_d i_q\big] \quad (3)$$

$$= \frac{3}{2}\frac{P}{2}\big[\Phi_m(t^\circ) I_s \cos\beta + \frac{1}{2}(L_q - L_d) I_s^2 \sin 2\beta\big], \quad (4)$$

where P denotes the number of poles,

$$I_s = \sqrt{i_d^2 + i_q^2} \quad (5)$$

the current magnitude, and $\beta = \tan^{-1}(-i_d/i_q)$ the current phase angle, respectively.

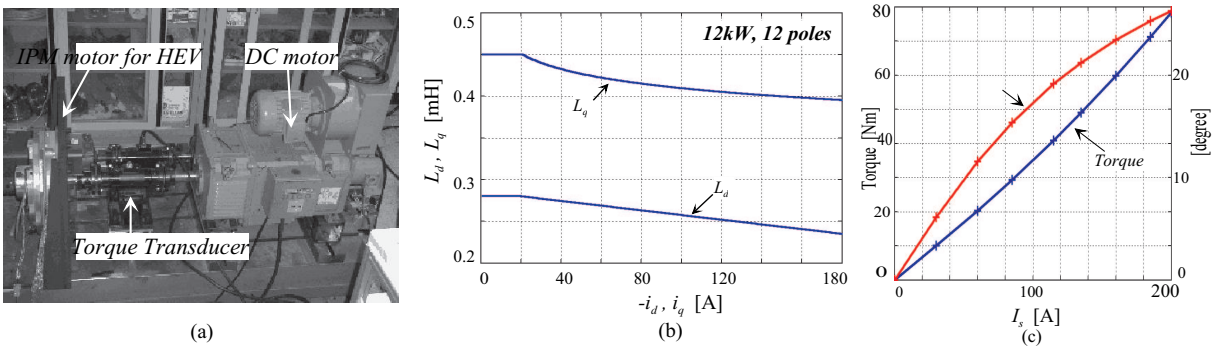

(a) (b) (c)

Fig. 1. (a) HEV motor used in the test. (b) L_d and L_q of the tested IPM motor. (c) Measured torque and current phase angle versus current for MTPA

To achieve MTPA for a given I_s, it should follow that $dT/d\beta = 0$ and $d^2T/d\beta^2 < 0$. Thus, we obtain from (4) the MTPA solution such that [9]

$$\beta = \sin^{-1}\frac{-\Phi_m(t^\circ) + \sqrt{\Phi_m(t^\circ)^2 + 8(L_q - L_d)^2 I_s^2}}{4(L_q - L_d)I_s} \quad (6)$$

Note that (5) and (6) are the transformation map from (i_d, i_q) to the polar coordinate (I_s, β). The inverse transformation is given by

$$i_d = -I_s \sin(\beta), \quad (7)$$

$$i_q = I_s \cos(\beta). \quad (8)$$

III. Look-up Table for MTPA Trajectory

Due to the strong magnetic field of the permanent magnet and the additional field generated by i_d and i_q, core is saturated and correspondingly L_d and L_q decrease. It is not straightforward to express the nonlinear saturation effects. Therefore, it is better to rely on the look-up table in the mapping between torque and (I_s, β).

In the rest of this section, we describe how we obtain the look-up table from experiments. To make the MTPA map, experiment has been done with the dynamo system shown in Fig. 1(a). The HEV motor is mechanically coupled to a 20 kW DC motor via a torque transducer. Parameters of the HEV motor are shown in Table. I. During the test, the PM temperature was kept around $20C^\circ$. Motor was running in speed-control mode, while the HEV motor was operating in current-control mode.

I_s and β are used to find the maximum torque in MTPA instead of (i_d, i_q), since MTPA condition is given by (6). The maximum torque for a given I_s was searched by measuring torque repeatedly while changing β from 0 to 90°. Then after increasing or decreasing I_s, the same search was performed. Repeating this procedure until it covers whole (I_s, β) space. Here, the torque was measured by a torque meter. The MTPA trajectory was represented by a bold line. For the convenience of notation, we denote by $f(I_s, \beta)$ the map from (I_s, β) to T. Fig. 2 shows the result of the test and the MTPA trajectory. The values that do not appear in the look-up table can be found by an interpolation technique.

It should be stressed here that the saturation effect was already reflected in the map $T = f(I_s, \beta)$. Specifically, with the increase of current the core will be saturated, and correspondingly L_d and L_q reduce. Fig. 1(b) shows L_d versus i_d and L_q versus i_q. Fig. 1(c) shows the measured torque and β versus I_s.

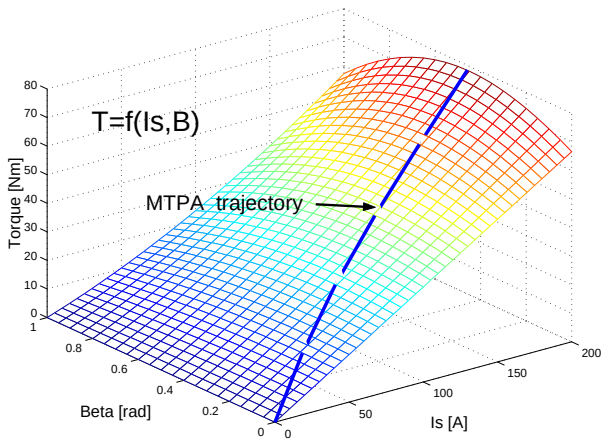

Fig. 2. Experimental result in order to find I_S and β for MTPA, and the MTPA trajectory.

IV. MTPA Control Scheme Considering PM Field Variation with Temperature

A. Flux Variation by Motor Temperature

Remanent flux-density B_r of PM decreases with temperature. This effect is specified in terms of the reversible temperature coefficient of B_r, quoted in % per $^\circ C$. If this coefficient is defined by α_{Br}, then the remanent flux density at temperature t° is given by

$$B_{r(t^\circ)} = B_{r(20^\circ C)}\left[1 + \alpha_{Br}\frac{t^\circ - 20}{100}\right] \quad (9)$$

where $B_{r(20^\circ C)}$ is the value of B_r at $20^\circ C$, i.e., room temperature. The coefficient α_{Br} is about $-0.1 \sim -0.12$ in the case of Nd-Fe-B magnet [12]. Further, the PM flux linkage at open-circuit operating point Φ_m is given by

$$\Phi_m = B_m A_m \quad (10)$$

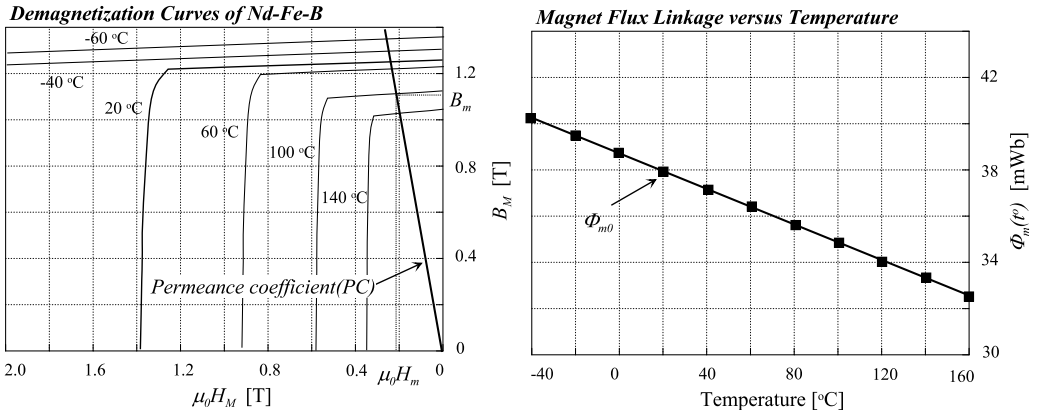

Fig. 3. Characteristics of Nd-Fe-B magnet : (a) Demagnetizing curves according to temperature. (b) Magnet flux linkages versus temperature[13].

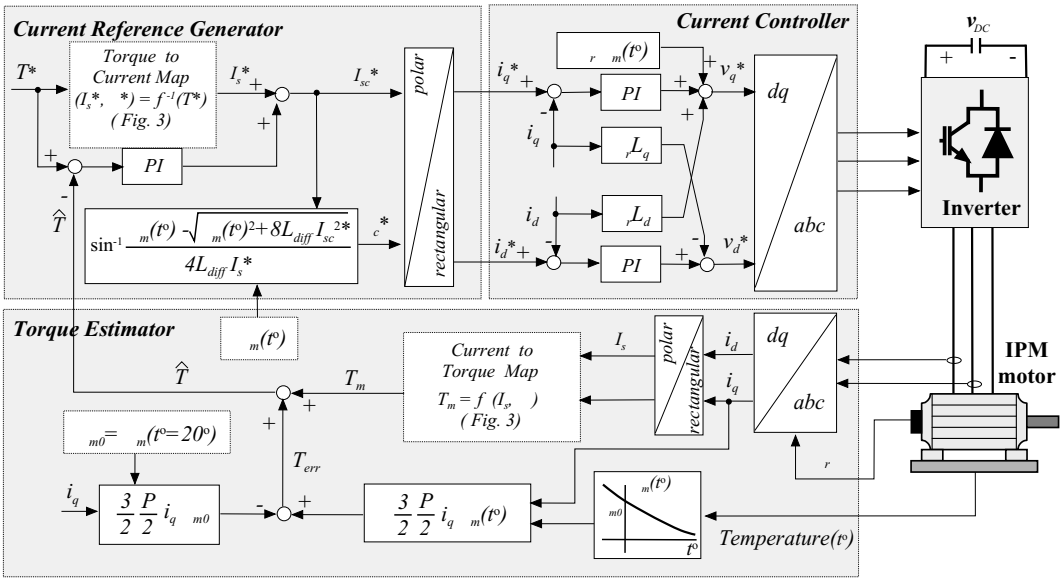

Fig. 4. Block diagram of the proposed MTPA control scheme.

where B_m denotes the PM flux density at open-circuit operating point and A_m the magnet pole area, respectively. Fig. 3(a) and (b) show the Nd-Fe-B magnet characteristics at different temperature and the magnet flux linkages versus temperature, respectively. It follows from (9) and (10) that the temperature dependence of PM flux is given by

$$\Phi_m(t^\circ) \quad = \quad \Phi_{m0}\Big[1 + \alpha_{Br}\frac{t^\circ - 20}{100}\Big], \tag{11}$$

where Φ_{m0} denotes the flux at the room temperature($20^\circ C$). In the real environments, PM temperature is assumed to vary in the range of $[-40C^\circ,\ 120C^\circ]$. In that temperature range, the flux varies from -8% to 4%.

B. MTPA Controller Considering PM Temperature Variation

The proposed torque control block diagram is shown in Fig 4. It is distinct from the existing MTPA controllers in that a temperature compensation algorithm is included in the torque controller. For the realization of MTPA, controller utilizes (I_s, β). The controller utilizes the look-up table, i.e., the map $(I_s, \beta) = f^{-1}(T)$ in generating the current command I_s^*, and utilizes its inverse map $T = f(I_s, \beta)$ in obtaining the torque estimate from current. But as was mentioned in the previous section, the saturation effect were reflected in the map f or f^{-1}. However, it is the table taken when the PM temperature is around $20^\circ C$.

To compensate for the torque offset due to temperature change, proportional-integral(PI) compensator is introduced such that

$$I_{sc}^* \quad = \quad I_s^* + \left(K_P + \frac{K_I}{s}\right)(T^* - \hat{T}) \tag{12}$$

where $K_P, K_I > 0$ denote proportional and integral gains and $\hat{T}$ is a torque estimate. The torque estimate is obtained such that

$$\hat{T} \quad = \quad T_m + T_{err} \tag{13}$$

$$\quad = \quad f(I_s,\, \beta) + \frac{3}{2}\frac{P}{2} i_q \big[\Phi_m(t^\circ) - \Phi_{m0}\big]. \tag{14}$$

Because of the flux variation with temperature, T_m from the current to torque map $f(I_s, \beta)$ is not equal to the

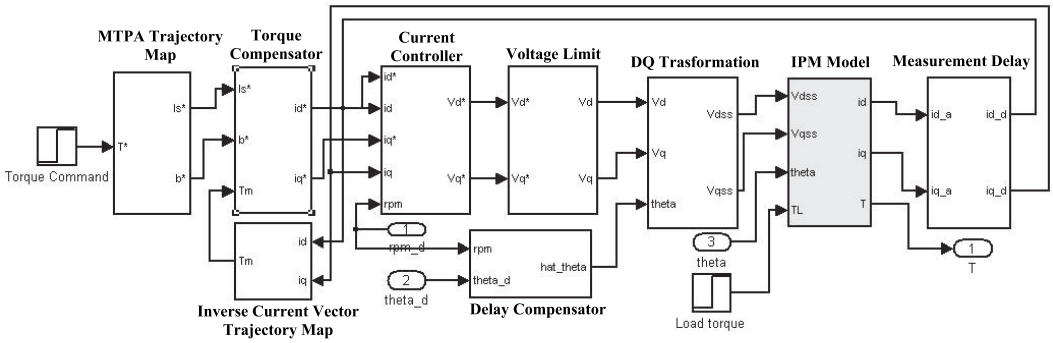

Fig. 5. Overall block diagram for simulation using MATLAB/Simulink.

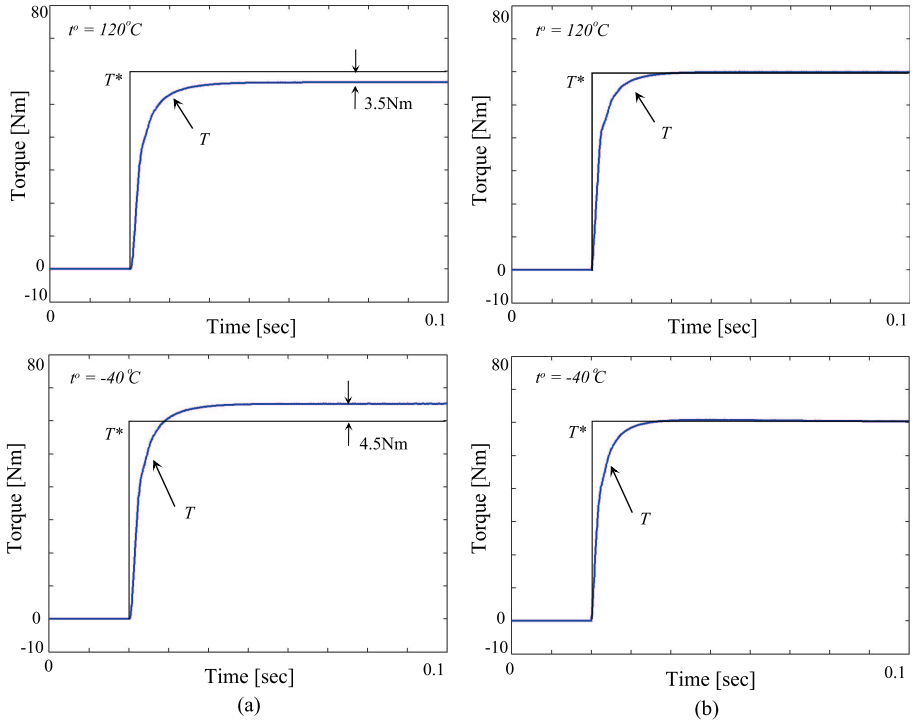

Fig. 6. Simulation results of torque with the MTPA control when the motor is running at 1500 r/min. (a) Without temperature consideration. (b) With temperature consideration.

real torque which is generated by IPM motor. The difference between T_m and the real torque causes the error of the torque. The torque error resulting in flux variation is caused by the first term in (3) ,which is called the excitation torque. Therefore, the torque error is expressed only in terms of the excitation torque.

In the proposed MTPA control, the new phase angle command β_c^* to satisfy MTPA control is obtained using (6).

V. Simulation Results

Simulation was performed with the following parameters of the HEV motor that we had: Output power = 12 kW, number of poles = 12, maximum torque = 75 Nm, DC link voltage = 150 V, maximum current = 200 A, R_s= 12 mΩ, $L_d = a_1|i_d| + b_1$ mH for $|i_d| > 20$ A; otherwise $L_d = 0.32$ mH, and $L_q = a_2|i_q|^{b_2}$ mH for $|i_q| > 20$ A; otherwise $L_q = 0.45$ mH, where $a_1 = -2.81 \times 10^{-7}$, $b_1 = 2.856 \times 10^{-4}$ and $a_2 = 5.4 \times 10^{-4}$, $b_2 = -0.06$, respectively. The simulation parameters of the IPM machine are listed in Table I. Fig. 5 shows the overall block diagram for simulation using MATLAB/Simulink. Fig. 6 shows the simulation results of the torque with the MTPA control when the motor is running at 1500 rpm. Fig. 6 (a) shows the torque responses with the MTPA control method without temperature consideration, while Fig. 6 (b) shows the torque responses with the proposed MTPA control method with temperature consideration. Without temperature consideration, as shown in Fig. 6(a), the torque error is about -3.5 Nm at $120°C$ and 4.5 Nm at $-40°C$, respectively. This substantiates that the effect of temperature becomes significant at a high or low temperature and that the proposed control scheme considering temperature yields the better performance.

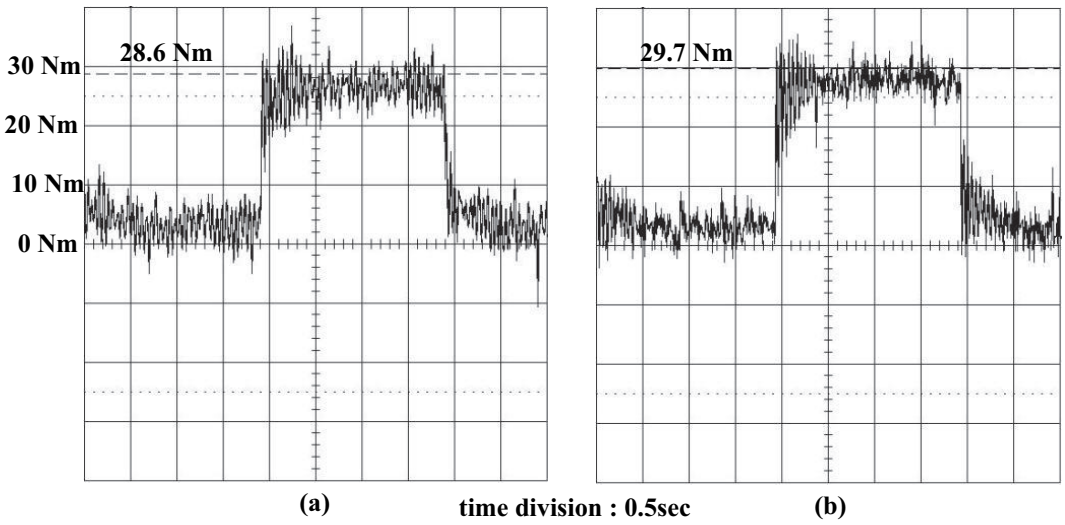

Fig. 7. Measured torque using CSD-807 when the motor is running at 1000 rpm and the torque command is 30 Nm. (a) Without temperature consideration. (b) With temperature consideration.

VI. Experimental Results

We constructed a dynamo system as shown in Fig. 1(a). The HEV motor is mechanically coupled to a 20 kW DC motor via a torque transducer. In the test, the DC motor was running in speed-control mode, while the HEV motor was operating in current-control mode. DC motor was running at 1000rpm, and the torque command was 30 Nm. The experiment has been done at $40°C$. The torque of the IPM motor was measured using the digital indicator CSD-807. The digital indicator CSD-807 also has an analog output, so displaying an analog signal is possible. Without using proposed scheme, the measured torque from CSD-807 digital output was 28.6 Nm when the torque command was 30.0 Nm. The measured torque was 29.7 Nm after using proposed scheme. Fig. 7 shows the measured torque when the torque command was 30 Nm. Here, the measured torque difference is small, but it is getting larger as temperature is getting higher as you've seen in simulation results.

TABLE I
List of the IPM machine parameters.

Power	12	kW
Current	200	A
Base/Max. speed	2000/6000	rpm
DC link voltage	150	V
R_s	0.012	Ω
L_{d0}/L_{q0}	0.32/0.45	mH
Φ_{m0} at $25°C$	0.037	Wb
P	12	

References

[1] T. M. Jahns "Flux-weakening regine operation of an interior permanent-magnet synchronous motor drive," *IEEE Trans. Ind. Applicat.*, vol.23, pp. 681-689, July/Aug. 1987.

[2] S. Morimoto, M. Sanada, and Y. Takeda, "Wide-speed operation of interior permanent magnet synchronous motors with high-performance current regulator," *IEEE Trans. Ind. Applicat.,* vol. 30, pp. 920-926, Sept./Oct. 1994.

[3] W. Soong and N. Ertugrul, "Field-weakening performance of interior permanent-magnet motors," *IEEE Trans. Ind. Applicat.,* vol. 38, pp. 1251-1258, Sep./Oct. 2002.

[4] R. Schiferl and T. A. Lipo, "Power capability of salient pole permanent magnet synchronous motors in variable speed drive applications," *IEEE Trans. Ind. Applicat.,* vol. 26, pp. 115.123, Jan./Feb. 1990

[5] J. M. Kim and S. K. Sul, "Speed control of interior permanent magnet synchronous motor drive for the flux-weakening operation," *IEEE Trans. Ind. Applicat.,* vol. 33, pp. 43-48, Jan./Feb. 1997.

[6] S.Morimoto,M.Sanada,and Y.Takeda, "Effects and compensation of magnetic saturation in flux-weakening controlled permanent magnet synchronous motor drives," *IEEE Trans. Ind. Applicat,* vol. 30, pp. 1632-1637,Nov./Dec.1994.

[7] T.Sebastian, "Temperature effects on torque production and efficiency of PM motors using NdFeB magnets," *Proc. IEEE/IAS Conf.Rec.*, PP.78-83,1993.

[8] J.W, Park; D.H, Koo; J.M, Kim; J.G, Kim, "Improvement of control characteristics of interior permanent-magnet synchronous motor for electric vehicle," *IEEE Trans. Ind. Applicat,* vol.37, pp. 1754-1760, Nov./Dec. 2001.

[9] S.Morimoto; K.Hantanaka; Y.Tong; Y.Takeda; T.Hirasa, "Servo drive system and control characteristics of salient pole permanent magnet synchronous," *IEEE Trans. Ind. Applicat,* vol.29, pp. 338-343, Mar./Apr. 1993.

[10] F. Fernandez-Bernal; A. Garcia-Cerrada,; and R. Faure, "Determination of parameters in interior permanent-magnet synchronous motors with iron losses without torque measurement," *IEEE Trans. Ind. Applicat., vol. 37,* pp. 1265-1272, Sep./Oct. 2001

[11] D. W. Novotny and T. A. Lipo, *Vector control and dynamics of AC drives,* Oxford: Clarendon Press, 1996.

[12] J. R. Hendershot and TJE Miller, *Design of brushless permanent-magnet motors,* Oxford: Clarendon Press, 1994.

[13] J & J magnetic corporation http://www.jnjmc.com/magnetic/product/product_03_2.htm

Advanced Hysteresis Control of Brushless DC Motors

Joachim Böcker
University of Paderborn, Germany
Institute of Power Electronics and Electrical Drives
boecker@lea.upb.de

***Abstract*—Brushless DC motor drives are typically employed in speed controlled applications. Torque control, particularly during regenerative mode, is not the standard domain of BLDC drives. However, it can be shown that the known BLDC control approach can be extended to control the torque in the regenerative mode even for low speed or at standstill. A hysteresis controller is proposed, which is specified by means of a state chart.**

I. Introduction

A brushless DC motor drive usually consists of a voltage source inverter and a three-phase permanent magnet motor quite similar to a standard three-phase drive (Fig. 1). However, the BLDC operation mode, using only two of three active phases at a time, enables a quite simple control approach compared, e.g., with the flux-oriented control of a three-phase permanent magnet motor. BLDC drives are mostly used for speed-controlled applications in driving operation. The torque-controlled operation, particularly in the regenerative mode, is not the usual domain of BLDC drives. This paper, however, shows how to revise the standard BLDC control approach to enable even regenerative operation.

II. Conventional BLDC Control

The typical BLDC operation mode is that, depending on the rotor position, one of the three inverter legs is kept inactive so that the current of that phase is then usually zero. There exists only one current path through both of the active inverter legs and the corresponding motor phases. One of the active inverter legs serves as buck converter in order to regulate the current, while the second active leg connects the motor to the positive or the negative DC link potential.

The control objective is mostly the speed. A speed controller may directly determine the duty cycle of a pulse width modulator (PWM), Fig. 2, or a cascaded control with an outer speed and an inner current control loop may be employed. The inner current control may be a PI-type controller with pulse width modulator as shown in Fig. 3, or a hysteresis controller, Fig. 4. This paper, however, will focus on the current control loop of the latter structure.

The motor phase currents resulting from that kind of control will show the typical square wave shapes. If a special BLDC motor with trapezoidal EMF is employed, the resulting torque is constant and proportional to the amplitude of the currents. The BLDC approach, however, can also be applied to permanent magnet motors with sinusoidal EMF, but the torque will then include a 6th-order harmonic content.

The control approaches with inner current control loop differs in the way, how the current feedback I is generated. The simplest solution is to use the DC link current,

$$I = i_{dc} \tag{1}$$

That method, however, may cause problems at standstill and low speed, because the DC link current is very small

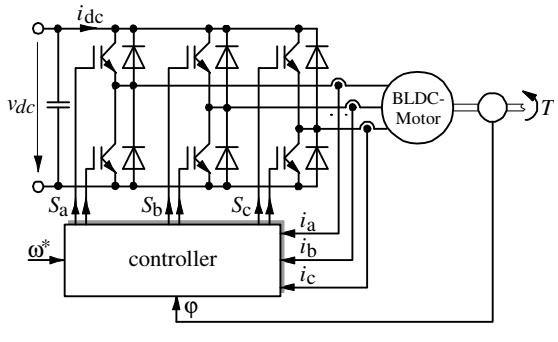

Fig. 1. BLDC drive

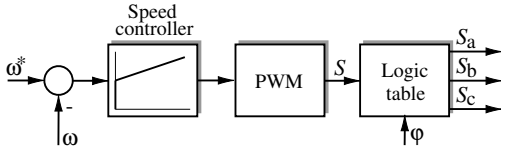

Fig. 2. Speed control with PWM

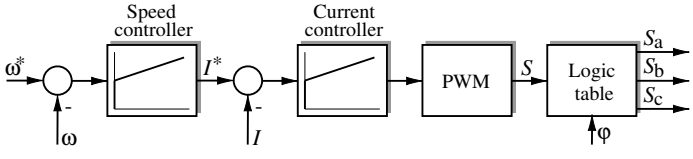

Fig. 3. Cascaded control with PWM

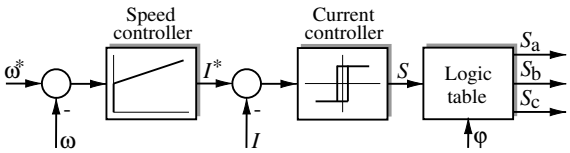

Fig. 4. Cascaded control with hysteresis current control

TABLE I
DETERMINATION OF THE CURRENT TO BE CONTROLLED

area	φ [1]	$2I$	V
1	-30°, 30 °	$i_b - i_c$	$v_b - v_c$
2	30°, 90°	$i_b - i_a$	$v_b - v_a$
3	90°, 150°	$i_c - i_a$	$v_c - v_a$
4	150°, 210°	$i_c - i_b$	$v_c - v_b$
5	210°, 270°	$i_a - i_b$	$v_a - v_b$
6	270°, 330°	$i_a - i_c$	$v_a - v_c$

[1] The angle $\varphi = 0$ is that position, the free motor will take with currents $i_a > 0, i_b = i_c = -i_a / 2$.

even with large motor currents. As alternative solution, e.g. [3], I can be generated from the motor phase currents by

$$I = \frac{1}{2} \sum_{k=a,b,c} |i_k| \quad \text{or} \quad I = \max_{k=a,b,c} \{|i_k|\} \qquad (2)$$

Because one of the phase currents should be zero, the sum yields the amplitude of the square wave. But this approach can handle only the driving operation. In view of governing also the regenerative mode, I should be better determined by selection of the appropriate phase current depending on the rotor position as proposed in Table I, where the correct signs of the phase currents are considered.

TABLE II
INVERTER SWITCHING COMMANDS FOR DRIVING OPERATION

area	φ	S_a	S_b	S_c
1	-30°, 30 °	0	+1	$-S$
2	30°, 90°	–1	S	0
3	90°, 150°	$-S$	0	+1
4	150°, 210°	0	–1	S
5	210°, 270°	+1	$-S$	0
6	270°, 330°	S	0	–1

The switching command S, either that of the PWM or of the hysteresis controller, can take only two values that are denoted as $S = \{+1,0\}$. Depending on the area of the rotor position, the command S is distributed to the inverter switching commands S_a, S_b, S_c by a logic table as specified by Table II. In that notation, "+1" or "–1" indicate that the upper transistor, or the lower one, respectively, is turned on. "0" indicates that both transistors are turned off. In this case, only the free wheeling diodes may conduct a current.

The result of this strategy is that the line-to-line voltage V between the active phases (see Table I for definition of

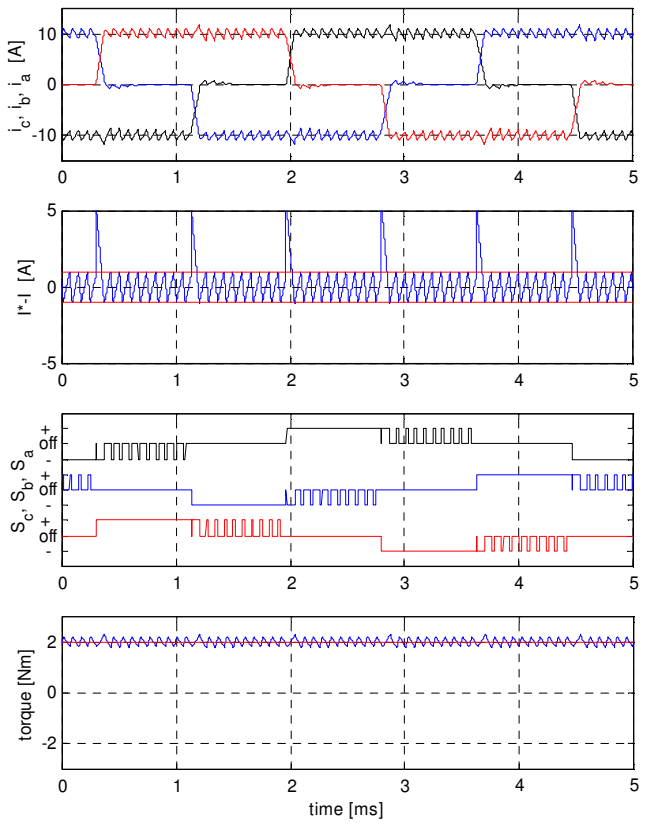

Fig. 5. Behavior in driving mode, $\omega/2\pi$ =200 Hz

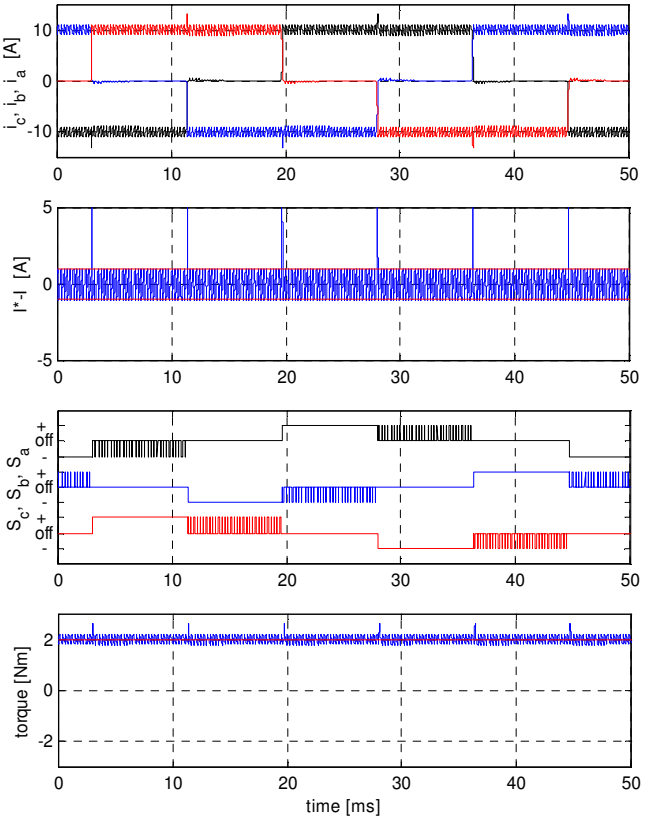

Fig. 6. Behavior in driving mode, $\omega/2\pi$ =20 Hz

V) is always

$$V = Sv_{dc} = \{0,+1\}v_{dc} = \{0,+v_{dc}\} = \{V_0, V_+\} \quad . \tag{3}$$

Neglecting the commutation between the phases, the current behavior will follow the simple differential equation

$$\begin{aligned} 2L\dot{I} &= V - 2E - 2RI \\ &= \{V_0, V_+\} - 2\omega\psi_f - 2RI \end{aligned} \tag{4}$$

where E is the electromotoric force (EMF) of one phase, and R and L are the resistance and the inductance of one phase. As long as the sliding condition

$$V_0 = 0 < 2\omega\psi_f + 2RI^* < V_+ = v_{dc} \tag{5}$$

is ensured, the hysteresis controller will hold the current within the tolerance band. $V_+ = v_{dc}$ lets the current I increase, $V_0 = 0$ lets it decrease. The torque

$$T = 2n_p\psi_f I \tag{6}$$

is proportional to the current I , so torque control is equal to current control. The numbers of pole pairs is n_p

A typical behavior of the hysteresis current approach is shown in Fig. 5 and 6. The figures show the three phase currents i_a, i_b, i_c of the motor, the control error $I^* - I$ together with the hysteresis width, the three inverter switching command signals S_a, S_b, S_c , and the torque compared with the desired value at constant speed. Fig. 5 shows the behavior for high speed, Fig. 6 for low speed.

III. Regenerative Operation

The described approach is even capable of regenerative operation with slight modifications: If, in case of driving operation, a transistor need not have to be turned on, because the parallel diode is conducting, it is now necessary to switch it on. Vice versa, a transistor, which is conducting in the driving mode, need not have to be switched on for regenerative operation. The result is a modified Table III.

The resulting behavior of the regenerative mode is shown in Fig. 7, which is quite satisfactory. However, with decreasing speed, the control behavior degrades essentially (Fig. 8). The control is no longer able to force the current back into the tolerance band, because the sliding condition

TABLE III
Inverter Switching Commands for Regenerative Operation

area	φ	S_a	S_b	S_c
1	-30°, 30 °	0	0	$1-S$
2	30°, 90°	0	$S-1$	0
3	90°, 150°	$1-S$	0	0
4	150°, 210°	0	0	$S-1$
5	210°, 270°	0	$1-S$	0
6	270°, 330°	$S-1$	0	0

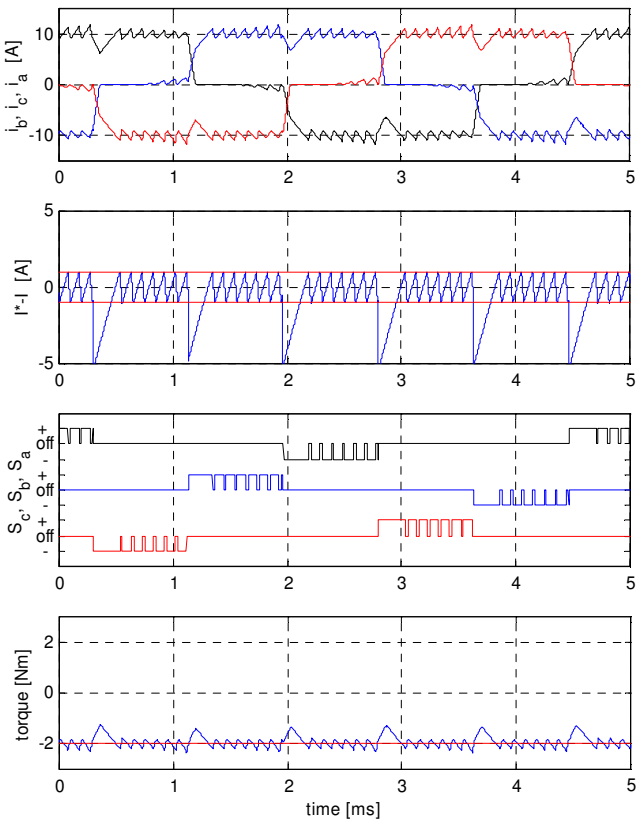

Fig. 7. Behavior in regenerative mode, $\omega/2\pi$ =200 Hz

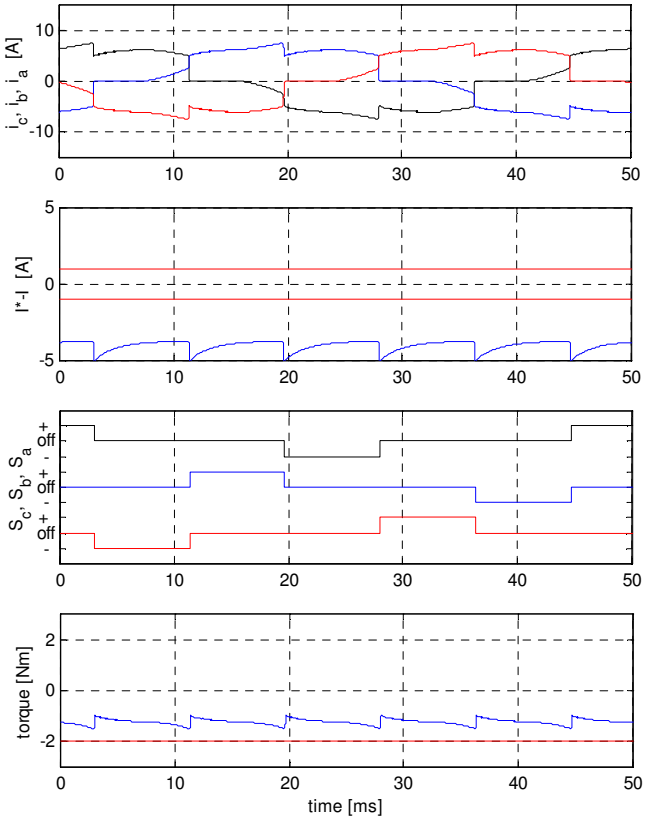

Fig. 8. Behavior in regenerative mode, $\omega/2\pi$ =20 Hz

(5) is violated. The minimum possible regenerative current can be calculated from (5) as

$$I > I_{\min} = -\frac{\omega \psi_f}{R} \quad . \tag{7}$$

IV. Improved Control Strategy

To overcome the problem of the regenerative mode and to exceed the limit (7), the controller should be allowed to use also the negative voltage $V = V_- = -v_{dc}$, which is possible by appropriate switching commands. The two active legs of the inverter work as four quadrant converter, which is able to apply positive and negative voltages as well. A difficulty is now that three switching states $V = \{-v_{dc}, 0, +v_{dc}\}$ have to be handled, which cannot be generated by a simple hysteresis controller with binary output S.

That is why the control concept was extended as shown in Fig. 9. The proposal incorporates now two tolerance bands $\pm\varepsilon_1$ and $\pm\varepsilon_2$. Usually, the controller works between the inner thresholds $\pm\varepsilon_1$ applying the voltages V_0 and V_+ alternatively. Only if the control error hits the second threshold $-\varepsilon_2$, the voltage V_- will be applied. As already shown for other converter topologies, [1], [2], state charts are an appropriate method to specify such control strategies pretty clear, which can be seen from Fig. 10. The state transitions are triggered by the events E_+, E_-, F_+, F_-, which

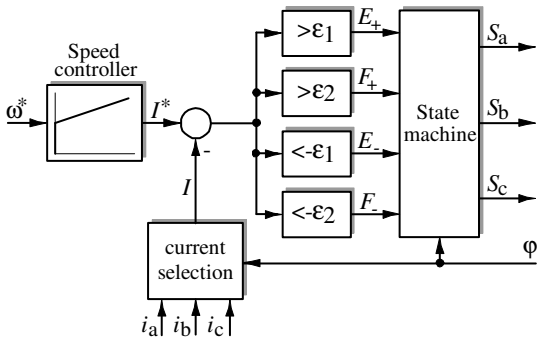

Fig. 9. Proposed control structure

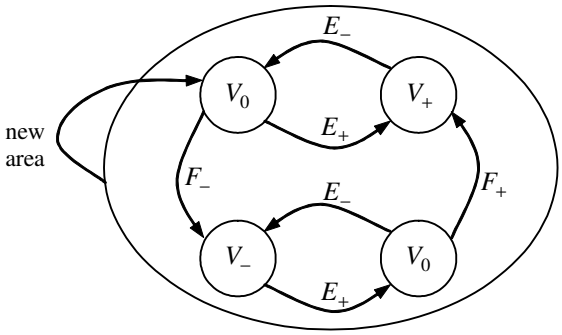

Fig. 10. State chart

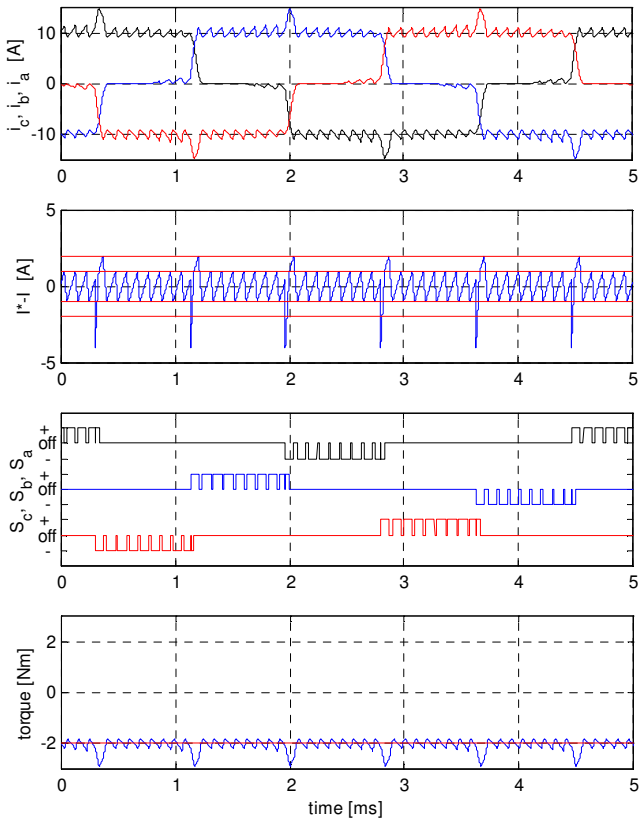

Fig. 11. Improved behavior in regenerative mode, $\omega/2\pi$ =200 Hz

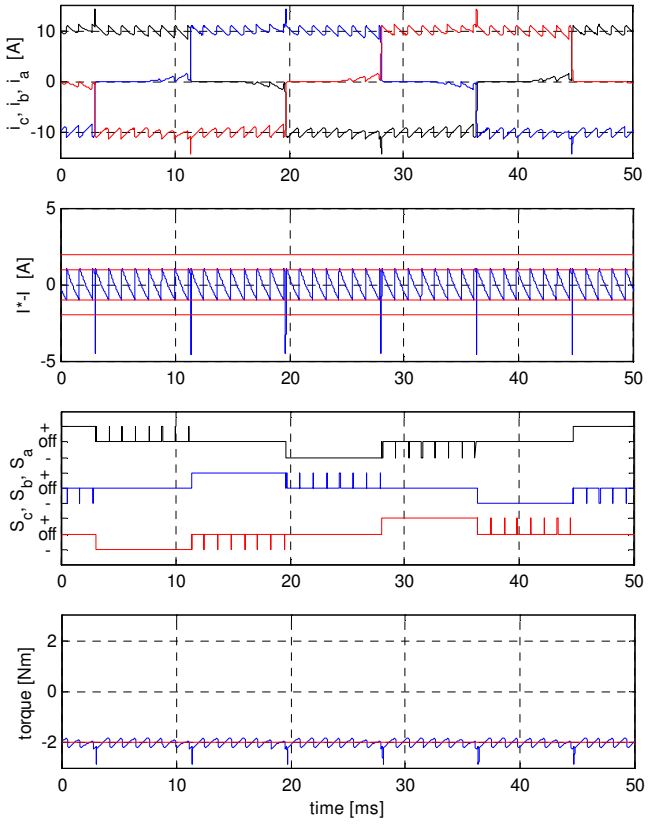

Fig. 12. Improved behavior in regenerative mode, $\omega/2\pi$ =20 Hz

TABLE IV
INVERTER SWITCHING COMMANDS FOR COMPLETE OPERATION RANGE

area	$I^* > 0$			$I^* < 0$		
	V_-	V_0	V_+	V_-	V_0	V_+
1	0, 0, 0	0,+1, 0	0,+1, –1	0,–1,+1	0, 0,+1	0, 0, 0
2	0, 0, 0	–1, 0, 0	–1,+1, 0	+1, –1, 0	0, –1, 0	0, 0, 0
3	0, 0, 0	0, 0,+1	–1, 0,+1	+1, 0, –1	+1, 0, 0	0, 0, 0
4	0, 0, 0	0, –1, 0	0, –1,+1	0,+1, –1	0, 0, –1	0, 0, 0
5	0, 0, 0	+1, 0, 0	+1, –1, 0	–1,+1, 0	0,+1, 0	0, 0, 0
6	0, 0, 0	0, 0, –1	+1, 0, –1	–1, 0,+1	–1, 0, 0	0, 0, 0

indicate, if a threshold is hit. Each time, a new area of the angle is entered, the state is reset to V_0.

The resulting states of the graph of Fig. 10 have to be mapped to the particular inverter switching commands S_a, S_b, S_c, which are given by Table IV. The resulting commands depend on the area and the mode of operation, driving or regenerative. The controller is completely specified by the structure (Fig. 9), the state chart (Fig. 10), and the mapping table (Table IV). As a proposal, most of that functions can be implemented using a field programmable logic gate array (FPGA).

The results with that new control strategy are shown in Fig. 11 and 12. The control error is now depicted with the thresholds $\pm\varepsilon_1$ and $\pm\varepsilon_2$. Particularly Fig. 12, which is the result for low speed, shows that the desired torque is now fully achieved (compare with Fig. 8). The states toggle only between V_0 and V_-, which is the case, if the ohmic voltage drop is larger than the EMF E.

Even Fig. 10 for higher speed shows a better result than Fig. 7 with the original strategy. The states toggle mainly between V_0 and V_+, which is not different to Fig. 7, but, during a commutation, the negative voltage V_- is now applied for a short time so that the control error is much faster back within the thresholds.

V. CONCLUSION

It has been shown how to extend the hysteresis control of BLDC drives for regenerative operation even at small speed and standstill. The control approach does not need any supplement of power electronics or sensors. As a particular point of interest, the controller has been specified by means of a state chart, which is an appropriate method for the design of switching controllers. The control may be realized using a microcontroller, or, as alternative, a field programmable gate array (FPGA).

REFERENCES

[1] J. Böcker, “Tolerance band controller for a three-level four-quadrant converter including DC link balancing”, PESC Conference, Aachen, 2004.

[2] J. Böcker, “Discrete-Event Converter Control”, European Conf. on Power Electronics and Applications, Toulouse, 2003.

[3] J. W. Dixon, I. A. Leal, Current Control Strategy for Brushless DC Motors Based on a Common DC Signal”, IEEE Trans. Power Electronics, Vol. 17, No. 2, March 2002, pp.232-240

[4] A. Murray, P. Kettle, F. Moynihan, “Advances in Brushless DC Motors”, American Control Conference, 1997, Vol. 6, pp 3985-3989

[5] T. J. E. Miller, “Brushless Permanent Magnet and Reluctance Motor Drives”, Oxford Science Publications, 1993

[6] P. Muir, C.P. Neuman; “Pulsewidth Modulation Control of Brushless DC Motors for Robotic Applications”, IEEE Trans. Industrial Electronics, Vol. 32, No. 3, August, 1985, pp. 222-229.

Experimental Precision Position Control of PMSM using Disturbance Observer with System Parameter Compensator

Jong-Sun Ko, and Soon-Chan Hong

Department of Electric Electronics and Computer Eng. Dankook University
San 8, Hananm-dong Yongsan-ku, Seoul City, Korea
e-mail: jsko@dku.edu

Abstract- **This paper presents external load disturbance compensation that used to deadbeat load torque observer and regulation of the compensation gain by parameter estimator. The position response of permanent magnet synchronous motor (PMSM) follows that of the nominal plant. The load torque compensation method is composed of a deadbeat observer that is well-known method. However it has disadvantage such as a noise amplification effect. To reduce of the effect, the post-filter, which is implemented by MA process, is proposed. The parameter compensator with recursive least square method (RLSM) parameter estimator is suggested to push real system to nomial operating point of the motor system. The proposed RLSM estimator is combined with a high performance torque observer to resolve the problems. As a result, the proposed control system becomes a robust and precise system against the load torque and the parameter variation. A stability and usefulness, through the verified computer simulation and experiment, are shown in this paper**.

I. INTRODUCTION

Recently, precision position control become more and more important in chip mount machines, semiconductor production machines, precision milling machines, high resolution CNC machines, precision assembly robots, high speed hard disk drivers and so on. Also one of a merging technology is a nanotechnology. This part almost works in nano-fabrication but now spreads to bio-engineering, optical equipment, and so on. It is also very important for direct drive systems. A PMSM has replaced many DC motors since the industry applications require more powerful actuators in small sizes. The PMSM has low inertia, large power-to-volume ratio, and low noise as compared to a permanent magnet DC servomotor having the same output rating [1][2]. However, the disadvantages of this machine are the high cost and the need for a more complex controller because of the nonlinear characteristic.

The proportional-integral (PI) controller usually used in PMSM control is simple to realize but makes it difficult to obtain sufficiently high performance in the tracking application. A new systematic approach was done in state space using digital position information in PMSM system [3]. However, the machine flux linkage is not exactly known for a load torque observer that creates problems of uncertainty. The cogging effect, some damage on permanent magnet, over current can affect the value of k_t. This caused small position or speed errors and increased the chattering effect, which should be reduced as much as possible. It also makes miss-estimated load torque in deadbeat observer system. In this paper the parameter compensator with RLSM parameter estimator is suggested to increase the performance of the load torque observer and main controller. This compensator makes real system as if it works in nominal system parameter. Therefore the deadbeat load torque observer has a good performance as if there is no parameter variation. Finally, this controller can be used in robot or vestibular system which is one of the simulators, that systems need the exact sinusoidal speed control even though unbalanced load is injected. Other production equipment also can take this controller to increase the production quality.

II. MODELING OF PMSM

The system equations of a PMSM model can be described as

$$\dot{\omega} = \frac{3}{2}\frac{1}{J}\left(\frac{p}{2}\right)^2 \lambda_m i_{qs} - \frac{B}{J}\omega - \frac{p}{2J}T_L \tag{1}$$

$$\dot{\theta} = \omega_r$$

$$T_e = \frac{3}{2}\frac{p}{2}\lambda_m i_{qs}. \tag{2}$$

where

p : number of poles
λ_m : flux linkage of permanent magnet
ω : angular velocity of rotor
J :inertia moment of rotor
B :viscous friction coefficient.

III. CONTROL ALGORITHM

3.1 Position controller

A new state is defined for the tracking controller as Eqn. (3). Where ω_r is the rotor speed reference [2]. The control input becomes Eqn. (4).

$$\dot{z} = \theta - \theta_r \tag{3}$$

$$i_{qc1} = -k_1\omega - k_2\theta - k_3 z\,. \tag{4}$$

The augmented system for the speed control of a PMSM is expressed as follows:

$$\begin{bmatrix} \dot{\omega} \\ \dot{\theta} \\ \dot{z} \end{bmatrix} = \begin{bmatrix} -\frac{B}{J} & 0 & 0 \\ 1 & 0 & 0 \\ 0 & 1 & 0 \end{bmatrix} \begin{bmatrix} \omega \\ \theta \\ z \end{bmatrix} + \begin{bmatrix} k_t \frac{p}{2J} \\ 0 \\ 0 \end{bmatrix} i_{qs} - \begin{bmatrix} \frac{p}{2J} \\ 0 \\ 0 \end{bmatrix} T_L - \begin{bmatrix} 0 \\ 0 \\ 1 \end{bmatrix} \theta_r \tag{5}$$

$$y = \begin{bmatrix} 0 & 1 & 0 \end{bmatrix} \begin{bmatrix} \omega \\ \theta \\ z \end{bmatrix}. \tag{6}$$

If the load torque T_L is known, an equivalent current command i_{qc2} can be expressed as

$$i_{qc2} = \frac{1}{k_t} T_L\,. \tag{7}$$

Then, the feeding forward an equivalent q axis current command to the output controller can compensates load torque effect. However, disturbances are unknown or inaccessible in the real system.

3.2 Load torque observer and MA process

It is well known that observer is available when input is unknown and inaccessible. For simplicity, a 0-observer is selected [3]. The system equation can be expressed as

$$\begin{bmatrix} \dot{\hat{\omega}} \\ \dot{\hat{y}} \\ \dot{\hat{T}}_L \end{bmatrix} = \begin{bmatrix} -\frac{B}{J} & 0 & -\frac{p}{2J} \\ 1 & 0 & 0 \\ 0 & 0 & 0 \end{bmatrix} \begin{bmatrix} \hat{\omega} \\ \hat{y} \\ \hat{T}_L \end{bmatrix} + \begin{bmatrix} k_t \frac{p}{2J} \\ 0 \\ 0 \end{bmatrix} i_{qs} + L \left(y - \begin{bmatrix} 0 & 1 & 0 \end{bmatrix} \begin{bmatrix} \hat{\omega} \\ \hat{y} \\ \hat{T}_L \end{bmatrix} \right). \tag{8}$$

To reduce disadvantage of deadbeat observer that is too sensitive of noise, moving average (MA) filter is considered [5].

$$\tilde{T}_L(k) = \frac{1}{2}(\hat{T}_L(k) + \hat{T}_L(k-1)) \tag{9}$$

3.3 Parameter estimator and compensator

The discrete dynamic equation of PMSM can be written as

$$y(k+1) = \alpha \cdot \omega(k) + \beta \cdot y(k) + \gamma \cdot i_{qs}(k) + \delta \cdot T_L(k) \tag{10}$$

where $\alpha = \frac{J}{B}(1 - e^{-\frac{B}{J}h})$, $\beta = 1$, $\gamma = k_t \frac{P}{2J}\frac{J}{B}(h - \frac{J}{B} + \frac{J}{B}e^{-\frac{B}{J}h})$, $\delta = \frac{P}{2J}\frac{J}{B}(\frac{J}{B} - h - \frac{J}{B}e^{\frac{B}{J}h})$.

Respectively, on the assumption that there is no effect of the load torque, a feed back gain and a feed forward gain are defined as C_1, C_2 and C_3 respectively[6]. Then a control input for a compensate parameter variation to make the system as a equivalent nominal system becomes as follow:

$$i_{qc}^*(k) = C_1(k) \cdot \omega(k) + C_2(k) \cdot y(k) + C_3(k) \cdot i_{qc}(k) \tag{11}$$

Therefore resultant compensated system is equal to the nominal equivalent system.

$$\begin{aligned} y(k+1) &= \alpha \cdot \omega(k) + \beta \cdot y(k) + \gamma(C_1(k)\omega(k) + C_2(k)y(k) + C_3(k)i_{qc}(k)) \\ &= \alpha_n \cdot \omega(k) + \beta_n \cdot y(k) + \gamma_n \cdot i_{qs}(k) \end{aligned} \tag{12}$$

where α, β, γ and α_n, β_n, γ_n are actual parameters and nominal parameters, respectively. These values can be obtained easily with Eqn. (12) as $C_1 = \frac{(\alpha_n - \alpha)}{\gamma}$, $C_2 = \frac{(\beta_n - \beta)}{\gamma}$, $C_3 = \frac{\gamma_n}{\gamma}$ respectively.

Parameter compensation requires real parameter estimation. Using a discrete system equation without disturbance Eqn. (13) we can separate a parameter and a measured parameter.

$$y(k+1) = \alpha \cdot \omega(k) + \beta \cdot y(k) + \gamma \cdot i_{qs}(k) = \theta^T \phi(k) \tag{13}$$

where $\theta^T = \begin{bmatrix} \alpha & \beta & \gamma \end{bmatrix}$, $\phi^T(k) = \begin{bmatrix} \omega(k) & y(k) & i_{qs}(k) \end{bmatrix}$.

A RLSM can estimate real parameter. Resultant equations are as follows [7][8]:

$$\hat{\theta}(k+1) = \hat{\theta}(k) + F(k+1)\tilde{\phi}(k)E(k+1) \tag{14}$$

$$F(k+1) = F(k) - \frac{F(k)\tilde{\phi}(k)\tilde{\phi}(k)^T F(k)}{1 + \tilde{\phi}(k)^T F(k)\tilde{\phi}(k)} \tag{15}$$

$$E(k+1) = y(k+1) - \hat{\theta}(k)^T \tilde{\phi}(k) \tag{16}$$

where $\hat{\theta}^T(k) = \begin{bmatrix} \alpha & \beta & \gamma \end{bmatrix}$,

$$\tilde{\phi}^T(k) = \begin{bmatrix} \omega(k) & y(k) & i_{qs}(k) - \frac{\hat{T}_L}{k_t} \end{bmatrix},$$

$$F(0) = \frac{1}{\delta} I \qquad (0 < \delta << 1)\,.$$

The resultant block diagram of proposed controller is shown in Fig. 1.

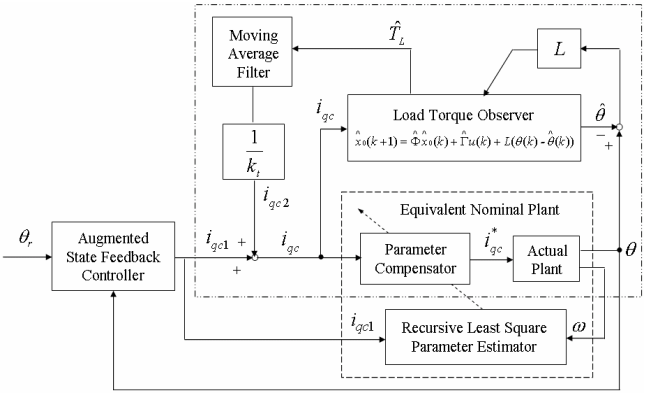

Fig. 1. Block diagram of the proposed algorithm

IV. CONFIGURATIONS OF OVERALL SYSTEMS

The total block diagram of the proposed controller is shown in Fig. 2. The C-Language program and a TMS320C31 DSP implement the digital control part. The MT method, which is realized by the FPGA, is used to reduce the quantization error.

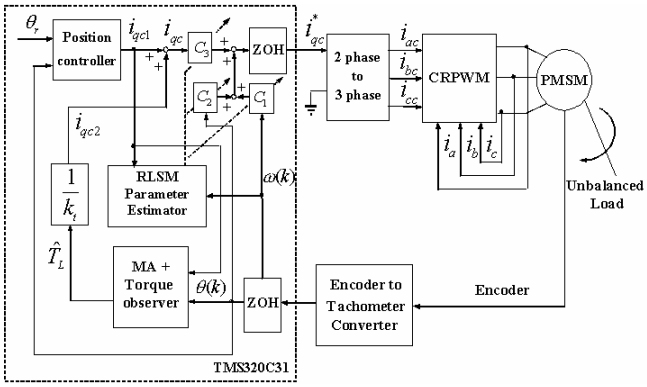

Fig. 2. Block diagram of the proposed control system.

Experimental load systems directly coupled to motor axis are depicted in Fig. 3. Fig. 5. This system creates time varying load torque to show effectiveness of the proposed algorithm.

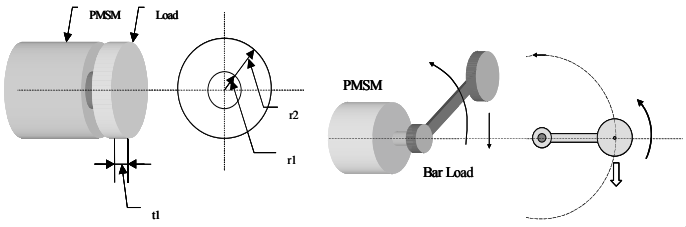

(a) Inertial load (b) bar load

Fig. 3 The figure of load for parameter and load variation

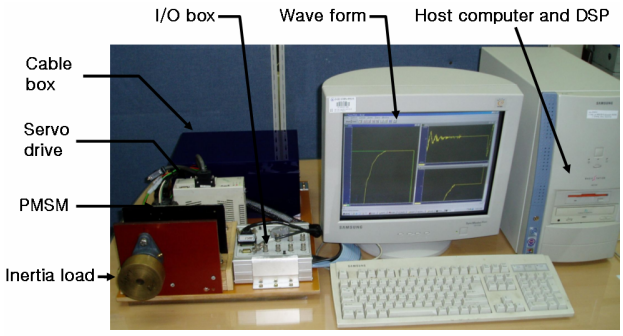

Fig. 4. The configuration of the experiment system.

V. SIMULATION AND EXPERIMENTAL RESULTS

The parameters of a PMSM motor used in this simulation and this experiment will be given as Table 1. The hysteresis band gap is chosen as 0.01[A] and the sampling time h is determined as 0.2 [ms]. The weighting matrix is selected as $Q = diag[0.1 \quad 60 \quad 1000]$, R = 1 and optimal gain matrix becomes $k = [0.0771 \quad 3.2321 \quad 11.4195]$ The deadbeat observer and the gain matrices are calculated from nominal values. The gain is obtained using the pole placement method at origin in z domain and becomes $L = [9623.9 \quad 2.7000 \quad -275.00]^T$. [4] The simulation results are shown in Fig. 5 and Fig. 6. Fig. 5 shows the speed response of the conventional controller, there is small speed ripple and small overshoot caused by a current ripple of hysteresis band gap and parameter variation

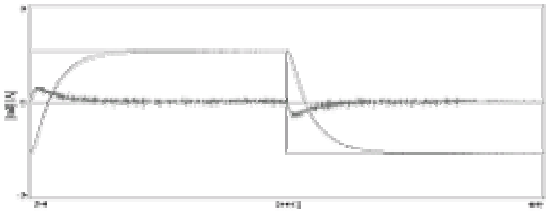

(a) Dead beat observer

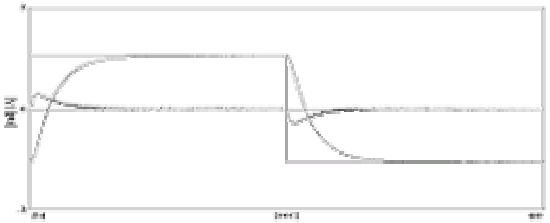

(b) Dead beat observer and parameter compensator algorithm

Fig. 5 simulation results of the rotor position, q phase current command for no load

The inertial parameter has 100 times of the permanent magnet value and 2 times of R and L value. This conventional algorithm makes large current ripple due to parameter variation. Fig. 6 shows the result of a proposed algorithm that is the same position command and a same disturbance condition as Fig.5. We can see this load effects are reduced by proposed algorithm of parameter compensation. In case of bar load, inertia variation is not so big. Therefore parameter algorithm does not work too large.

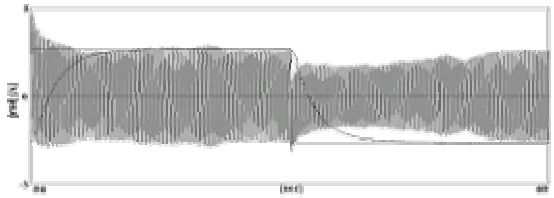

(a) using disturbance observer

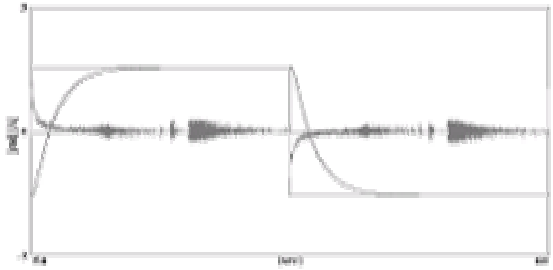

(b) disturbance observer and parameter compensator

Fig. 6 simulation results of the rotor position, q phase current command for inertia load, inertia parameter of 30 times and variation of R and L

Fig. 7 presents 0.1[rad] scaled simulation results to show the comparison between two controllers. Conventional controller Fig. 6(a) has large position ripple compare with proposed system Fig 6(b). These phenomena come from a parameter compensator.

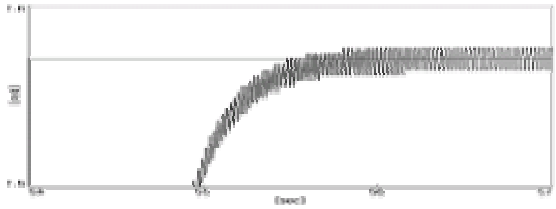

(a) disturbance observer

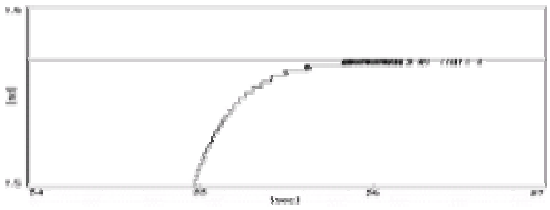

(b) disturbance observer with parameter compensator

Fig. 7 Performance comparison of two controllers for the parameter variation

Some experimental results are depicted in Fig. 8 and Fig. 9. In this experiment, real observer gains are reduced about 30% to obtain some effectiveness of the parameter compensation. The parameter compensator calculates real parameter and compensates a current to fit for present miss tuned gain. Fig. 8 shows experimental results of the position with current command about 3 sec durations. There is current ripple ins steady state and large position overshoot in transient state in Fig. 8(a). However, after 20 minutes, there is no current ripple and position error in the proposed system as shown in Fig. 8(b)

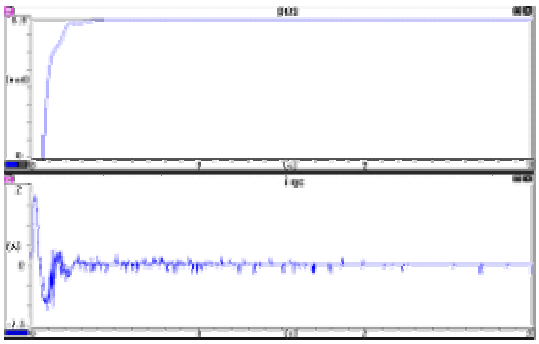

(a) disturbance observer

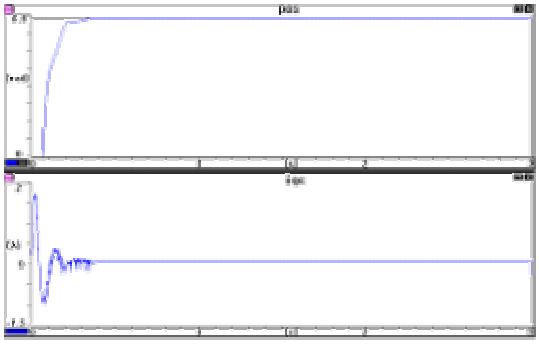

(b) disturbance observer and parameter compensator (after twenty minute)

Fig. 8 experiment results of the rotor position, q phase current command for inertia load

More detailed figure is shown in Fig. 9 from 0 minute to 20 minutes. This figure has a scale between 0.1[rad] (0.7[rad] ~ 0.8[rad]) to see a zooming data and it shows that the position error decrease gradually after times go on.

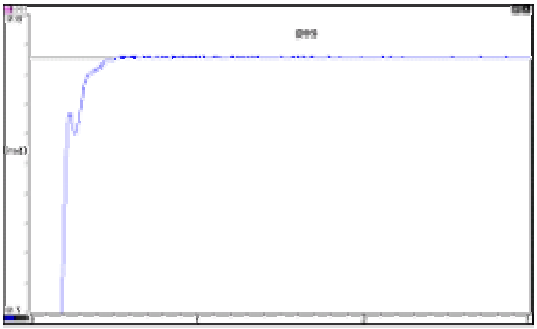

(a) disturbance observer algorithm

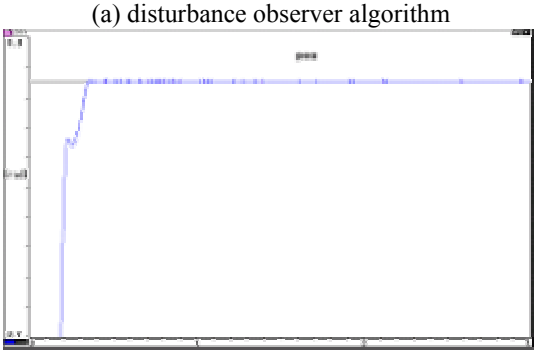

(b) disturbance observer and parameter compensator (after one minute)

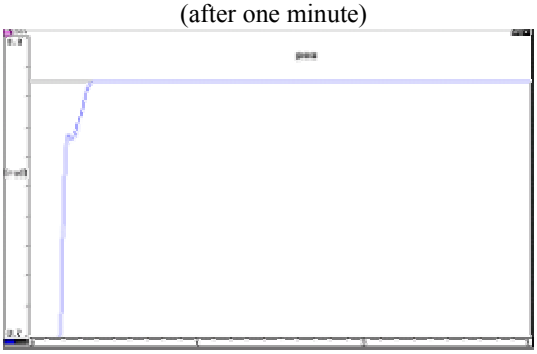

(c) disturbance observer and parameter compensator (after twenty minutes)

Fig. 9 experiment results of zoom in the rotor position for inertia load

VI. CONCLUSIONS

A new deadbeat load torque observer with a system parameter compensator is proposed to obtain better performance from the PMSM in a precision position control system. This compensator makes real system work as in nominal parameter system. Therefore the deadbeat load torque observer has a good performance as if there is no parameter variation. To reduce of the effect of the noise, the post-filter implemented by MA process, is adopted. The system response comparison between the deadbeat gain observer and the parameter compensated system with deadbeat observer has been done. Since parameter compensated system acts as there is no parameter variation, the conventional deadbeat load torque well adapts to real system. It can be used to cancel out the steady state and the transient position error due to the external disturbances, such as various friction, load torque and small chattering effect of deadbeat control.

ACKNOWLEDGMENT

This work has been supported by EESRI (00-036), which is funded by MOCIE (Ministry of commerce, industry and energy)

REFERENCES

[1] D. W. Novotny and R. D. Lorentz "Introduction to field orientation and high performance AC drives" *IEEE-IAS Tutorial Course*, 1986

[2] P. C. Krause, *Analysis of electric machinery*, McGraw-Hill, 1984

[3] K. J. Å ström and B. Wittenmark *Computer controlled system*, Prentice Hall, International, 1997

[4] J. S. Ko, J. H. Lee, S. k. Chung, and M. J. Youn "A Robust Position Control of Brushless DC motor with Dead Beat Load Torque Observer" *IEEE Transaction on Industrial Electronics,* vol. 40, no. 5, pp. 512-520, 1993

[5] C. T. Chen, *Linear System Theory and Design*, Holt, Rinehart and Winston, Inc., 1984

[6] C. Y. Huang, T. C. Chen, C. L. Huang "Robust Control of Induction Motor with A Neural-Network Load Torque Estimator and A Neural-Network Identification" *IEEE Transaction on Industrial Electronics*, vol. 46, no. 5, pp 990-998, 1999

[7] J. D. Landau, *System Identification and Control Design*. Englewood Cliffs, NJ, Prentice-Hall, 1990

[8] G. C. Goodwin, K. S. Sin, *Adaptive Filtering Prediction and Control*. Englewood Cliffs, NJ, Prentice-Hall, 1984

[9] J. S. Ko and S. K. Youn, "A Study of Adaptive Load Torque Observer and Robust Precision Position Control of BLDD Motor", *Transaction on KIPE*, Vol. 4. No. 2, pp. 138-143, 1999.

[10] J. S. Ko and Y. J. Lee, "Precision Speed Control of PMSM Using Neural Network Distrubance Observer and Parameter Compensator", *Transaction on KIEE*, Vol. 51B. No. 10, pp. 573-580, 2002.

[11] J. S. Ko, T. H. Lee, B. L. Park, and C. W. Jeon " Precision Speed Control of PMSM for Stimulation of the Vestibular System Using Rotatory Chair" *Transaction on KIPE*, Vol. 5. No. 5, pp. 459-466, 2000.

[12] J. S. Ko, T. H. Lee, C. W. Jeon, S. S. Lee "Precision Speed Control of PMSM Using Distrubance Observer and Parameter Compensator", *Transaction on KIPE*, Vol. 6. No. 1, pp. 98-106, 2001.

Speed-sensorless stator-flux-oriented control of induction motor drives in traction

Manfred Depenbrock
Ruhr-University Bochum
D-44780 Bochum, Germany
depenbrock@eele.rub.de

Andreas Steimel
Ruhr-University Bochum
D-44780 Bochum, Germany
steimel@eele.rub.de

***Abstract*- Indirect Stator-Quantities Control (ISC) combines the principle of stator-flux-orientation proven successful in Direct Self Control (DSC) with Pulse-Width Modulation (PWM). High torque dynamics and robust behaviour against input voltage disturbance are achieved in the whole operation range including field-weakening. After careful correction of inverter-voltage errors and dc portions in the stator fluxes and currents not necessary for the actual operation point the difference of the stator-current space vectors in the machine and in the controlled model is employed for speed and stator resistance estimation, allowing to dispense with speed sensors. A special flux management allows infinitely slow change between driving and braking.**

I. INTRODUCTION

In the eighties of the last century Vector Control of Induction Machine already successful with industrial drives was introduced in traction, too [1]. As well known it impresses the components of the stator current space vector in orientation to the rotor flux space vector by means of control. In traction drives with high power this approach was limited as the switching frequency is in general too low to impress the currents sufficiently well.

In 1984 M. Depenbrock invented ([2], [3], [4], [1]) to orient the space vector of the stator voltage directly to the space vector of stator flux which is obtained in a very simple manner as integral of the magnetising stator voltage, according to Faraday's Law. In Direct Self Control (DSC) the stator flux activates the suited next voltage switching when it reaches predetermined thresholds. Thus it guides itself on its trajectory symmetrical to the origin and controls the magnetization of the machine. Torque is controlled by the track speed, in DSC simply by a torque hysteresis controller which guides pulsing and makes a separate Pulse Width Modulator unnecessary. Flux Self Guidance makes the drive insensitive to input voltage disturbations met typically in traction, as e. g. by pantograph bouncing. Asynchronous pulsing exploits the limited switching frequency best compared to synchronized pulse patterns [6] used elsewhere.

In the nineties IGBT inverters superseded GTO inverters in the range of low and medium powers as typical for Light Rail and Metro applications, allowing distinctly higher switching frequencies. In the first years of this century the same happened with inverters for locomotives and high-speed trains. The question arose how to transfer the advantages of Direct Stator Flux Control to these new inverters which made some of the old restrictions obsolete. With sufficient ratio of switching to stator base frequency sinusoidal PWM can be used without drawback making the traction drive easier to adapt to severe line harmonics limitations. It was already employed with DSC-controlled GTO inverters in the starting region [4] where DSC shows some complications [1].

As Stator-Flux-Oriented Control uses the complete machine model already it can be well applied for estimation of speed from the terminal quantities. As often additional broadband voltage sensors are not wanted careful compensation of the inverter voltage errors is applied when the voltage is modelled from measured dc-link voltage and switching commands. Then robust estimator schemes can be applied to estimate two parameters, e.g. rotational speed and stator resistance, from the difference of the space vectors of machine and model currents. As the model is of the linear fundamental-wave type the system is unobservable at stator frequency being permanently zero. Nevertheless a special management of the flux magnitude enables the drive to operate permanently at any speed at and around zero.

II. MODEL OF THE MACHINE

Each highly dynamic flux-oriented control needs a model of the induction machine as exact as possible to calculate the non- measurable fluxes. On the other hand it must be calculable in sufficiently short time on a Digital Signal Processor (DSP). Space Vector (SV) notation [8] is used for description, denoted by arrows under the letter symbols. For stator-flux orientation the „canonical" Γ-Equivalent Circuit Diagram (ECD) (with the leakage inductance L_σ concentrated in the rotor mesh) using the stator-fixed reference system is most convenient (Fig. 1):

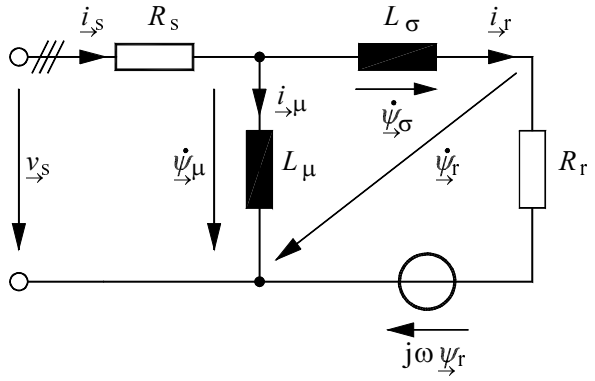

Fig. 1. Equivalent Circuit Diagram of induction machine in space-vector notation, stator-fixed reference frame

It describes the fundamental values of all quantities correctly. Saturation of the main inductance L_μ is measured off-line and taken into account by a characteristic dependent on stator flux magnitude. The stator resistance R_s must be identified on-line.

The state equations can be derived according to this ECD:

$$\dot{\underrightarrow{\Psi}}_{\mu} = \underrightarrow{v}_S - R_S \cdot \underrightarrow{i}_S \tag{1}$$

$$\dot{\underrightarrow{\Psi}}_{r} = R_r \cdot \underrightarrow{i}_r + j \cdot \omega \cdot \underrightarrow{\Psi}_r \tag{2}$$

The stator current is:

$$\underrightarrow{i}_S = \underrightarrow{i}_\mu + \underrightarrow{i}_r = \left[\frac{1}{L_\mu} + \frac{1}{L_\sigma}\right] \cdot \underrightarrow{\Psi}_\mu - \frac{1}{L_\sigma} \cdot \underrightarrow{\Psi}_r \tag{3}$$

Torque can be calculated by two equations

$$T = \tfrac{3}{2} \cdot p \cdot \mathrm{Im}\left\{\underrightarrow{\Psi}_\mu^* \cdot \underrightarrow{i}_S\right\} \tag{4}$$

$$T = \tfrac{3}{2} \cdot p \cdot \frac{1}{L_\sigma} \cdot \left|\underrightarrow{\Psi}_\mu\right| \cdot \left|\underrightarrow{\Psi}_r\right| \cdot \sin\vartheta \tag{5}$$

with $\vartheta = \chi(\underrightarrow{\Psi}_\mu) - \chi(\underrightarrow{\Psi}_r)$ and p number of pole pairs. The first equation is used within the DSP program, the second is better suited for basic deliberations. It is well known from the Synchronous Machine, and it will be taken to illustrate the basic idea of torque control.

III. STATOR-FLUX-ORIENTED CONTROL

The basic task of machine control is to produce the demanded torque and to keep the (stator) flux intensity on its demanded value.

Stator-flux orientation leads the tip of the stator flux SV on a predetermined trajectory – in the case of high switching frequency a multi-corner polygon, nearly a circle ([4], [5]. The radius of the ideal trajectory will be defined by control of the modulus of the stator-flux SV. The tracking speed – in the sampled system expressed by the angular increment per sampling period – results from the output of a linear torque controller [9]. In the following we assume that the modulation period T_m equal to the half switching period is small against the rotor leakage time-constant $T_\sigma = R_\mathrm{r}/L_\sigma$ and the fundamental period T_s.

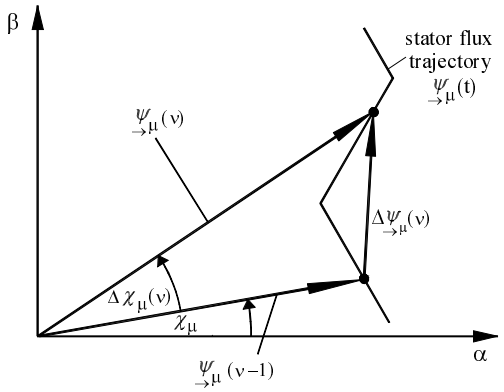

Fig. 2. Stator-flux trajectory and stator-flux increment $\Delta\underrightarrow{\Psi}_\mu(\nu)$ per modulation period ν

Fig. 2 shows the stator flux SV at the beginning and the end of a modulation period T_m (equal to processor cycle); in the most general case the stator flux is stretched by $k_\psi(\nu)$ and rotated by $\Delta\chi_\mu(\nu)$:

$$\underrightarrow{\Psi}_\mu(\nu) = \{(1 + k_\psi(\nu)) \cdot e^{j\Delta\chi_\mu(\nu)}\} \cdot \underrightarrow{\Psi}_\mu(\nu - 1) \tag{6}$$

and thus changed by

$$\Delta\underrightarrow{\Psi}_\mu(\nu) = \underrightarrow{\Psi}_\mu(\nu) - \underrightarrow{\Psi}_\mu(\nu-1) = \{(1 + k_\psi(\nu)) \cdot e^{j\Delta\chi_\mu(\nu)} - 1\} \cdot \underrightarrow{\Psi}_\mu(\nu - 1) \tag{7}$$

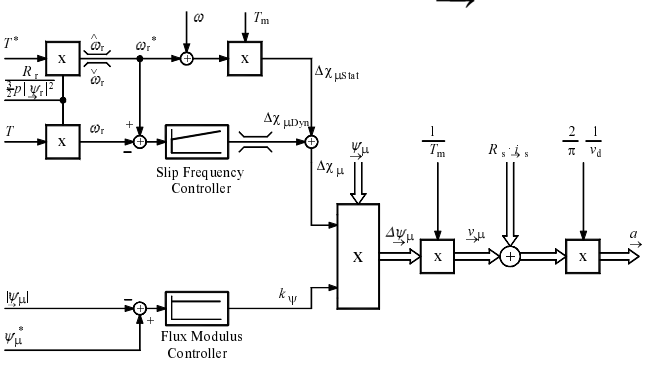

Fig. 3. Basic structure of Indirect Stator-Quantities Control (ISC)

Fig. 3 shows the basic structure of the controller; all quantities are mean values per sampling period. $k_\psi(\nu)$ is delivered by a P-type flux-modulus controller. Torque set (T^*) and actual value (T) are first transformed to slip angular frequencies by multiplication with $R_r/(\frac{3}{2}p \cdot \Psi_r^2)$. Thus breakdown can easily be prevented by limiting the set value. Then both angular frequencies are compared in a PI-type controller delivering the dynamic part of the angular increment, $\Delta\chi_{\mu\mathrm{Dyn}}$. The integral channel will be relieved by a stationary feed-forward

$$\Delta\chi_{\mu Stat} = (\omega + \omega_r^*) \cdot T_m \tag{8}$$

The following block calculates $\Delta\underrightarrow{\psi}_\mu(\nu)$ by developping equ. (7) in a Taylor series, broken after the fourth member:

$$\Delta\underrightarrow{\Psi}_\mu(\nu) = k_\psi(\nu) \cdot \left\{1 - \tfrac{1}{2}\Delta\chi_\mu^2(\nu)\right\} \cdot \underrightarrow{\Psi}_\mu(\nu-1) - \left\{\Delta\chi_\mu(\nu) - \tfrac{1}{6} \cdot \Delta\chi_\mu^3(\nu)\right\} \cdot \underrightarrow{\Psi}_\mu(\nu-1). \tag{9}$$

The stator-flux increment SV will then be multiplied with $1/T_\mathrm{m}$ yielding the magnetizing voltage $\underrightarrow{v}_\mu$, to which the resistive stator voltage drop $R_S \cdot \underrightarrow{i}_S$ will be added. Finally division by $v_d \cdot \pi/2$ delivers the voltage control SV $\underrightarrow{a}$ handed to the PWM unit ([9], [10]).. Please note that there are no underlayed current component controllers anymore.

Now the issue of low frequencies shall be addressed in detail. The stator flux in the model will always be controlled correctly, even at zero frequency. But at low frequency the correspondence of model and real machine currents will be unsufficient, mainly due to errors of the temperature-dependent stator resistance and of the inverter voltages modelled from measured dc-link voltage v_d and switching signals.

Fig. 4 shows the complete machine model acc. to equ. (1)...(3). The very left blocks, in dashed lines, are current balancing controllers comparing measured ($i_{s\alpha(\beta)w}$) and model current ($i_{s\alpha(\beta)}$) coordinates, to correct these errors in a Luenberger observer structure. The gain has to be decreased

with increasing speed, so that the model works as an *i-n*-model at low and as a *v-i*-model at high speed [5].

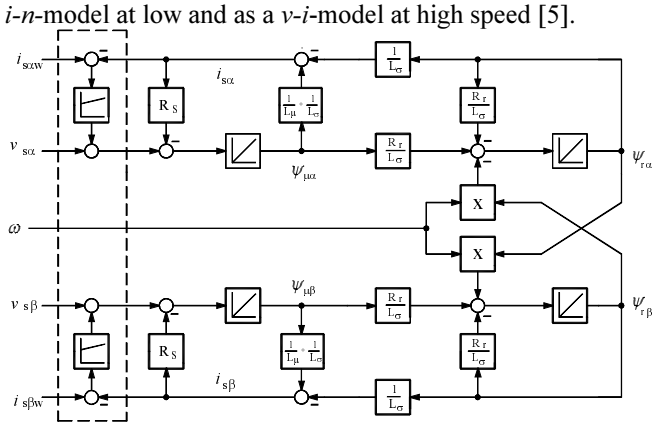

Fig. 4. Complete induction machine model (with current-balancing controllers)

If as shown the stator-voltage drop is calculated with the model currents the control acts only on the model, the true machine will only be „chained" to the model by the current-balancing controllers. This enables e. g. testing of the control without powering the real drive.

IV. FIELD-WEAKENING OPERATION

For high power traction drives the limitation of output voltage by sinusoidal PWM to less than 90% of the maximum possible value of the fundamental at square-wave modulation is disadvantageous as the break-down torque at high speed will be limited to less than 80%. By means of suited overmodulation schemes [10] some 95% can be reached, with comparable dynamics. But finally the transition to square-wave modulation has to be performed. When the maximum voltage – it may be sinusoidal, „overmodulated" or square-wave – has be reached, the torque (constant power range) can only be controlled by field-weakening.

Fig. 5 shows the completion of the control structure by a field-weakening controller. The stationary field-weakening via the factor $1/\gamma_F$ ($\gamma = \psi_\mu/\psi_{\mu rated}$; left part) works in forward mode by amplifying the flux modulus feed-back. The angular increase $\Delta\chi_\mu$ necessary for torque increase cannot be gained as before as the voltage is already at its maximum. Here Dynamic Field Weakening developped for DSC [1] is helpful again [9].

Fig. 6 shows the transient for a torque step out of idling operation, connecting the two stationary circular flux trajectories with radii γ_{FA} (before) and γ_{FC} (after the step). For short time the rotor-flux SV moves further-on on the trajectory with the radius γ_{FA}, while the stator-flux SV takes the „cut-off" trajectory AC having the same length as AB, weakening the stator flux modulus intermediately to γ_{min},. The angle ϑ is increased from zero to the stationary value in the fastest possible way.

The command for the dynamic field-weakening $1/\gamma_D$ is derived from the dynamic response of the slip frequency controller, $\Delta\chi_{\mu Dyn}$, increasing the flux feedback additionally.

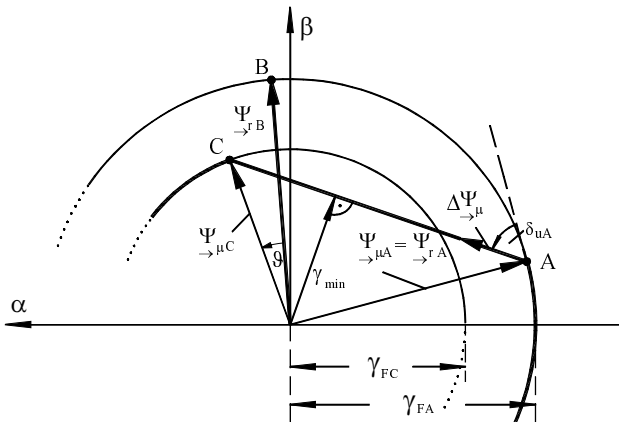

Fig. 6: Trajectories of stator and rotor flux SV at Dynamic Field Weakening

A torque increase is thus performed in less than 1/3 of the base period, without any voltage margin!. At a negative torque step dynamics are achieved only by variation of the control factor $\underrightarrow{a}$. After that the stator-flux modulus is guided rather slowly (taking into account the rotor leakage time-constant) to the new stationary value, to avoid excessive leakage flux and thus overcurrent.

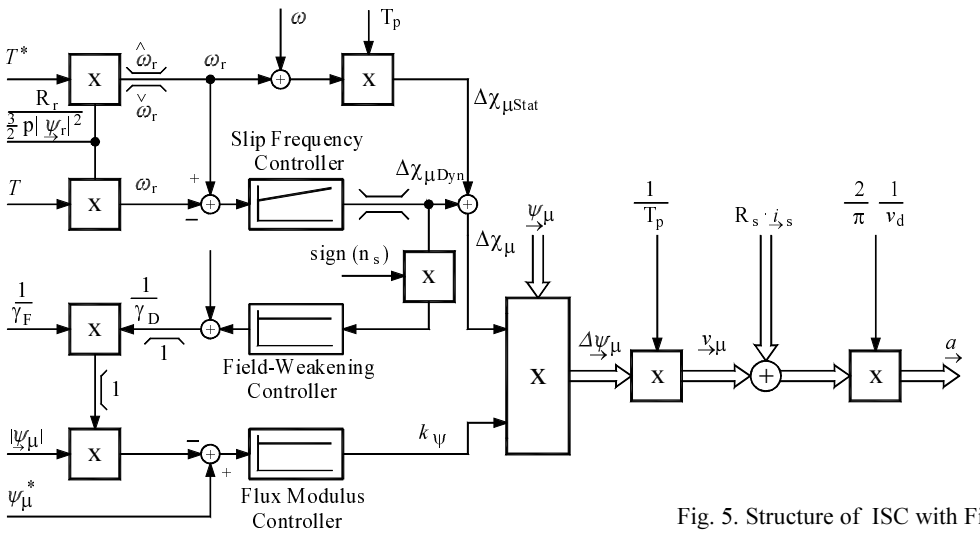

Fig. 5. Structure of ISC with Field-Weakening Controller

V. CORRECTION OF INVERTER VOLTAGE ERRORS

Each model-based control structure is as good as the quality of the modelled quantities and parameters. The major source of incertainty is the modelling of the stator voltage from the measured dc-link voltage and the switching signals. Errors are due to

- Voltage drop of semiconductor devices
- Differences in the switching delay times
- Different influence of the interlocking time dependent on the sign of the inverter output (= stator) current

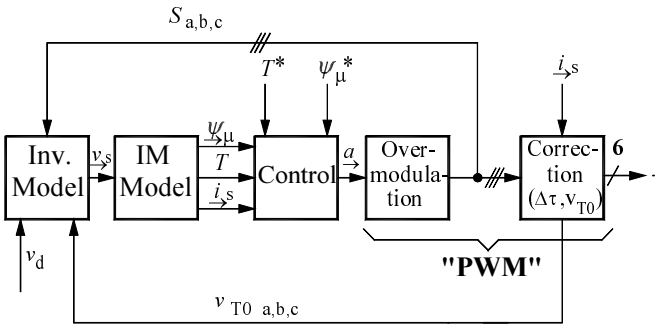

Fig. 7. Correction scheme for inverter errors in recent ISC

These errors depend mainly on the value and the sign of the inverter output current. In the structure described up to now the current-coordinate balancing controller will compensate them, but only to that degree limited by the stability of the control.

Fig. 7 shows the block structure of the correction system applied with ISC today [10], [12]. Control hands the set value for the (normalized) stator-voltage SV $\underrightarrow{a}$ to the Overmodulation block, where the zero-sequence system for Symmetrized Sinusoidal Modulation is added and overmodulation is performed, if needed.

In the correction block the switching-time errors are corrected and the device-voltage drops calculated, based on the model stator current SV. Now the real switching edges will coincide with the ideal ones. The demanded switching commands $S_{a,b,c}$ are given back – together with the correction voltage drops – to the Inverter Model calculating the model stator voltages identical to those of the real motor.

It is now possible to operate the drive without current-balancing controllers. The information set free by this can now be used to estimate e.g. the speed. The most important ECD parameter at low frequency is stator resistance as it influences the stator current severely. It must be estimated on-line for high performance drives.

VI. SENSORLESS IDENTIFICATION OF SPEED

Speed sensors in traction induction motors have always been a bottleneck as spoiling the robustness and/or control performance of the simple squirrel-cage motor: Either they are robust - then the angular resolution is limited and the signal delay at low speed is high. Or they have a high resolution and good dynamic response, but then they are sensitive to shock and hazard.

In the last years the demand on the speed sensor grew, e.g. for the aforementioned speed feed-forward or for speed control as part of adhesion control systems. In low-floor Light Rail Vehicles sensors increase the volume of the individual small motors reasonably. Cost is not negligible, for the sensor itself and for planning, mounting and commissioning, and is an important component of Life Cycle Cost.

Open-loop speed estimation schemes are already widely introduced in industrial application. They are extremely dependent on parameters. Much more robust are observer schemes, as e. g. that described in [11], which has been extended and especially improved by the following scheme ([10], [12], [13]).

Basis is the linear fundamental-wave model used already in ISC; no parasitic effects as slotting or saliency are used. The real machine is described by an identically structured ECD; the quantities in the real machine shall be designated by the index 'w'. The differences are $\Delta x = x - x_w$.

If as supposed both machine and model are fed with identical voltages and show no difference in the parameters the same current would flow in each. If the difference of the stator-voltage drops due to different currents is not too big both current SVs can be described in steady-state by the same Heyland circle diagram (Fig. 8), assuming a constant stator-flux SV.

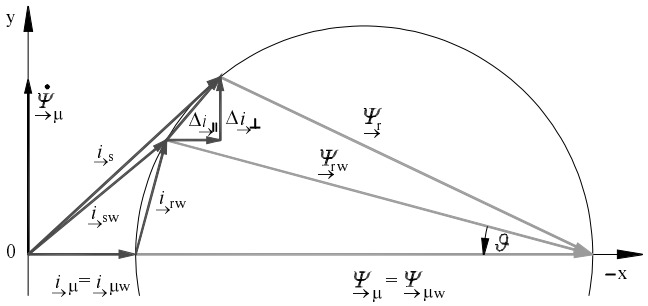

Fig. 8. Heyland Circle Diagram for real machine (x_w) and model (x) at identical stator-flux SV

It is obvious that the different speeds lead to different slip values and thus to different stator currents. If all other parameters are identical this difference can be employed to speed estimation. From the figure it can be seen that e.g. the component of $\underrightarrow{\Delta i_s}$ being perpendicular to the stator-flux SV $\underrightarrow{\psi_\mu}$ will be suited as indicator under thr conditions assumed.

At the critical point of stator frequency being zero speed identification is not possible in the stationary state: The whole dc stator voltage drops over the stator resistance, the rotor mesh is short-circuited by the magnetizing inductance. Only a change of flux or speed can induce a current difference which may be evaluated for speed identification.

The mathematical analysis of the stator-current difference leads to a space-vector differential equation of second order. To make it more compact some abbreviations and normalizations shall be introduced before, the time-constant factor

$$\rho = \frac{L_r/R_r}{L_s/R_s} = \frac{L_\sigma + L_\mu}{L_\mu} \cdot \frac{R_s}{R_r} \qquad (10)$$

and the leakage factor

$$\sigma = \frac{L_\sigma}{L_\mu + L_\sigma}. \qquad (11)$$

The angular frequency is normalized to rotor breakdown value $\omega_{rb} = L_\sigma/R_r$ and designated by 'n', time is normalized to the inverse of ω_{rb}. The derivatives to the normalized time are marked by $\dot{x}$. Then the differential equation can be written as:

$$\underrightarrow{\Delta i_S}^{\circ\circ} + (\rho + 1 - j\,n_w) \cdot \underrightarrow{\Delta i_S}^{\circ} + \rho(\sigma - j\,n_w) \cdot \underrightarrow{\Delta i_S} = j \cdot \frac{1}{L_\sigma} \cdot \left[\Delta n \cdot \underrightarrow{\psi_r}^{\circ} \right] \qquad (12)$$

The excitation of the system and by that the stator current difference vanishes if the following conditions are fulfilled:

- The speed difference or the rotor flux are permanently equal to zero (trivial case)
- The derivatives of both quantities are zero

The last condition marks the case that speed identification fails at stator frequency zero.

In the stationary case under symmetrical sinusoidal conditions the first and second time-derivative of the stator current difference can be expressed by the difference itself and the normalized stator frequency n_s:

$$\underrightarrow{\Delta i_S}^{\circ} = j \cdot n_s \cdot \underrightarrow{\Delta i_S}, \quad \underrightarrow{\Delta i_S}^{\circ\circ} = -n_s^2 \cdot \underrightarrow{\Delta i_S} \qquad (13)$$

Then the solution of the differential equation for stationary operation is given by

$$\underrightarrow{\Delta i_S} = \frac{n_s}{[\rho\sigma - (n_r + \Delta n)n_s] + j \cdot [\rho(n_r + \Delta n) + n_s]} \cdot \frac{\Delta n}{L_\sigma} \cdot \underrightarrow{\psi_r} \qquad (14)$$

This is a rotating space vector containing the information about the speed difference. After multiplication with the conjugate-complex rotor-flux SV, the leakage inductivity L_σ, an additional suited working-point-dependent complex factor $\underline{K}$ and normalization by multiplication with $1/\Psi_r^2$ a resting quantity is obtained. The real part is parallel and the imaginary part perpendicular to the product of $\underrightarrow{\Psi_r}$ and $\underline{K}^*$.

$$\mathrm{Im}\left\{ \frac{\underrightarrow{\Psi_r^*}}{\Psi_r^2} \cdot \underline{K} \cdot \underrightarrow{\Delta i_S} \cdot L_\sigma \right\} = G_{i2} \cdot \Delta n \qquad (15)$$

The perpendicular component to be used for speed identification in an observer structure is proportional to the speed difference and a function of the machine and operating parameters and shall be summarized in a factor G_{i2}. In the prevailing operation range the factor $\underline{K}$ is chosen equal to

$$\underline{K} = (1 + j \cdot n_r)/\sqrt{1 + n_r^2}, \qquad (16)$$

showing a rather uniform negative gain. Only in the range of very small stator frequency with opposite signs of torque and speed the indicator would change its sign [9] and defeat a stable control. The factor is then to be chosen as shown in [13] to

$$\underline{K} = (1 + j \cdot n_r/\sigma)/\sqrt{1 + (n_r/\sigma)^2} \qquad (17)$$

The corresponding gain is depicted in Fig. 9 dependent on stator frequency n_s, up to about double rated speed, with the normalized slip frequency n_r as main parameter.

At the critical stator frequency zero the gain G_{i2} vanishes always, the machine is unobservable. Outside this region the left part of equ. (15) can be used as error function for a PI-controller adjusting the speed signal in the observer. The practical settling time is about one third of the rotor leakage time-constant T_σ [12].

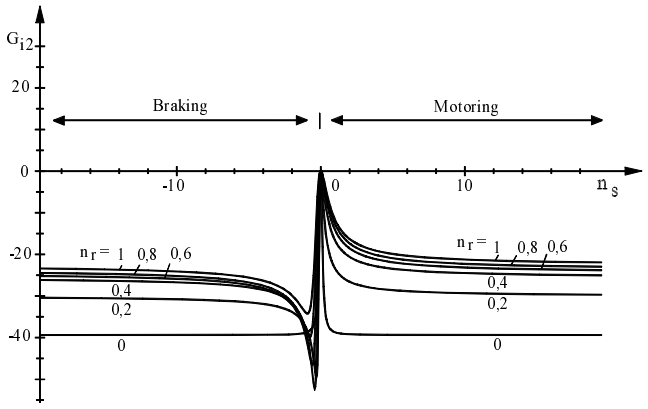

Fig. 9. Factor $G_{i2} = f(n_s, n_r)$; equ. (17)

The excellent quality of this speed observer scheme shall be demonstrated by experimental results of a 120-kW traction motor fed from a 500-kVA IGBT traction inverter with a nominal dc-link voltage of 750 V.

Fig.10 shows speed estimation under dynamic conditions. A torque set value step sequence is given on the induction machine coupled with a dc machine, speed follows mainly in a triangular fashion. Real speed ω_w (measured with an incremental encoder with 2000 pulse/rev.) and estimated speed ω are shown, together with the torque functions.

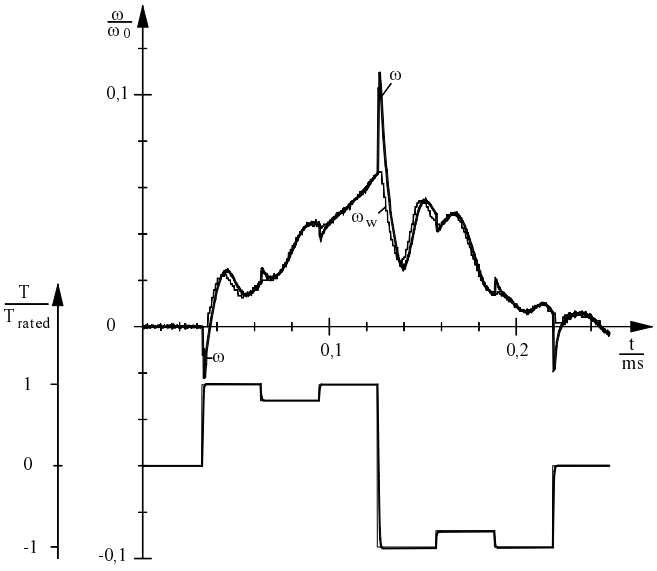

Fig. 10. Estimated (ω) and measured speed (ω_w) at acceleration and braking with up to 100 % rated torque

Estimated speed follows the measured speed astonishingly exactly, including the oscillation of the two-masses-spring-system.

The peaks visible in ω when the torque changes very fast are due to current displacement effects in the rotor bars reducing $L_{\sigma w}$. So the real rotor currents rise faster than those in the model which cannot take care of this effect due to limited calculation time. It will be interpreted by the speed estimator as a negative speed error. But it has no vital consequence on the quality of speed estimation as set value and actual torque differ anyway during such extremely fast transients.

With such a scheme speed reversals with a change rate of 24 min^{-1}/s and permanent full load operation at a minimum stator frequency of only 0.33 Hz can be safely managed. But it must be kept in mind that at still lower values or rates of change the scheme will fail. An escape of the problem will be given in Section IX.

VII. STATOR RESISTANCE ESTIMATION

An undispensable prerequisite is exact on-line identification of the stator resistance which changes severely with temperature. Obviously thermal sensors are not wanted.

The same change of temperature in stator and rotor shall be assumed as first approach. So the value of ρ is not changed, when R_s changes. Then an equation similar to (14) can be found for the appertaining stator-current SV difference $\underrightarrow{\Delta i_s}_R$ caused by the difference ΔR_s [14]. For small ΔR_s and $\rho = \rho_w$ this equation can be written as:

$$\underrightarrow{\Delta i_s}_R = \frac{n_r^2 - \sigma^2 - j \cdot 2\sigma n_r}{\underline{Z}} \cdot \frac{\Delta R_s}{L_\sigma \cdot R_r} \cdot \underrightarrow{\Psi_r} \qquad (18)$$

with

$$\underline{Z} = [\rho \cdot \sigma - n_r \cdot n_s] + j \cdot [\rho \cdot n_r + n_s]. \qquad (19)$$

Multiplying the sum of equ. (14) and equ. (18) with the conjugate-complex rotor flux SV, L_σ, the complex (mainly imaginary) factor $\underline{Z}$ and $1/\Psi_r^2$ yields again a resting quantity. The imaginary part of this is only proportional to ΔR_s:

$$\mathrm{Im}\left\{ \frac{\underrightarrow{\Psi_r^*}}{\Psi_r^2} \cdot (\underrightarrow{\Delta i_s} + \underrightarrow{\Delta i_s}_R) \cdot L_\sigma \cdot \underline{Z} \right\} = G_{\mathrm{Rs}} \cdot \frac{\Delta R_s}{R_r} \qquad (20)$$

In steady state Δn has no influence on the result, as it is contained only in the real part. As the stator resistance changes only slowly an integral controller will be used for identification. The left side of equ. (20) multiplied with the sign of n_r is its input. This method is independent of the speed identification scheme for small differences of speed and stator resistance.

Fig. 11 shows that speed estimation at very low stator frequency needs correct values of R_s. The drive (same as in Fig. 10) operates at standstill with 100% rated torque (= 35% of breakdown torque T_b). The model stator resistance value is initialized to 80% of its nominal value. Due to this mismatch the estimations of stator flux and correspondingly of speed are wrong. The ripple frequency is six times stator frequency due to malfunctioning of the inverter correction circuit (Fig. 7) by a severe difference between $\underrightarrow{i_s}$ and $\underrightarrow{i_{sw}}$. The initial error in speed is 1% of rated speed.

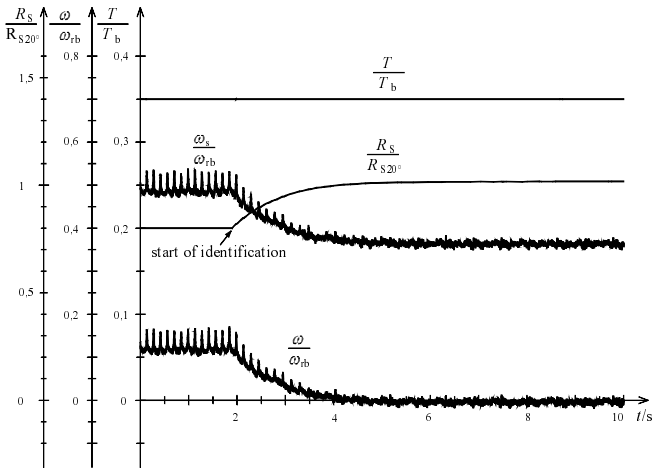

Fig. 11: On-line identification of stator resistance at standstill

At t = 1.9 s the identification of R_s starts, the actual value of 1.018 $R_{s20°C}$ is found within 2...3 s. Simultaneously all state variables converge to their correct values, the ripple vanishes and speed reaches the correct value zero**.** The method operates well in the range of small frequencies where the influence of the stator resistance is relevant and where this identification is necessary.

VIII. SUPPRESSION OF PARASITIC DC VOLTAGES

As in the ISC structure only the mathematical model in the DSP is controlled, unwanted dc components in voltage and fluxes are of only numerical order and can thus be neglected. As will be shown later there are possible operation points in which – under steady-state conditions – dc portions must be allowed in the stator fluxes and stator currents, which the control must handle without problems. But of course inspite of all sophisticated parameter identification and compensation of inverter voltage errors in the real inverter drive parasitic dc voltage portions cannot be prevented. In standard field-oriented control schemes the dc portions of the measured motor voltages and (sometimes) wrongly the stator fluxes are cancelled by filtering.

In ISC another way has been found: In a rather quick-acting circuit the dc portions in the stator-current differences are detected. To that purpose the stator-current-difference SV is sampled at time intervals corresponding to e.g. about 5° of χ (see Fig. 12). The dc-portion SV is then approximately [15]

$$\underrightarrow{\Delta i_-} \approx \left[\frac{1}{2} \cdot \left(\underrightarrow{\Delta i_s}_2 + \underrightarrow{\Delta i_s}_1 \right) + j \cdot \frac{1}{\Delta\chi} \cdot \left(\underrightarrow{\Delta i_s}_2 - \underrightarrow{\Delta i_s}_1 \right) \right] \qquad (21)$$

and given on two PI-controllers, whose outputs are acting as $\underrightarrow{\Delta v_{s-}}$ on the stator-flux integrator input, compensating any (parasitic) dc difference between the model voltages and the real inverter voltages, but not suppressing necessary dc portions in the stator fluxes or the stator currents.

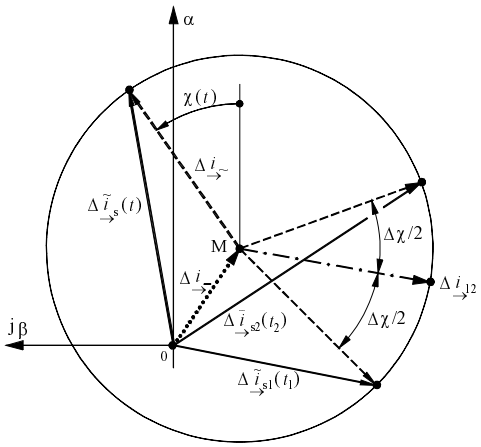

Fig. 12. Space vector of stator-current differences caused by a parasitic dc voltage, at speed identification

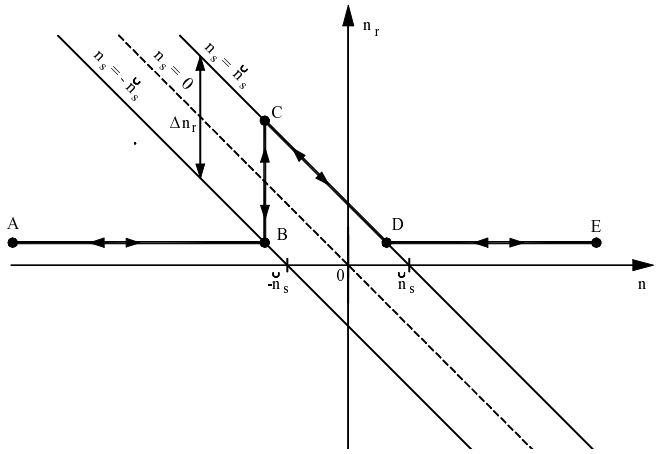

Fig. 13: Normalized slip frequency n_r vs. normalized speed n at constant torque

IX. OPERATION WITH INFINITELY SLOW CHANGE BETWEEN DRIVING AND BRAKING

The speed of a linearly modelled induction machine cannot be observed at zero stator frequency without injecting test signals providing a change of flux. Test signals are often not wanted as they may disturb e.g. signalling circuits, or they cannot be injected sufficiently with the low switching frequency of high power inverters.

As it has been shown slow passings through the region of very small stator frequency can be safely managed. The question is whether an operation mode is possible which simply avoids stationary working in the region below 0.4...0.5 Hz, a value that can safely be mastered with the described control structure.

To that purpose a scheme has been proposed and successfully implemented [14] which avoids operation with too low stator frequency by manipulating the modulus of the stator-flux SV. For a given (non-zero) torque a reduction of the rotor flux modulus raises the necessary slip frequency:

$$\omega_r = \frac{R_r \cdot 2}{3 \cdot p \cdot \Psi_r^2} \cdot T \qquad (22)$$

The function of the operation management is explained for a reversing of speed at constant torque. Fig. 13 shows the normalized slip frequency n_r as a function of normalized speed. In the diagram working points with constant normalized stator frequency n_s are straight lines with gradient –1. Speed identification works safely for stator frequencies with an absolute value $\geq \check{n}_s$. Thus the drive must not work stationarily in the region between the lines $n_s = -\check{n}_s$ and $n_s = \check{n}_s$ in Fig. 13.

Starting at point A, the machine brakes with negative speed and positive (non-zero) torque and slip frequency; the absolute values of speed and stator frequency decrease. At point B the stator frequency reaches the limit $-\check{n}_s$. Now there are two choices to produce the wanted torque:With full flux, minimal slip frequency and negative stator frequency (point B) or with reduced flux magnitude and a slip frequency increased by Δn_r (point C), where the stator frequency is already positive and $\geq +\check{n}_s$.

The operation management decides to decrease the flux such that the crossing of the stator frequency through the „forbidden zone" is sufficiently fast. On the other hand the transition must be slow in regard to the rotor leakage time-constant T_σ, to avoid an inadmissibly dynamic increase of the leakage flux and thus stator current.

As speed changes further the operation point moves along the line $n_s = +\check{n}_s$ towards D, while the flux is continuously increasing again, so that the drive is operated $n_s = \check{n}_s$ with maximum permissible flux and minimum stator current. This is done by stator frequency control. At D normal motoring operation with full flux and constant slip frequency is reached again and maintained until E.

The opposite reversing starts at point E in motoring mode. With decreasing speed point D and $n_s = +\check{n}_s$ is reached. For further decreasing speed the flux must be decreased continously to keep the stator frequency at its upper limit $+\check{n}_s$. The control supervises whether the torque can be produced with full flux and negative stator frequency $\leq -\check{n}_s$, too. When at point C the condition is fulfilled, the drives changes sharply to B.

In practical operation an additional hysteresis avoids jittering. Fig. 14 shows the time functions of such a very slow speed reversal, measured at the 120-kW drive. The dc load machine is speed-controlled and impresses the triangularly changing speed; the IM is torque-controlled.

The two upper traces show stator flux modulus and torque, the middle the observed stator frequency and the lower traces the nearly perfectly coinciding values of true and observed speed. For $T_{\text{rated}} = 0.35\ T_b$ the rated slip frequency is $0.187 \cdot \omega_{rb} = 2\pi \cdot 0.89\ \text{s}^{-1}$, which is more than the double of the above-mentioned minimum frequency of $\check{\omega}_s = 2 \cdot \pi \cdot 0.33\,\text{s}^{-1}$; the frequency hysteresis is 0.02 ω_{rb}. Stator flux is reduced down to 50%. [14] shows how at practical no-load condition safe transition is reached by switching on a minimum torque of less than 3.5% of rated torque. [16] reports on practical tests on a Combino® low-floor tram-car. It shows that vehicles running down a slope can be smoothly stopped, held at zero speed and accelerated in the opposite direction, without speed sensors.

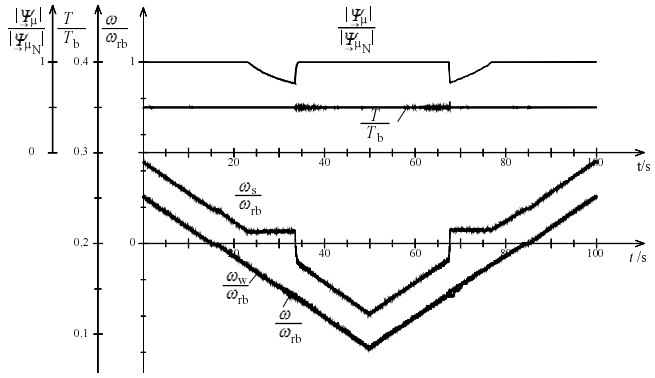

Fig. 14: Very slow speed reversing operation with rated torque. 120-kW motor.

[17] finally states that the speed-sensorless operation will be implemented in the new SITRAC Siemens traction control and intensively tested in different light-rail and metro applications in Spain, U.S.A. and Taiwan.

X. ADVANTAGEOUS DIFFERENCE OF INDIRECT STATOR-QUANTITIES CONTROL AND DIRECT VECTOR CONTROL

Fig. 15 shows in an overview the whole control system of speed-sensorless Indirect Stator-Quantities Control (ISC).

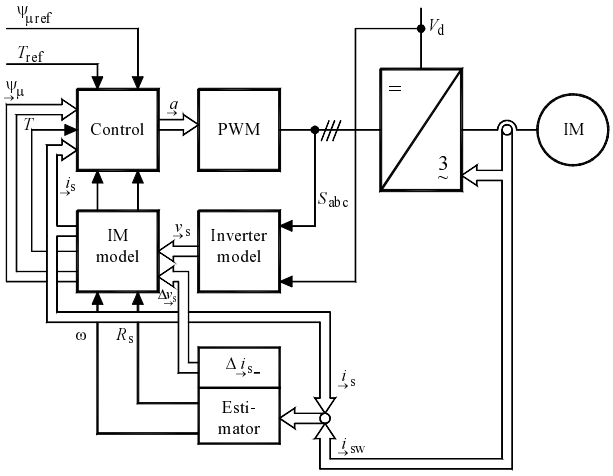

Fig. 15. Overall block structure of speed-sensorless ISC

In the Control block stator-flux modulus and torque reference values are computed together with the actual values of stator-flux and stator-current SVs and torque, delivered by the IM model (sections III, IV). The normalized output voltage SV $\underrightarrow{a}$ is transformed in the PWM block to the switching commands for the inverter (voltage error correction (section V) indicated only by the input arrow to the inverter block). From the switching commands and the dc-link voltage the stator-voltage SV is calculated in the inverter model and handed to the IM model. The necessary speed and stator-resistance informations for the *v-i-n*-model are obtained from the comparison of the manipulated stator-current SVs of model and machine (section VI). Finally the Δi_s-block suppresses parasitic dc portions in the stator voltages (section VIII).

As claimed in section VIII there may be operation points where dc portions in the stator fluxes and currents must be admitted. Such a point is depicted in Fig. 16: The (very low) speed reference is modulated with – mainly – stator frequency 0.65 Hz.

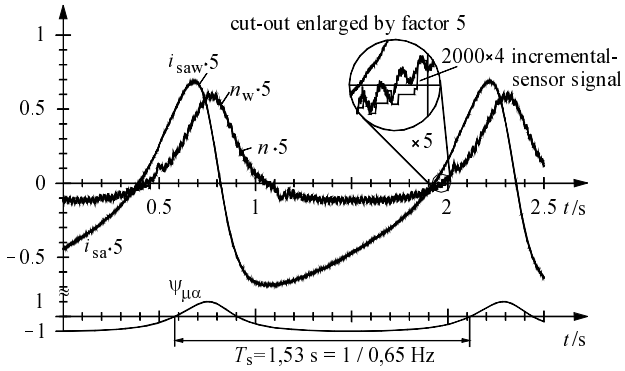

Fig. 16. Operation with stator-frequency-modulated speed reference. Stable operation in spite of dc portions in stator fluxes and currents

In stator-flux and stator current dc portions are clearly visible. The slight 50-Hz oscillation in the speed signal is due to such a disturbation in the armature current of the dc brake machine, which demonstrates on the other hand the excellent resolution of the speed identification scheme.

This operation is not allowed with direct vector control systems (e.g. [1, 18]) suppressing all dc portions in the measured stator voltages and perhaps the stator flux [18], as those cancel the necessary dc portions too. Though this may be regarded a somewhat hypothetic working-point, it makes clear the extended operation possibilities of Indirect Stator-Quantities control, compared with usual Direct Vector Control at very low speeds.

XI. CONCLUSION

Indirect Stator-Quantities Control (ISC) unifies the advantages of stator-flux-orientation proven successful in Direct Self Control with Pulse Width Modulation well suited for fast-switching IGBT inverters. Using the signals available in the control model motor speed can be estimated so that no speed sensors are needed anymore. Careful feed-forward correction of inverter voltage errors and especially the on-line cancelling of their unwanted parasitic dc portions is indispensable for safe operation in the zero-speed zone with unrestricted speed reference. Additional work not described here has been necessary on automatic identification procedures of machine and inverter model parameters and on procedures for magnetizing the machine with unknown speed and residual flux without speed sensor.

ACKNOWLEDGEMENTS

The authors would like to thank their Ph.D.s Christoph Evers, Christian Foerth, Frank Hoffmann, Stephan Koch and Markus Weidauer for their contribution to this project.

REFERENCES

[1] A. Steimel, „Control of the Induction Machine in Traction“, in *Proc. 8th International Power Electronics and Motion Control Conference (PEMC 98), Prague 1998, K 4* and *Elektrische Bahnen 96* (1998), No. 12, pp. 361–369

[2] M. Depenbrock, „Direkte Selbstregelung (DSR) für hochdynamische Drehfeldantriebe mit Stromrichterspeisung“, *etzArchiv* 7 (1985), H. 7, pp. 211-218

[3] M. Depenbrock, „Direct Self-Control of the Flux and Rotary Moment of a Rotary-Field Machine“, *US Patent* 4,678,248; 07.07.1987 (filed 18.10.1985).

[4] M. Depenbrock, „Direct Self-Control (DSC) of Inverter-Fed Induction Machine“, *IEEE Transactions on Power Electronics*, vol. 4, pp. 420–429, 1988

[5] U. Baader, „Hochdynamische Drehmomentregelung einer Asynchronmaschine im ständerflußbezogenen Koordinatensystem“, *EtzArchiv* 6 (1989), H. 1, S. 11–16

[6] A. Steimel, „Steuerungsbedingte Unterschiede von wechselrichtergespeisten Traktionsantrieben“, *Elektrische Bahnen 92* (1994), No. 1/2, pp. 4–36.

[7] M. Jänecke, R. Kremer, G. Steuerwald, „Direct Self Control (DSC), A Novel Method Of Controlling Asynchronous Machines in Traction Applications“, *Elektrische Bahnen 88* (1990), No. 3, pp. 81–87

[8] K. P. Kovacs, I. Racs, *Transiente Vorgänge in Wechselstrommaschinen*. Verlag der Ungarischen Akademie der Wissenschaften, Budapest 1959.

[9] M. Jänecke, F. Hoffmann, „Fast Torque Control of an IGBT-Inverter-Fed Three-Phase A.C. Drive in the Whole Speed Range – Experimental Results“, *in Proc. 6th EPE Conference 1995*, Sevilla, vol. 3, pp. 399–404

[10] F. Hoffmann, „Drehgeberlos geregelte Induktionsmaschinen an IGBT-Pulsstromrichtern“, Ph. D. Dissertation, Ruhr-Universität Bochum, Germany, 1996.

[11] H. Kubota, K. Matsuse, T. Nakano, „DSP-Based speed adaptive flux observer of induction motor“, *IEEE Transactions on Industry Applications*, 1993, No. 2, pp. 344–348

[12] M. Depenbrock, F. Hoffmann, St.Koch, „Speed Sensorless High Performance Control For Traction Drives“, in *Proc. 7th EPE Conference 1997*, Trondheim, Vol. 1, pp. 1.418–1.423

[13] F. Hoffmann, St. Koch, „Steady State Analysis of Speed Sensorless Control of Induction Machines“, in *Proc. IECON '98* (Aachen), Vol. 3, pp. 1626–1631

[14] M. Depenbrock, Ch. Foerth, St. Koch, „Speed Sensorless Control Of Induction Motors At Very Low Stator Frequencies“, in *Proc. 8th EPE Conf. 1999*, Lausanne

[15] Ch. Foerth, „Traktionsantrieb ohne Drehzahlgenber mit minimiertem Messaufwand“, Ph. D. Dissertation, Ruhr-Universität Bochum, Germany, 2001

[16] T. Frenzke, F. Hoffmann, H.-G. Langer, „Speed Sensorless Control of Traction Drives – Experiences on Vehicles“, in *Proc. 8th EPE Conference 1999*, Lausanne

[17] G. Amler, F. Sperr, F. Hoffmann, „Highly dynamic and speed sensorless control of traction drives“, in *Proc. 10th EPE Conference 2003, Toulouse.*

[18] M. Cirrincione, M. Pucci, G. Cirrincione, G.-A. Capolino, „A New Adaptive Integration Methodology for Estimating Flux in Induction Machine Drives“, *IEEE Transactions on Power Electronics*, vol. 19, No.1, pp. 25–34, January 2004.

A 10KW SOFC-Low Voltage Battery Hybrid Power Processing Unit for Residential Use - A Student Project

Jinhee Lee, Jinsang Jo, Minsoo Jang, and Sewan Choi*
Seoul National University of Technology
Department of Control & Instrumentation Eng.
Seoul, Korea
*E-mail: schoi@snut.ac.kr

***Abstract*—This paper outlines a 10kW power processing unit for 5KW SOFC-low voltage battery hybrid power generation which has been developed for participation in the 2003 Future Energy Challenge Competition organized by U.S. Department of Energy and IEEE. The objective of the competition was to develop a fuel cell inverter with minimum requirement for cost of $40/KW and efficiency of 90%. The proposed power processing unit consists of the front-end DC-DC converter, the DC-AC inverter and the bi-directional DC-DC converter. Practical issues such as component rating calculation, high frequency transformer design, heat sink design, and protection are detailed aiming at the cost and efficiency targets. A low-cost controller design is discussed along with current-mode control, output voltage regulation with capacitor balancing and a SOC control for battery management. A 10kW hardware prototype was successfully built and tested in the steady-state as well as in the transient-state. Experimental performances are compared to minimum target requirements of the fuel cell inverter. The cost analysis is done based on the spreadsheets evaluation forms provided in the competition.**

1. INTRODUCTION

A Fuel cell power generation systems are expected to see increasing use in various applications such as stationary loads, automotive applications, and interfaces with electric utilities due to the several advantages over conventional generation systems. These advantages include 1) low environmental pollution 2) highly efficient power generation 3) diversity of fuels(natural gas, LPG, methanol and naphtha) 4) reusability of exhaust heat 5) modularity and 6) faster installation [1].

Fuel cells are generally characterized by the type of electrolyte that they use. Solid oxide fuel cells (SOFC) have grown in recognition as a viable high temperature fuel cell technology. The most striking quality of SOFCs is that the electrolyte is in solid state and is not a liquid electrolyte. The high operating temperature up to 1000°C allows internal reforming, promotes rapid kinetics with non-precious materials and produces high quality byproduct heat for cogeneration or for use in a bottoming cycle. A number of different fuels can be used from pure hydrogen to methane and carbon monoxide. The major advantage of SOFC lies in its efficiencies raging from 55 to 60% [2].

In general, the function of a power processing unit (PPU) in a fuel cell generation system is to convert the DC output power from the fuel cell to regulated AC power. The power conditioning unit that basically consists of an inverter is required to have the following characteristics: 1) allowable for wide output voltage regulation of fuel cell 2) controllability of output voltage 3) available for isolated operation and line parallel operation 4) fast reactive power dispatch 5) low output harmonics 6) high efficiency and 7) suitable for high power system [3]. Fuel cell production costs are currently decreasing and have nearly achieved energy costs that are competitive with local utility rates. The inverter cost must also decrease while at the same time increasing efficiency, reliability, and power quality levels. The cost reduction of a PPU will enable the fuel cell systems to penetrate rapidly into the utility market.

Table I. System Specification

Design item	Minimum Target Requirement	
Manufacturing cost	Less than US$40/kW in high volume protection	
Output Power	nominal	5kW continuous @ DPF 0.7
	overload	10kW overload for 1 minute @ DPF 0.7 5kW from fuel cell and 5kW from battery
Energy source	Primary source (SOFC)	29V nominal, 22~41 VDC, 275A max. from 5kW fuel cell
	Battery	48V nominal, +10% ~ -20%, 500Wh
Output voltage	Split single-phase 120V/240V, 60Hz	
	Voltage regulation	± 6%
	Frequency regulation	± 0.1Hz
	THD	Less than 5%
Acoustic noise	Less than 50dBA @ 1.5 m distance	
Overall efficiency	Higher than 90%	
Protection	Over current, over voltage, short circuit, over temperature, and under voltage	

2. PROPOSED POWER PROCESSING UNIT

Fig. 1 shows the block diagram of the SNUT fuel cell inverter system. The DC voltage from the fuel cell, $29V_{DC}$ nominal, is first converted to $400V_{DC}$ via an isolated high frequency DC-DC converter. The 400V DC-DC converter output is then converted to 120V/240V, 50/60 Hz, single-phase AC by means of a PWM inverter stage. The 48V battery bank is connected to the 400V DC link via a bi-directional DC-DC converter for charge and discharge modes of operation.

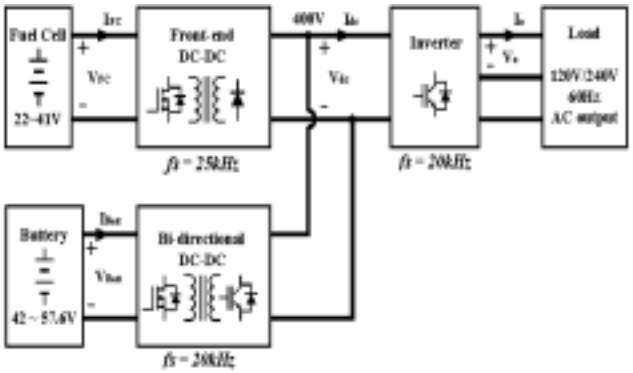

Fig. 1 Block Diagram of the SNUT Fuel Cell Inverter System

2.1 Front end DC-DC converter

A front end DC-DC converter is required to boost an unregulated fuel cell voltage of 29V nominal to a regulated 400V. As shown in Fig. 2, the full-bridge type with two diode bridges connected in series at the secondary is a topology of choice. High frequency transformers are employed to allow a low voltage to be boosted to two split $200V_{DC}$ buses for the DC link to the Inverter. The reason why two 2.5kW high frequency transformers are employed instead of using a 5kW high frequency transformer is to reduce the leakage inductances and therefore to reduce the duty loss. The reduced duty loss also reduces turns ratio of the transformer. This in turn reduces the voltage rating of diodes in the secondary side and the current rating of MOSFETs in the primary side. The voltage source type has been chosen because the inductor in the current source type should have a large peak current rating of 275A.

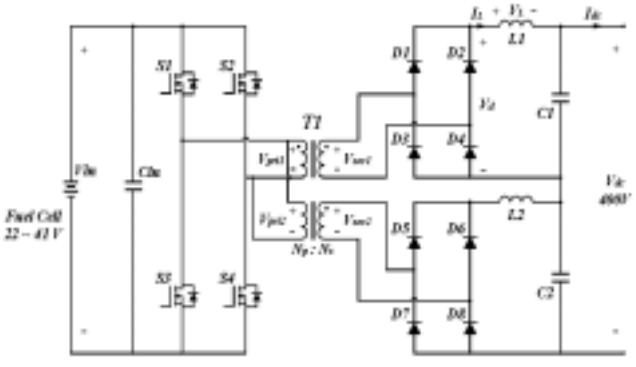

Fig. 2 Front-end DC-DC Converter

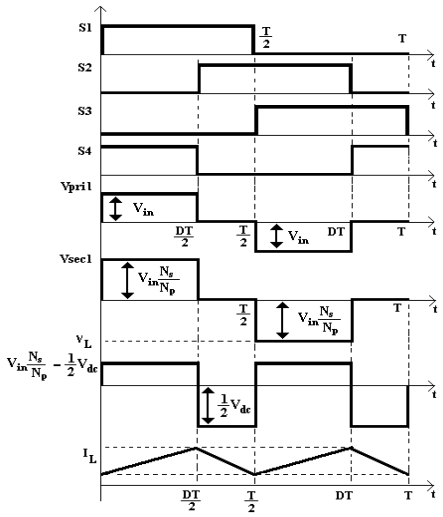

Fig. 3 Main waveforms of the front-end DC-DC converter

Fig. 3 shows the main waveforms of the front-end DC-DC converter. From the inductor voltage V_L an equation can be written as,

$$(V_{in} \cdot \frac{N_s}{N_p} - \frac{1}{2} \cdot V_{dc}) \cdot \frac{DT}{2} = \frac{1}{2} \cdot V_{dc} \cdot \left\{ \frac{T \cdot (1-D)}{2} \right\} \quad (1)$$

Therefore, the duty cycle of the proposed front-end DC-DC converter is obtained by,

$$D = \frac{N_p \cdot V_{dc}}{4 \cdot N_s \cdot V_{in}} \quad (2)$$

According to eqn.(2), the duty cycle ranges 0.24 to 0.45 to regulate the dc link voltage of 400V when the fuel cell voltage varies between 22V and 41V.

Fig. 4 shows the block diagram for feedback control of the front end DC-DC converter. The first goal of the control is to regulate the dc link voltage. A PI compensator is used for the voltage control. A current control is also implemented to improve the dynamic characteristic of the system and to reduce current ratings of the power components during load transient. The current reference is restricted by a current limiter whose value is adjusted by a command from the fuel cell controller so that the power drawn from the fuel cell does not exceed its capability. A low-cost phase-shift PWM controller, UC3895, is employed for control of the front-end DC-DC converter. It allows constant frequency PWM in conjunction with resonant zero-voltage switching to provide high efficiency at high frequency [9].

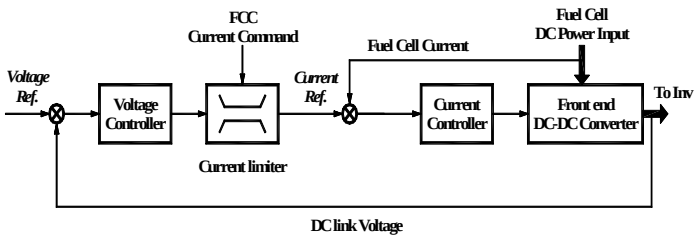

Fig. 4 Control block diagram for the front end DC-DC converter

2.2 DC-AC Inverter

The inverter system consists of two half-bridge inverters, utilizing center tapped dc link capacitors to generate a split single-phase 120/240V_{ac}, 60Hz output as shown in Fig. 5. An output L-C filter stage is employed to reduce the ripple component and to draw a low THD AC waveform.

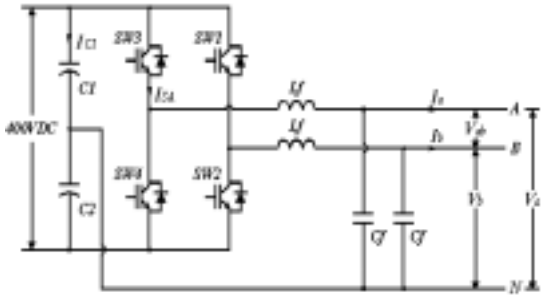

Fig. 5 DC-AC Inverter

A low cost DSP Texas Instrument TMS320LF2407 DSP is implemented to provide the control for the inverter system. The DSP control will offer increased flexibility and will minimize component cost. The goal of the DSP control is as follows: 1) Supervise the whole PPU. 2) Generate the PWM gating signals for IGBTs in the inverter stage. 3) Implement output voltage regulation under varying load conditions. 4) Send the bi-directional DC-DC converter a current reference. 5) Communicate with the fuel cell controller.

To meet the output voltage tolerance requirement the AC output voltage is sensed and a closed-loop control is implemented with a digital PI compensator in the DSP. In the meanwhile, unbalance in dc-link capacitor voltages causes generation of even harmonics in the inverter output voltages. A simple output voltage regulation method with capacitor voltage balancing function is implemented as shown in Fig. 6. Suppose output voltage V_a has a positive dc offset, which means that the upper capacitor voltage is greater than the lower capacitor voltage. The output voltage V_a is sensed and passed through a low pass filter to obtain a dc component of voltage V_a. This causes addition of a positive value to the reference output voltage V_b^* resulting in a decrease in upper capacitor voltage and an increase in lower capacitor voltage.

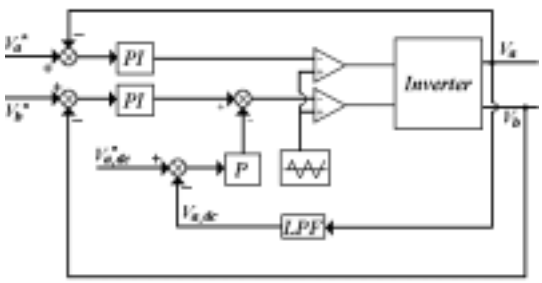

Fig. 6 Output voltage regulation and capacitor voltage balancing

2.3 Bi-directional DC-DC Converter

The fuel cell has a slow response, and therefore the power demand from the load and the power supply from the fuel cell does not coincide during a transient load. Therefore, a secondary energy source is required to match the power difference between the fuel cell and the load. High voltage batteries could be directly connected to the 400V dc link without any intermediate power converter, but the high voltage battery is relatively expensive and may have the battery cell unbalance problem in the long run. A 48V lead acid battery pack is connected to the 400V dc link via a bi-directional DC-DC converter shown in Fig. 7. A current-source push-pull converter employing MOSFETs is operated to discharge the battery whereas a voltage-source full-bridge converter employing IGBTs is operated to charge the battery.The control block diagram for the bi-directional DC-DC converter is shown in Fig. 8. The DSP in the inverter system determines the current reference for the bi-directional DC-DC converter by calculating the difference in real power between the PPU input and the load. The two PWM controllers, UC3825 and UC3895, are employed for charge and discharge modes of operation, respectively. One should be in idle state while the other is in operation. Fig. 9 shows the inductor voltage and current waveforms for charge and discharge modes, respectively. Let us define turns ratio n_2 of the high frequency transformer T_2 to be (See Fig. 7),

$$n_2 = \frac{N_s}{N_p} \tag{3}$$

During the charge mode, we have

$$-(V_{batt} - \frac{V_{dc}}{n_2}) \cdot DT_S = V_{batt} \cdot (\frac{1}{2} - D)T_S \tag{4}$$

which gives

$$\therefore \frac{V_{batt}}{V_{dc}} = \frac{2D}{n_2} \quad \text{(where, } 0 < D < 0.5\text{)} \tag{5}$$

During the discharge mode, we have

$$V_{batt} \cdot D_d T_S = -(V_{batt} - \frac{V_{dc}}{n_2}) \cdot (\frac{1}{2} - D_d)T_S \tag{6}$$

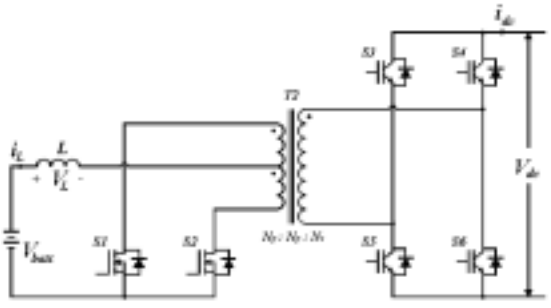

Fig. 7 Bi-directional DC-DC Converter

which gives

$$\therefore \frac{V_{dc}}{V_{batt}} = \frac{n_2}{(1-2D_d)} \quad (0<D_d<0.5) \tag{7}$$

$$\therefore \frac{V_{dc}}{V_{batt}} = \frac{n_2}{2(1-D)} \quad (0.5<D<1, \text{ where } D = 0.5+D_d) \tag{8}$$

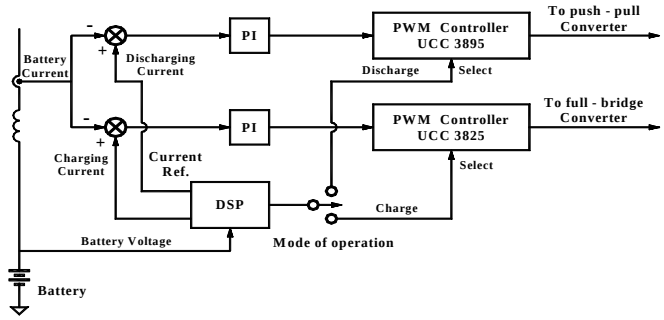

Fig. 8 Control block diagram for the bi-directional DC-DC converter

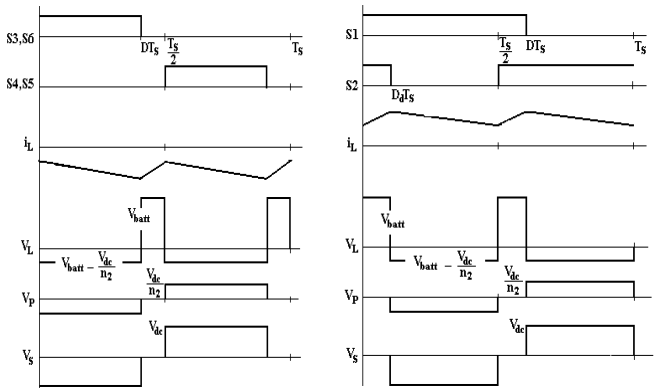

(a) Charge mode (b) Discharge mode

Fig. 9 Inductor voltage & current waveforms

2.4. Battery management

An optimum use of battery combined with fuel cell can reduce the cost of the fuel cell system, or improve the system performance such as reliability and lifetime. To cope with the slow dynamic response of the fuel cell(Maximum Slew Rate = 200 watts/minute), a 48 V battery pack is used as a secondary energy source to supply transient load since the fuel cell system including a reformer is sluggish even if the fuel cell stack has a fast response.

During an overload condition the PPU is supposed to draw 5kW from the fuel cell and 5kW from the battery for maximum 1 minute. Charging and charge management must be provided such that charge is unchanged at the end of a 24 hour test sequence [8]. The SNUT fuel cell inverter determines the mode of operation based on battery state of charge (SOC). The SOC could be measured simply by integrating the battery charging current I_{bat} as follows,

$$SOC = \frac{Q_0 - \int i_{bat}\, dt}{Q_n} \tag{9}$$

where Q_o is initial charge and Q_n is rated ampere-hour of battery. The initial charge Q_o is set to be Q_n when the system starts from full battery charge. More accurate measurement requires in-depth considerations of various parameters such as temperature, discharge rate, age and cumulative calculation errors [5,6]. But this research is out of paper's scope and it is the authors' intention to show the mode of operation determined by SOC as an index.

In hybrid electric vehicle system where regeneration braking is considered, the SOC is maintained between 0.4 and 0.8. However, the SOC is controlled to maintain 1 for residential use, which is the case of the competition. Detailed operational procedure is as follows. When the load power exceeds 5kW, which is the maximum output power of the fuel cell, battery discharges its energy to the load through a bi-direction converter until the overload condition is removed. When the load jumps, but not overloaded, the battery should also discharge until the fuel cell power increases and is able to supply the demanded load power. After the discharging mode ends, the fuel cell power continues to increase to charge the battery until the SOC reaches 1. In charging mode, the fuel cell charges the battery with a current proportional to depth of discharge, but limits the current to a maximum value recommended by manufacturer. The magnitude of the charging current in the SNUT fuel cell inverter system is determined as shown in Fig. 10.

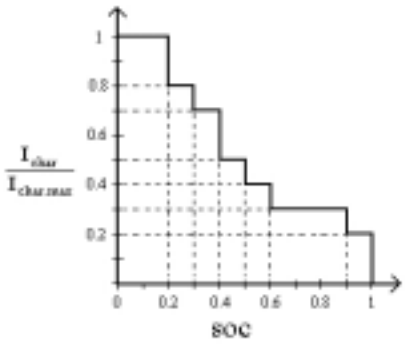

Fig. 10 Battery charging current

2.5. Protection and Diagnostic

The proposed PPU provides the protection capability of over current, short circuit, over/under voltage and over temperature in the circuit. Table II lists all the protection implemented in the proposed PPU. The PWM control IC such as UC3895 provides the capability to detect any fault signal through an input pin of the

chip and will shut down the chip by disabling all the gate signals to the switches. Temperature protection is implemented by using a bimetal as a temperature sensor that is mounted on the heat sink. If the temperature of the sensor rises over 60°C a fan on the heat sink starts to operate. If the temperature of the sensor rises over 80°C a signal is sent to the gate drive for immediate shutdown. A PC is connected to the inverter system so that the output phase voltage, the output phase current, the output power, the frequency of the output voltage and some inverter status including faults, etc. could be monitored. All the data monitored are also recorded in the PC and updated every two minutes so that inverter status could be interpreted after the fault has occurred.

Table II. Protection

Fuel Cell	OV (over 41V), UV (under 22V), OC (over 275A)
DC-link	OV (over 500V), UV (under 300V)
Load	OC (100%~110%, 1min.), SC (over 110%)
Battery	OV (over 56.7V), UV (under 42V)
Heatsink	Over 60°C → Fan Start, Over 80°C → Shutdown

3. POWER COMPONENT DESIGN

The power components of the proposed PPU are designed with the following system parameters.

- Switching frequency for the front-end DC-DC converter : 25kHz
- Switching frequency for the DC-AC converter : 20kHz
- Switching frequency for the bi-directional DC-DC converter : 20kHz
- DC link voltage V_{dc} : 400V
- Transformer turns ratio N_{p1}: N_{s1} = 1 : 10
- Permissible ripple current ΔI_{L1} = 50% of maximum dc link current
- Permissible ripple voltage ΔV_{c1} = 10% of the dc link voltage

Power switches

The ratings of the power switching devices used in each section of the converters are listed in Table III. A safety margin for MOSFETs and diodes in the front-end DC-DC section should be considered due to voltage spikes originated from the leakage inductance and/or the ringing phenomenon at the secondary winding of the high frequency transformer. A ultra-fast recovery diode is chosen to lower the switching loss due to the high switching frequency operation. Since the maximum battery discharge current is much larger than the maximum battery charge current, the switch ratings of the bi-directional DC-DC converter should also be determined based on the discharge mode of operation at full load (5KW, 1min.).

Table III. Ratings of the Power Switching Services

Section	Component	Designed value		Actual device Selection
Front-end DC-DC converter	MOSFET (S1~S4)	V_{peak} (V)	41	IXFN180N10 (100V, 180A, 8mΩ)
		I_{rms} (A)	177.4	
	Diode (D1~D8)	V_{peak} (V)	410	DSEI2X31-10B (1000V, 30A, trr = 35ns)
		I_{rms} (A)	8.8	
DC-AC Inverter	IGBT (SW1~SW4)	V_{peak} (V)	420	2MBI200N-060 (600V, 200A, $V_{CE(sat)}$ 1.5V)
		I_{rms} (A)	50	
Bi-directional DC-DC converter	MOSFET (S1,S2)	V_{peak} (V)	140	IXFN180N20 (200V, 180A, 10mΩ)
		I_{rms} (A)	88.4	
	IGBT (S3~S6)	V_{peak} (V)	420	MG50J2YS50 (600V, 50A, $V_{CE(sat)}$ 2.1V)
		I_{rms} (A)	11.9	

High Frequency Transformer

Ferrite core is chosen as a material of a high frequency transformer. The power handling capacity of a transformer core can be determined by its area product $\boldsymbol{W_aA_c}$, where $\boldsymbol{W_a}$ is the available core window area, and $\boldsymbol{A_c}$ is the effective core cross-sectional area.
The area product $\boldsymbol{W_aA_c}$ is given by[9],

$$W_a A_c = \frac{P_{dc} \cdot C \cdot 10^8}{4 \cdot e \cdot B \cdot f_s \cdot K} = 23.47\, cm^4 \qquad (10)$$

where $\boldsymbol{P_{dc}}$ is output power, $\boldsymbol{C}$ is current capacity which is $5.07\times10^{-3} cm^2/Amp$ for '**EER**' core, $\boldsymbol{e}$ is transformer efficiency which is assumed to be 90%, $\boldsymbol{B}$ is flux density which is assumed be 2000(gauss), $\boldsymbol{f_s}$ is switching frequency and $\boldsymbol{K}$ is winding factor which is 0.3 for primary side only. Using the core selection table by area product distribution, the core of 47054-EC was selected. Once a core is chosen, the calculation of primary and secondary turns and their wire sizes are readily accomplished. The number of primary turns is given by [9],

$$N_p = \frac{V_P \cdot 10^8}{4 \cdot B \cdot A \cdot f_s} = \frac{41 \cdot 10^8}{4 \cdot 2000 \cdot 3.39 \cdot 25000} = 3.18 turns \qquad (11)$$

Here, $\boldsymbol{V_p}$ is the peak primary voltage and $\boldsymbol{A}$ is the cross-sectional area of the core. Considering duty loss of 20% at the secondary winding of the transformer originated from the leakage inductance, the final number of turns for primary and secondary windings are determined to be N_p : N_s = 6 : 90. The wire sizes AWG 0 and AWG 12 are selected from AWG table for the primary and secondary wires whose circular mil requirements are 93,500 and 5,900, respectively. Ritz wires were used to reduce the copper loss due to skin effect.

DC Link Inductor and Capacitors

From eqn.(1), the inductance can be obtained by,

$$L = \frac{(1-2D)\cdot(\frac{N_s}{N_p})\cdot V_{in}\cdot D}{\Delta I \cdot f_s} = 100\ \mu H \qquad (12)$$

At displacement factor of 0.7 the maximum output VA becomes,

$$VA_{out} = \frac{10000}{0.7} = 14280 \ VA \tag{13}$$

The full load current of each phase is given by,

$$I_{a,rms} = \frac{14280}{2 \cdot 120} = 59.5 \ A \tag{14}$$

For the sake of simplicity, the output current i_a is assumed to consist of only fundamental ($I_{a,1}$) and third harmonic ($I_{a,3}$). Further, assuming $I_{a,3} = 0.7 I_{a,1}$ since this is a typical case of a single phase rectifier type nonlinear load [4],

$$I_{a.rms} \cong \sqrt{I_{a,1}^{\ 2} + I_{a,3}^{\ 2}} = 1.22 I_{a,1} \tag{15}$$

The most dominant component of the DC-link capacitor current i_{c1} is the fundamental frequency current, the rms value of which equals,

$$I_{c1,1} \cong \frac{1}{2} \cdot I_{a,1} = 24.3 \ A \tag{16}$$

Capacitance can be obtained by,

$$C_1 = \frac{I_{c1,1}}{\omega \Delta V_{c1}} = \frac{24.3}{2\pi \cdot 60 \cdot 20} = 3222 \ \mu F \tag{17}$$

Output filter

Based on the design procedure in [4], the filter inductance and capacitance become,

$$L_f = \frac{X_L}{2\pi f_1} = \frac{0.035}{2\pi \cdot 60} = 92.84 \ \mu H \tag{18}$$

$$C_f = \frac{1}{2\pi \cdot f_1 \cdot X_c} = 16 \ \mu F \tag{19}$$

Battery Inductor

The ripple component in the charging current should be restricted by an inductor on the battery side. The magnitude of the charging current depends on the capacity of the battery. The maximum charging current is assumed to be 45A for battery of 48V, 155Ah. We allow the ripple current to be 20% of the maximum charging current, that is, $\Delta i_L = 9$A.

During the charge mode, the duty ratio D lies between $0.33 < D < 0.5$.

When the switches S3 and S6 are turned on during the charge mode we have (See Fig. 9),

$$\frac{(V_{dc} / n_2) - V_{batt}}{L} = \frac{\Delta i_L}{DT_S} \tag{20}$$

Then, the worst case inductance is obtained by,

$$\therefore L = \frac{(1-2D) \cdot D}{n_2 \cdot \Delta i_L \cdot f_s} \cdot V_{dc} = 39 \ \mu H \tag{21}$$

The current rating of the inductor is dominated by discharge mode of operation. The rms inductor current at a maximum discharge becomes $I_L = 113$ (A).

Heat sink

The heat sink is a crucial and a costly component of the PPU. The first step is to calculate the power dissipation of switching devices. Then, a thermal equivalent circuit for analyzing thermal characteristic of the heat sink is defined as shown in Fig. 11, where two different power devices are mounted on a heat sink. Given power loss P_l (where, l = 1 or 2) of a switching device, junction to case thermal resistance $R_{jc,l}$ case to heat sink thermal resistance $R_{ch,l} = 0.3$°C/W, ambient temperature $T_a = 40$°C, and juntion temperature $T_{j,l}$, heat sink to ambient thermal resistance R_{ha} can be obtained in the following procedure. The case temperature $T_{c,l}$ can be given as,

$$T_{c,l} = T_{j,l} - P_l \cdot R_{jc,l} \tag{22}$$

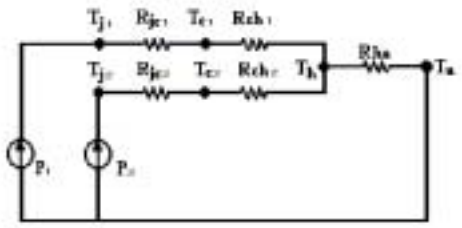

Fig. 11 Thermal equivalent circuit

Then, heat sink temperature $T_{h,l}$ can be given as,

$$T_{h,l} = T_{c,l} - P_l \cdot R_{ch,l} \tag{23}$$

Then, the total heat sink temperature T_h is,

$$T_h = T_{h,1} + T_{h,2} \tag{24}$$

Finally, heat sink to ambient thermal resistance R_{ha} is obtained by,

$$R_{ha} = \frac{T_h - T_a}{P_1 + P_2} \tag{25}$$

Table IV summarizes the thermal calculation required for the heat sink design. Using the heat sink to ambient thermal resistance, the area of the heat sink required can be calculated or the heat sink can directly be selected from a manufacture by the heat sink to ambient thermal resistance obtained.

Table IV. Thermal Characteristics for the Heat Sink Design

Section	Device	Power loss per unit (W)	R_{jc} (°C/W)	T_j (°C)	T_c (°C)	T_h (°C)	R_{ha} (°C/W)
Front-end DC-DC	MOSFET	48.9	0.21	70.26	60	45.4	0.11
	Diode	13.2	1.25	65.85	49.3		
Inverter	IGBT	120.9	0.22	112.5	85.9	49.7	0.08
Bi-directional DC-DC	MOSFET	107.7	0.18	103.3	80.9		
	IGBT	39.9	0.31	67.5	55.2		

4. EXPERIMENTS AND PERFORMANCE EVALUATION

The output voltage and current waveforms for a steady state condition at 4.4KW load level are shown in Fig. 12. The experimental waveforms were also obtained for a discharge mode of operation, that is, a load increase from 2kW to 2.7kW. In this experiment a DC power supply emulates the fuel cell. The lower trace in Fig. 13(a) shows an increase of the output phase current, and the upper trace in Fig. 13(a) shows the output phase voltage, which is well regulated during the load increase. The upper trace in Fig. 13(b) shows the output current of the front end DC-DC converter whose average value did not change after the transient even if the ripple was slightly increased due to operation of bi-directional DC-DC converter. The lower trace in Fig. 13(b) shows the dc link voltage, which undergoes an overshoot and is stabilized. Fig. 13(c) shows the PWM current waveform on the dc link side of the bi-directional DC-DC converter. Fig. 13(d) shows the current waveform on the battery side of the bi-directional DC-DC. This demonstrates that for a sudden load increase the output voltage is well regulated while the bi-directional DC-DC converter would quickly draw the power difference from battery. Fig. 14 shows variations in SOC and in real power of the PPU input, load and battery sides. Initially, the fuel cell is supplying a load of 600W, and the SOC is being kept at 1. The load power jumps to 2000W at t = 2.13 min., and the battery immediately starts to discharge with a current corresponding to the power difference. The SOC starts to decrease from this moment. As the PPU input power increases at a rate of 200W/minute, the battery power decreases at the same rate until it reaches the demanded load power plus losses. Since the SOC is supposed to be maintained at 1 in the SNUT system, the PPU input power continues increasing to charge the battery until a charging current is set up. The PPU keeps charging with the constant charging current and finishes the battery charge mode when the SOC reaches 1. Photograph of the SNUT fuel cell inverter system is shown in Fig. 15. Experimental performances of some important design items have been obtained and listed in Table V. As shown in Table V, the SNUT prototype inverter met the minimum target requirements for most of the design items such as frequency regulation, THD of the output voltage, output voltage regulation and input current ripple. The cost analysis is based on the spreadsheets evaluation forms provided in the competition. The values in the table indicate only preliminary, relative cost estimates, not dollars.

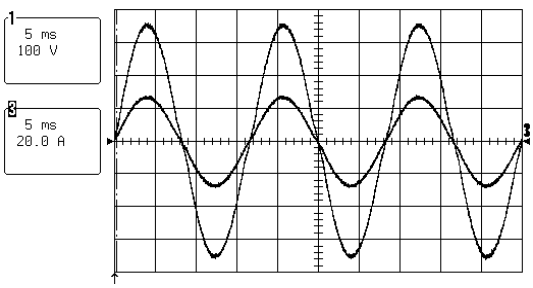

Fig. 12 Experimental waveforms (4.4kW load): output voltage and current : phase AB

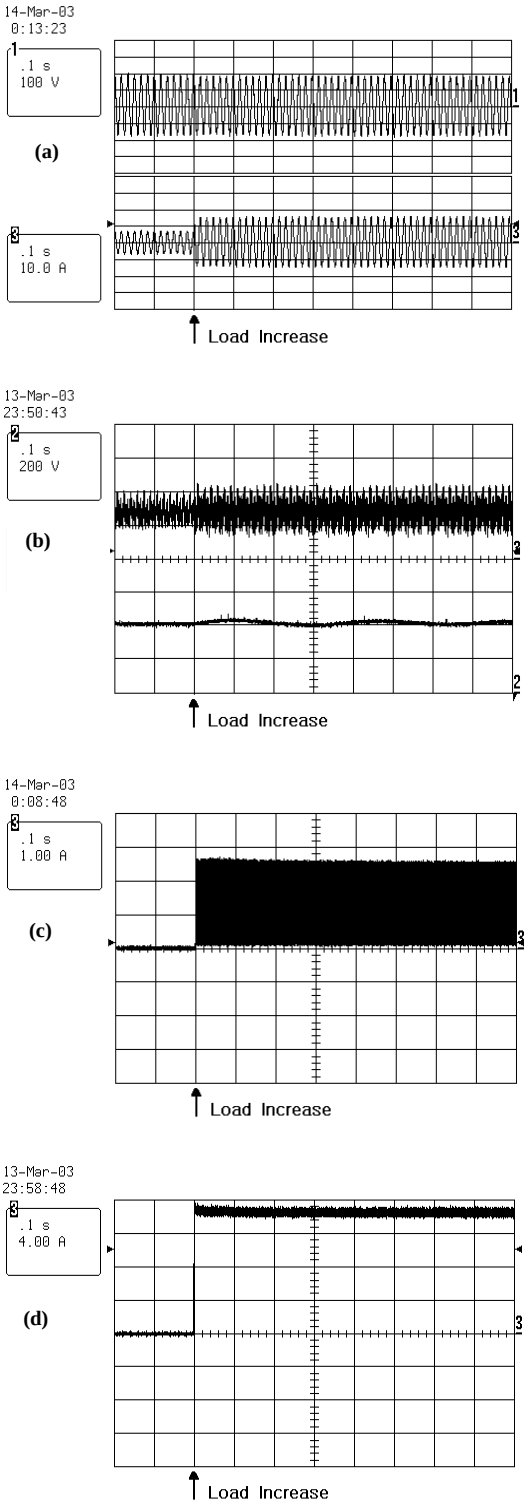

Fig. 13 Experimental waveforms (2KW→ 2.7KW), (a) output phase voltage and current (b) upper : output current of the front end converter ; lower: dc link voltage, (c) output current of the bi-directional converter, (d) battery current

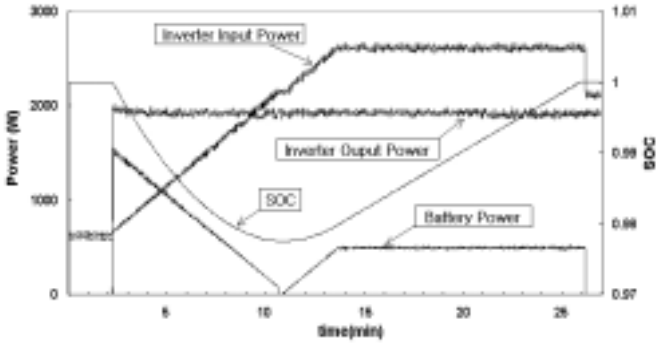

Fig. 14 SOC control for battery management

Fig. 15 Photograph of the SNUT fuel cell inverter

Table V. Experimental performance (no load to 4.4kW load)

Design Item	2003 FEC Specification performance	SNUT team Experimental performance
Frequency	60Hz ±0.1Hz	59.95Hz ~ 60.09Hz
THD (Output voltage harmonic)	5%	Lower than 1.94%
Regulation	±6%	-2.4% ~ +0.2%
Input current ripple	3%	Lower than 2.2%
Efficiency	Higher than 90%	Total 88% at 4.4kW load (DC-DC:90%, INV:97%)
Cost	$40/KW	$45.18/KW

5. CONCULSION

In this paper a 10kW power processing unit for 5KW SOFC-low voltage battery hybrid power generation has been proposed for the 2003 Future Energy Challenge Competition organized by U.S. Department of Energy and IEEE. The objective of the competition was to develop a fuel cell inverter with minimum requirement for cost of $40/KW and efficiency of 90%. Many practical issues such as component rating calculation, high frequency transformer design, heat sink design, and protection have been detailed. Battery management has been performed by a SOC control. The SNUT prototype inverter met the minimum target requirements and demonstrated a good performance in most of the design items.

REFERENCES

[1] R. Anahara, S. Yokokawa and M. Sakurai, “Present Status and Future Prospects for Fuel Cell Power Systems”, Proceedings of the IEEE, March 1993, vol 81, no. 3, pp399-407

[2] M.W. Ellis, M.R. Von Spakovsky, D.J. Nelson, “Fuel cell systems: efficient, flexible energy conversion for the 21st century”, Proceedings of the IEEE, vol. 39, no. 12, pp. 1808-1818,2001

[3] N. Azli, A. Yatim, “DSP-based Online Optimal PWM Multilevel Control for Fuel Cell Power Conditioning Systems”, IEEE IECON 2001 conf. Rec., 29 Nov-2 Dec.2001, vol. 2, pp.921-926

[4] R. Gopinath, D. Kim, J. H. Hahn, M. Webster, J. Burghardt, S. Campbell, D. Becker, P. N. Enjeti, M. Yeary, J. Howze, “Development of a Low Cost Fuel Cell Inverter System with DSP Control”, IEEE PESC 2002 Conf. Rec. , June 2002, vol. 1, pp. 309-314

[5] A. H. Anbuky and P. E. Pascoe, “VRLA Battery State-of-Charge Estimation in Telecommunication Power Systems”, IEEE Trans. on Indus. Elec., vol. 47, no3, , pp. 565-573, 2000

[6] X. Wang and T. Stuart, “Charge Measurement Circuit for Electric Vehicle Batteries”, IEEE Trans. on Aerospace and Electronic systems, vol. 38, no. 4, pp. 1201-1209, 2002

[7] K. Wang, C.Y. Lin, L. Zhu, D. Qu, F.C. Lee, J.S. Lai, “Bi-directional DC to DC Converters for Fuel Cell Systems”,in Conf. Rec. 1998 IEEE Workshop on Power Electronics In Transportation, pp.47-51

[8] The 2003 International Future Energy Challenge Web Site; http://www.energychallenge.org/

[9] Texas Instruments, http://www.ti.com/

[10] Design application note MAGNETICS. INC.

[11] A. I. Pressman, Switching Power Supply Design.McGRAW-HILL INTERNATIONAL, 1999.

Impedance Control of flexible Structures

F. Palis, S. Sokolov
Institut für Elektrische Energiesysteme
Otto-von-Guericke-Universität Magdeburg, Germany
39106 Universitätsplatz 2
Magdeburg (Germany)
frank.palis@e-technik.uni-magdeburg.de

Abstract: Depending on the problem to be solved different control strategies can be used. All strategies can be classified as feedforward or feedback control systems. Its advantages and disadvantages are discussed in the paper. Special emphasis is put on the analogy between mechanical and electrical phenomena. It will be shown that some times the representation of complex mechanical systems in form of electric equivalent schemes can give a better understanding of physical interactions and open new ways of vibration damping. As example for the convenience of electric equivalent schemes impedance control is considered. The later turns out to be very robust and appropriate for practical applications. Using internal acceleration, speed or position feedback of the actuator its own dynamics can be neglected and some times system integration is facilitated. However, rigid control of one or more state variables of the system changes the boundary conditions of the system that must be taken into consideration when modeling plant dynamics.

1 INTRODUCTION

Owing to the development of new types of actuators and progress in the field of hardware technology for real time operation more and more attention has been paid to the problem of vibration damping in mechanical structures. Depending on the problem to be solved there are two fundamentally different approaches which have been used in the past for vibration suppression. In the case, if the exciting force changes its position or the structure is excited by distributed forces a system of actuators can be used to compensate vibration at the desired point. Vibration damping of an elastic beam using piezoelectric patches placed on a beam [1] can serve as example. Another solution is to decouple the vibration source from the receiver with active mounts. To this aim the vibration transmission paths from the beam to the supports must be interrupted. This approach guarantees more efficient vibration reduction than traditional passive supports for which the loss of performance at low frequencies (below 500 Hz) is typical [2]. The best isolation rate is generally obtained when an active system is used in combination with a passive bearing [1,2]. This method enables a compromise between high-frequency isolation due to passive isolation system and good low-frequency isolation without static problems. Typical examples of isolation systems are: car suspension design [3] and isolation of equipment from a vibrating body [4,5].

In recent years a number of researchers have been investigating the use of intelligent algorithms as e.g. adaptive filters or neuronal networks to control the actuators. Very often, if on the one hand the impacting force is known or the signal related to the disturbance input can be obtained and on the other hand the error signal is available the concept of feedforward control is used [1,6]. In case, if there is a noise on the feedforward sensor, vibration suppression performance can be improved using a hybrid control system [7]. Otherwise a feedback controller has to be implemented [2]. Impedance control, as will be shown in the paper, offers good possibilities for designing robust damping systems.

The paper deals with different vibration damping strategies when using piezoelectric actuator systems. In previous works is has been shown that acceleration, speed or position controlled piezoelectric actuator systems facilitate their system integration. It has been proved that current feed piezoelectric actuators systems in sliding mode operation are characterised by linear dynamics and can be easily integrated in complex control schemes. In addition, they allow multi-actuator operation with energy recovering [8].

2 TWO PROACHES FOR VIBRATION CONTROL

2.1 Feedforward Vibration Isolation Techniques

In a feedforward control structure the actuator signal is calculated from measured reference signals or from statistic data that are obtained from the perturbation (fig. 1). Here the structure response to actuator signal must be compensate the

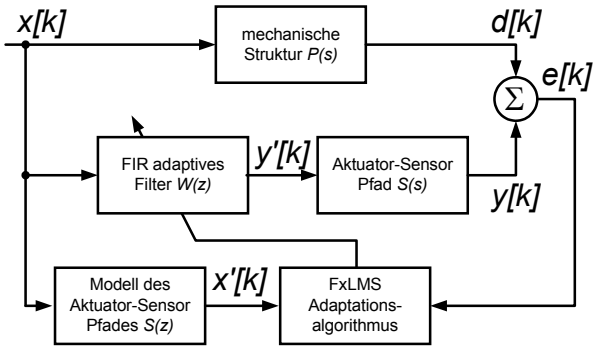

Fig.. : 1: Feedforward control structure

vibration due to the outer excitation force. The control sig

nal is generated by an adaptive filter to cope with changing structure parameters. Since the resulting system represents an open loop system and the investigated mechanical structure is stable the stability of the feedforward controller determines the stability of the whole system. It is known, that all poles of a FIR filter are situated in the origin of the z-plane. Moreover a FIR controller can not cause instability in an open loop system while the adaptation algorithm is stable. The filter coefficients are calculated using the gradient method [9].

$$\underline{\omega}[k+1] = \underline{\omega}[k] - \mu \underline{x}'[k] e[k] \qquad (1)$$

Here $\underline{x}'[k]$ is the vector of the last N values of the reference signal filtered with the transfer function of the sensor-actuator-path:

$$\underline{x}'[k] = s[k] \underline{x}[k] \qquad (2)$$

The algorithm (1) is known as FxLMS–algorithm minimising the medium square error $E\{e^2[k]\}$. The phase of the transfer function from the actuator to the sensor must be identified with an accuracy of $\pm 90^\circ$ to guaranty convergence of the algorithm [9]. On the other hand time of convergence, stability and the choice of parameters depend on the step width μ whose maximum value is limited by the number of coefficients and the performance of the filtered reference signal [9].

$$\mu_{max} = \frac{2}{N P_{x'}} \qquad (3)$$

Since the optimal filter coefficients depend on the signal the steady state perturbation signal x[k] must be available for adaptation. That is why transition processes increase the time of convergence of the algorithm [10].
To compensate several tonal perturbation the reference signal can be generated using the frequencies of the perturbations [9 ,11]. The identification of the frequency is realised by an adaptive notch filter (ANF) shown in figure 2. For the adaptation of the ANF the RLS-algorithm (Rekursive Least

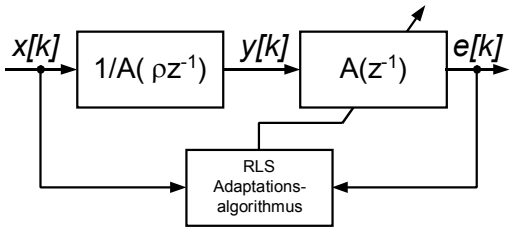

Fig.:. 2: Adaptives Notch Filter

Square) is used that guaranties a faster convergence in comparison with the LMS but demands, however, more operations per summation step. In accordance with [11] ANF possesses a symmetrical numerator and, consequently, the properties of an ideal notch filter with stable poles in the z-plane. The denominator coefficients results from the numerator coefficients by multiplication with a fixed factor ρ

$$N(z^{-1}) = \frac{1 + a_1 z^{-1} + \ldots + a_p z^{-p} + \ldots + a_1 z^{-(2p-1)} + z^{-2p}}{1 + \rho a_1 z^{-1} + \ldots + \rho^p a_p z^{-p} + \ldots + \rho^{(2p-1)} a_1 z^{-(2p-1)} + \rho^{2p} z^{-2p}} \qquad (4)$$

to the corresponding power. So the poles of the tranfer function (4) are placed independently of the zeros [11].

$$P_i = \rho^{-1} Z_i \qquad (5)$$

The observed frequencies of the signal x can be calculated from the zeros

$$\hat{f}_i = \frac{1}{2\pi} angle(Z_i \mid A(z^{-1}) = 0) \qquad (6)$$

When using a separate feedforward controller for each of the identified frequency convergence of LMS algorithm can be improved [9].

2.2 Robust feedback control

Let us start from the supposition that sensor and actuator cannot always be placed in the same point of the structure (collocated). Moreover, a mechanical structure with distributed parameters often possesses positive zeros [11, 12]. Zeros in right part of the complex plane, however, cause a large phase shift between the control signal and the measure signal and affect the stability margin. In many cases, using parameter adaptation accurate models can be obtained only within a limited range of frequencies (in our case from 50 to 900 Hz). The H_∞-theory permits a direct specification of the model error using the frequency response.
The transfer function from the disturbance input d to the

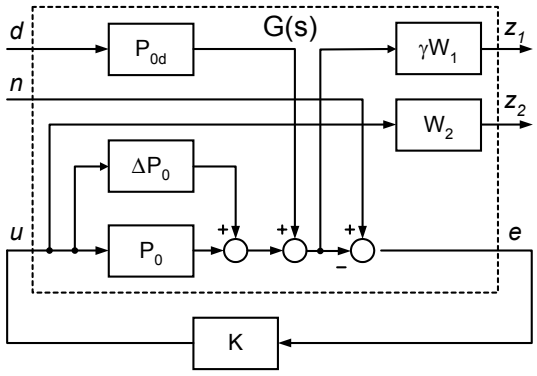

Fig. 3: Interpretation of the H∞ -Theorie

first structure output z_1 (see figure 3) without consideration of the uncertainty $\Delta P(s)$ corresponds to the weighed function of sensitivity $S(s)$:

To solve the problem in the context of H_∞-control we must apply a sensor noise to the structure (equ. 8).

$$P_{z_1 d} = \frac{z_1(s)}{d(s)} = \gamma W_1(s)(1 + P_0(s)K(s))^{-1} P_{0d}(s) = \gamma W_1(s) S(s) \qquad (7)$$

To solve the problem in the context of H_∞-control we must apply a noise to the structure (equ. 8).

$$P_{z_2 n} = \frac{z_2(s)}{n(s)} = W_2(s)K(s)(1 + P_0(s)K(s))^{-1} = W_2(s)T(s) \quad (8)$$

Taking into account the model uncertainty at high frequencies as additive uncertainty $\Delta P(s)$ the closed loop system is stable if yields [12]:

$$\left\| \Delta P(s)T(s) \right\|_\infty < 1 \quad (9)$$

Choosing an optimal $H\infty$-controller the ∞-norm of the closed loop system is minimised:

$$\left\| \begin{matrix} \gamma W_1(s)S(s) & * \\ * & W_2(s)T(s) \end{matrix} \right\|_\infty < 1 \quad (10)$$

From (9 and 10) can be obtained the stability condition of the closed loop system for the transfer function $\Delta P(s)$ [12]:

$$\bar{\sigma}\left[\Delta P(j\omega)\right] \le \bar{\sigma}\left[W_2(j\omega)\right] \quad (11)$$

Here $\bar{\sigma}[\ ]$ characterises the maximum singular value of the corresponding transfer function.

Experimental investigations were carried out at a beam fixed on both sides as shown in fig. 4. The applied weight functions and the frequency responses of the controlled and uncontrolled system are depicted in fig. 5.

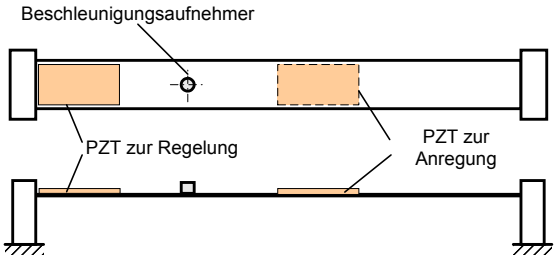

Fig.: 4: Draft of the experimental equipment

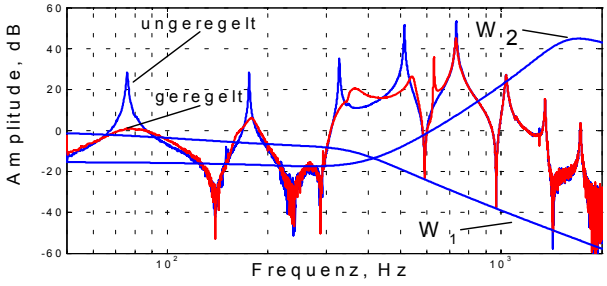

Fig. 5: Experimental results

3 IMPEDANCE CONTROL OF FLEXIBLE STRUCTURE SYSTEMS

3.1 Modal representation and electric equivalent scheme of flexible structure systems

As known, the dynamics of flexible structures can be represented using modal transformation. To illustrate the proposed approach let's consider flexural vibrations of a beam

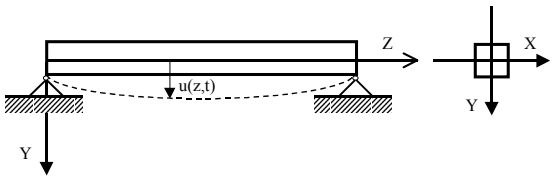

Fig. 6: *Flexural vibration of a beam*

(see fig.6). Using modal transformation and considering only one exciting force vibration of n modes can be described by the following system of differential equations.

$$\begin{aligned} & m_1 q_1 + d_1 q_1 + k_1 q_1 = V_1 F \\ & m_2 q_2 + d_2 q_2 + k_2 q_2 = V_2 F \\ & \quad \ldots\ldots\ldots\ldots \\ & m_n q_n + d_n q_n + k_n q_n = V_n F \\ & y = V_1 q_1 + V_2 q_2 + \ldots . V_n q_n \end{aligned} \quad (12)$$

with

m_i - equivalent masses

d_i - equivalent damping factor

k_i - equivalent spring constant

V_i - eigenvectors

q_i - modal coordinates

or in matrix notation

$$\mathbf{A} * \mathbf{q} = \mathbf{V} * F \quad (13)$$

with

$\mathbf{A}$ - modal vector

Drawing the well known analogy between mechanical and electrical systems [9] equations (12) can be rewritten in the form

$$\begin{aligned} & L_1 \frac{di_1}{dt} + R_1 i_1 + \frac{1}{C_1} \int i_1 dt = u_1 \\ & L_2 \frac{di_2}{dt} + R_2 i_2 + \frac{1}{C_2} \int i_2 dt = u_2 \\ & \quad \ldots\ldots\ldots\ldots\ldots\ldots \\ & L_n \frac{di_n}{dt} + R_n i_n + \frac{1}{C_n} \int i_n dt = u_n \end{aligned} \quad (14)$$

$$i = \sum_{i=1}^{n} i_i$$

The system of equations (14) can be represented by the equivalent electric scheme in fig. 7. Here currents stand for velocities, voltages for forces, inductances for masses, resistances for damping factors and capacitances for spring constants. Dividing equation (12) by the corresponding eigenvector $\mathbf{V}$ the feeding voltage U_i in equation (14) will be the same and the equivalent scheme can be simplified as shown in figure 8. The presented approach can be

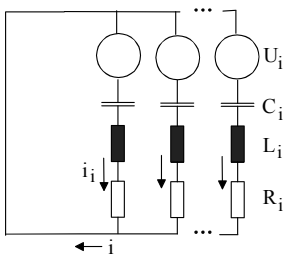

Fig. 7.: Electric equivalent scheme

generalised for k exciting or actuator forces using the superposition law. Consequently, the same equivalent scheme with the corresponding eigenvectors can be used independently k times and the resulting currents have to be summed up. As will be shown later, reasoning in terms of electric schemes may be useful for physical interpretation and for control structure design.

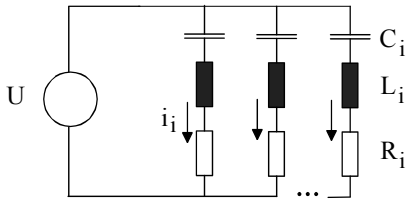

Fig. 8: Transformed electric equivalent scheme

3.2 *Impedance control of a flexible beam*

Damping of an elastic structure can be reached by using impedance control. To this aim the displacement is measured and applied via an impedance function to the actuator.

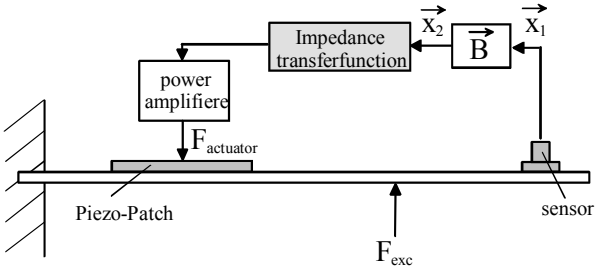

Fig. 9:: Principle of impedance control

The notion of impedance is common in electrical and mechanical engineering [9]. In electrical engineering impedance is defined as a complex resistance $\underline{Z} = \underline{U}/\underline{I}$ whereas in mechanical engineering it represents the quotient of the force vector and the velocity vector $\underline{Z} = \underline{F}/\underline{v}$. The general scheme is given in fig. 9. To make the working principle clearer let us represent the control scheme as electrical equivalent scheme. In accordance with equation (13) vibration in the point of measurement can be written as

$$\mathbf{q} = \mathbf{A}^{-1}\left[F_{ex} * \mathbf{V}_{ex} + \mathbf{F}_{\mathbf{ac}} * \mathbf{V}_{\mathbf{ac}}\right] \qquad (15)$$

or graphically represented as shown in fig. 10 Taking into account that currents stand for velocities and voltages stand

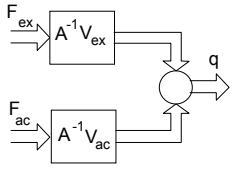

Fig.11: Matrix representation of the damping system

for mechanical forces the mechanical system can be represented as electrical system described by the equation

$$\begin{aligned}\mathbf{i} &= \mathbf{i_{ex}} + \mathbf{i_{ac}} \\ &= \mathbf{Z^{-1}}\left(U_{ex} + \mathbf{V_{ex}}^{-1}\mathbf{V_{ac}}U_{ac}\right)\end{aligned} \qquad (16)$$

or

$$\mathbf{i}^* = \mathbf{Z}^{-1}U_{ex} + \mathbf{Z}^{-1}U_{ac} \qquad (17)$$

with

$\mathbf{i}^* = \mathbf{i_{ex}} + \left(\mathbf{V_{ex}}^{-1}\mathbf{V_{ac}}\right)\mathbf{i_{ac}}$, reduced current vector

$\mathbf{Z}$ - impedance vector.

It is obvious that decomposing the current into the excitation and actuator components and utilising the reduced current vector $\mathbf{i}^*$ the mechanical system represented in fig 9 can be described by the equivalent scheme given in fig. (11). The advantage of this representation consists in utilising the same scheme both for the excitation and the actuator circuit.

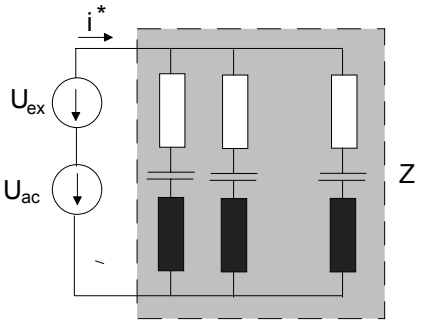

Fig. 11: Electrical equivalent scheme

The aim of impedance control consists in designing a filter for the flexible structure by introducing a virtual impedance in the mechanical structure. As known, electric filters can be designed in T- or Π -structure. Figure 12 shows the scheme with T-filter. A virtual impedance can be realised by introducing a velocity depending force into the mechanical structure or, in electrical terms, by introducing a current depending voltage as depicted in figure (13). It can be shown that the system with T-filter (fig. 12) and the system with virtual impedance (fig. 13) are electrically identical when choosing

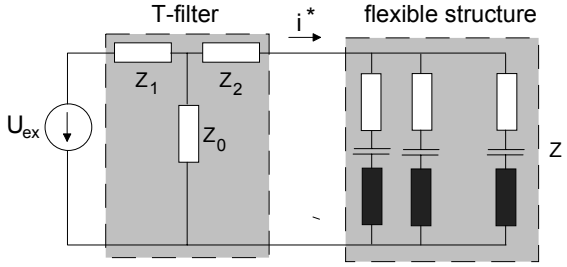

Fig. 12: Impedance control using T-filter

$$U_{ac} = I^* \frac{Z_1Z_2 + Z_2Z_0 + Z_1Z_0 + Z_1Z + Z_0Z}{Z_0} \qquad (18)$$

Let us introduce a low pass supposing

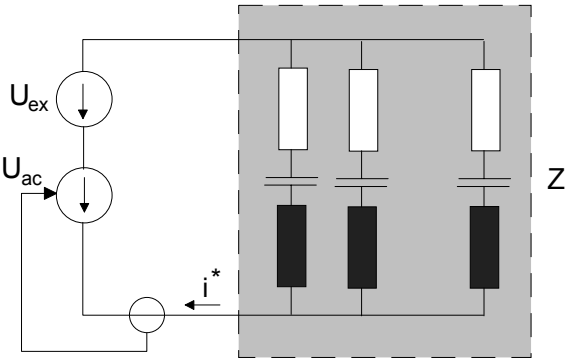

Fig. 13: Vibration damping with virtual T-filter

$$Z_1 = R_1$$

$$Z_0 = \frac{1}{j\omega C_0}$$

$$Z_2 = 0$$

Consequently, equation (18) can be simplified

$$U_{ac} = I^*\left[Z_1 + Z\left(1 + \frac{Z_1}{Z_0}\right)\right] = I^*\left[R_1 + Z\left(1 + j\omega C_0 R_1\right)\right] \quad (19)$$

From equ. (18 and 19) can be seen when designing a virtual filter with transversal impedance Z_0 we need the system impedance Z to calculate the control signal (actuator force, voltage U_{ac} in the equivalent scheme). This disadvantage can be avoided by using the disturbance observer principle. To this aim the vibration exciting force F_{ac} is reconstructed using the adaptive filter described in chapter 2.1. This force is directly related to the voltage $\left(I^* Z\right)$ and can be introduced in equ. (19). To investigate this scheme and different filter design methods will the focus of future works.

Figure 15 shows results when utilising different longitudinal impedances are used.

4. CONCLUSION

Several approaches for vibration isolation and vibration damping were investigated. It was shown that drawing the well known analogies between mechanical and electrical phenomena dynamics of flexible structures can be represented in form of equivalent electric schemes. Reasoning in terms of electric schemes may be useful for physical interpretation and for control structure design. As example for the convenience of electric equivalent schemes impedance control is considered. The later turns out to be very robust and appropriate for practical applications. In contrast, usual feedforward and feedback systems suffer from parameter sensitivity.

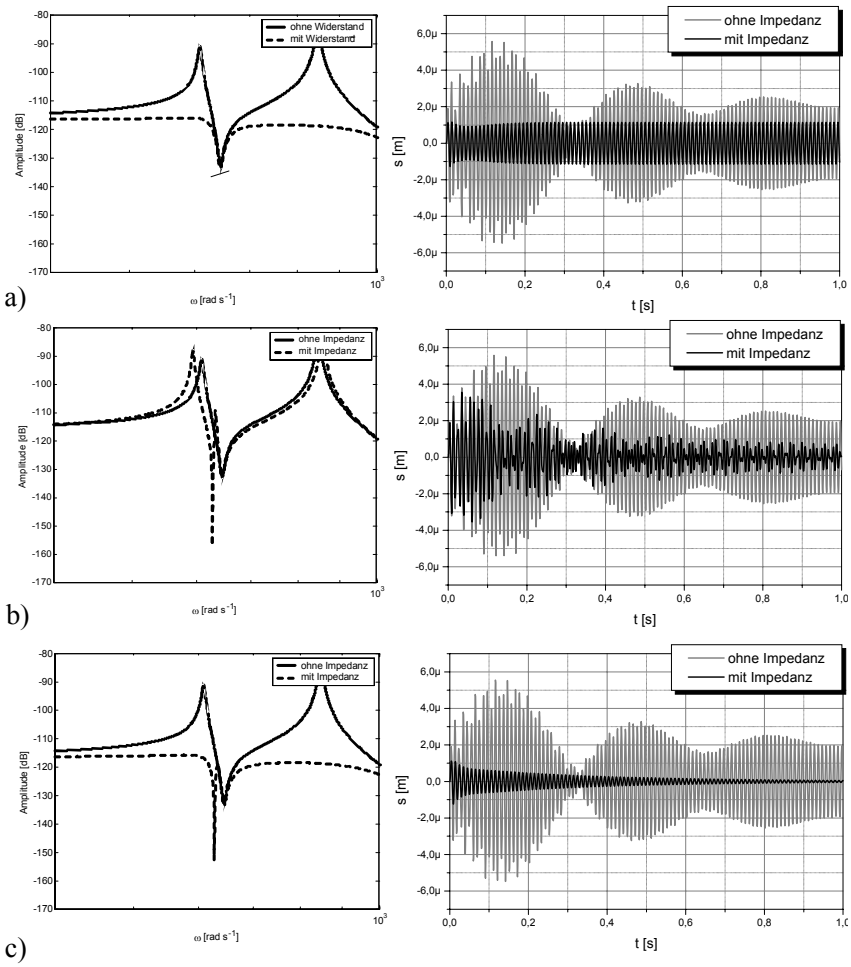

Fig. 14: *Impedance control with different longitudinal filters*
- *a) with resistance*
- *b) with parallel oscillating circuit*
- *c) with parallel oscillating circuit and resistance*

REFERENCES

[1] Colin H. Hansen, Scott D. Snyder, *Active control of noise and vibration*, E&FN SPON, Cambridge University Press, Great Britain (1997)

[2] M. Serrand, S. J. Elliott, *Multichannel feedback control for the isolation of base-excited vibration*, Journal of Sound and Vibration, Vol. 234, No. 4, Academic Press (2000), pp. 681-704

[3] T. Yoshimura, A. Kume, M. Kurimoto, J. Hino, *Construction of an active suspension system of a quater car model using the concept of sliding mode control*, Journal of Sound and Vibration, Vol. 239, No. 2, Academic Press (2001), pp. 187-199

[4] M. D. Jenkins, P. A. Nelson, R. J. Pinnington, S. J. Elliott, *Active isolation of periodic machinery vibrations*, Journal of Sound and Vibration, Vol. 166, No. 1, Academic Press (1993), pp. 117-140

[5] Jiaqiang Pan, Colin H. Hansen, Jie Pan, *Active isolation of vibration source from a thin beam using a single active mount*, The jour

nal of the Acoustical Society of America, Vol. 94, No. 3, pt. 1, Acoustical Society of America (1993), pp. 1425-1434

[6] S. M. Yang, G. S. Lee, *Vibration control of smart structures by using neuronal networks*, Journal od Dinamic Systems, Measurement, and Control, Vol. 119, Transactions of the ASME (1997), pp. 34-39

[7] T. E. Pare, J. P. How, *Hybrid H_2 control design for vibration isolation, Journal of Sound and Vibration*, Vol. 226, No. 1, Academic Press (1999), pp. 25-39

[8] Palis, F., Sokolov, S., Heller, D.: *Converter Design and Control of Piezo-Electric Multiactuator Systems in Sliding Mode Operation*, 8th International Conference on New Actuators, 10-12 Juni, 2002, Bremen, pp. 502-505

[9] Kuo, S. M., Morgan, D. R.: *Active Noise Control Systems. Algorithms and DSP Implementations*, John Whiley&Sons, New York, 1996

[10] Saunders, W. R., Robertshaw, H. H., Burdisso, R. A.: *Hybrid Structural Control Approach for Narrow-Band and Impulse Disturbance Rejection*, Noise Control Engineering Journal, Vol. 44, No. 1, 1996, pp. 11-21

[11] Kim, S., Park, Y.: *Active Control of Multi-Tonal Noise with Reference Generator Based on On-Line Frequency Estimation*, Journal of Sound and Vibration, Vol. 227, No. 3, 1999, pp. 647-666

[12] Xie, S. L., Zhang, X. N., Zhang, J. H.: *$H\infty$ Robust Vibration Control of a Thin Plate Covered with a Controllable Constrained Damping Layer*, Journal of Vibration and Control, Vol. 10, No. 1, 2004, pp. 115-133

Performance Analysis of Unified Power Flow Controller Based on H-Bridge Modules

Byung M. Han, Seung T. Baek, Young I. Son
Department of Electrical Engineering, Myongji University,
South Korea
Email: erichan@mju.ac.kr

Abstract— **This paper proposes a new configuration of UPFC based on H-bridge modules, which are isolated through single-phase multi-winding transformers. The dynamic performance of proposed system was analyzed by computer simulations, assuming that the UPFC is connected with the 138-kV transmission line of one-machine-infinite-bus power system. The proposed system can be directly connected to the transmission line without series injection transformers. It has flexibility in expanding the operation voltage by increasing the number of H-bridge modules.**

I. INTRODUCTION

UPFC was proposed as the most promising FACTS device to improve the dynamic performance of power transmission system. The presently developed UPFC operates in a dc link voltage much lower than the operation voltage of power transmission system [1]. The reason for low dc link voltage is limitation on the maximum sustain voltage of high-power semiconductor switches, which is about 6000V for the commercially available GTO.

A technique called series connection of GTOs was developed to increase the dc link voltage of UPFC. However, still there is limitation in the maximum allowable number of units. Step-down transformers are normally used for properly matching the inverter operation voltage with the transmission voltage [2]. Multi-level inverter was proposed to increase the system operation voltage avoiding series connection of switching units [3]. But the multi-level inverter has many back-connection diodes to share the dc link voltage, which are connected in series for increasing the sustain voltage.

In order to improve this weak point, multi-bridge inverter with five H-bridge modules connected in series for one phase was proposed by Peng for STATCOM application [4]. The system operation was verified through experimental works with a scaled model [5]. A commercial STATCOM of 75 MVar with H-bridge modules was developed and installed in National Grid Company in UK [6,7].

A multi-bridge inverter with several H-bridge connected in series was proposed in reference [8,9] for SSSC application. This system can operate without series injection transformers and has flexibility in expanding the operation voltage by means of adding the number of modules.

This paper proposes a new configuration of UPFC based on H-bridge modules, which are isolated through single-phase multi-winding transformers. The operation of proposed UPFC was verified through computer simulations. The feasibility of hardware implementation was confirmed through experiment with a scaled prototype. The proposed system can be directly connected to the transmission line without series injection transformers.

II. PROPOSED UPFC

Fig. 1 shows the configuration of UPFC proposed in this paper, which is based on several pairs of H-bridge modules connected in series for each phase. Each pair has two H-bridge modules connected in parallel through a common dc link capacitor. The H-bridge module in shunt part is connected through single-phase multi-winding transformer for isolation, while the H-bridge module in series part is directly inserted in the transmission line. The whole converter, its shunt part as well as its series part, must be insulated to the full insulation level of line-to-line voltage.

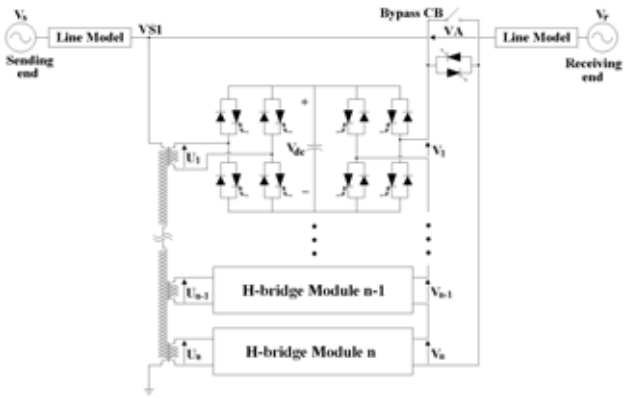

Fig. 1 Configuration of novel UPFC

The proposed UPFC has bypass functions to remove the series inverter from service during system faults. The bypass function is implemented by the operation of thyristor switch and mechanical circuit breaker. The line over-current can be bypassed first by the thyristor switch and then by the mechanical circuit breaker. However, when the maximum fault current is lower than the maximum current rating of series inverter switches, it is possible to attempt a bypass scheme using the inverter control, instead of adding separate thyristor switch. The proposed series inverter has two possible bypassing ways by making a short circuit at the ac terminal. One is to turn on all the upper two switches in series

part simultaneously and another is to turn on all the lower two switches in the series part simultaneously.

TABLE I
SWITCHING PATTERN OF MULTI-BRIDGE INVERTER

V1 A	Switching State	Mode
V_{dc}	S1, S4 : on and S2, S3 : off	M1
0	S1, S3 : on and S2, S4 : off S2, S4 : on and S1, S3 : off	M2 M3
$-V_{dc}$	S2, S3 : on and S1, S4 : off	M4

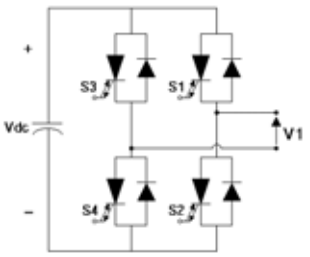

(a) H-bridge structure

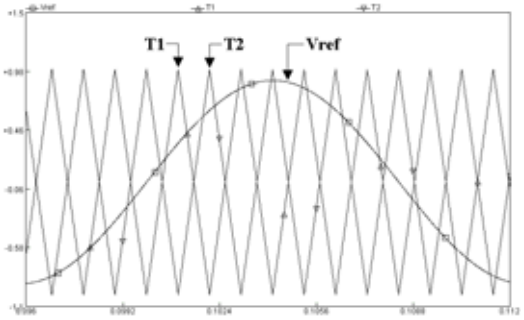

(b) Carrier and reference signal

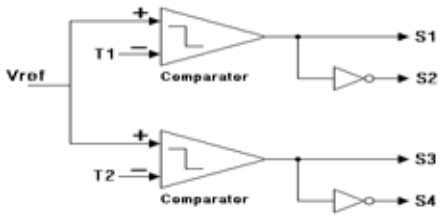

(c) Gate pulse generation scheme

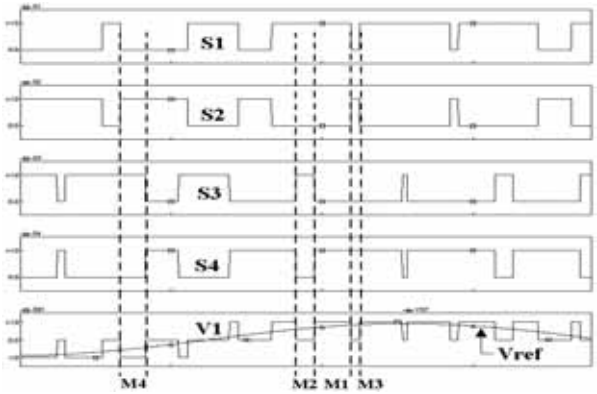

(d) Gate pulse and inverter output

Fig. 2 H-bridge gate pulse generation

Fig. 2 shows the principle of PWM gate-pulse generation for the H-bridge module. Fig. 2(a) shows the basic structure of H-bridge module, whose switching states can be explained using Table 1. The output of each module has three states $+V_{dc}$, 0, $-V_{dc}$ depending on states of switch S1～S4. By changing the modulation index, the output voltage can be adjusted.

Fig. 2(b) shows two carrier signals and the reference signal to generate the gate pulses for inverter module INV1. The frequency of carrier T1, T2 is 360 Hz. Each of two carriers has 180° phase shift with each other. The reference signal V_{ref} has maximum value of 0.9 in per unit and has a sinusoidal waveform of 60Hz. Fig. 2(c) shows how to generate the gate pulses using the reference and carrier signals. Carrier T1 and T2 are compared with the reference signal. The gate pulses for switches S1 and S3 are inversed to make gate pulses for switches S2 and S4. Fig. 2(d) shows four gate pulses supplied to switch S1, S2, S3, and S4, and the output voltage of inverter module INV1 with the reference signal V_{ref}. This figure indicates that each switch S1～S4 is properly operated according to the switching state in Table I.

Fig. 3 shows the output voltage build-up of one phase and the harmonic analysis results of the output voltage. Fig. 3(a) shows the output voltage waveforms of each inverter modules, V1, V2, V3, and the total output voltage of three inverter modules, where the dc voltage V_{dc} is 1.0 per unit. As explained before, two carriers shown in Fig. 2(b) are used to generate gate pulses for building up the output voltage V1. Two sets of each two carriers, which are 180°phase shift each other, are needed to generate gate pulses for building up output voltage V2 and V3. These sets of carriers have 120° phase-shift with each other. Since each carrier has a frequency of 360 Hz and total output voltage VA has an equivalent switching effect of N*360Hz, where N is the number of modules. Fig. 3(b) shows the spectrum analysis result for the output voltage of one module and the output voltage of cascaded three modules. Large number of harmonics are involved in the output of one module, while significantly small number of harmonics are involved in the output of cascaded three modules. Fig. 3(c) shows THD analysis results for the inverter output voltage with respect to the number of modules. The THD of output voltage is significantly decreases as the number of modules increases. In the same number of modules it is relatively high when the modulation index is less than 0.4. So, the desirable operation range of modulation index is located between 0.5 and 1.0.

The proposed UPFC has three dc link capacitors for each phase. Each capacitor in the same phase might have a voltage deviation from the average voltage because each capacitor is isolated from others. This voltage unbalance is due to the unequal leakage current of the dc capacitor, the dead time of inverter, unsymmetrical operation caused by the transient or the disturbance. By making the dc capacitor voltage balanced, it is possible to reduce the harmonics level of the inverter

output voltage.

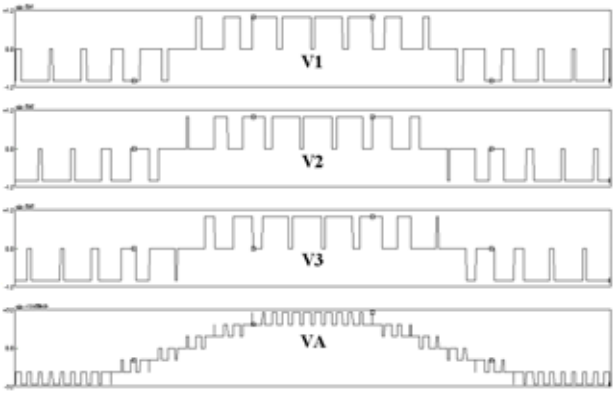

(a) Inverter output voltage

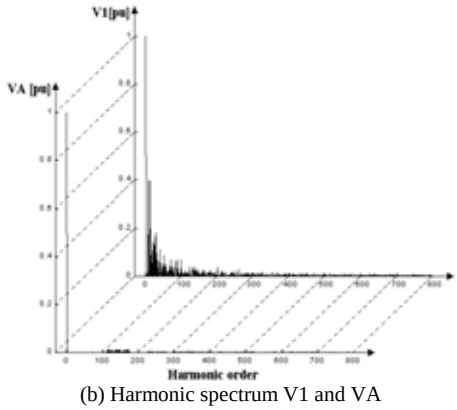

(b) Harmonic spectrum V1 and VA

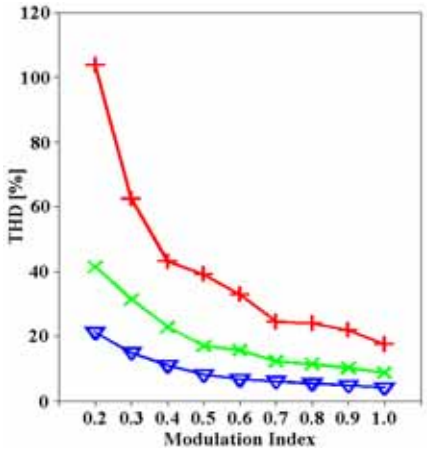

(c) THD of output voltage (+:N=3, ×:N=6, ▽:N=12)

Fig. 3 Output voltage build-up and harmonic analysis

Fig. 4 shows the configuration of DC voltage unbalance controller for the dc capacitor. There are three controllers in the proposed UPFC because separate control was considered for each phase. The controller measures the voltage at the common connection point of shunt inverter. This value is used to calculate the phase-lock angle θ by passing through the phase-lock loop. This value is adjusted by means of adding 2π/3 and 4π/3 for other two phases.

The total dc link voltage is obtained by means of measuring each capacitor voltage with an isolated sensor and adding together. This voltage is used to obtain the average voltage of each capacitor by means of dividing by three. The average voltage is compared with the measured voltage of each capacitor and the error is passed through the PI controller and the limiter to obtain the phase-angle deviation Δα. The phase-angle deviation Δα is added to the phase-angle α and the phase-lock angle θ. The total phase-angles are sent to the sine wave generator to obtain the reference signals Ref1, Ref2, Ref3, which have the phase deviation.

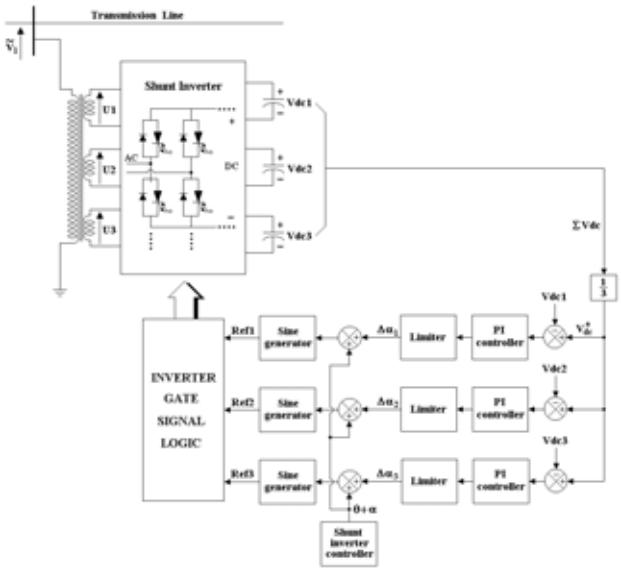

Fig. 4 DC voltage unbalance controller

III. COMPUTER SIMULATION

In order to analyze the operation of proposed UPFC, computer simulations with PSCAD/EMTDC(Power System Computer Aided Design / Electro-Magnetic Transient for DC Transmission System) were performed. The power system is represented by one-machine-infinite-bus pattern. The transmission line is modeled considering lumped line reactance and resistance. The circuit parameters used in the simulation are shown in Table 2.

TABLE II
SIMULATION PARAMETER

Base voltage	112.676 kV
Base current	946 A
Rate voltage	138 kV
Power angle	20°
Line model 1	1.0053 Ω
	19.73 mH
Line model 2	3.0159 Ω
	59.19 mH
DC capacitor	1000 μF
Tr. leakage reactance	0.12 p.u.

Fig. 5 shows a configuration of the UPFC controller used

in the simulation. Fig. 5(a) shows the controller structure of series inverter in automatic power flow control mode, while Fig. 5(b) shows the controller structure of shunt inverter in bus voltage regulation mode. The automatic power flow control is achieved by means of a vector control scheme that regulates the transmission line current using a synchronous frame, in which the control quantities appear as dc signals in the steady state. The appropriate reactive and real current components, i_q^* and i_p^*, are determined for a desired P_{Ref} and Q_{Ref}. These are compared with the measured line currents, i_q and i_p, and used to drive the magnitude and angle of the series inverter voltage, V_{pq} and α_{pq}, respectively. In the control scheme for the shunt inverter, the magnitude of the output voltage is directly proportional to the dc voltage and only its angle is controllable. The outer voltage loop regulates the ac bus voltage and also controls the dc capacitor voltage. It changes the phase angle α of the output voltage with respect to the ac bus voltage until the dc capacitor voltage reached the value necessary to achieve the reactive power compensation demanded.

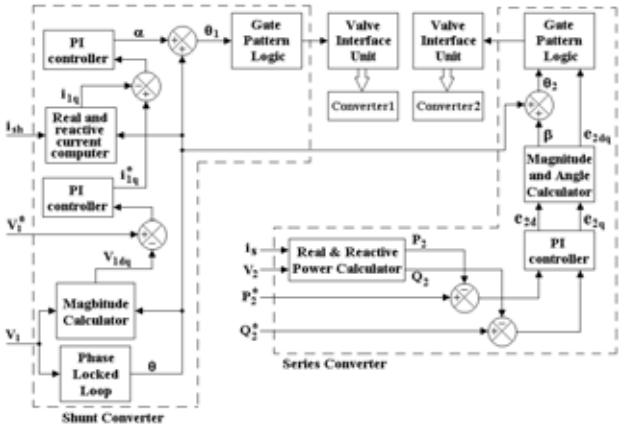

(a) Series inverter control

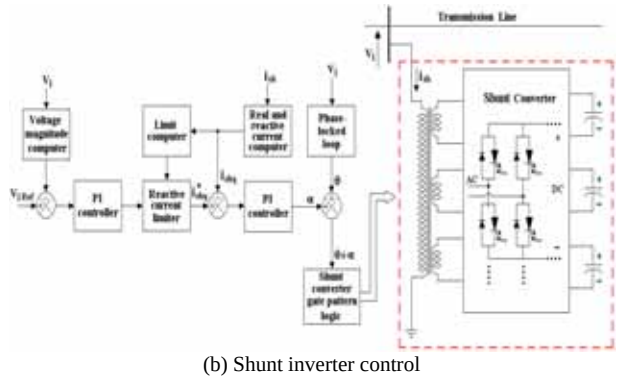

(b) Shunt inverter control

Fig. 5 Controller structure of proposed UPFC

The scenario considered in this simulation is shown in Table III. It is assumed that the maximum simulation time is 5.5 second. The reference value of P, which is initially 250 MW, suddenly changes at 1.5, 2.5, 3.5, and 4.5 second as shown in the Table 3. The reference value of Q, which is initially 0 MVar, suddenly changes at 2.5 second as shown in Table III.

TABLE III
SIMULATION SCENARIO

Time(sec)	0-1.5	1.5-2.5	2.5-3.5	3.5-4.5	4.5-5.5
V_{ref}(p.u.)	1.0	1.0	1.0	1.0	1.0
P_{ref}(MW)	250	350	450	450	450
Q_{ref}(MVar)	0	0	50	100	150

Fig. 6 shows the simulation results for the performance analysis of the proposed UPFC. Fig. 6(a) and 6(b) shows the tracking capability of the proposed UPFC with respect to the step-changes of P and Q reference values. The series inverter injects a proper voltage into the transmission line to make the P and Q through the transmission line follow the reference values of P_{ref} and Q_{ref}. Fig. 6(c) shows that the shunt inverter maintains the bus voltage constant by means of STATCOM operation. Fig. 6(d) shows the variation of each dc link capacitor in phase A. Although there is dispersion due to the PWM switching, it is known that the voltage of each capacitor is balanced evenly. Fig. 6(e) shows the output voltage waveform of the shunt inverter. Since the shunt inverter has coupling transformers, its output voltage waveform has lower level of harmonics. Fig. 6(f) shows the variation of dc capacitor voltage Vdc1, Vdc2, Vdc3, and the average dc link voltage V_{dc}^*, when the unbalanced controller works. It is assumed that each capacitor voltage, which is balanced initially, falls suddenly into the unbalanced state at 1.4 second. The voltage unbalance controller is activated at 1.8 second. This result confirms that the controller shown in Fig. 5 operates perfectly to make the dc link voltage balanced. Fig 6(g) shows the phase-angle deviation of the reference signal when the unbalance controller detects the DC capacitor voltage unbalance. Since the capacitor voltage Vdc2 has more deviation from others, the reference signal ref2 has more phase-angle deviation.

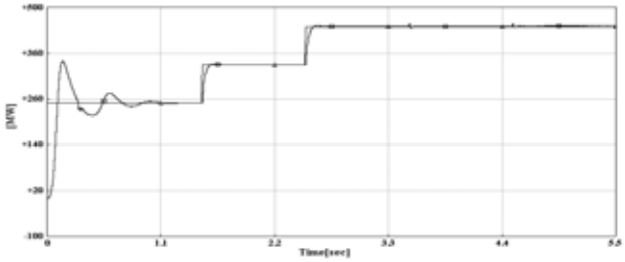

(a) Desired real power(P_{ref}) and line real power(P)

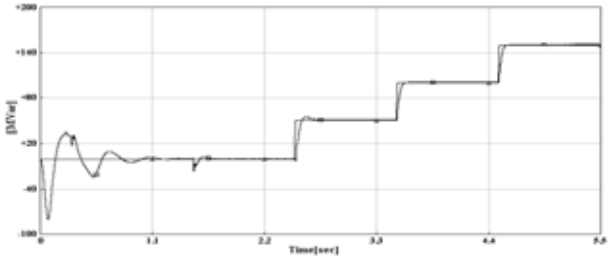

(b) Desired reactive power(Q_{ref}) and line reactive power(Q)

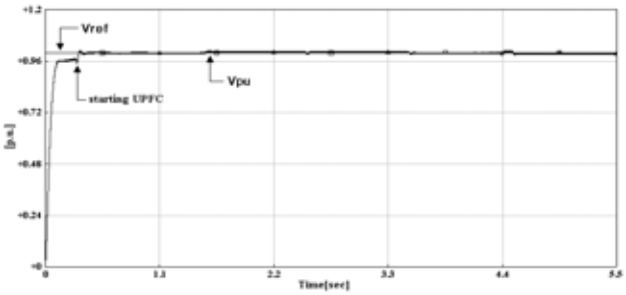

(c) Reference bus voltage (V_{ref}) and actual bus voltage(V_{pu})

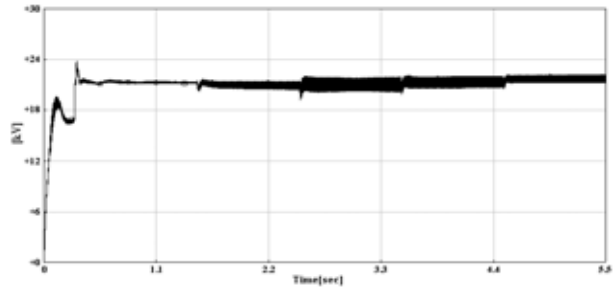

(d) DC capacitor voltages in phase A

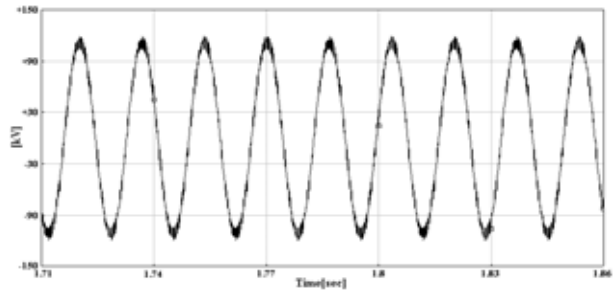

(e) Output voltage of shunt inverter

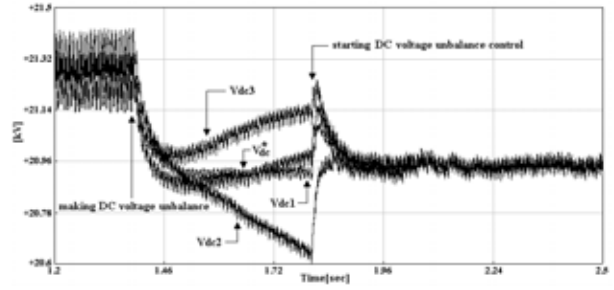

(f) DC link capacitor voltage

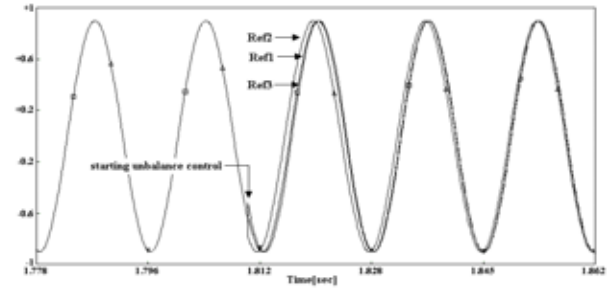

(g) Reference signal for unbalance control

Fig. 6. Simulation results for normal operation

IV. EXPERIMENTAL RESULTS

A scaled hardware model of proposed UPFC was built based on the analysis results through computer simulation. Fig. 7 shows the power circuit diagram of the experimental set-up including the proposed UPFC and the transmission system. It is assumed that the shunt and series converters consist of three sets of H-bridge modules for each phase respectively. The switching frequency is assumed to be 480Hz. The multi-winding transformer has three secondary windings to make the three H-bridge modules isolated.

The model transmission system was built as described in the reference paper [10], in which V_S and V_R represent the bus voltage at sending end and receiving end respectively and the L_1 and L_2 represent the line inductance of the transmission line. The sending-end voltage was implemented using three phase-shifting transformers and one variac. The phase-shifting transformer works to inject a 90^o phase-shifted voltage to the source voltage. The shifting angle is determined to adjust the magnitude of injected voltage. It is assumed that the shifted phase angle is 20^o.

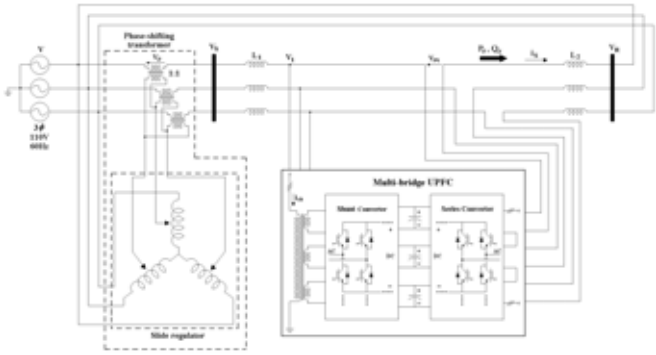

Fig. 7 Experimental set-up for multi-bridge UPFC

The circuit parameters used in the experimental work are shown in Table 4. The shunt converter controller operates to regulate the bus voltage when the proposed UPFC works in normal mode, while it operates to compensate the reactive power when the proposed UPFC works in special mode. The series converter controller operates to inject a voltage with proper magnitude and phase for making the active power and the reactive power through the transmission line follow the reference values of active power and reactive power.

TABLE IV
EXPERIMENTAL PARAMETER

Parameter		Nominal Value
Source Voltage(V)		110V
Switching frequency		480Hz
Shunt Transformer		2kVA, 6:1
Line model	L_1	28mH
	L_2	15mH
DC capacitor		560μF

Fig. 8 shows the variations of the line current, the shunt-inverter voltage, the series-inverter voltage, the active power through, and the reactive power through the line, when the reference value of active power changes from 25W to 160W. The active component of line current increases while

the reactive component of line current is maintained. The line current increases suddenly at the instant of the active-power change.

Fig. 9 shows the variations of the line current, the shunt-inverter voltage, series-inverter voltage, the active power through line, and the reactive power through the line, when the reference value of reactive power changes from –140Var to 180Var. The reactive component of line current increases while the active component of line current is maintained. The injecting voltage has transient phenomenon during the state change from the capacitive mode to the inductive mode.

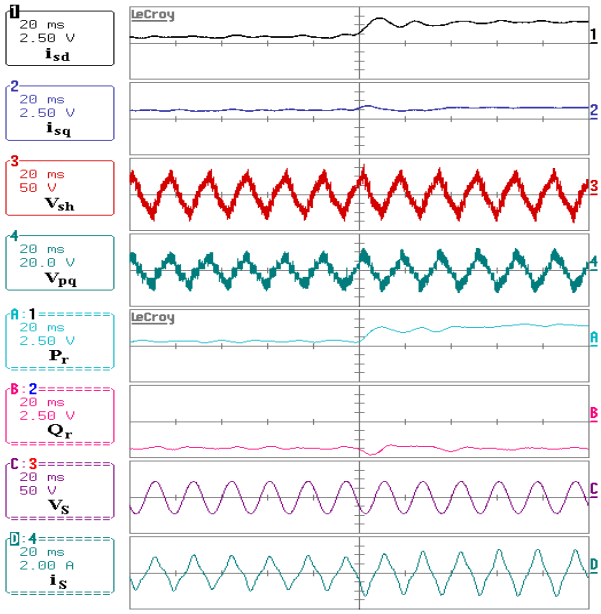

Fig. 8. Experimental results for the step change in active power flow from 25W to 160W

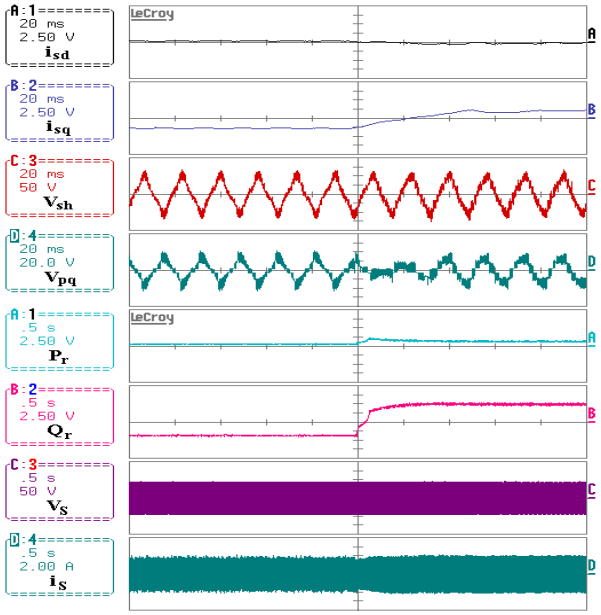

Fig. 9. Experimental results for the step change in reactive power flow from –140Var to +180Var

V. System Realization

The system realization aims at the development of a practical system that can be built with commercially available and reliable components. A commercially available high-power GTO, Mitsubishi FG6000AU-120D, was considered for the building block of H-bridge. It has ratings of 6kV peak off-state voltage (4.8kV DC off-state voltage) and 6kA controllable on-state current (1.5kA average on-state current). In order to guarantee the safety, 4kV DC off-state voltage and 1.25kA average on-state current were considered for the system design.

It is assumed that the proposed UPFC has 138kV of nominal operating voltage and 150MVA of power rating. There are twelve pairs of H-bridge modules for each phase in the proposed UPFC. The maximum injection voltage in series part is assumed 30% of the operation voltage (phase voltage of 24kV). The turn-ratio of primary to each secondary winding in the single-phase multi-winding transformer is designed to be 36:1. The RMS voltage to be handled by each H-bridge is 2.0kV, which has enough safety margin because the GTOs in one H-bridge have rating of 4kV DC off-state voltage.

Fig. 10 shows the conceptual diagram of the proposed UPFC including the simple power system. The proposed UPFC has twelve pairs of H-bridge module for each phase. There are total thirty-six pairs of H-bridge module, in which each pair of H-bridge has eight GTOs. Therefore, there are total two hundred eighty-eight GTOs in the proposed UPFC.

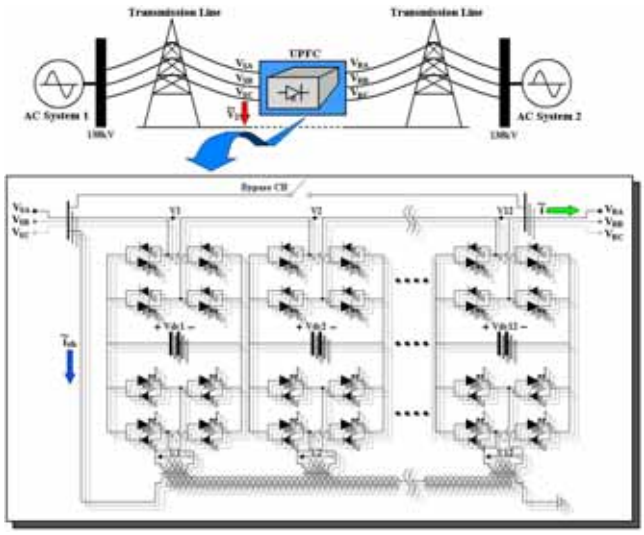

Fig. 10. Conceptual diagram for system realization

VI. Conclusion

This paper proposes a novel UPFC based on H-bridge modules, isolated through single-phase multi-winding transformers. The dynamic performance of proposed system was analyzed by computer simulations, assuming that the UPFC is connected with the 138-kV transmission line of one-machine-infinite-bus power system. The feasibility of

hardware implementation was confirmed through experiment with a scaled prototype. The proposed system can be directly connected to the transmission line without series injection transformers. It has flexibility in expanding the operation voltage by increasing the number of H-bridge modules.

The contribution of this paper is to propose a novel structure of UPFC to be connected in the transmission line directly without series injection transformer. The series transformer is a critical item in UPFC because it should have low saturation effect and low leakage impedance. The developed simulation model could be used to obtain design data for the actual hardware system.

REFERENCES

[1] C. D. Schauder, L. Gyugyi, M. R. Lund, D. M. Hamai, T. R. Rietman, D. R. Torgerson, A. Edris, "Operation of the Unified Power Flow Controller(UPFC) under Practical Constraints," IEEE Trans. on Power Delivery, Vol. 13, No. 2, pp.630-639, April 1998.

[2] Renz, B. A., Gyugyi, L., "AEP Unified Power Flow Controller Performance," IEEE Trans. on Power Delivery, Vol. 14, No. 4, pp.1374-1381, October 1999.

[3] Yiqiang Chen, Mwinyiwiwa, B, Z. Wolanski, Boon-Teck Ooi, "Regulating and Equalizing DC Capacitance Voltages in Multilevel STATCOM," IEEE Trans. on Power Delivery, Vol 12, No.2, pp.901-907, April 1997.

[4] F. Z. Peng, J. S. Lai, " A Multilevel Voltage-Source Inverter with Separate DC Sources for Static Var Generation," IEEE/IAS Annual Meeting. pp. 2541-2548, Orlando, FL, Oct. 8-12, 1995.

[5] F .Z. Peng, J. S. Lai, " Dynamic performance and control of a static var compensator using cascade multilevel inverter," IEEE/IAS Annual Meeting. pp.1009-1015, San Diego, CA, Oct. 6-10, 1996.

[6] J. D. Ainsworth, M. Davies, P. J. Fitz, K. E. Owen, D. R. Trainer, "Static Var compensator(STATCOM) based on single-phase chain circuit converters," IEE Proc.-Gener. Transm. Distrib., Vol. 145, No. 4, pp.381-386, July 1998.

[7] D. J. Hanson, C. Horwill, B. D. Gemmell, D. R. Monkhouse, "A STATCOM-Based Relocatable SVC Project in the UK for National Grid," IEEE/PES Winter Meeting, pp.532-537, Vol. 1, 2002.

[8] G. Joos, X. Huang, B. Ooi, "Direct-Coupled Multilevel Cascaded Series Var Compensator," IEEE Trans. on Industry Application, Vol. 34, No. 5, pp.1156-1163, September/October 1998.

[9] B. Han, S. Baek, H. Kim, G. Karady, "Dynamic Characteristic Analysis of SSSC Based on Multibridge Inverter," IEEE Trans. on Power Delivery, Vol. 17, No. 2, pp.623-629, April 2002.

[10] H. Fujita, H. Akagi, et al, "Transient Analysis of a Unified Power Flow Controller and its Application to Design of the DC-Link Capacitor," IEEE Transaction on Power Electronics, Vol. 16, No. 5, pp. 735-740, Sept. 2001.

A New Family of High Efficiency ZVS PWM Converter without Output Filter

Gun-Woo Moon and Sang-Kyoo Han
DEPT. OF ELECTRICAL ENGINEERING AND COMPUTER SCIENCE,
Korea Advanced Institute of Science and Technology (KAIST),
373-1 Guseong-Dong, Yuseong-Gu, Daejeon, 305-701, Republic of Korea
Phone: +82-42-869-3475, Fax: +82-861-3475
Email: gwmoon@ee.kaist.ac.kr

***Abstract*—A family of high efficiency ZVS-PWM bridge-type converters suited to high-voltage and low-current applications is proposed in this paper. To achieve the zero-voltage-switching (ZVS) of power switches along a wide load range, a small additional inductor, which also acts as an output filter inductor, is serially inserted to the transformer primary side. The problem related to ringing in the secondary rectifier caused by the additional inductor can always be completely solved by employing a structure without an output filter inductor. In addition, since it has no large output inductor filter, it features a simpler structure, lower cost, less mass, and lighter weight. Moreover, since all energy stored in the additional inductor is transferred to the output side, the circulating energy problem can be completely solved and the overall system efficiency along a wide load range is as high as above 96%. The proposed circuit is expected to be well suited to high-voltage and low-current applications. The operational principle, theoretical analysis, and design considerations are presented. To confirm the operation, validity, and features of the proposed circuit, experimental results from a 425W, 385-170Vdc prototype are presented.**

I. INTRODUCTION

In the field of power conversion system, various ZVS-PWM bridge-type converters such as an active-clamp forward, asymmetrical half-bridge, and phase-shifted full-bridge converters have been proposed to reduce the component current/voltage stress and switching losses in the traditional PWM converter [1-5]. However, since all these converters are required to have the large leakage inductor to achieve the ZVS of power switches along the wide load range, they have several common serious problems as follows. The first problem accompanied by increasing the leakage inductor is that it can bring relatively large circulating energy and reduce the overall system efficiency as a consequence [1-3]. The second problem accompanied by it is the serious parasitic ringing in the secondary rectifier. Thus, the device current/voltage stress and the system temperature are increased and the low noise output voltage is difficult to obtain [1-5]. Especially, in the case of the high output voltage applications, the resistor-capacitor (RC) snubber to absorb the serious ringing voltage across the secondary rectifier degrades the overall system efficiency, since the energy stored in the snubber capacitor is not only very large but also all dissipated through the snubber resistor [4,5].

Moreover, since the leakage inductor is the parasitic component, which cannot be tuned arbitrarily, the additional large inductor enough to achieve the zero-voltage-switching (ZVS) of power switches would be required along the wide load range [1-5].

Therefore, to solve all these drawbacks, a family of high efficient ZVS-PWM bridge-type converters is proposed in this paper as shown in Fig. 1. These converters can be classified into three groups according to their structure of the output stage. They are the FBR type, the HBR type, and double ended HBR type. The output voltage of the latter is twice as high as that of the former by its voltage doubling action of the half bridge configuration in the output side. The features of proposed converters in this paper will be described in the next chapter.

Among various ZVS-PWM DC/DC converters hitherto developed, a half bridge converter suitable for the mid power (about 400W~500W) application like the PDP power module has been proposed to reduce the component current/voltage stress and switching losses as shown in Fig. 2. However, since this converter is required to have the large leakage inductor to achieve the ZVS of power switches for the wide load range, it has several serious problems such as a large circulating energy, low system efficiency, serious parasitic ringing in the secondary rectifier, considerable heating, bulky cooling system, and noisy output voltage. Especially, in the case of the high output voltage applications like the PDP sustaining power module, the resistor-capacitor (RC) snubber to absorb the serious ringing voltage across the secondary rectifier degrades the overall system efficiency, because the energy stored in the snubber capacitor is not only very large but also all dissipated through the snubber resistor. Moreover, since the leakage inductor is the parasitic component, which cannot be tuned arbitrarily, the additional large inductor enough to achieve the ZVS of power switches would be required [4, 5]. Therefore, a new family of the high efficiency ZVS-PWM asymmetrical bridge type converter well suited to the applications of high voltage and low current is proposed in this paper as shown in Fig. 1. It can effectively overcome the abovementioned all problems of the prior circuit and realize the high power density, high performance, and high efficiency.

II. STURCTURE AND FEATURES OF THE PROPOSED CONVERTER

To simply show the structure and features of the proposed converters, the half bridge converter with voltage double rectifier will be explained in this section. To achieve the ZVS of power switches for the wide load range, an additional inductor is inserted to the transformer primary side like the prior approach as shown in Fig. 3, where C_1, C_2, D_1 and D_2 are not additional components but parasitic capacitors and anti-parallel diodes of MOSFETs and L_{lkg} represents the additional inductor including the transformer leakage component. However, same abovementioned problems as the prior circuit caused by the additional inductor are inevitable. To solve the

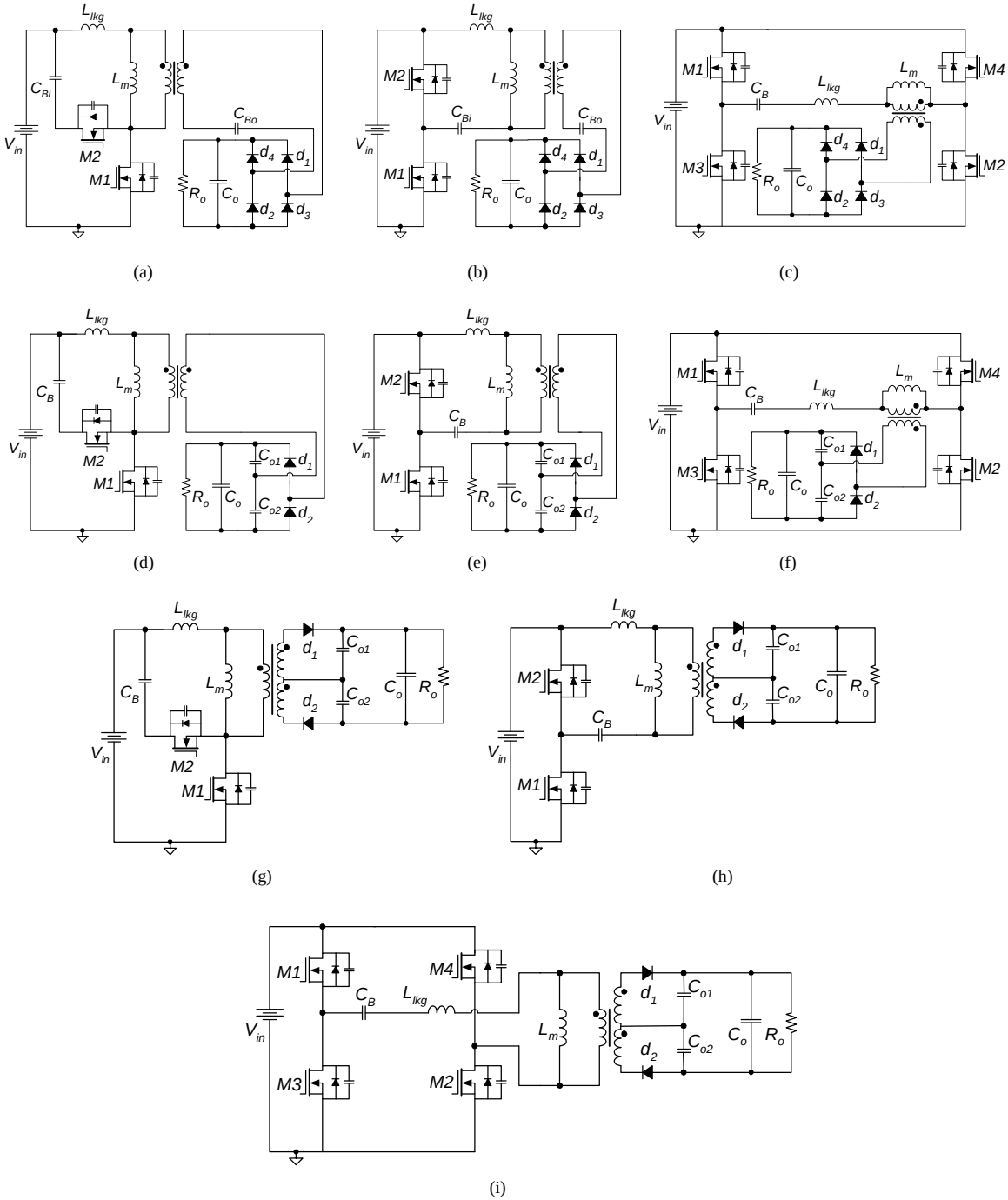

Fig. 1. A family of ZVS PWM bridge type DC/DC converter, (a) Active clamp forward converter with full bridge rectifier (b) Asymmetrical half bridge converter with full bridge rectifier (c) Phase shifted full bridge converter with full bridge rectifier (d) Active clamp forward converter with voltage-doubler rectifier (e) Asymmetrical half bridge converter with voltage-doubler rectifier (f) Phase shifted full bridge converter with voltage doubler rectifier (g) Active clamp forward converter with double ended voltage-doubler rectifier (h) Asymmetrical half bridge converter with double ended voltage-doubler rectifier (i) Phase shifted full bridge converter with double ended voltage doubler rectifier

problem related to the ringing in the secondary rectifier, the voltages across the output rectifier diodes has to be clamped at any voltage source, which can be effectively accomplished by removing the output filter inductor. Therefore, an RC snubber to absorb the ringing voltage is not necessary and the high efficiency as well as low noise output voltage can be realized. In addition, since it has no large output filter inductor but also employs only a small additional leakage inductor, it features a simpler structure, lower cost, less mass, and lighter weight. Although the output filter inductor does not exist, L_{lkg} can function as a filter inductor beside that for ZVS operation, which counts for nothing in high-voltage and low-current applications such as a PDP sustaining power module. Moreover,

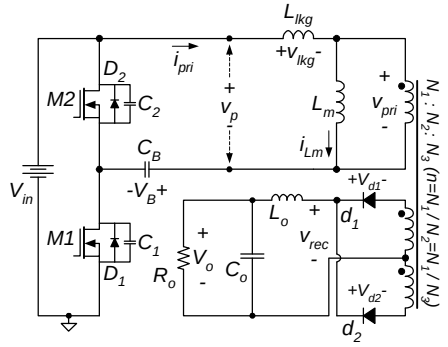

Fig. 2 Conventional half bridge converter

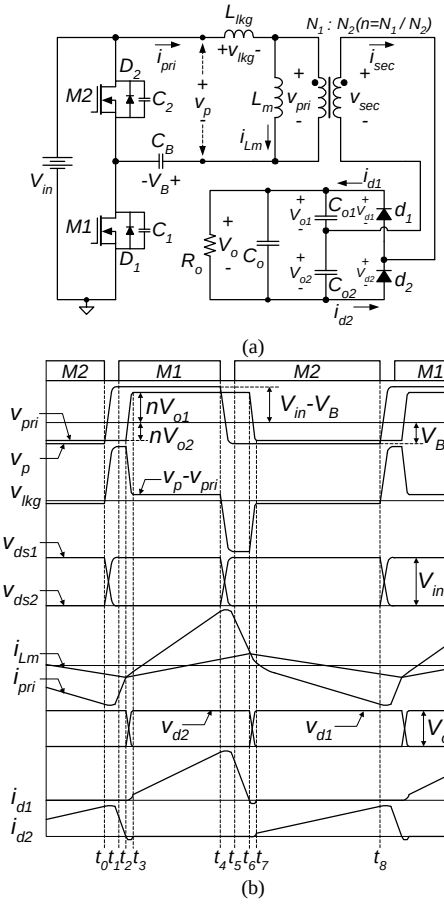

Fig. 3. Proposed converter (a) Schematic diagram of the proposed circuit (b) Key waveforms

since all energy stored in L_{lkg} is transferred to the output side until the current flowing through L_{lkg} becomes 0A, the circulating energy problem can be effectively solved.

Meanwhile, from the fact that the DC value of the current through the capacitor is 0A, the DC values of i_{pri}, i_{Co1}, and i_{Co2} (i. e. $<i_{pri}>$, $<i_{Co1}>$, and $<i_{Co2}>$, respectively) are all 0A, where $<\bullet>$ means the DC value of '$\bullet$'. Since i_{sec} is equal to i_{Co1}-i_{Co2}, $<i_{sec}>=<i_{Co1}>-<i_{Co2}>=0$A. Since i_T is equal to i_{sec}/n, $<i_T>=<i_{sec}/n>=0$A. And, since i_{Lm} is equal to i_{pri}-i_T, $<i_{Lm}>=<i_{pri}>-<i_T>=0$A, which means that the DC offsets of the transformer magnetizing current and flux can be completely blocked. Therefore, the

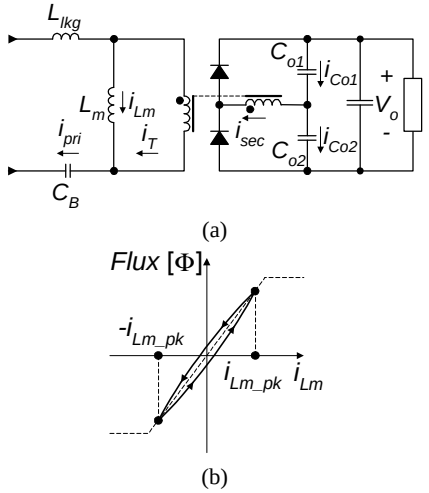

Fig. 4. Zero DC offsets of the transformer magnetizing current and flux (a) transformer magnetizing current (b) B-H curve of the magnetic core

transformer magnetic core can be fully utilized as shown in Fig. 4, and thus, its power density can be considerably increased.

III. CIRCUIT OPERATION

Figs. 3 (a) and (b) shows the circuit diagram and key waveforms of the half bridge converter with voltage double rectifier among the proposed family of high efficiency converters without output inductor, respectively. One cycle period of a proposed circuit is divided into two half cycles, t_0~t_4 and t_4~t_8. Since the operation principles of two half cycles are symmetric, only the first half cycle is explained. The driving method of the proposed circuit is the same as those of the conventional circuit. The switches M_1 and M_2 are turned on and off in a complementary way to each other. And, M1 is driven with the duty ratio D, which is less than 0.5. To illustrate the steady-state operation, all parasitic components except for those specified in Fig. 3(a) are assumed to be neglected. The switch M_2 is assumed to be initially in turn-on states before t_0. Therefore, the energy stored in C_B is powered to the output stage as shown in Fig. 5 (a) and at the same time, the primary current is linearly decreased with the slope of $-(V_B-nV_{o2})\}/L_{lkg}$. The analysis of the proposed circuit begins when the switch M_2 is turned off.

Mode 1 (t_0~t_1): When M2 is turned off at t_0, mode 1 begins as shown in Fig. 5 (b). With the initial conditions of $i_{pri}(t_0)=I_{t0}$, $v_{ds1}(t_0)=V_{in}$, and $v_{ds2}(t_0)=0$, the current i_{pri} flowing through L_{lkg} charges C_2 and discharges C_1 as $v_{ds1}(t)=V_{in}-I_{to}/(2C_{oss})(t-t_0)$ and $v_{ds2}(t)=I_{to}/(2C_{oss})(t-t_0)$ where C_1 and C_2 are equal to C_{oss} and L_{lkg} acts as a current source with the value of I_{t0} in this interval. After the voltage across C_1 is decreased to 0V, D_1 starts conducting. Therefore, the voltage across M1 is maintained to 0V.

Mode 2 (t_1~t_2): Since D_1 is conducting before t_1, M1 can be turned on with the ZVS at t_1. Since the primary current i_{pri} is larger than the magnetizing current i_{Lm}, the secondary current i_{sec} is still flowing in the same direction as that of the previous mode and output rectifier diode d_2 is also on the conductive state as shown in Fig. 5 (c). At the same time, the primary current is linearly increased with the slope of $(V_{in}-V_B+nV_{o2})/L_{lkg}$.

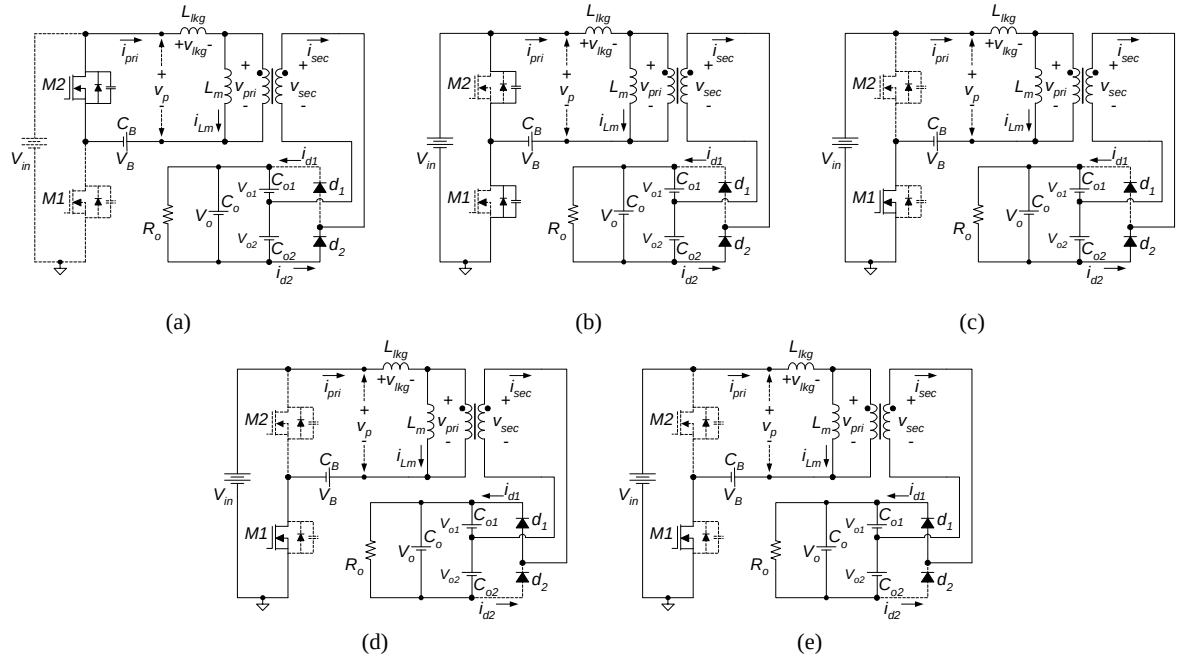

Fig. 5. Operation modes of the proposed converter, (a) Before t_0 (b) Mode 1 (t_0~t_1) (c) Mode 2 (t_1~t_2) (d) Mode 3 (t_2~t_3) (e) Mode 4 (t_3~t_4)

Mode 3 (t_2~t_3): When the primary current i_{pri} becomes equal to the magnetizing current i_{Lm}, mode 3 begins as shown in Fig. 5 (d). Since the primary current i_{pri} becomes smaller than the magnetizing current i_{Lm}, the direction of the secondary current i_{sec} is reversed and the commutation between d_1 and d_2 begins.

Mode 4 (t_3~t_4): After the commutation of output rectifier diodes, d_1 is conducting and d_2 blocked as shown in Fig. 5 (e). Therefore, the input source energy is powered to the output stage and at the same time, the primary current is linearly increased with the slope of $(V_{in}-V_B-nV_{o1})/L_{lkg}$.

The circuit operation of t_4~t_8 is similar to that of t_0~t_4. Subsequently, the operation from t_0 to t_4 is repeated.

IV. ANALYSIS OF THE PROPOSED CONVERTER

A. Voltage conversion ratios

For the convenience of the analysis of the steady-state operation, several assumptions are made as follows:

- All parasitic components except for the leakage inductor are neglected
- The dead time between M_1 and M_2 is discarded.
- The conductive period DT_s of M1 is less than $0.5T_s$.
- The commutation time between two pairs of output diodes is discarded.
- The blocking capacitors C_B, C_{o1}, C_{o2} and output capacitor C_o are large enough to be considered as a constant voltage source V_B, V_{o1}, V_{o2}, and V_o, respectively.
- Since time intervals t_1~t_2 and t_5~t_6 (as shown in Fig. 3 (b)) are much smaller than the switching period T_s, they can be discarded for the simplicity of the analysis.
- The magnetizing inductor L_m is so large that $i_{Lm}=0$.

By imposing the volt-second balance rule on the leakage inductor L_{lkg}, the steady state equation can be obtained as

$$D(V_{in}-nV_{o1}-V_B)=(1-D)(V_B-nV_{o2})\,. \qquad (1)$$

From equation (1), the voltage V_B across C_B can be expressed as

$$V_B = DV_{in}\,. \qquad (2)$$

By imposing the volt-second balance rule on the magnetizing inductor L_m, the steady state equation can be obtained as

$$D(V_o-V_{o2})=(1-D)V_{o2}\,. \qquad (3)$$

From equation (3), the voltage V_{o2} across C_{o2} can be expressed as

$$V_{o2} = DV_o\,. \qquad (4)$$

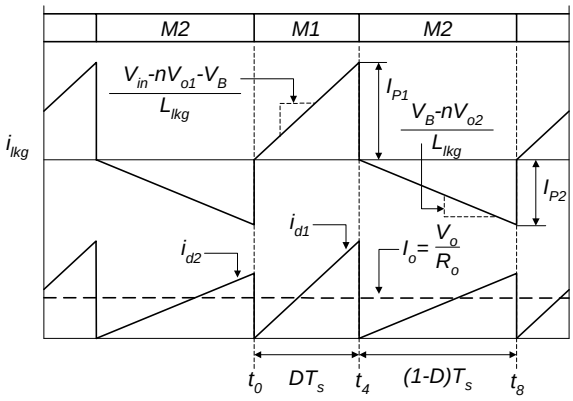

Fig. 6 Simplified current waveforms

Since V_{o1} is equal to V_o-V_{o2}, the voltage V_{o1} across C_{o1} can be easily obtained as

$$V_{o1} = V_o - V_{o2} = (1-D)V_o \,. \tag{5}$$

Fig. 6 shows that simplified current waveforms and the average value of the sum of i_{d1} and i_{d2} is equal to the load current I_o. Therefore, the following steady state equation is satisfied.

$$\begin{aligned} I_o &= \frac{V_o}{R_o} = avg\left\langle i_{d1} + i_{d2} \right\rangle \\ &= \frac{n}{T_s}\left[\frac{V_{in} - nV_{o1} - V_B}{2L_{lkg}} D^2 T_s^2 + \frac{V_B - nV_{o2}}{2L_{lkg}} (1-D)^2 T_s^2 \right]. \end{aligned} \tag{6}$$

where avg<•> means the average value of '•'.

Form equations (2), (4), (5), and (6), the steady state voltage conversion ratio of the overall system can be derived as follow

$$M = \frac{V_o}{V_{in}} = \frac{1}{\dfrac{2L_{lkg}}{nR_o T_s D(1-D)} + n}. \tag{7}$$

B. Zero-voltage switching

From Fig. 3(b), to achieve the ZVS of switches, the energy E_{lkg_t4} stored in the leakage inductor L_{lkg} at t_4 must be large enough to fully charge C_1 and discharge C_2 before the switch M_2 is turned on. Similarly, the energy E_{lkg_t8} stored in the leakage inductor at t_8 must fully charge C_2 and discharge C_1 before the switch M_1 is turned on. Therefore, to assure the ZVS of switches M_1 and M_2, the following equation must be satisfied.

$$E_{lkg\_t_4} = \frac{1}{2} L_{lkg} I_{lkg\_t_4}^2 \geq E_{lkg\_t_8} = \frac{1}{2} L_{lkg} I_{lkg\_t_8}^2 \geq \frac{1}{2} 2C_{oss} V_{in}^2 \tag{8}$$

where C_1 and C_2 are assumed to be equal to C_{oss} and I_{lkg_t4} and I_{lkg_t8} are the peak currents through the leakage inductor at t_4 and t_8, respectively. From the simplified current waveforms shown in Fig. 6, I_{lkg_t4} and I_{lkg_t8} are assumed to be equal to I_{p1} and I_{p2}, respectively, which can be also expressed as follows

$$I_{lkg\_t_4} \triangleq I_{P1} = \frac{V_{in} - nV_{o1} - V_B}{L_{lkg}} DT_s \tag{9}$$

$$I_{lkg\_t_8} \triangleq I_{P2} = \frac{V_{in} - nV_{o2}}{L_{lkg}} (1-D)T_s \,. \tag{10}$$

C. Duty cycle loss and circulating current

The typical waveforms of the conventional half bridge converter and the proposed converter are compared as shown in Fig. 6. The operating duty cycle of the conventional circuit can be expressed as $D=D_{eff1}+D_{loss1}$ and $1-D=D_{eff2}+D_{loss2}$, where D_{eff1} and D_{eff2} mean the effective duty cycle and D_{loss1} and D_{loss2} mean the losses of the duty cycle.

The D_{loss1} and D_{loss2} can be expressed as

$$D_{loss1} = \frac{L_{lk}(I_1 + I_2)}{(1-D)T_s V_{in}}, \; D_{loss2} = \frac{L_{lk}(I_3 + I_4)}{DT_s V_{in}} \tag{11}$$

where I_1, I_2, I_3, and I_4 are defined in Fig. 6 (a).

For the conventional half bridge converter, the leakage inductance should be large enough to provide a reasonable ZVS range. So, the loss of the duty cycle D_{loss1} and D_{loss2} are very large from the equation (11) and therefore, the effective powering period is decreased as shown in Fig. 7 (a), resulting in the increased circulating current and subsequent serious conduction loss. On the other hand, the proposed converter does not have any duty cycle loss and all energy stored in L_{lkg} is transferred to the output side until the current flowing through L_{lkg} becomes 0A as shown in Fig. 7 (b). Consequently, the circulating energy problem can be effectively solved.

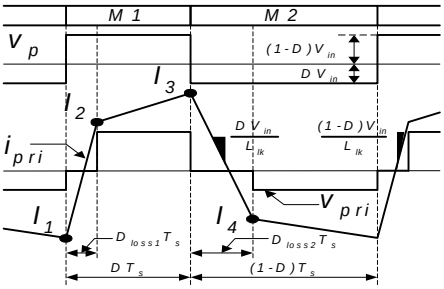

(a)

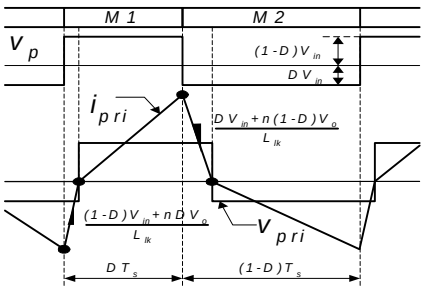

(b)

Fig. 7 Comparison of primary voltage and current waveforms, (a) Conventional half bridge converter (b) Proposed converter

D. Comparisons of device stresses

Table I shows the comparisons of device stresses between the conventional and proposed circuits. As shown in this table, the voltage stresses of the output diodes d_1 and d_2 in the conventional circuit are so high as V_{in} at D=0.5 compared with V_o of the proposed circuit. Furthermore, the output diode of the conventional circuit suffers from the serious voltage ringing, which results in the increased voltage rating, forward voltage drop, and cost of the output diode. Therefore, the well-designed RC snubber must be used to protect the output diode from this voltage ringing, which could also generate serious power losses.

Meanwhile, the current stresses of the output diodes d_1 and d_2 in the proposed circuit are rather large compared with that in the conventional circuit. This is because the proposed converter employs the output structure of the half bridge configuration, which features the voltage/current doubling effects and simple structure. However, this is not so serious in low current and high voltage applications such as the PDP sustaining power module.

Table. I Comparisons of device stress

Part	Conventional circuit	Proposed circuit
Voltage stress of M1 and M2	V_{in}	V_{in}
Current stress of M1 and M2	$2(1-D)I_o/n_{con}$, $2DI_o/n_{con}$	$n_{pro}I_o/D$, $n_{pro}I_o/(1-D)$
Voltage stress of d_1 and d_2	$2DV_{in}/n_{con} + a$, $2(1-D)V_{in}/n_{con} + a$ (a=voltage ringing)	V_o
Current stress of d_1 and d_2	I_o	$2I_o/D$, $2I_o/(1-D)$
DC offset current of L_m	$(1-2D)I_o/n_{con}$	0
Transformer turn ratio	n_{con}	$n_{pro}=2n_{con}$

V. EXPERIMENTAL RESULTS

The prototype of the proposed circuit is implemented with specifications of V_{in}=385V, V_o=170V, rated power P_o=425W, L_{lkg}=32uH, C_B=2uF, C_{o1}=C_{o2}=4.4uF, C_o=560uF/ 250V, transformer turns ratio N_1:N_2=21:11, M1 and M2= 2SK2837(C_{oss}=1.165nF), d_1 and d_2=15ETH03, and switching frequency=72kHz. Fig. 8 shows an industrial sample of a PDP power module employing the proposed converter.

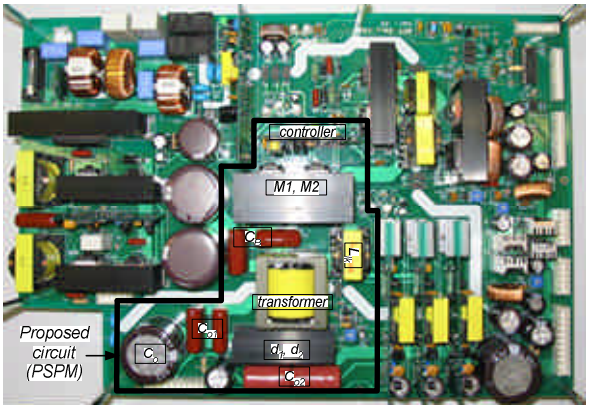

Fig. 8 Industrial sample of a PDP power module employing the proposed converter

Fig. 9 (a) and (b) shows the key waveforms at the full load. From these figures, since the voltages across d_1 and d_2 are clamped to the output voltage, there is no serious voltage ringing in those diodes. Moreover, since all energy stored in L_{lkg} is transferred to the output side, no circulating energy exists. Fig. 9 (c) shows that the ZVS of M1 and M2 can be achieved at the 40% load condition. Fig. 9 (d) shows that while the ZVS of M2 is obtained at 10% load, that of M1 not. However, since the current though M1 are very small at this point, the switching loss is not serious. Fig. 10 shows heat dissipations of the proposed engineering sample. As seen in this figure, low temperatures of the components as low as 60 degree can be obtained. Fig. 11 shows the measured efficiency compared with conventional asymmetrical half bridge converter. The efficiency along a wide load range is as high as above 96%.

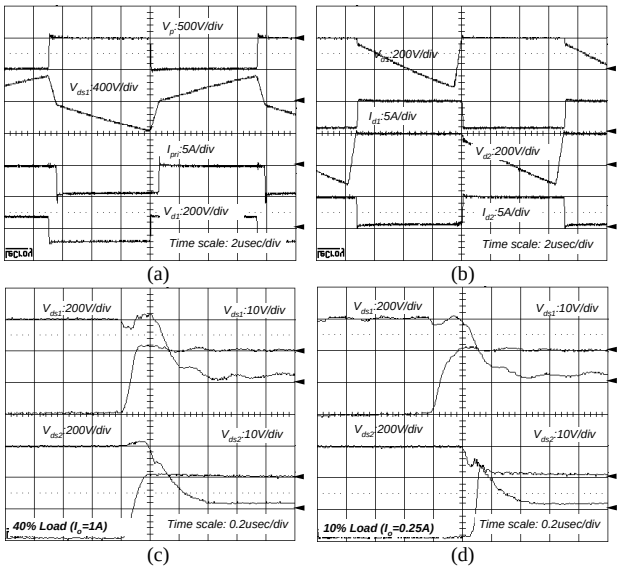

Fig. 9 Experimental waveforms, (a) Key waveforms of v_p, v_{ds1}, i_{pri}, and v_{d1} (b) Key waveforms of v_{d1}, i_{d1}, v_{d2} and i_{d2}, (c) ZVS turn on at 40% load (d) Hard switching and ZVS turn on at 10% load

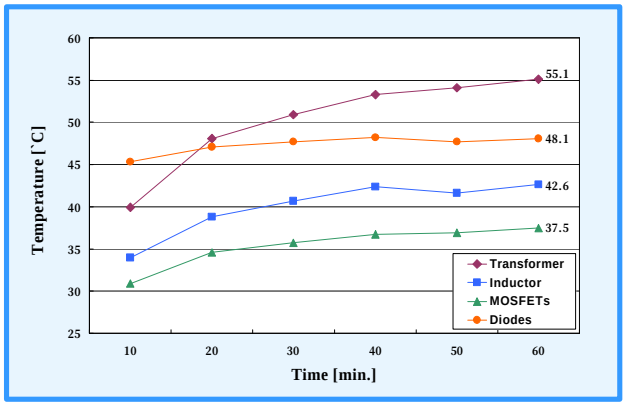

Fig. 10. Heat dissipations of engineering sample

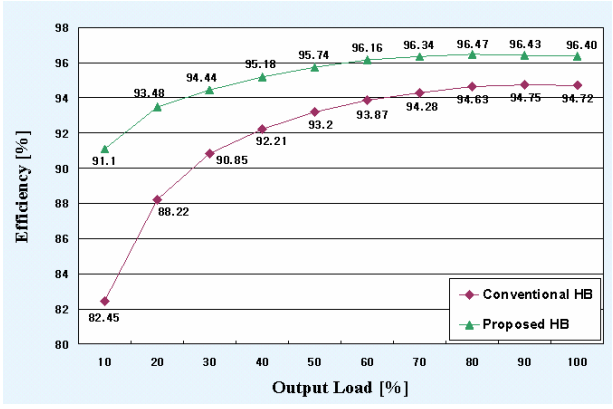

Fig. 11. Measured efficiency compared with conventional half bride converter

VI. CONCLUSION

A family of high efficient ZVS-PWM bridge-type converters has been presented in this paper. A small additional inductor, which also acts as an output filter inductor, can achieve the ZVS of power switches for the wide load range. And, the problem related to ringing in the secondary rectifier caused by the additional inductor can be completely solved by employing a structure without an output filter inductor. In addition, since it has no large output inductor filter, it features a simpler structure, lower cost, less mass, and lighter weight. Moreover, since all energy stored in the primary inductor is transferred to the output side, the circulating energy problem can be effectively solved and the overall system efficiency along a wide load range is as high as above 96%.

REFERENCES

[1] J. A. Sabate, V. Vlatkovic, R. B. Ridley, F. C. Lee, and B. H. Cho, "Design considerations for high-voltage high-power full-bridge zero-voltage-switched PWM converter," in Proc. IEEE Appl. Power Elecrton. Conf., 1990, pp.275~284.

[2] Jung-Goo Cho, Ju-Won Baek, Chang-Yong Jeong, Dong-Wook Yoo, and Kee-Yeoun Joe, "Novel Zero-Voltage and Zero-Current-Switching Full Bridge PWM Converter Using Transformer Auxiliary Winding", IEEE Trans. Power Electron., Vol. 15, No. 2, pp.250~256, Mar. 2000.

[3] H. K. Ji, H. J. kim, "Active clamp forward converter with MOSFET synchronous rectification**",** PESC 1994, vol. 2, pp.895-901.

[4] Marcelo Lobo Heldwein, Alexandre Ferrari de Souza, and Ivo Barbi, "A Primary Side Clamping Circuit Applied to the ZVS-PWM Asymmetrical Half-Bridge converter", PESC 2000, vol. 1, pp.199-204.

[5] Jim H. Liang, Po-Chueh Wang, Kuo-Chien Huang, Chern-Lin Chen, Yi-Hsin Leu, and Tsuo-Mim Chen, "Design Optimization for Asymmetrical Half-Bridge Converters", APEC 2001, vol. 2, pp. 697-702.

Multi-Phase Converter System as a Testing Generator for medium power applications

Petzoldt, J.; Büttner, J.; Ellinger, T.; Rosenbaum, T.

1. Introduction

Certain functional testing processes in the electrical industry require that the applied testing voltage should have accurate magnitude, wave shape and also have exact required frequency. The power rating of the applied testing voltage ranges upto several hundred kVA depending on the testing object. The proposed converter system to generate these applied voltages not only guarantees the exactness of the voltage magnitude and wave shape but can also generate them in a wide range of frequency. A fast dynamic response is obviously required in case of fast load variations or changing reference values.
Therefore with the proposed system it is possible to generate a three phase voltage with nearly unlimited unbalances and with fast dynamic response for voltage magnitude variations. With this type of converter it is possible to generate a 50Hz or 60 Hz grid with additional voltage harmonics of defined magnitude and phase upto 50^{th} harmonic. Also grid frequencies as far as some kHz can be generated with this setup.
The paper presents the novel power electronics topology as well as a new control strategy for a 50kVA test bench. Simulation and experimental results shows the theoretical as well practical feasibility of the proposed concept.

2. Power circuit topology

The AC- test generator power circuit topology is shown in Figure 1 below. It principally consist of three sections namely AC to DC converter - DC to DC converter - AC Sinusoidal generator.

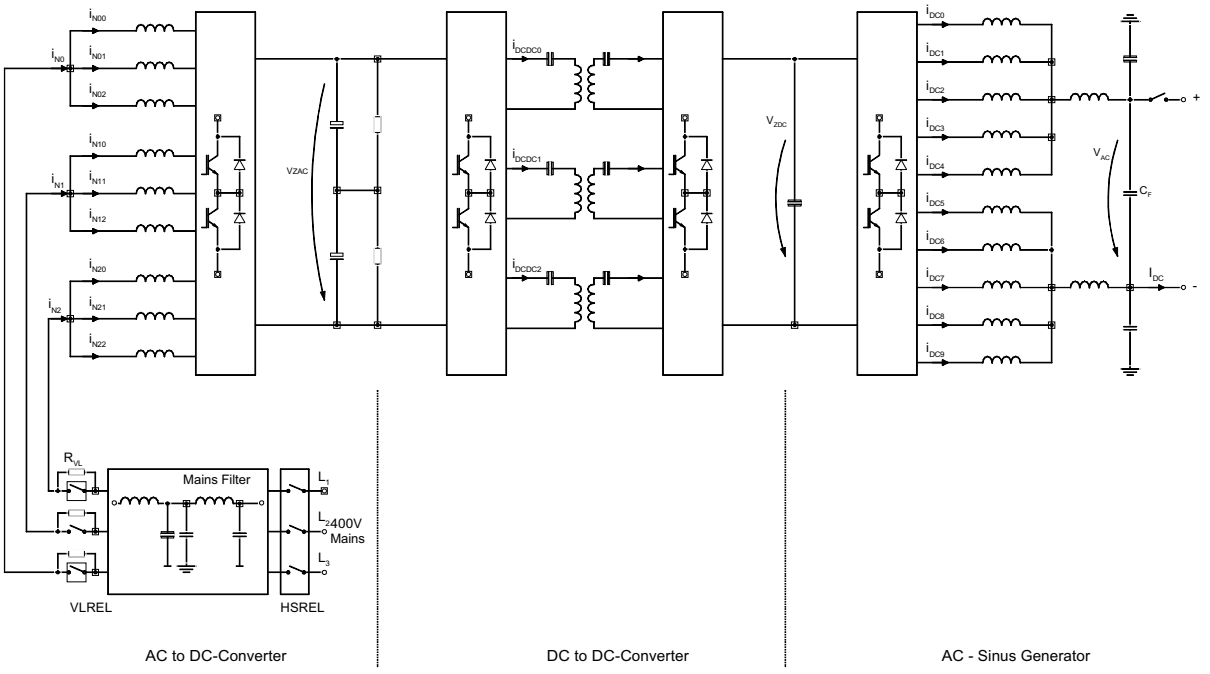

Figure 1: Power Circuit Topology of the proposed System

The AC to DC Converter section is connected to the mains voltage under purpose of maintaining a constant DC Voltage V_{ZAC} at the DC bus. Otherwise the AC to DC converter limits the disturbance in the mains. The DC to DC converter provides the potential isolation between the mains and the AC test generator. Through generation of a middle frequency current (20-25 kHz) based on resonant concept it is possible to realise fast current variation in the output with very little disturbance in the DC bus voltage. The main task of the AC-test generator is generating a precise sinusoidal output voltage from the unregulated DC bus voltage $V_{ZDC.}$

2.1 AC to DC converter:

The AC to DC converter is connected to the mains and provides a constant DC-bus voltage U_{ZAC} (about 700 volts). The DC voltage control of the AC/DC converter is implemented by using a DSP controller card. The control maintains a constant DC voltage while limiting the disturbance caused in the mains due to charging the DC bus. The precharging of the capacitor is provided by a precharging contactor in parallel with a resistor. The contactor is operated through relay VL_REL. The grid connection is realised through another contactor relay arrangement (HS_REL). The requirement of fast energy exchange between three phase mains and the AC-DC converter is realised by supplying each converter phase with three single phase connection which works at 120 degree phase shift to each other. Therefore a total of 9 single phase connections are synchronised for operation of the AC- DC converter. All the phases are working together to produce a constant DC voltage U_{ZAC} upon a common DC bus capacitor of 6mF. To provide proper voltage distribution/division among the DC capacitor, balancing resistors are used, as shown in Figure 1. The limitation of the mains current harmonics is achieved by an additional control block, which contains a separate control loop for each of the harmonics from the 5^{th} up to the 25^{th} of the mains frequency. This control loops are equipped with Low-Pass to Band-Pass transformed controllers (will be described in the following) to obtain low current distortion and a short computation time. The distortion control block operates in parallel to the control loops for the fundamental current.

2.2. DC to DC converter:

The DC to DC converter is used to provide potential separation between the mains and the AC test generator. The left IGBT half bridges inject a resonant middle frequency current (20-25kHz) into the transformer primary windings. The energy flow from the mains to the AC-output can be controlled by variation of the delay angle between the phase of the resonace current $I_{DC/DC}$ and the switching time of the right IGBT halfbridges. This concept also prevents a dropping or sinking of the DC bus voltage and realises a bidirectional energy flow. Due to the work of three 120 degree shifted DC to DC converters, the resulting ripple in the DC Voltage V_{ZDC} is around the frequency greater than 120 kHz.

2.3 AC Test Generator:

Figure 2 shows the topology of the AC Sinus Generator. The main task of the AC test generator is providing a very accurate AC output voltage V_{AC}. Two groups each consisting of 5 IGBT-half bridges are used to achieve the output voltage on the output capacitor which connects the AC test device. The circuit is symmetrical. This will minimise the disturbing influence of one group over the other and so minimising the EMI disturbances. Through the half bridge topology small AC-output voltage can be realised as well as fast voltage and current variations. Thereby a high dynamic response can be achieved. An integrated 16 bit accurate AD conversion technique is surely required for a precise measurement of the actual output value. Since a phase shift between the pulse pattern for each bridge is used, as described in section 2.1, the ripple in the output voltage is decreased by the factor of

ten. The realized system provides an output voltage ripple frequency of about 100kHz. Due to this high ripple frequency the output capacitor is very small and therefore the dynamic response is fast.

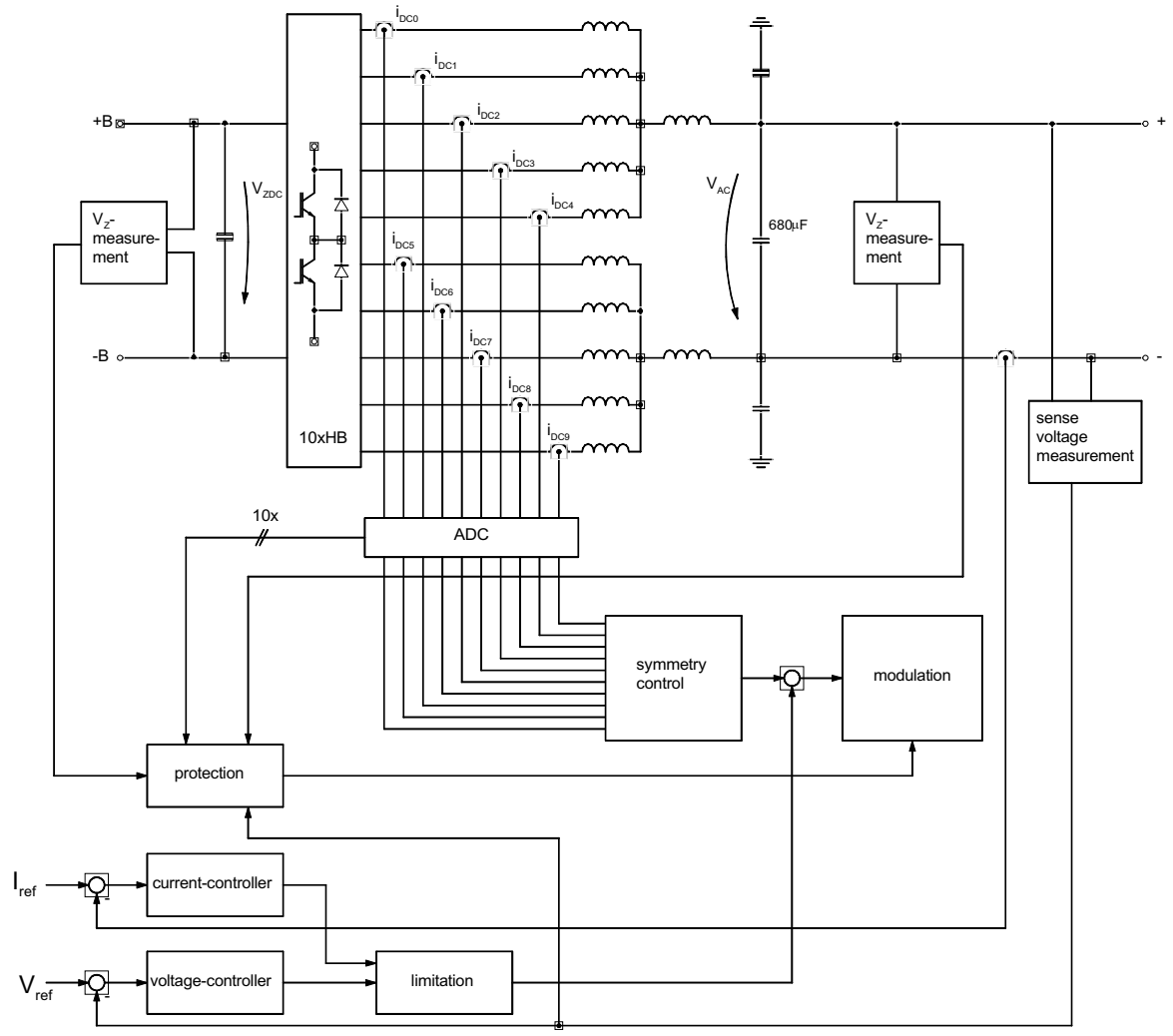

Figure 2: Topology of the AC Sinus Generator

3. Control System Topology

The control system for the AC and DC/DC converters correspond to the state of the art. The mains connection includes a harmonic current compensation up to the 25^{th} harmonic. An appropriate control concept was developed for realizing the high dynamic demands to the AC-generator. The implemented control system is described in the following subchapter.

3.1. Control design for amplitude modulated system values

The demand for compliance of a given AC-reference value is based on the theory by generating a sinusoidal voltage with a stationary constant amplitude. This amplitude is to be influenced by a power electronic converter in combination with a adequate control system in a desired way.
For that purpose often a controller with transformed coordinates is used.

The implementation of such a method requires a twice online transformation of coordinates (demodulation DM and modulation M) which calls for additional computation time. However this method gives the possibility to use DC-controllers ($G_{R\_}$) and a DC set value (w-) which represents the amplitude. For avoiding the permanently made coordinate transformation the use of a control method is proposed which is based on the low-pass to band-pass transformation (in the following LP-BP-Transformation). This method is described in [1]. The amplitude of an AC-component can be stationary exactly controlled by omitting the demodulation and the modulation blocks.

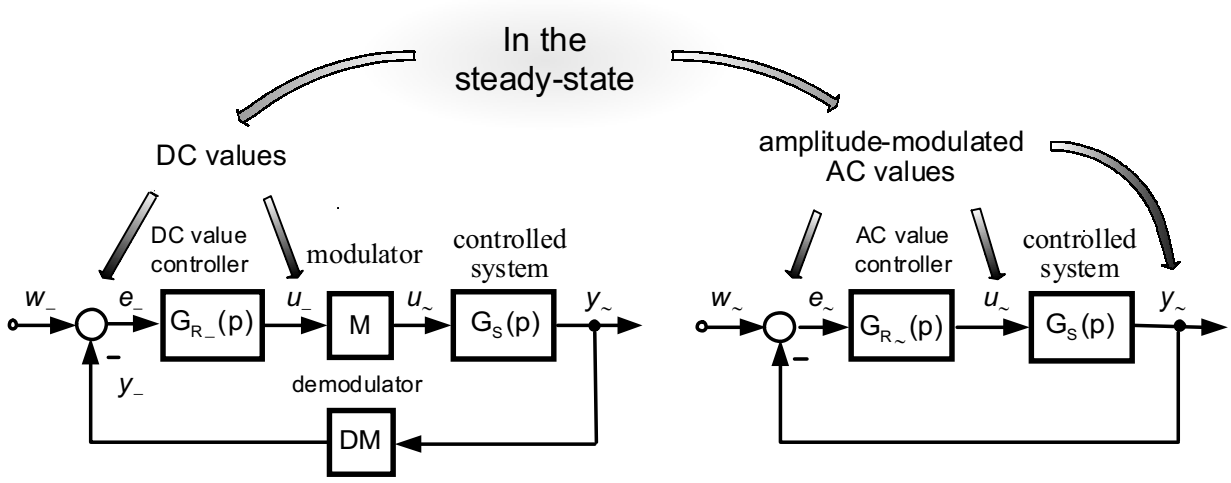

Figure 3: fundamental structure of AC-component control systems

Figure 3 shows the difference between the two possibilities. In case of a LP-BP-Transformation the set value is an AC-component.
The proposed concept is rarely common up to now. In this connection an example will give an explanation. Based on the transfer function of a well known DC-component PI-controller $G_{R\_}$ the LP-BP-Transformation by using the parameter Ω_T leads to a transfer function for AC-components $G_{R\sim}$.

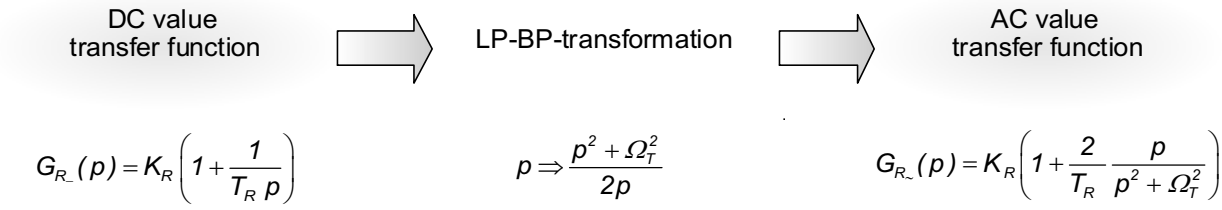

Figure 4: needed steps to to generate a AC-component controller

Figure 4 illustrates the needed steps to find the transformed transfer function. The definition of the LP-BP-transformed controller requires three parameters. K_R represents the gain, T_R the time constant and Ω_T the frequency of the reference value.

3.2. Control Topology of the AC-Sinus Generator

The control loop of the AC-Generator consists of the voltage controller and the controlled output-filter L_F, C_F. The good dynamic response results from the cascaded control structure. In this case the output filter current i_F is controlled to a defined reference value apart from the

output voltage V_{CF}. The reference value of the current control loop is delivered by the voltage controller. This inner loop improves only the dynamic behaviour. Therefore the current controller can have a proportional characteristic (G_{R-}). The outer voltage control loop guaranties the steady-state precision and for that a transformed PI-controller ($G_{R\sim}$) has to be implemented. It fits the output voltage to the sinusoidal reference $V_{CF,ref}$.

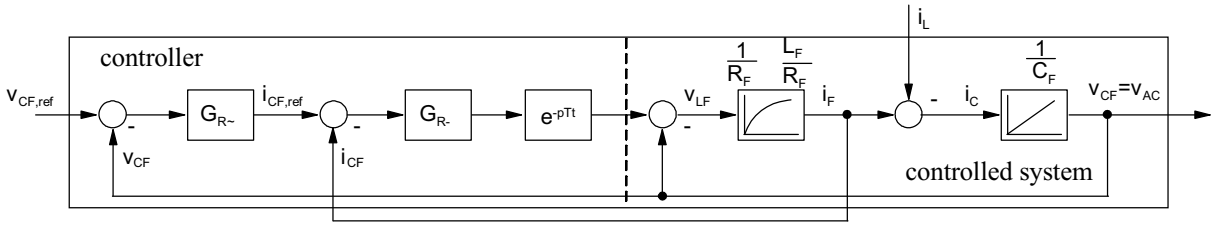

Figure 5: control structure of the AC-Generator

4. Simulation Results

The in-house Simulation System DIGSIM was used to analyse the proposed system. The extensive simulations will be demonstrated by showing characteristic values for a defined operation point. Figure 6 shows the reference value and the output voltage of the system in case of a set-point jump generating a sinusoidal voltage for the 11-th harmonic of a 50Hz-grid.
The system is able to meet the referenced phase condition only the amplitude is delayed by approximately 5 ms.

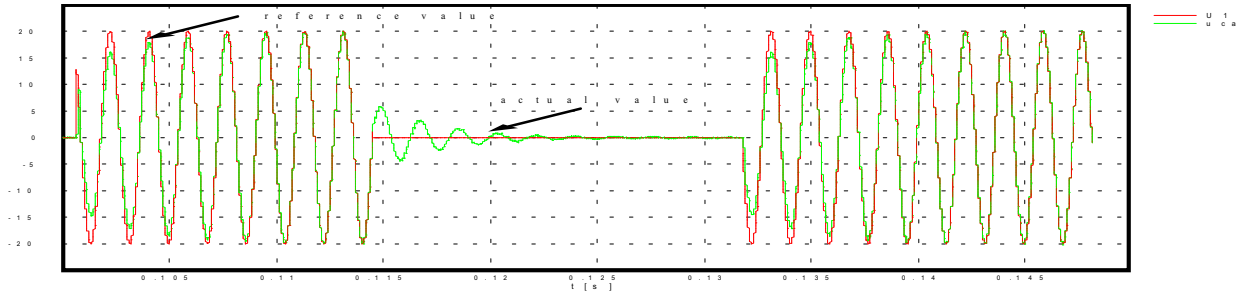

Figure 6: Simulations for a 550Hz voltage step, reference and actual value

In case of a steady-state 5000Hz voltage generation there is no difference between the reference and the output voltage (compare **Figure 7**).

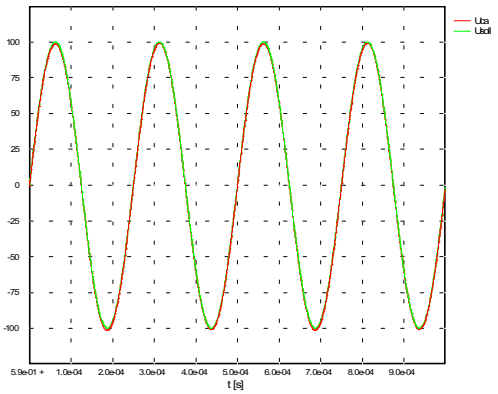

Figure 7: Simulation result for 4000Hz frequency

Figure 8 shows the the discrete currents in the shifted phases for operation with 4000Hz.

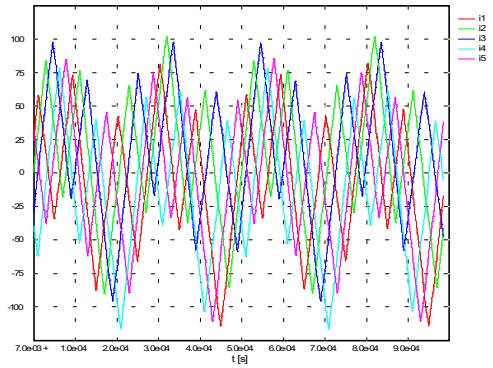

Figure 8: discrete currents in shifted phases

It can be seen, that the discrete currents have a DC component. The reason is the

switching behaviour of the power electronic system and it is necessary to implement a control loop for avoiding circulating currents.

5. Eperimental Measurements

Figure 9 confirms the made simulations. The response time corresponds to the simulations. The over-shoot of the amplitude is a little higher. The peak current of the resistive load reaches the amount of approximately 35A.

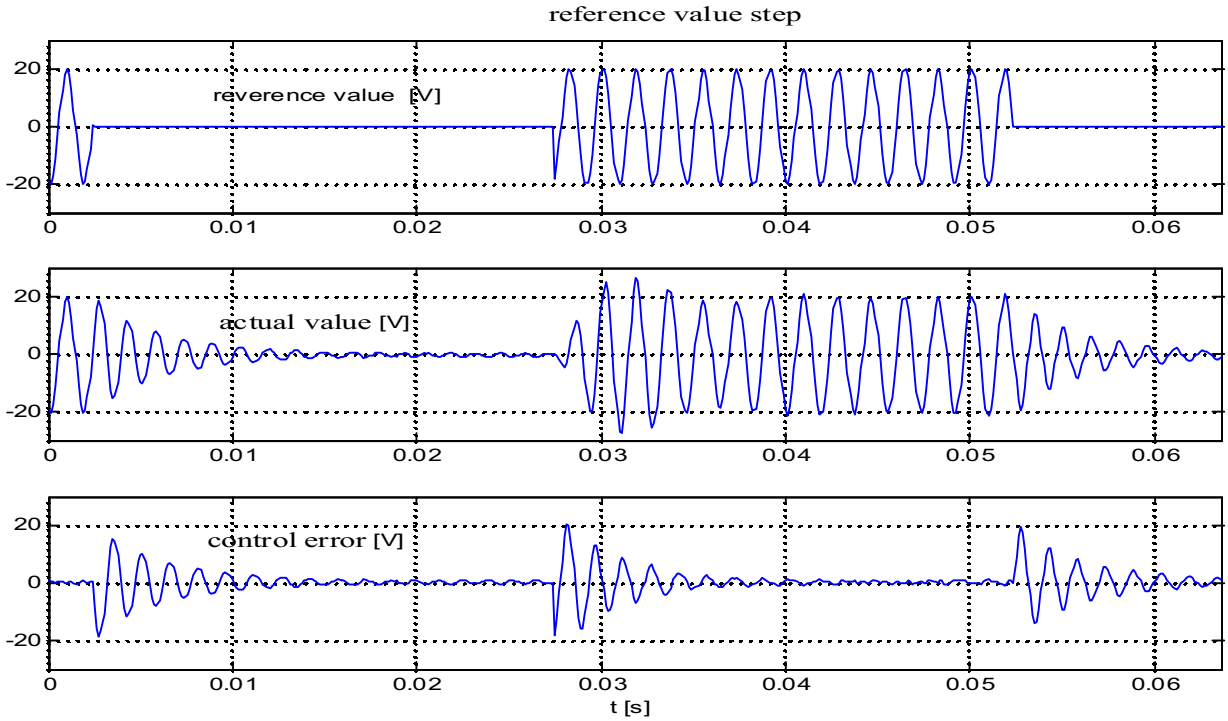

Figure 9: experimental measurement of a 550Hz voltage step, reference and actual value

6. Conclusion

The paper presents the characteristic properties of a proposed power electronic topology and introduces to the control concept realizing a testing generator for sinusoidal voltage. High quality demands concerning the dynamic and the resolution of the provided voltage could be more satisfied by using the proposed innovative topology and adapted control concept. The proposed Low-Pass to Band-Pass transformed control loops give the possibility to reach a fast dynamic response without phase error in case of a set-point step variation. The high cut-off frequency of the system permits to synthesise a output voltage consisting of several frequency components each controlled by a separate control loop. So it is possible to generate a sinusoidal fundamental voltage with defined harmonics as well as a triangular, rectangular or a DC voltage.

References:

[1]Solodownikow, W. W.: Grundlagen automatischer Regelungssysteme. Verlag Technik, Berlin, 1971.

Authors:

Dr. J. Büttner, Prof. Dr. J. PetzoldtDr. T. Ellinger, cand. Ing. T. Rosenbaum
Ilmenau Technical University, Germany
98684 Ilmenau Postfach 100565
Faculty Electrical Engeneering and Information Technology
Department Power Electronics and Control

Analysis of DC Link Ripple Current in Three-Phase AC/DC/AC PWM Converters

Young-Wook Park Dong-Choon Lee Jul-Ki Seok

School of Electrical Engineering and Computer Science, Yeungnam University

214-1, Daedong, Gyongsan, Gyongbuk, 712-749, Korea

mcath@dreamwiz.com *dclee@yu.ac.kr* *doljk@yu.ac.kr*

Abstract **- This paper proposes a spectral analysis of the dc link ripple current in three-phase ac/dc/ac PWM converter system for induction motor drives. The expression of the harmonic currents is developed by using switching functions of the PWM and the complex exponential form of the Fourier series. The effect of the displacement angle between the PWM periods of line-side converters and motor-side inverters on the dc link ripple currents is investigated. Also, the influence of asynchronization in the PWM is observed. The result of analysis coincides well with the frequency spectrum which results from the PSIM simulation. The proposed scheme is very useful to model the equivalent circuit of the dc electrolytic capacitor in a high frequency range as well as to understand analytically the principles of the pulse width modulation.**

Index terms**: Ac/dc/ac/ PWM converters, dc link ripple current, harmonic spectrum, exponential Fourier series**.

I. INTRODUCTION

In recent, the three-phase ac/dc/ac PWM converter is increasingly used for industrial applications such as mill drives, elevators, uninterruptible power supply(UPS) [1], active power filters [2], wind power generation [3] and so on, since it has advantages such as constant dc voltage control, sinusoidal line current control, unity power factor control, and bi-directional power flow [4]. The ac/dc/ac PWM converter usually has a dc link with large electrolytic capacitors as an energy storage element. The sizing of the dc capacitor depends on the operating frequency. Also, the performance deterioration of the dc electrolytic capacitor is diagnosed by identifying its equivalent series resistance (ESR) which is a function of the operating frequency and temperature [5], [6]. So, for these purposes, it is required to analyze the frequency spectrum of the dc link ripple currents.

There have been some research results to analyze the dc link ripple currents [7], [8], where only the rms value of the ripple currents was developed. The previous studies which dealt with the frequency spectrum of the dc link current are very a few [9], [10]. In [9], the dc link current in PWM inverters only was analyzed and in [10] the harmonic spectrum measured experimentally was presented without analysis.

In this paper, the dc link ripple currents for the three-phase ac/dc/ac PWM converters feeding induction motors are analyzed in a frequency domain. The expression of the harmonic currents is developed by using switching functions of the PWM and the complex exponential form of the Fourier series. Also, the effect of the displacement angle between the switching periods of the line-side converter and the motor-side inverter on the dc link ripple currents is investigated, where it is known that the displacement angle of 0 and π gives the minimum dc link ripple current. The validity of the proposed analysis method has been verified by simulation results using the PSIM.

II. PROCEDURE OF ANALYSIS

Fig. 1 shows the main circuit of a three-phase ac/dc/ac PWM converter feeding an induction motor, which consists of the line-side PWM converter and the motor-side PWM inverter. The procedure to derive the dc link ripple current mathematically, which basically comes from the method in [9] where analysis of the inverter input current only was developed, is described below:

i) At first the switching function S_k of the PWM is expressed, where k (=1, 2, 3) represents the phase number. Its detail derivation will be described in the following sections.

ii) Using the switching function, the dc link current due to each phase current i_k is obtained as

$$i_{dck} = i_k \cdot S_k \tag{1}$$

where i_k is found from the ratio of the harmonic voltage to the harmonic impedance.

iii) The sum of each contribution of the three phases gives the total dc link current drawn by the inverter such as

$$i_{dcI} = \sum_{k=1}^{3} i_{kI} \cdot S_{kI} \tag{2}$$

where the subscript "*I*" means the inverter-referred term.

iv) In the same way as in (iii), the dc link current of the converter output terminal, i_{dcR}, is calculated as

$$i_{dcR} = \sum_{k=1}^{3} i_{kR} \cdot S_{kR} \,. \tag{3}$$

v) The ripple current of the dc link capacitor is calculated by adding vectorially both the n-th harmonics of the converter output and the inverter input terminals,

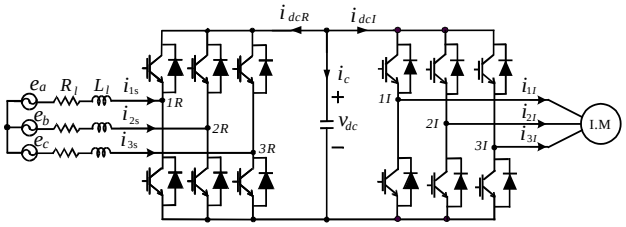

Fig. 1. Three-phase ac/dc/ac/ PWM converter.

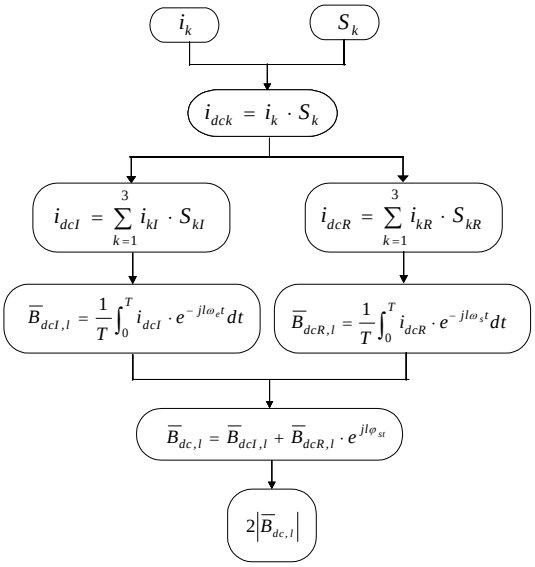

Fig. 2. Procedure of analysis.

considering a displacement angle, which is expressed as

$$\vec{i}_{dc,n} = \vec{i}_{dcI,n} + \vec{i}_{dcR,n} \cdot e^{-jn\varphi_{st}} \tag{4}$$

where, φ_{st} is an angle displaced between the two switching periods of the inverter and the converter.

The flow chart for analysis is shown in Fig. 2.

III. EXPRESSION OF SWITCHING PULSES

The derivation of the switching function in this section is referred to in [9]. Fig. 3(a) shows the principle of the sinusoidal PWM, switching pulses, and corresponding pole voltages, where a synchronous PWM is assumed. Fig. 3(b) shows one modulated pulse in a switching period. The fundamental period is subdivided into *p* short pulses of equal width Δ.

$$\Delta = 2\pi / p \tag{5}$$

The angle of δ_{1i} and δ_{2i} means a pulse width in a switching period. The δ_o is the quarter of a switching period. If $\delta_{1i} = \delta_{2i} = \delta_o$, the average voltage over the pulse is zero.

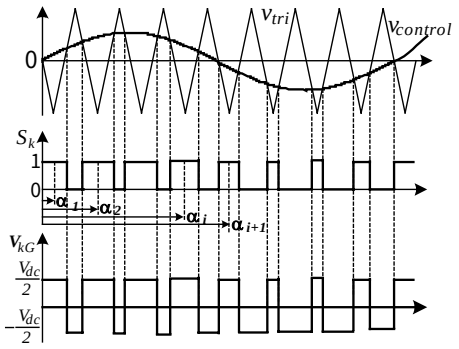

(a)

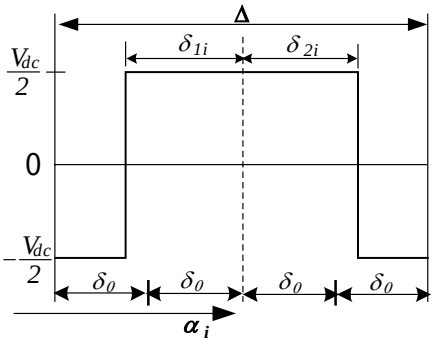

(b)

Fig. 3. Switching pattern of PWM.
(a) PWM (b) switching pulse.

Considering the left-half pulse, the average voltage over this period, V_{1i}, is

$$V_{1i} = \beta_{1i}(0.5V_{dc}) \tag{6}$$

where,

$$\beta_{1i} = \frac{\delta_{1i} - \delta_o}{\delta_o} \tag{7}$$

and V_{dc} is the dc link voltage.

In high switching frequency PWM, the average voltage during a half period of the modulated pulse is proportional to the amplitude of the sine wave V_m at the midpoint of the half pulse. So,

$$\beta_{1i}(0.5V_{dc}) \propto V_m \sin(\alpha_i - \delta_o) \tag{8}$$

When the amplitude of the sine wave is expressed with the modulation index, M,

$$V_m = M(0.5V_{dc}) \tag{9}$$

Then,

$$\beta_{1i} = M \sin(\alpha_i - \delta_o). \tag{10}$$

Similarly,

$$\beta_{2i} = M \sin(\alpha_i + \delta_o) \tag{11}$$

By substituting for β using (7), (10) and (11) are expressed in an alternative form as

$$\delta_{1i} = \delta_o[1 + M \sin(\alpha_i - \delta_o)], \tag{12}$$

$$\delta_{2i} = \delta_o[1 + M \sin(\alpha_i + \delta_o)] \tag{13}$$

If the modulation index is given, the switching instants are determined by (12) and (13).

The switching function is the set of *p* pulses of which level is unity or zero, with modulating angles calculated by (12) and (13). Applying the exponential Fourier series to the *i*-th pulse, the amplitude of its *n*-th harmonic component, C_{ni}, is given by

$$C_{ni} = j(\frac{1}{2\pi n})(e^{-jn\delta_{2i}} - e^{-jn\delta_{1i}})e^{-jn\alpha_i} \tag{14}$$

where "*j*" means an imaginary unit in complex number.

For the p pulses in a fundamental period,

$$C_n = \sum_{i=1}^{p} C_{ni} \tag{15}$$

The harmonic coefficients of the modulated pole voltage are also derived in the same expression as (15) except that the average term is absent and the amplitudes are multiplied by V_{dc}.

IV. ANALYSIS OF DC LINK CURRENTS

Using the harmonic coefficient of the switching function and the pole voltages, the dc link current of the two converters can be found.

A. Derivation of phase currents of inverter

The per-phase harmonic equivalent circuit of the inverter-side is shown in Fig. 4(a). If the amplitude of the *n*-th harmonic component of the pole voltage is denoted by v_n, the corresponding harmonic current i_{kn} is given by

$$i_{kn} = \frac{v_n - e}{Z_{kn}} \cdot e^{-2\pi(k-1)/3} \tag{16}$$

where e is the motor back-emf which is assumed to be sinusoidal, and Z_{kn} is the harmonic impedance to the *n*-th harmonic frequency between terminals of each leg and virtual dc midpoint. The back-emf is expressed as

$$e = E_m e^{j(\omega_e t - \gamma)} \tag{17}$$

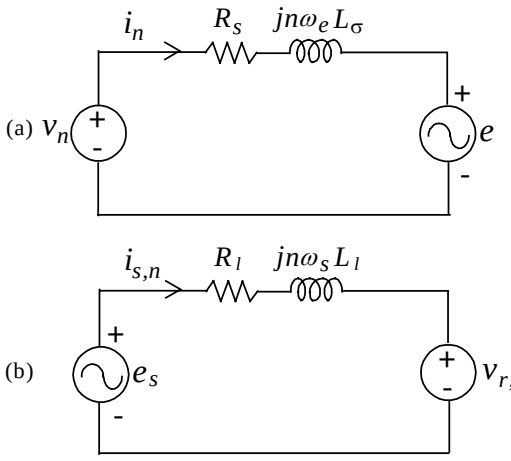

Fig. 4. Per-phase harmonic equivalent circuits. (a) inverter-side (b) converter-side.

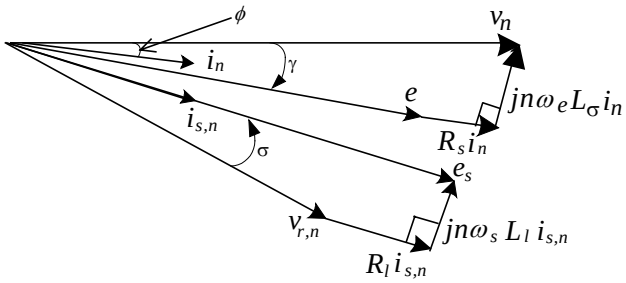

Fig. 5. Phasor diagram for current and voltage.

where E_m is the magnitude of the back-emf, ω_e is the angular velocity of the inverter output frequency, and γ is the angle between the inverter output voltage and the back-emf.

Fig. 5 shows a phase diagram illustrating the relationship between the currents and the voltages, which is referred to Fig. 4. It is assumed that the line-side converter is, as usual, operated at unity power factor and that the motor is operated at lagging power factor. The inverter output voltage is chosen as a reference phasor and the phase of the converter input voltage is adjusted to be equal to that of the reference phasor.

The leg current is given by

$$i_k = \sum_{n=-\infty}^{\infty} (\frac{v_n - e}{Z_{kn}})e^{jn(\omega_e t - \phi)}e^{-jn2\pi(k-1)/3} \tag{18}$$

The last term in (18) means that the three leg currents are displaced by $2\pi/3$ one another.

The sum of all the leg currents is given by

$$i_o = \sum_{k=1}^{3} i_k$$

$$= \sum_{k=1}^{3} \{(\frac{v_n - e}{Z_{kn}})e^{jn(\omega_e t - \phi)} \sum_{n=-\infty}^{\infty} e^{-jn2\pi(k-1)/3}\} \tag{19}$$

If the impedances in all legs are the same, i.e. $Z_{kn} = Z_n$,

(19) can be rearranged as

$$i_o = \sum_{n=-\infty}^{\infty} \{(\frac{v_n - e}{Z_n}) e^{jn(\omega_e t-\phi)} \sum_{k=1}^{3} e^{-jn2\pi(k-1)/3}\} \quad (20)$$

In (20), by a geometric series,

$$\sum_{k=1}^{3} e^{-jn2\pi(k-1)/3} = e^{-jn2/3} \frac{\sin(n\pi)}{\sin(n\pi/3)} \quad (21)$$

The sine quotient in (21) is zero for any integer *n* except when $n = 3s,\ s = 0, \pm 1, \pm 2, \cdots$.

Since the triplen harmonic components cannot exist at the load of the three-phase inverter, (18) is expressed as

$$i_k = \sum_{n=-\infty}^{n=\infty} (\frac{v_n - e}{Z_n}) e^{jn(\omega_e t-\phi)} \cdot e^{-jn2\pi(k-1)/3} \quad (22)$$

where $n \neq 3s,\ s = 0,\pm 1,\pm 2,\cdots$.

B. Derivation of switching function S_k

The switching function S_k is expressed as

$$S_k = \sum_{m=-\infty}^{\infty} C_m \cdot e^{jm\omega_e t} \cdot e^{-jm2\pi(k-1)/3} \quad (23)$$

where C_m is the same as in (15).

C. Derivation of total dc link currents on inverter input side

Substituting (22) and (23) into (2), the total DC link current can be obtained as

$$i_{dcI} = \sum_{k=1}^{3} \{ \sum_{n=-\infty}^{\infty} (\frac{V_{dc} \cdot C_n - e}{Z_n}) \cdot e^{jn(\omega_e t-\phi)} e^{-jn2\pi(k-1)/3} \times \sum_{m=-\infty}^{\infty} C_m e^{jm\omega_e t} \cdot e^{-jm2\pi(k-1)/3} \} \quad (24)$$

where the term of v_n in (22) has been replaced by $V_{dc} C_n$.

By geometric series,

$$\sum_{k=1}^{3} e^{-j2\pi(k-1)(m+n)/3} = e^{-j2\pi(m+n)/3} \frac{\sin \pi(m+n)}{\sin \pi(m+n)/3} \quad (25)$$

Substituting (25) into (24), i_{dcI} becomes zero unless $m + n = 3s', (s' = 0, \pm 1, \pm 2, \cdots)$, where the sine quotient becomes equal to 3. Hence, (24) is simplified to

$$i_{dcI} = \sum_{n=-\infty}^{\infty} \sum_{m=-\infty}^{\infty} 3(\frac{V_{dc}}{Z_n} C_n C_m e^{j((m+n)\omega_e t - n\phi)}) \times \sum_{n=-\infty}^{\infty} \sum_{m=-\infty}^{\infty} 3(\frac{E_m}{Z_n} C_m e^{j((m+n+1)\omega_e t - \gamma - n\phi)}) \quad (26)$$

where, $n \neq 3s,\ s = 0,\pm 1,\pm 2,\cdots, m + n = 3s', s' = 0,\pm 1,\pm 2,\cdots$. Eq. (26) is the general expression for the total dc current in time domain.

On the other hand, the complex exponential form of the Fourier series of i_{dcI} and its *l*-th harmonic coefficient, $\overline{B}_{dcI,l}$, is defined as [11]

$$i_{dcI}(t) = \sum_{-\infty}^{\infty} \overline{B}_{dcI,l} e^{jl\omega_e t} \quad (27)$$

$$\overline{B}_{dcI,l} = \frac{1}{T} \int_0^T i_{dcI}(t) e^{-jl\omega_e t} dt \quad (28)$$

which consists of the complex number. For the complex exponential form of the Fourier series, the magnitude of each harmonic component is obtained by doubling that of the complex coefficient, except for the dc term.

Substituting (26) into (28) and simplifying,

$$\overline{B}_{dcI,l} = \sum_{n=-\infty}^{\infty} \sum_{m=-\infty}^{\infty} 3 \cdot (\frac{V_{dc} \cdot C_n}{Z_n}) \cdot C_m \cdot e^{-jn\phi} \cdot e^{-j2\pi s'} - \sum_{n=-\infty}^{\infty} \sum_{m=-\infty}^{\infty} 3 \cdot (\frac{E_m}{Z_n}) \cdot C_m \cdot e^{-j(\gamma+n\phi)} \cdot e^{-j2\pi s'} \quad (29)$$

where,
$n \neq 3s,\ s = 0,\pm 1,\pm 2,\cdots,\ m + n = 3s', s' = 0,\pm 1,\pm 2,\cdots,$ and $l = 3s'$ are the only nonzero harmonics present.

Eq. (29) is the general expression for the harmonic content of the dc link current in frequency domain. It should be noted that the only harmonic currents present in the dc link of a three-phase inverter are triplen harmonic components.

V. DC LINK CURRENT THROUGH CAPACITORS

The dc link current of the line-side converter is derived just as in (26) except that the back-emf of the induction motor in (17) is replaced by the source voltage as

$$e_s = E_s e^{j(\omega_s t + \sigma)} \quad (30)$$

where, E_s and ω_s are the magnitude and the angular velocity of the source voltage, respectively, and σ is the phase angle between the converter input voltage and the source voltage as shown in Fig. 5. In this case, σ is substituted for $-\phi$ since the source power factor is controlled as unity.

After tedious mathematical manipulation, we can obtain a series of complex coefficients of $\overline{B}_{dcR,l}$ similar to (29) for the PWM converter side. By summing the complex coefficients of the same harmonic components in the two exponential Fourier series and taking the magnitude of each coefficient, the harmonic spectrum of the capacitor ripple currents is obtained.

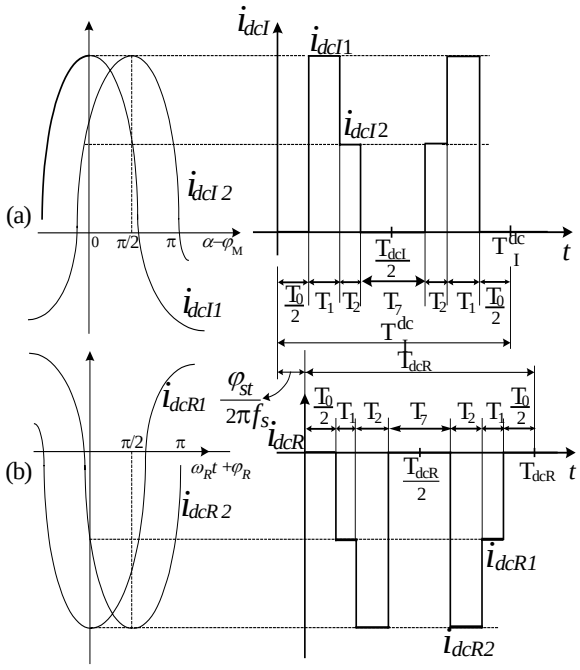

Fig. 6. Relation of phase current and dc link current. (a) inverter side (b) converter side.

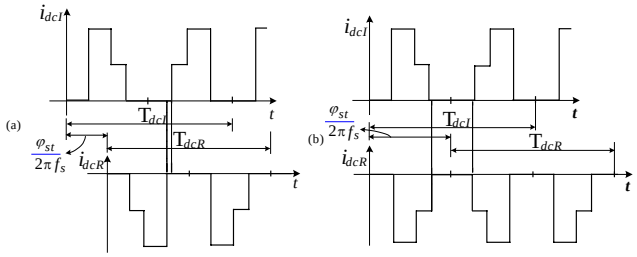

Fig. 7. Superposition of freewheeling states with regard to displacement angle. (a) $\varphi_{st} = \pi/2$ (b) $\varphi_{st} = \pi$.

If the switching frequency of the line-side converter and the motor-side inverter is unequal, the harmonics in the dc link currents are independent of each other and form their own rms values. For the equal switching frequency, the superposition of both the harmonics yields the rms value, which depends on the displacement angle between the switching pulse patterns of both the converters.

In this paper, the switching frequency for the two converters is assumed to be equal. If the displacement angle φ_{st} is not zero, its effect should be considered in summing the two Fourier series, as

$$\overline{B}_{dc,l} = \overline{B}_{dcI,l} + \overline{B}_{dcR,l} \cdot e^{-jl\varphi_{st}} \qquad (31)$$

Finally, taking the absolute value of $\overline{B}_{dc,l}$ in (31) and doubling it, except the dc term, the magnitude spectrum of the dc link capacitor current is obtained.

Fig. 6 shows the relationship between the phase current and the dc link current waveforms in the PWM converter and inverter, which is redrawn from in [10]. What is the displacement angle, φ_{st}, is shown obviously in the figure. Since the magnitude of the capacitor current is the summed amount of the inverter input current and the converter output current, it is seen from Fig. 6 that the current flowing through the dc capacitor becomes less as the superposition of the zero voltage vector duration for the PWM switching state on the both-side converter is larger. The rms ripple current of the capacitor is minimum at $\varphi_{st} = 0, \pi, 2\pi$ since at these angles the superposition duration of the freewheeling states of both converters is maximum. Fig. 7(a) and (b) show the dc current pulse waveforms of the converter and inverter, for example, at $\varphi_{st} = \pi/2$ and π, respectively. At $\varphi_{st} = \pi/2$, the superposition of the freewheeling states is minimum. So, the capacitor ripple current is maximum. In case of $\varphi_{st} = \pi$, the superposition of the freewheeling states is maximum and then the capacitor ripple current is minimum. To minimize the capacitor ripple current, it is necessary to set the displacement angle φ_{st} to $0, \pi, 2\pi$.

VI. ANALYSIS RESULTS AND DISCUSSIONS

The results of the analysis are illustrated by using the MathCAD tool. To verify the validity of analysis, the PSIM simulation has been carried out. The operating conditions of the system are listed in Table I. The dc link voltage V_{dc} is 350[V] and the dc link capacitor is 3300[μF]. The induction motor parameters are listed in Table II.

Fig. 8 (a)-(c) show the current waveforms of the converter output side, the inverter input side, and the dc capacitor, respectively, where the inverter output frequency is equal to that of the source voltage of 60[Hz].

Fig. 9 and 10 show the frequency spectrums corresponding to the dc link currents in Fig. 8, which resulted from analysis and simulation, respectively. Here, the displacement angle was set to zero degree. Both spectrums coincide well with each other, from which the analysis method is proved to be valid.

Table I Operating conditions

	Converter side	Inverter side
R, L	0.02[Ω] 3.3[mH]	induction motor (in Table II)
Power factor	1	0.8
Modulation index	0.95	0.81
Switching/fundamental Frequency	3420/60 [Hz] 57 pulses/cycle	3420/60 [Hz] 57 pulses/cycle

Table II Ratings and parameters of induction motor

3-phase, 220[V], 3 [Hp], 4Poles
$R_s = 0.83[\Omega],\ R_r = 0.91[\Omega]$
$L_{ls} = L_{lr} = 3.25[mH],\ L_M = 166[mH]$

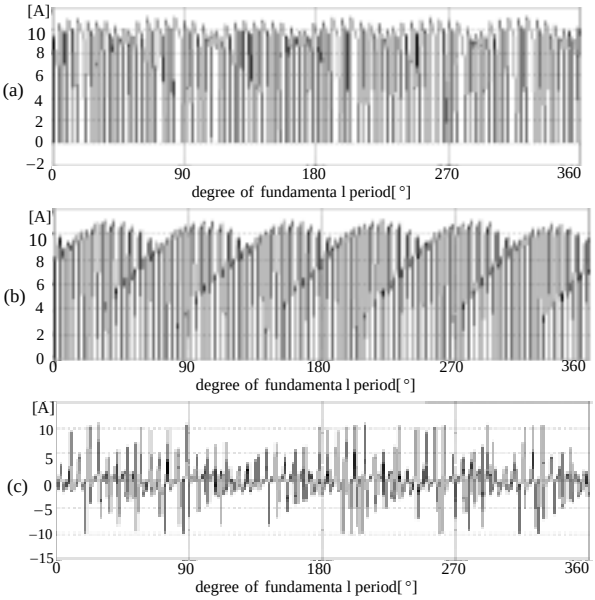

Fig. 8. DC link current waveforms (simulation).
(a) converter output side (b) inverter input side
(c) capacitor current.

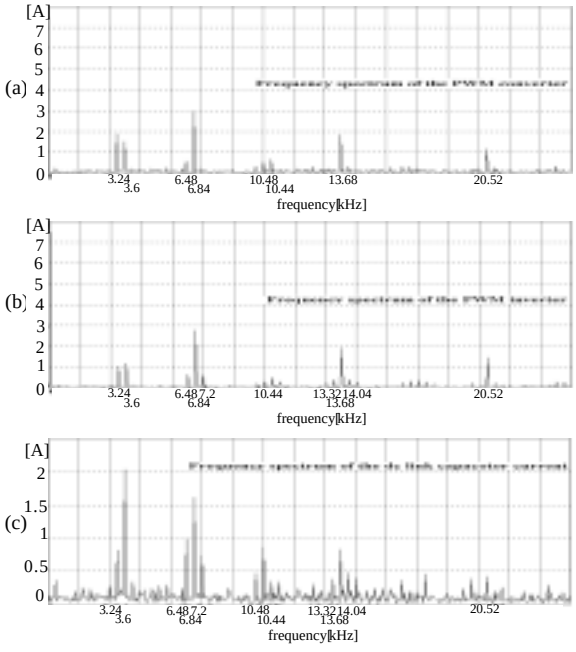

Fig. 9. Harmonic spectrum of dc link currents (simulation).
(a) converter output side (b) inverter input side(60Hz)
(c) capacitor current

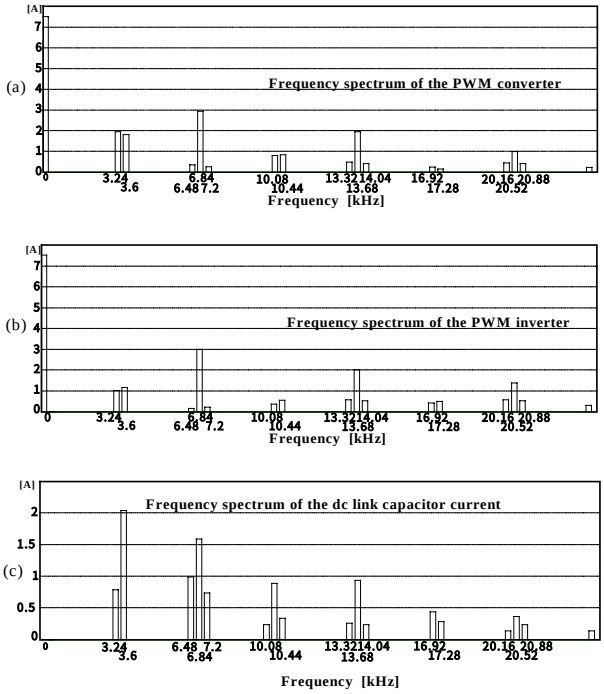

Fig. 10. Harmonic spectrum of dc link current(analysis).
(a) converter output side (b) inverter input side(60Hz)
(c) capacitor current.

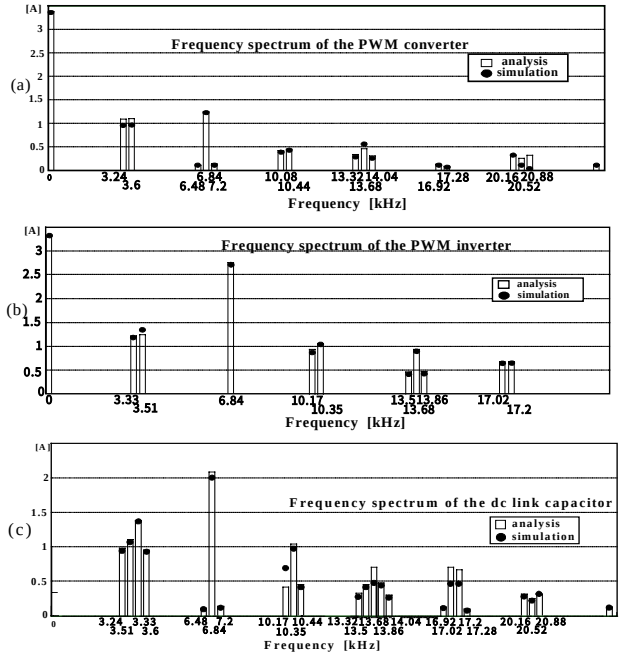

Fig. 11. Comparison of harmonic spectrum of dc currents.
(a) converter output side (b) inverter input side (20Hz)
(c) capacitor current.

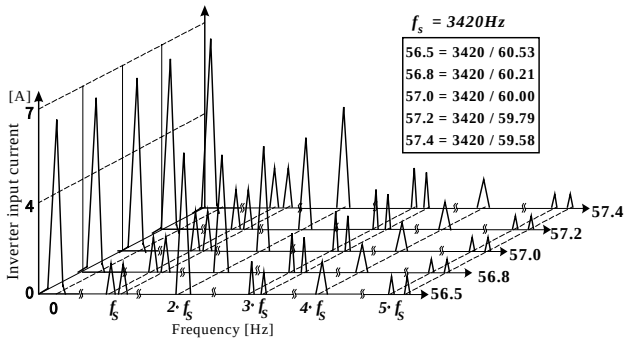

Fig. 12. Harmonic spectrum of inverter input current for asynchronous PWM.

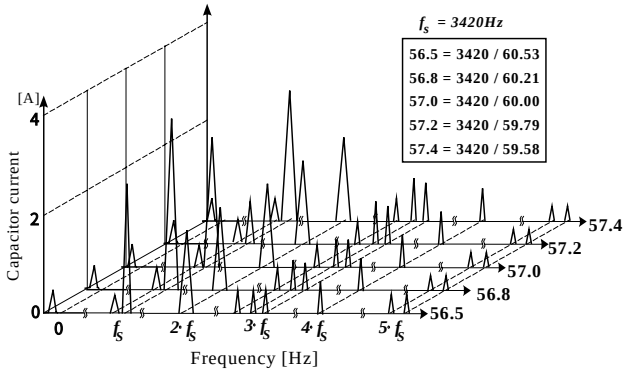

Fig. 13. Harmonic spectrum of dc capacitor current for asynchronous PWM.

Table III Magnitude of harmonic components in inverter-side dc currents

	dc	f_s		$2f_s$	$3f_s$		$4f_s$	$5f_s$	
56.5	6.5	1.9	1.95	3.2	1.1	0.9	1.5	1.1	1.1
56.8	6.5	1.9	1.95	3.2	1.0	1.1	1.8	1.1	1.0
57.0	6.5	1.9	1.95	4.2	1.0	0.9	1.2	1.0	1.0
57.2	6.5	1.95	2.05	4.95	0.9	1.1	1.2	1.1	1.0
57.4	6.5	1.8	1.9	4.5	1.1	1.0	1.2	1.1	1.0

Table IV Magnitude of harmonic components of dc capacitor currents

	dc	f_s		$2f_s$	$3f_s$		$4f_s$	$5f_s$	
56.5	0.5	0.2	2.45	1.2	1.1	1.1	1.1	0.8	0.8
56.8	0.6	0.2	2.45	2.4	1.1	1.4	1.1	1.2	1.1
57.0	0.3	0.4	2.8	3.5	1.2	1.0	1.1	1.2	1.1
57.2	0.6	0.7	2.8	3.4	0.9	1.2	1.1	1.2	1.2
57.4	0.4	0.6	2.9	2.9	0.8	1.6	0.9	0.9	1.2

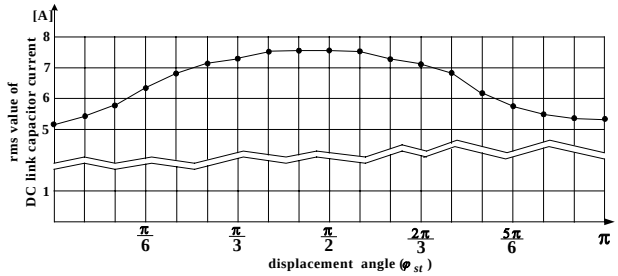

Fig. 14. RMS value of dc link ripple currents as a function of displacement angle φ_{st}.

Fig. 11 shows the comparison of analysis and simulation results for the harmonic spectrums of the dc link currents when the inverter output frequency is changed to 20[Hz]. Even though the inverter output frequency may be different from that of the source voltage, the analysis result is still valid. Thus, the proposed method can be applied to the analysis of the dc link ripple currents for adjustable speed ac drive systems.

Fig. 12 and 13 show the harmonic spectrums of the inverter-side dc current and the capacitor ripple current, respectively, for the asynchronous modulation. Here, the inverter output frequency is varied in four steps from 59.58[Hz] to 60.53[Hz] centered at 60[Hz] and so the frequency modulation ratio is not an integer. For easy comparison, their numerical values are listed in Table III and IV. In the tables, the top row represents the dominant frequency of which side bands are centered at and the most left column represents the frequency modulation ratio. It is observed that a small amount of the dc component exists due to the asynchronous PWM. However, the dc term will be cancelled in the long term since its polarity may be opposite in other cycles. On the whole, the magnitude of the harmonic current is not changed so significantly with the asynchronous modulation since the frequency modulation ratio is as high as about 57. So, the result of the analysis for the synchronous modulation may be applied to the case of the asynchronous modulation without any remarkable loss of reliability.

Fig. 14 shows the rms value of the dc link ripple currents as a function of the displacement angle φ_{st}. As expected, the ripple current is maximum at $\pi/2$, and minimum at 0 and π.

VII. CONCLUSIONS

In this paper, analysis of the dc link ripple currents for the three-phase ac/dc/ac PWM converters feeding ac machines has been proposed. The analysis is based on the switching function of the PWM and the complex exponential form of the Fourier series. The analysis results coincide well with those of simulation. In addition, the effect of asynchronous modulation and the displacement angle on the dc link current has been investigated. The

proposed analysis method for the dc link ripple current is useful for specifying the capacitor and for predicting the lifetime as well as for understanding analytically the PWM switching operation.

REFERENCES

[1] F. Kamran and T. G. Habetler, "A novel on-line UPS with universal filtering capabilities," *IEEE Trans. on Power Elec.*, vol. 13, no. 3, pp. 410-418, 1998.

[2] H. Fujita and H. Akagi, "The unified quality conditioner: the integration of series and shunt active filters," *IEEE Trans. on Power Elec.*, vol. 13, no. 2, pp. 315-322, 1998.

[3] R. Pena, J. C. Clare, and G. M. Asher, "Doubly fed induction generator using back-to-back PWM converters and its application to variable speed wind-energy generation", *IEE proc.-Electr. Power Appl*., vol. 143, no. 3, pp. 231-241, 1996.

[4] J. W. Dixson, A. B. Kulkarni, M. Nishimoto, and B.-T. Ooi, "Characteristics of a controlled-current PWM rectifier-inverter link," *IEEE Trans. on Ind. Applicat.*, vol. 23, no. 6, pp. 1022-1028, 1987.

[5] M. L. Gasperi, "Life prediction model for aluminum electrolytic capacitors," *IEEE IAS Conf. Rec.*, pp. 1347-1351, 1996.

[6] M. L. Gasperi, "A method for predicting the expected life of bus capacitors," *IEEE IAS Conf. Rec.*, pp. 1042-1047, 1997.

[7] P. A. Dahono, Y. Sato, and T. Kataoka, "A novel method for analysis of inverter currents," *IEE PEVDS proc*., pp. 407-412, Oct., 1994.

[8] P. A. Dahono, Y. Sato, and T. Kataoka, "Analysis of ripple components of the input current and voltage of PWM inverters," *Int. J. Electronics*, vol. 80, no. 2, pp. 265-276, 1996.

[9] P. D. Evans and R. J. Hill-Cottingham, "DC link current in PWM inverters," *IEE proc.-Electr. Power Appl.*, vol. 133, no. 4, July, 1986.

[10] L. Sack, "DC link current in bidirectional power converter with coordinated pulse patterns," *EPE proc*., in *Trondheim*, pp. 239-244(vol. 4), 1997.

[11] W. D. Stanley, *Network Analysis with Applications.*, NJ: Prentice-Hall, 1993.

Integration Possibilities in Ballast Design

M. Radecker, A. Knoll, F. Bisogno
Fraunhofer-Institut für
Autonome intelligente Systeme AiS
Sankt Augustin, Germany

Mario Pacas
Institute for Power Electronics and
Electrical Drives
University of Siegen, Germany
jmpacas@ieee.org

Abstract—**Integrated circuits for electronic ballasts are a growing market today. Driven by the telecommunication industry, powerful technologies have been developed to handle both, the large scale integrated signal processing and the power stage driving and control. These technologies are delivering the fundament for IC solutions, which meet both, the cost requirements of ballasts, as well as the aiming at miniaturization. Special custom integrated solutions make sense for high-end comfort ballasts with extended signal processing. For the mass market, a modular system is desirable, which allows the flexible change of product characteristics. The paper gives an overview of ongoing developments and future trends in this area.**

I. INTRODUCTION

The growing demand for ballast integration concepts is a result of tasks faced in ballast design:

- different features are hard to implement by using discrete components in a modular concept of a ballast family
- miniaturization requires a low number of discrete components and a reduction of the PCB-board area
- some features can only be implemented utilizing integrated solutions (high-performance dimming, digital interface)

Today's ballasts show three suitable parts for integration:

- The power stage for lamp driving
- The power stage for PFC (and possibly the input rectifier)
- The control and driving of power
- The Interface and signal processing functions

Fig. 1 shows a typical block diagram of concepts and components for integration. This diagram is applicable for the wide spread low pressure fluorescent lamp ballasts (FLB), for the HID ballasts, and for the halogen lamp ballasts, regarding line applications (230V and 120V AC). However, it makes sense to design different integration concepts for different ballast families. The FLB families can be divided into:

- Compact fluorescent lamp ballasts (B1)
- Non dimming external ballasts (B2)
- Dimming external ballasts (B3)
- Controls (for ballast interfaces) (B4)

Another important criterion is the power level of the ballast. It shall be made the following distinctions for line ballasts:

- low power ballasts (< 30 Watts) (P1)
- medium power ballasts (<70 Watts) (P2)
- high power ballasts (> 70 Watts) (P3)

So the integration task has to be examined under the above mentioned diversity of systems [1].

II. TOPOLOGIES, TECHNOLOGIES AND CONCEPTS

In the following only line-powered ballasts are considered. Battery powered and low voltage input ballasts often consist of a push-pull power stage combined with an input boost stage [2]. The consideration of suitable topologies for integration in line-powered ballasts leads to single stage and dual stage concepts [3].

Single stage topologies can be used for low cost solutions with PFC, but they can hardly enable the dimming feature down to brightness of 1 %. Besides, dimming combined with bus voltage limiting, preheating and ignition control might require additional auxiliary circuits in a single stage ballast, which provides PFC from the lamp power stage [4]. Providing the PFC option, a single stage ballast is well suited, using a driver IC for fault protection. Preheating and ignition control can be implemented with moderate expense. The bus voltage does not need to be higher than in dual stage ballasts because the voltage stress of the power transistors is the same [4].

When a half-bridge topology is used for the power stage, two n-channel transistors need a high-side driver. The combination of one n-channel and one p-channel transistor (mixed transistor type) allows a low side driver only [5]. The mixed transistor type stage has the disadvantages of the different gate capacitances of the transistors and of a larger chip area of the p-channel type. Besides, the combination of driver IC's in dual stage ballasts with a mixed transistor type half bridge is not simple and requires the high-side option.

Alternatively, a single transistor power stage can be used with a low-side driver. It has the disadvantage of an excessive voltage over the transistor, which leads to high blocking voltages of 4 to 5 times the maximum line input voltage. As a result switches with blocking voltages of 1000V or 1600V for the single transistor topology are necessary, compared

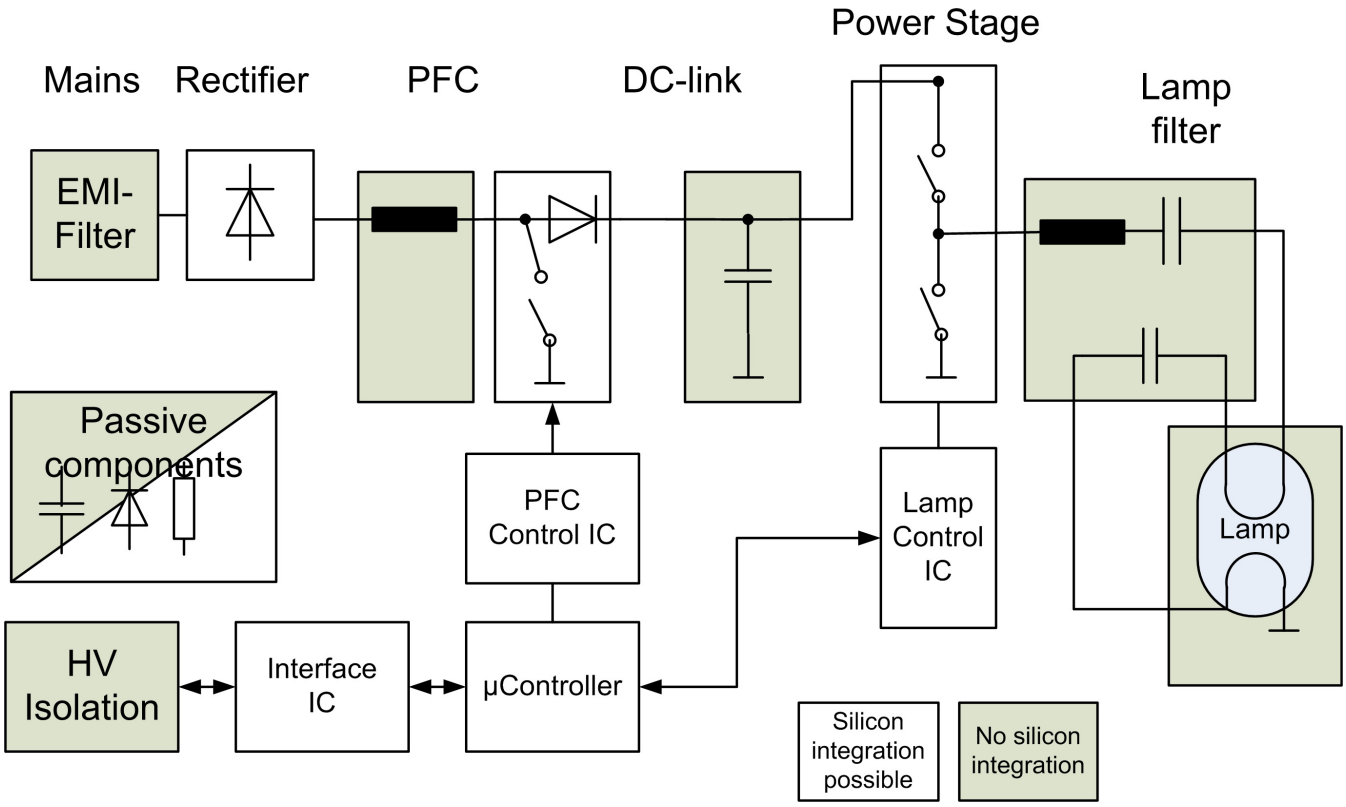

Fig. 1. Different parts and functions of a ballast and possible integration on silicon

to only 500 V to 650 V for the half-bridge topology in line applications of 230V AC. Table 1 shows different combinations of power transistors, topologies and driver technologies with their respective advantages and disadvantages. By using the most common high-side drivers, combined with a n-channel MOSFET half-bridge, there is a choice between „genuine" high-side technologies and chip-on-chip, or chip-by-chip solutions, respectively. When both, the high-side driver IC and the low-side driver IC are designed in low-voltage technology, a blocking voltage of only 15 V to 30 V is sufficient for the driver transistors. Such drivers are available today in sub-micron technologies, down to a quarter-micron technology. The packaging of chip-on-chip solutions with bidirectional data transfer between the low side and the high-side driver chip is not simple, but it can be handled today for reliable solutions

This solution presented by Knodgen in [6] makes sense for driver ICs for B2 and B3 ballasts and for all power levels P1 to P3, when a modular concept is used as it is shown in Fig. 1. For the modular concept the dual stage topology has some advantages, because some of the P1 ballasts do not need PFC. The control IC can then be provided in two versions, one version with PFC driver and one version without PFC driver (e.g. the IR215x and IR216x series). In a single stage topology, the driver IC must include the PFC function, which makes it more difficult to use a simple phase control concept for dimming ballasts [7]. For P3 ballasts external driver ICs should be combined with discrete power transistors. Integration of the power transistors together with the driver ICs at one chip is usual up to power levels of 70 Watts (P1 and P2). Therefore an SOI technology is proposed, due to its minimized space for voltage blocking structures, compared to junction isolation. It is possible to integrate the PFC power transistor, the half-bridge transistors, and the needed driver and control circuits at one chip (Fig. 1): PFC IC and Lamp Control IC, integrated with PFC and Lamp power stage, including the bridge rectifier [6]).

For designing a dimming ballast B3, even the microcontroller can be integrated in SOI technology [6]. The so-called „resurf technique" for the lateral MOS power transistors up to 650 V blocking voltage offers the opportunity of a small active silicon area, which is smaller than that of discrete standard vertical power MOSFET. Such full-integration concepts are limited by the power losses, which have to be handled by the heat sink on the housing. Losses of more than 0.5 Watts in one component may cause problems due to the excessive temperatures of 80 to 100°C inside of the ballast. Heat spreading is usual for power levels higher than 70 Watts, regarding the inductors of the PFC boost converter, as well as the resonant inductors for multi-lamp ballasts. Using discrete transistors for the half-bridge, a useful heat spreading is provided between them (P3). A small silicon area can be achieved when a so-called Cool-MOS technology is used [8]. Unfortunately, these vertical transistors are not well suited for complete

integration. On the other hand, bipolar technology require excessive base driving current, and may be used only in combination with serial MOSFETS, better known as BIMOS technology devices, when a driver IC is applied [6].

For a single transistor power stage, a MOSFET is mostly not efficient, because of its high blocking voltage. This results in larger chip area, compared to the half-bridge transistors. For higher voltage levels a new generation of IGBTs should be used [9]. Due to the fact that the tail current is negligible even for low current levels of about 1.0 A, switching frequencies of 30 to 100 kHz should be reached without significant dynamic losses in ballast applications. For the single transistor power stage, a low side driver is required only. However, the additional size of the resonant inductor and the high voltage resonant capacitor in a simple class-E topology should not result in higher costs, compared to the half-bridge topology. This can be achieved because of reduced packaging costs.

For high-performance applications the half-bridge, combined with a PFC boost converter, is the most usual concept. The symmetric half-bridge helps to adjust the nominal lamp power (100%), and power levels down to 1%, by simple trimming. If the trimming is done by a digital IC concept, a low number of external components will be possible. For a class-E topology, as it was shown in [10], high-performance dimming is hardly possible, when using analog concepts, due to the complexity of control. For partial dimming ballasts, or for button switched different levels of brightness, analog technique is sufficient. From Table 1 it can be summarized, that low-cost concepts tend to single-stage PFC ballasts without dimming, at least including fault protection. Low-cost concepts for partial dimming -with or without PFC- may tend to a single-switch topology e.g. class-E inverter, combined with a boost converter. High-performance dimming ballasts -with or without PFC- make use of the n-channel MOSFET half-bridge, combined with a boost converter. Then, of course, interface ICs can be added separately (B4) [6]. Finally, for low-cost concepts without PFC, the n- and p-channel half-bridge is well suited, requiring only a low-side driver. Other topologies are less suited for integration, due to a restricted performance in one or more of the following features:

- low crest factor
- high power factor
- dimming
- fault protection, restart
- preheating and ignition control - sufficient line filtering
- end-of-life-, brown-out-protection, frequency variation, low number of passive elements, transformer-less topology
- low voltage and low current stress of transistors and passive components.

New opportunities are less given by new topologies, but by new technologies of the ballast components, including the light source itself. The substitution or elimination of the inductors and transformers in ballasts is highly desired due to the possible size and weight reduction. Therefore, the introduction of piezo-electric transformers (PT) will lead to acceptable size reduction at even low costs. Because of the non-dimming and instant-start behavior of such PT ballasts, the applications are restricted to special markets. Further, the expected cost reduction of LEDs will provide an alternative in the next years, as it is already to be seen in the automotive market. Summarizing, we can state that new components technologies always open the door to new topologies and driving solutions.

III. CONTROL STRATEGIES FOR DMMING BALLASTS

As already described, the functionality of a ballast may be very different, depending on the market sector and on the power level respectively. For achieving the dimming performance, usual control strategies for half-bridge and for single-transistor ballasts are shown in Table 2. It can be seen that analog concepts are well suited for optimum high-performance dimming, if phase control is implemented [7]. The external trimming needs more expense for analog ICs than for digital ones. For high-performance dimming, a digital concept is recommended, if the number of external components should be minimized and if different lamp types are chosen for one ballast type.

IV. THEORETICAL COMPARISON OF CONCEPTS

There are two well-suited topologies for dimming and for power control of a line ballast. These are the half-bridge and the class E converter, which was introduced by N. O. Sokal in 1975 [11]. Even if the half-bridge is an optimum topology regarding the voltage stress and the size of resonant components, a theoretical comparison is of interest because the single-transistor solution leads to cost-effective solutions as fast high-voltage IGBTs and low-cost low-voltage technologies are available. For this purpose, an average transfer function analysis was made for both, the half-bridge, and the class E converter. The circuits are shown in Fig. 2 and Fig. 6, respectively. The fundamentals of the description of load resonant converters by average transfer functions can be found in [12]. The approach is based on wide-range parametric analysis including the parameters D (duty-cycle), the normalized frequency a, and the load factor Q, as defined in Eq. (1).

Derived from a simple series resonant circuit, driven by a sinusoidal AC supply an average static transfer function $\frac{R_L}{R_{dc}}$ can be defined, which represents the average value of the static transfer function, when the parameters are changed within a wide range.

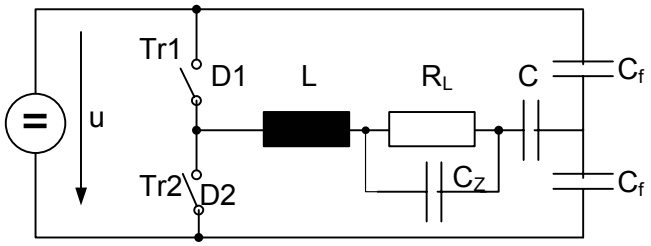

Fig. 2. Class D half-bridge converter

It can be shown, that for specific parameter constellations there is only a slight change of the static transfer function. Other parameter constellations lead to extreme changes of the static transfer function, when only changed slightly. Neglecting C_Z, and assuming $C_f = \infty$ and defining:

$$D = \frac{t_{on}}{T}; \quad a = \frac{f_{res}}{f} = \frac{\omega_{res}}{\omega}; \quad Q = \frac{1}{R_L}\sqrt{\frac{L}{C}} \tag{1}$$

where f is the operating frequency and f_{res} is the series resonant frequency an average static transfer function for a half-bridge can be derived as:

$$\left.\frac{R_L}{R_{dc}}\right|_{predict} = \frac{(2D)^2}{\frac{2}{\nu} + \frac{k}{2}} \tag{2}$$

$$\nu = a\left(D - \frac{1}{4\pi}\sin(4\pi D)\right); \quad k = 2Q + 1 \tag{3}$$

The results of this approach are shown in Fig. 3, Fig. 4 and Fig. 5, where frequency and duty-cycle are the parameters influencing the load power taking into account the wide range of change of the values of the elements R_L, C, and L. In this approach, the capacitor C_Z is neglected in lamp burning mode. For dimensioning the dimmable class-D half-bridge converter a more exact solution has to be used. In case of dimming, the load factor Q, including the blocking capacitor C from Fig. 2 is not of interest, because Q is always within a range of 1.0< Q <2.0. By neglecting the filament resistance of the lamp and assuming a large value of capacitor C, the following complex expression can be derived [7]:

$$\frac{R_L}{R_{dc}} = \frac{0.25(1 + j\omega R_L C_Z)}{(1 + j\omega R_L C_Z)\left(1 + \frac{j\omega L}{R_L}\right) - j\omega R_L C_Z} \tag{4}$$

At 100% lamp power the value of $j\omega R_L C_Z$ can be neglected and the lamp current can be adjusted by choosing the inductor value L for a given minimum frequency $\omega = 2\pi f$.

For dimming, C_Z has to be taken in account; it has to be large enough to ensure sufficient filament current at higher frequencies. Otherwise, the lamp could extinguish in dimming mode. To prevent the lamp from overheating and from degrade lamp life in dimming mode, an increasing lamp voltage has to be considered, due to the negative incremental lamp impedance [7].

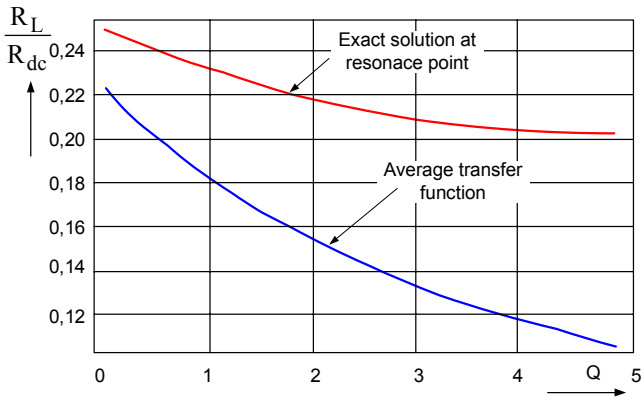

Fig. 3. Average transfer function of a class-D half-bridge converter a=1 and D=0,5

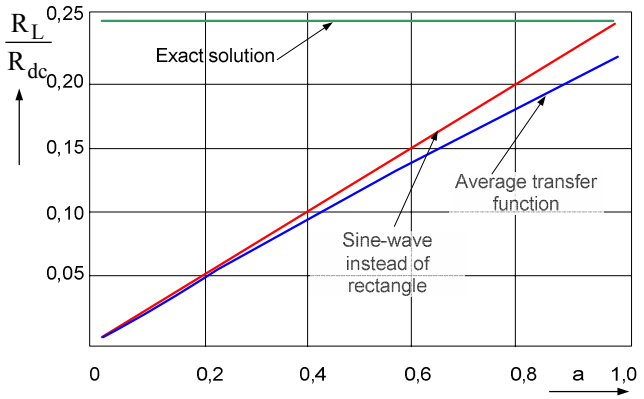

Fig. 4. Average transfer function of a class-D half-bridge converter a=1 and D=0,5

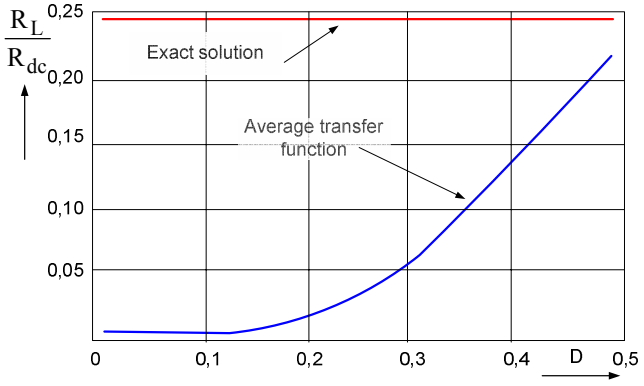

Fig. 5. Average transfer function of a class-D half-bridge converter Q=0 and a=1

Because of the symmetrical topology of a half-bridge, dimming is possible by using a phase-control technique, as it is described in [7]. Other dimming concepts should be similar, and the filament current has to be detected in any operation mode. Future generations of integrated solutions should have the opportunity to calculate lamp parameters during operation as lamp voltage-current-curves and the filament resistance, to ensure a sufficient heating performance. Long-term effects and errors due to tolerances can be partially handled by chip-internal adjustment and calculation. If a

single-transistor concept is used for integration, dimming should be possible as well. From the approach of an average transfer function for the class-E converter the characteristics depicted in Fig. 7 can be calculated.

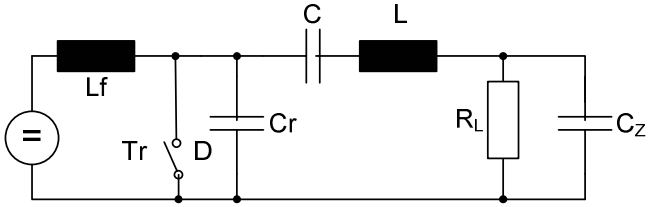

Fig. 6. Class-E Converter (N. Sokal)

With (1) follows for this topology

$$\left.\frac{R_L}{R_{dc}}\right|_{predict} = (2D)^2\left(\sqrt{z^2+\frac{1}{2\nu^2 k}}-z\right) \tag{5}$$

$$\nu = \frac{2\cos^2(\pi D)+1}{(\cos(\pi D)+1)^2};\quad z=\frac{1}{2}(1+\frac{1}{4\nu^2}) \tag{6}$$

$$k = \frac{1}{2}(1+\frac{1}{2Q+1}) \tag{7}$$

This „parametric" or „predictive" transfer function, here called average transfer function, shows only a slight dependence on the load factor Q, which is not shown in the diagram. A low value of Q should be chosen. The maximum transistor voltage will be slightly decreased, and the normalized current stress of the blocking capacitor C is lower [13]. On the other hand, there is a higher amount of harmonics, compared to the half-bridge, due to the asymmetric topology. Increasing Q means fewer harmonic at the load, but does not result in significant reduction of the input current harmonics.

For PFC a pre-converter is recommended. As an alternative, similar AVF circuits are suitable as for the half-bridge (AVF=Active Valley Fill). It was shown in [14] that a good estimation of the real static transfer function can be found empirically for low Q values, when a transistor-current control is used [10]:

$$\frac{R_L}{R_{dc}} = \frac{D\cdot R_L}{2\cdot f\cdot L_f} \tag{8}$$

Equation (5) is only valid for transistor current control, adjusting approximately constant output power, independent of the input voltage. For low values L_f of the smoothing inductor, the input current is changing between zero and maximum, due to the appropriately chosen current reference function. For dimming it is possible to increase the frequency f starting from each point of the input voltage level [10]. This solution -compared to the voltage-fed half-bridge- allows dimming concepts without regulation of the DC bus voltage. Even for universal input, this concept would be applicable. Unfortunately, due to the asymmetric lamp current, a simple phase control is not sufficient for dimming down to low power levels. It has to be a more complex combination of lamp current detection in both directions and of the transistor-current control, which will allow a high-performance dimming concept. Nevertheless this topology has the potential for integration because of its parameter-independent-behavior over a wide input voltage range, regarding resonant inductor L and capacitor C_r [14].

V. TOPOLOGIES WITH PIEZO-TRANSFORMERS

Recent developments in the area of Piezo-transformers are very promising and make this technology attractive for new designs and applications. Power supplies with Piezoelectric Transformers (PT) allow size and cost reduction in many low power applications, such as CCFL backlighting inverters, DC to DC converters and off-line power supplies. Therefore they can also be taken into consideration for the integration of ballasts. As an emerging technology several aspects have to be examined especially the suitable topology to be used.

In [15] a complete parameter analysis is provided to optimize both, the PT, and the converter topology, mainly for step-down off-line applications. The most suited topologies for high voltage input (85 to 260 V) are the half-bridge and the class-E. Typical output voltages of 1 V to 60 V, combined with power levels between 1 and 100 Watts, are achievable with today's PT Transoner®-type technology. So, the Class-E converters results to be suitable for low power levels, using a PT at low expense, due to the only required low-side driving. On the other hand the half-bridge, requiring an expensive high-side driver, is suited for larger power levels where efficiency becomes more important for size reduction. The input inductor of class-E, considered as a "bulky" component in the past, can be reduced to small sizes, at high input voltages.

VI. CONCLUSION

For medium requirement up to high-end systems, the half-bridge topology is now and in the next future the most suitable one for the implementation in silicon. Besides the dimming and safety control can easily be realized in a robust way.

The results concerning piezo transformers lead to the conclusion that for miniaturized systems the load side can be equipped with a piezo transformer. This system is especially attractive for the substitution of conventional ballast by electronic ones as it is necessary due to the new European regulations. The aspect of flatness should also be considered as piezo transformers allow flat miniaturized power supplies.

One aspect not considered in this paper will become very important in the next time. The application of LED in automotive applications is a growing one, so it can be expected that the importance of LEDs in general lightning applica-

tions will grow in the near future. Here piezo transformers are a very attractive solution due to their EMI characteristics, their high efficiency and their size.

REFERENCES

[1] M. Radecker, F. Dawson:Ballast on a chip; Realistic expectation or technical disillusion, IEEE Industry Applications Magazine , Jan/Feb 2004

[2] F. Goodenough: „IC molds Power for LCD's Backlit Fluorescent Lamp", Electronic Design, No. 43, July, 8th 1993

[3] Böhme, Frank: Elektronische Vorschaltgeräte für Niederdruckentladungslampen, Diss. University of Dresden, Germany,2001

[4] H. Güldner, K. Lehnert, F. Bohme, F.Raiser: „Principles of Electronic Ballasts for Fluorescent Lamps - an Overview", IEEE Proc., PESC'99, pp. 19-25

[5] L.R. Nerone: „A Complementary Class D Converter", 1998 IEEE IAS Annual Meeting, St. Louis, IEEE Proc., pp. 2052-2059

[6] 1999 IEEE IAS Annual Meeting, Panel Session: „Ballast-on-a-Chip: Realistic Expectation or Technical Delusion ?", Phoenix, AZ, U.S.A., Oct., 6th 1999

[7] T.J. Ribarich, J.J. Ribarich: „A New Control Method for Dimmable High-Frequency Electronic Ballasts", 1998 IEEE IAS Annual Meeting, St. Louis, IEEE Proc., pp. 2038-2043

[8] L. Lorenz, et al: ‚COOL MOS from SIEMENS", Internal Report, Siemens, from March, 27h, 1998

[9] M. März, A. Knapp, M. Billmann:„Schnelle 600-V-IGBTs als MOSFET-Alternative fur Schaltfrequenzen bis uber 300 kHz", elektronik industrie 5 - 1998, pp. 28-32

[10] M. Radecker, Y.-L. Nguyen: „Application of Single-Transistor Smart-Power IC for Fluorescent Lamp Ballast", 1999 IEEE IAS Annual Meeting, Phoenix, AZ, IEEE Proc., pp. 262-268

[11] N. Sokal, A. Sokal: " Class E- A New Class of High- Efficiency Tuned Single-Ended Switching Power Amplifiers", IEEE Journal of Solid State Circuits, Vol. SC-10, Nr. 3, June 1975

[12] M. Radecker: "Effiziente Berechnung and Entwicklung energieubertragender Systeme", Thesis, 1999, Technische Universitat Chemnitz

[13] M. Kazimierczuk, K. Puczko: „Exact Analysis of Class E Tuned Power Amplifier at any Q and Switch Duty Cycle", IEEE Trans.on Circuits and Systems, Vol. CAS-34, No. 2, Febr. 1987, pp. 149-159

[14] Radecker, M.: "Integrated circuit design and application for electronic ballasts", IEEE IAS Annual Meeting Conference Record, Rome 2000

[15] F.E. Bisogno, M. Radecker, A. Knoll et.al.: Comparison of Resonant Topologies for Step-Down Applications Using Piezoelectric Transformers, Proceedings of the PESC04 Aachen, 2004

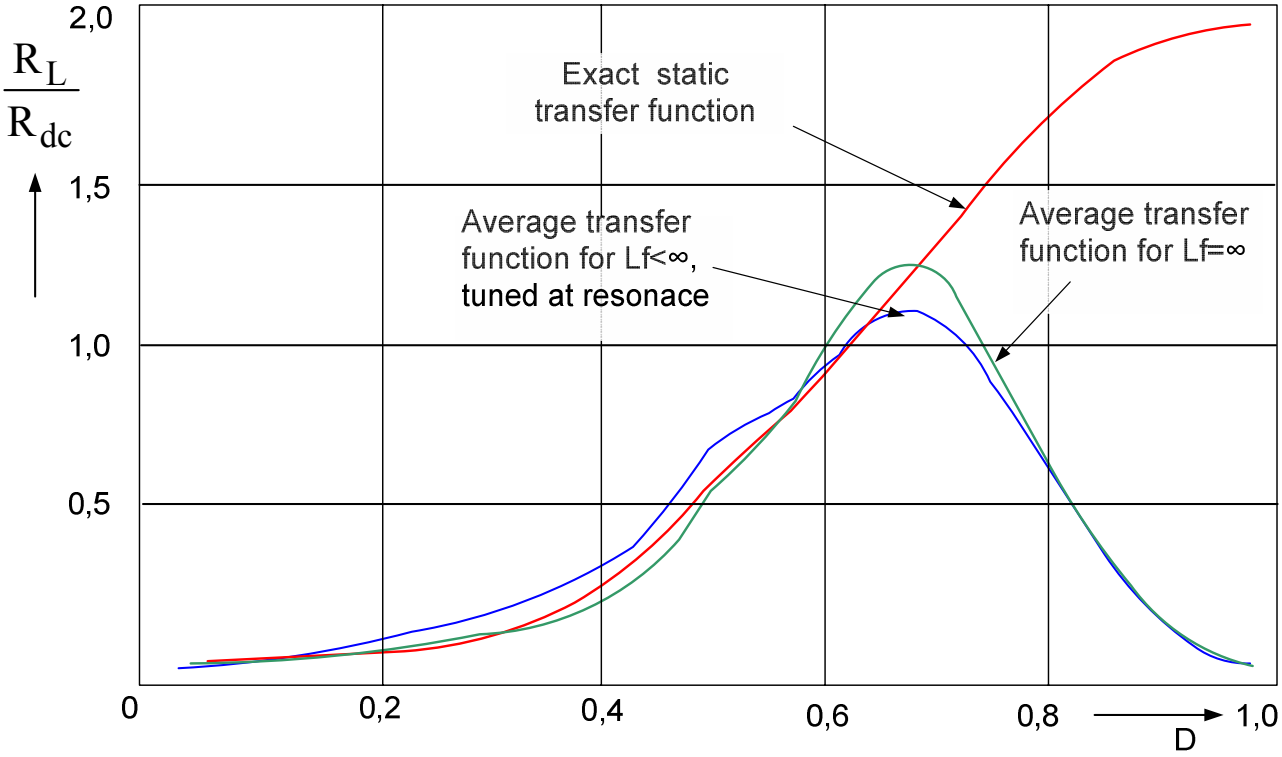

Fig. 7. Average Transfer Functions of a Class-E Converter for Q = O

TABLE 1: ADVANTAGES (+) AND DISADVANTAGES (-) OF TOPOLOGIES AND TECHNOLOGIES

	Topology				
	Power Stage (Lamp)			PFC Stage (Pre-Converter)	
	Half-Bridge		Single-Transistor	Boost-Converter	Single-Stage Ballast (AVF)
Power Transistors	2 n-channel Mosfets	1 n-+ 1 p-chan. Mosfet	IGBT, or BIMOS	1 n-channel Mosfet	-
Blocking Voltage for an input of 230V AC	500 ... 650 V	500 ... 650 V	1200 ... 1600V	500 ... 650 V	-
Driver - IC	High-Side and Low-Side	Low-Side	Low-Side	Low-Side	-
Technology of Driver- IC + and -	- Low-scaled High-side + Single-chip - Chip-by-chip solution + High-scaled Low-side (2 chips)	- combination with Boost Converter not simple + Only one Low-side chip	+ Only one Low-side chip	+ Only one Low-side chip	-
Ballast Features + and -		- additional losses at p-channel Transistor	- additional losses at transistor + wide input voltage range	+ PFC	- no advanced dimming + PFC
Passive Components + and -			- larger inductor size - larger voltage stress		- advanced line filter - additional inductor and capacitors

TABLE 2: COMPARISON OF CONTROL STRATEGIES FOR DIMMING BALLASTS

	Half-Bridge		Single-Transistor	
	Phase-Control	Additional Frequency-Control and Voltage-Control possible		Frequency-Control
Dimming Performance	Optimum up to approx. 1 %	Optimum up to approx. 1 %	Possibly up to approx. 1 %	Optimum up to approx.. 10
Control IC Concept	Analog High-Side and Low-Side, 1.0 to 5.0 µm Technology	Digital High-Side and Low-Side, 0.25 to 0.8 µm Technology	Digital Low-Side, 0.25 to 0.8 µm Technology	Analog Low-Side, 1.0 to 5.0 µm Technology
External Trimming	Medium Number of Components	Low Number of Components	Low Number of Components	Low Number of Components

Improved Adaptive Predictive Filter for Generating Reference Signal in Active Power Filters

Byung M. Han, Byong Y. Bae, Seung T. Baek
Department of Electrical Engineering, Myongji University,
South Korea
Email: erichan@mju.ac.kr

Abstract— **The performance of an active power filter (APF) depends on the inverter characteristics, applied control method, and the accuracy of the reference signal generator. The accuracy of the reference generator is the most critical item in determining the performance of active power filters. This paper introduces an efficient reference signal generator composed of an improved adaptive predictive filter. The performance of the proposed reference signal generator was first verified through a simulation with MATLAB. Furthermore, the application of feasibility was evaluated through experimenting with a single-phase APF prototype based on the proposed reference generator, which was implemented using the TMS320C31 floating-point signal processor. Both simulations and experimental results confirm that our reference signal generator can be used successfully in practical active power filters.**

I. INTRODUCTION

Harmonic current generated in the non-linear load is a remarkable issue, as more power electronic equipment have come into wide use in offices and factories. The distortion of terminal voltage in the power system due to the harmonic current brings about over-heating and vibration problems of power devices connected to the power system. Thus, the harmonic current causes degradation of power devices and faults in the power system [1].

An active power filter is a power electronic device used to effectively eliminate the harmonic current generated by non-linear loads. The operational principle of the active power filter is to inject a harmonic current with the same magnitude and a 180-degree phase shift in parallel with the load, so that the source can supply the fundamental component of a load current only. The performance of an active power filter depends on the extraction method for the current reference signal, the control method for the harmonic current, and the dynamic characteristic of the related inverter [2]. A comprehensive review of active power filters is available in reference [7].

One method in extracting the current reference signal from the load current is to make the load current pass through a notch filter. Another method is to obtain the reference signal by means of the instantaneous power theory through the rotational coordinate transform. The weak point in using the notch filter is the inherent phase shift. This phase shift can bring about an enormous performance degradation of the active power filter. In the case that the instantaneous power theory is used, it is required to detect the load current, source voltage, and injecting current from the active power filter, as well as perform the complicated coordinate transform. Also, this method requires a lowpass filter to remove the fundamental component from the transformed load current [4], [6].

The adaptive predictive filter under consideration was first introduced by Väliviita and Ovaska for generating the current reference signal without a phase shift for the active power filter application in 1998 [5]. Their paper proposes a multi-stage reference signal generator composed of a fixed pre-filter, adaptive predictive filter, peak detector, and a Lagrange interpolator. It also demonstrates the performance of the proposed scheme that was evaluated through computer simulations with MATLAB. However, it only deals with the performance of the reference signal generator based on simulation results within a short time period of 2 seconds. Moreover, it does not present any experimental performance analysis of an active power filter (prototype) using the proposed reference signal generator.

In order to evaluate the feasibility of the above reference signal generator, the present authors verified its performance using the TMS320C31 digital signal processor and C programming language. According to our verification results, the reference signal extracted from the load current using the proposed reference signal generator has practically no distortion up to 2 or 3 seconds. However, it has severe harmonic distortion after a lapse of 20 seconds. Consequently, it is verified that the proposed reference signal generator cannot be applicable for any active power filter as it is. The principal reason for this unexpected behavior is the common weight-drift problem of the standard LMS algorithm [8].

To fix the undesired behavior of the original reference generator [5], the present authors modified the algorithm block of the adaptive predictive filter in the reference signal generator and added an algorithm block of magnitude correction. The performance of an improved reference signal generator was first analyzed by means of a simulation with MATLAB. Moreover, it was verified by implementing an algorithm programmed by C language in the TMS320C31 DSP. In order to evaluate the feasibility of practical application, hardware models of the entire active power filter and a single-phase diode rectifier were built and connected together for experimental analyses.

II. ACTIVE POWER FILTER

The basic function of active power filters is to attenuate the harmonic components of the load current supplied to the non-linear load. The operational principle and system configuration of the active power filter was proposed first by Gyugyi and Strycula in 1976 [1]. Furthermore, a comprehensive study was performed by Akagi *et. al.* in reference [2]. Such an active power filter can be connected to the load in parallel or in series, but typically, it is connected in parallel as shown in Fig. 1.

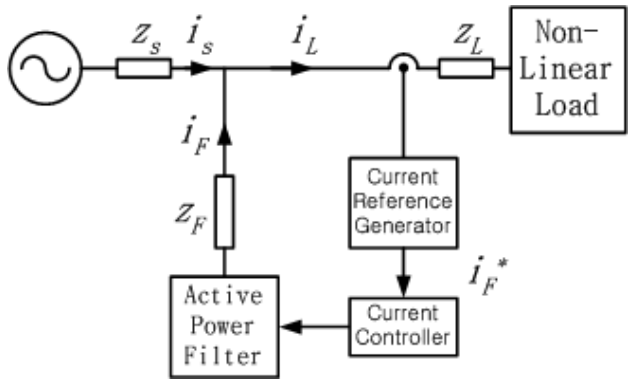

Fig. 1 Parallel-type active power filter

The active power filter provides a current of the opposite magnitude and the same phase angle with the harmonic components of a load current. Therefore, in accordance with Kirchhoff's current law, the source current contains only the fundamental component. In order to implement the active power filter, a processor measures the load current and extracts the fundamental component for constructing the reference signal. So, the reference signal i_F^* can be represented as:

$$i_F^* = i_L - i_{L1} \qquad (1)$$

where i_L is the load current distorted by the nonlinear load and i_{L1} is the fundamental component of the load current. The reference current i_F^* is used to generate the inverter switching pulses, so that the inverter output current follows it.

The reference generation described in Eq. (1) is theoretically simple. But the more difficult issue is how to obtain the harmonic components from the distorted load current by eliminating the fundamental component. A notch filter was first proposed for this purpose. Notch filters can extract the harmonic components from the distorted load current, but they introduce a harmful phase shift to the harmonic components. In order to solve the phase shift problem, the instantaneous power method was proposed for the three-phase non-linear load, in which the three-phase load current is measured and converted by the rotational *dq*-transform. The transformed value is passed through a lowpass filter to extract the fundamental component and finally to obtain the harmonic components as a current reference signal. The disadvantage of this method is that it requires a large number of sensors for input measurements and complicated computations for coordinate transform.

III. ORIGINAL CURRENT REFERENCE GENERATOR

Figure 2 shows a data flow diagram of the reference signal generator, which was proposed in reference [5]. The reference signal generator consists of the peak detector, prefilter, adaptive predictive filter, and the Lagrange interpolator.

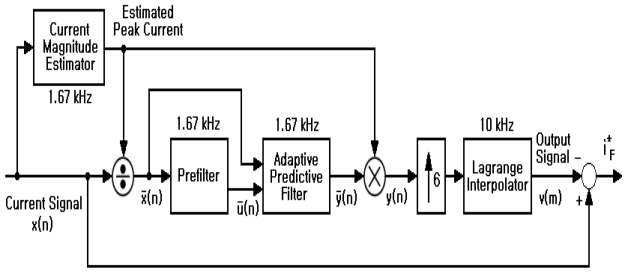

Fig. 2 Original reference signal generator [5]

The input signal is first normalized in order to mitigate the difficulty of processing the adaptation algorithm. Normalization is implemented by dividing the input signal by its estimated peak value. After passing through the adaptive predictive filter, the signal is de-normalized by multiplying the output signal by the peak value again. The normalized signal is filtered through a lowpass filter to eliminate undesired frequency components. If the original distorted signal were applied directly to the adaptive predictive filter, it would disturb the adaptation process, because the LMS algorithm is sensitive to all correlating signal components.

The applied prefilter was a fifth-order Chebyshev type II infinite impulse response (IIR) filter whose passband cut-off frequency and stopband ripple are 0.17 π and 10 dB, respectively. Since the sampling rate of the prefilter is 1.67 kHz, the passband cut-off frequency is 142 Hz. Thus, the 5th, 7th, and higher order harmonics are attenuated trough the prefilter. Also, the phase shift, which results from passing through the prefilter, is compensated through the adaptive predictive filter.

The sampling rate of 1.67 kHz is rather slow in application for the pulse-width modulation (PWM) switching of the inverter in the active power filter. Therefore, it is required that the sampling frequency be increased by up to 10 kHz to reduce the harmonics generated by sampling. A second-order Lagrange interpolator was applied for this up-sampling.

A. Adaptive Predictive Filter

The adaptive predictive filter must predict one step ahead in order to allow interpolation for sampling up to 10 kHz. The adaptive predictive filter processes the signal from the prefilter after delaying it by one step as illustrated in Fig. 3. Basically, the adaptive predictive filter behaves as a one-step-ahead predictor.

The predictive filter is a finite impulse response (FIR)

filter. Such a filter should converge to predict the dominating (fundamental) sinusoidal component only. The adaptation of the FIR filter is realized by means of the Widrow-Hoff LMS algorithm for filter coefficient adaptation. Below is the formula for adapting the filter coefficients:

$$H(n+1) = H(n) + 2\mu \bar{e}(n)\overline{U}(n-1) \qquad (2)$$

The output error related to the coefficient adaptation is defined below:

$$\bar{e}(n) = \bar{x}(n) - H^T(n)\,\overline{U}(n-1) \qquad (3)$$

where, $H(n) = [h(0), \cdots, h(N-1)]^T$ and $\overline{U}(n-1) = [\bar{u}(n-1), \cdots, \bar{u}(n-N)]^T$ are the filter coefficient vector and the data vector in the FIR window, respectively, and *N* is the length of the FIR filter.

The adaptation gain factor μ in Eq. (2) is selected to be small enough to guarantee the stability of the LMS algorithm. The choice of μ is always a trade-off between the adaptation rate and the overall stability of the system. In this study, μ=0.002 (with *N*=22) is selected as an appropriate compromise.

Finally, the output of the adaptive predictive filter $\bar{y}(n)$ is calculated as:

$$\bar{y}(n) = H^T(n)\,\overline{U}(n) \qquad (4)$$

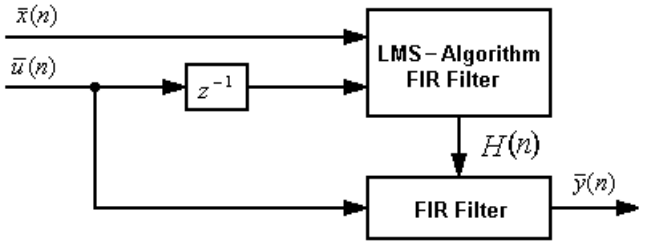

Fig. 3 Adaptive predictive filter

B. Interpolator

The output of the predictor is sampled at a rate of 1.67 kHz. However, the time resolution can be improved to any reasonable value by up-sampling and interpolation. The interpolation rate is mainly determined considering the available software and hardware resources. On the other hand, the switching frequency of the active power filters is typically from a few kHz up to 10 kHz.

A general-purpose approach for interpolation is considered, which is a second-order Lagrange interpolator. The advantage of this interpolator is its computational simplicity and low output distortion. Such an interpolator can be conveniently implemented with a poly-phase structure for interpolation by a factor of six.

The interpolator is composed of six poly-phase filters operating on the de-normalized samples $y(n)$, $y(n-1)$, $y(n-2)$, which come from the adaptive predictive filter. For each new input sample, the output side collects one sample from each of the six poly-phase filters. The coefficients of the poly-phase filters, $p_i(n)$, $i \in \{0, 1, 2, \ldots, 5\}$, are given below [5]:

$$p_0(n) = [0,\ 1,\ 0] \qquad p_1(n) = \left[\frac{7}{72}, \frac{25}{36}, -\frac{5}{72}\right]$$

$$p_2(n) = \left[\frac{2}{9}, \frac{8}{9}, -\frac{1}{9}\right] \qquad p_3(n) = \left[\frac{3}{8}, \frac{3}{4}, -\frac{1}{8}\right]$$

$$p_4(n) = \left[\frac{5}{9}, \frac{5}{9}, -\frac{1}{9}\right] \qquad p_5(n) = \left[\frac{55}{72}, \frac{11}{36}, -\frac{5}{72}\right] \qquad (5)$$

Finally, the output signal $v(m)$ of the interpolator is obtained as:

$$v(m) = p_i(n)\,Y(n) \qquad (6)$$

where, $Y(n) = [y(n),\ y(n-1),\ y(n-2)]^T$ is the data vector in the filter window. The poly-phase filter index i rotates at a rate of 10 kHz after the division of m/n, because the output time index m increments six times faster than the input time index n.

C. Peak Detector

The variation of the current magnitude may cause instability of the adaptive predictive filter. Therefore, the input signal is normalized to make the peak amplitude approximately one. This is simply done by dividing the input signal with the estimated peak amplitude. The peak detector is realized by choosing the maximum value of the input samples during a one half period of the fundamental frequency. If 1.67 kHz is used as a sampling frequency, 22 samples are needed to be stored in the 60 Hz power system for peak value estimation.

IV. Improved Reference Generator

The reference signal generator discussed in the previous section brings about severe distortion in the output after an elapse of about 20 seconds. This is due to the weight-drift problem of the coefficient vector $H(n)$. Such a drifting problem is common when the standard LMS algorithm is used in environments that do not satisfy a certain persistence of excitation condition [8]. In order to remove the drift phenomenon, the present authors propose a modified reference signal generator as shown in Fig. 4.

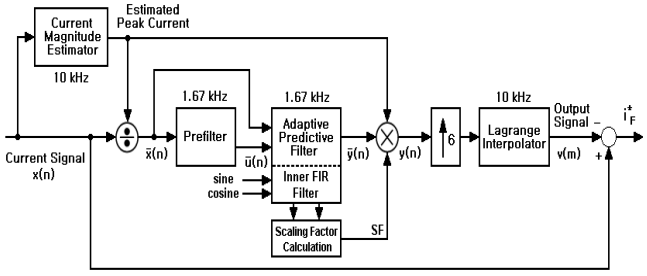

Fig. 4 Improved reference signal generator

The output interpolator of the proposed reference signal

generator is the same as that of the reference signal generator explained in the previous section. Other components are modified as discussed below in order to solve the severe operational problem.

A. Peak Detector

The function of the peak detector is to mitigate the harmonic distortion that is the same as that of the peak detector in the original reference signal generator. The peak detector in the original reference signal generator operates at a sampling rate of 1.67 kHz, which can be disturbed by harmonics with higher frequency than 835 Hz. Consequently, it affects the output stability of the adaptive predictive filter. In order to minimize this effect, the input signal is filtered through a lowpass filter with a 180 Hz cut-off frequency.

B. Prefilter

The fifth order Chebyshev II IIR filter was originally used as a prefilter to extract the fundamental component from the input signal. This prefilter has advantages such as a good skirt characteristic and a small phase shift. Nevertheless, its disadvantage is related to aliasing, which disturbs the operation of the adaptive predictive filter, because the harmonics with higher frequency than 835 Hz still exist after passing through the prefilter. In the following study, a fifth order Butterworth IIR filter is used instead of the earlier Chebyshev II filter, which is insensitive to the aliasing phenomenon, although it has better phase and skirt characteristics.

C. Adaptive Predictive Filter

In order to eliminate the harmful drift of the adaptive filter coefficients, Eq. (2) is modified as the following equation, considering a leakage factor [8]:

$$H(n+1) = \delta \cdot H(n) + 2\mu \bar{e}(n)\overline{U}(n-1) \qquad (7)$$

The error calculation is the same as in Eq. (3). The coefficient vector $H(n)$, data vector $\overline{U}(n-1)$, and adaptation gain μ are taken the same as in the above discussion. The output is determined by the FIR filter, which is illustrated in Eq. (4).

Fig. 5 shows the total harmonic distortion (THD) of the calculated output of the predictive adaptive filter with respect to the leakage factor, when it is changed from 0.5 to 0.999. The optimal leakage factor was determined as δ =0.999, so that the THD of the calculated output of the predictive adaptive filter is at the minimum and no coefficient drifting exists. A similar leakage factor was also used by Nishida *et al.* in their active power filter implementation [9] .

When the leakage factor is used, the filter coefficient vector $H(n)$ is improved to avoid drifting. But the magnitude response characteristics of the adaptive predictive filter bring about losses in the important frequency band. In order to compensate for these losses, the magnitude of the fundamental component should be corrected.

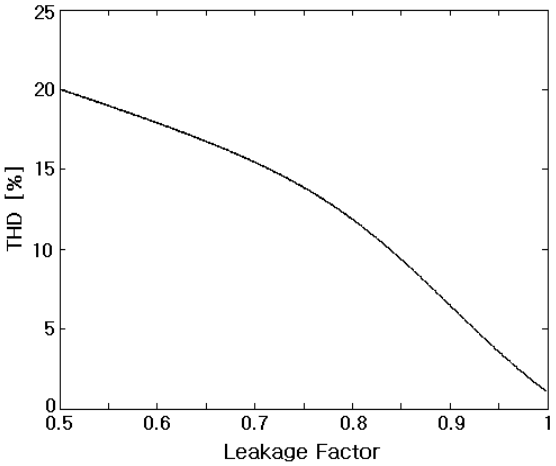

Fig. 5 Output signal THD with respect to leakage factor

D. Fundamental Component Compensation

The magnitude attenuation of the fundamental component due to considering the leakage factor in the adaptive predictive filter is compensated by means of a scaling factor (SF) to adjust the output amplitude. The attenuation of the fundamental component is first detected through measuring the orthogonal component losses of the FIR filter. In order to implement such a compensation scheme, two orthogonal sinusoidal signals with a magnitude of unity are passed through the FIR filter, as represented in Eq. (8). The two orthogonal signals are defined as two vectors on the orthogonal coordinates, whose vector sum has a magnitude of unity. SF is obtained by taking the inverse of the magnitude of the vector sum for the two components, and multiplying it to the output of the predictive adaptive filter for appropriate de-normalization.

$$ds(n) = \sin(\omega \Delta t \cdot n) \quad qs(n) = \cos(\omega \Delta t \cdot n) \qquad (8)$$

V. Performance Verification

For the purpose of performance comparisons before and after the improvement of the reference signal generator, the steady state of the waveform and its frequency response was analyzed in detail using MATLAB simulations. It is assumed that a steady state begins after about 20 seconds, as experience from the simulation portrays.

TABLE I
HARMONIC COMPONENTS OF TEST INPUT SIGNAL

Harmonic order	Amplitude [%]
Fundamental	100
5th	22.6
7th	10.5
11th	7.3
13th	4.7

Table I shows the existing frequency components and their magnitudes in the test input signal whose waveform is shown in Fig. 6 (a). Using this signal as the input for the reference

signal generator, the performance comparison was performed through the evaluation of the fundamental component, obtained from the simulation after 20 seconds.

Figures 6 (b) and (c) show the extracted fundamental component and the magnitude response of the entire filter, when the input signal is passed through the reference signal generator before improvement. The simulation results indicate that the harmonics level is very low as shown in Figs. 6 (b) and (c), after one second of simulation. So, the reference signal generator seems to work well.

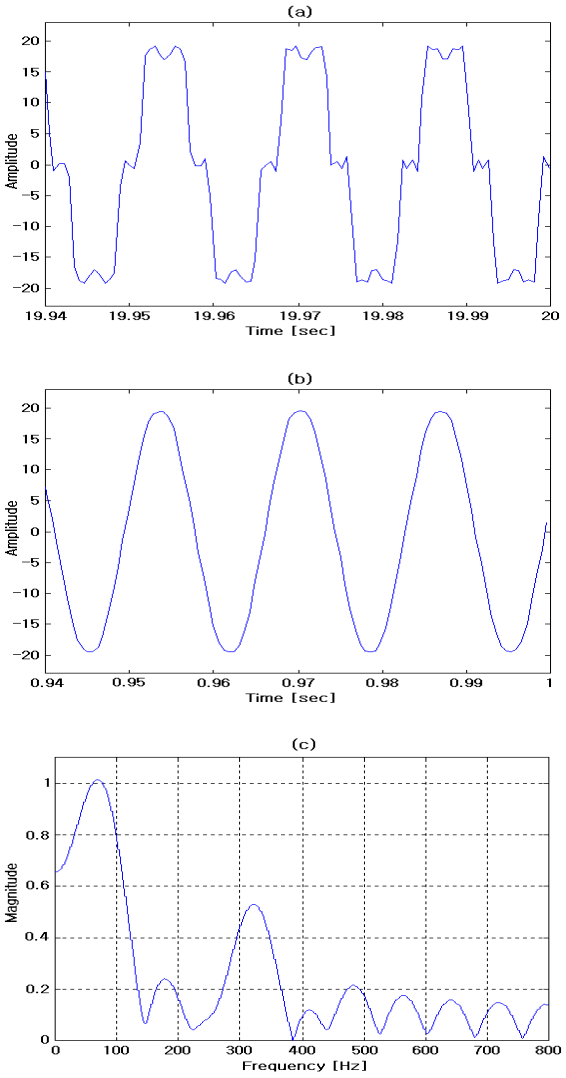

Fig. 6 Simulation results of the original reference signal generator at 1 second: (a) Output waveform, (b) Extracted fundamental component, (c) Magnitude response of the entire filter

The graphs in Fig. 7 show the fundamental component and the magnitude response of the entire filter when the simulation was performed for 20 seconds. Now, the extracted fundamental component has severe distortion, which means that the reference signal generator no longer works. This result can be distinguished clearly in the frequency response of the entire filter (Fig. 7 (b)); there is a considerable gain-peak of 3.5 at the fifth harmonic.

The disturbing gain-peak builds up, because the reference signal of the original adaptive filter is taken before the lowpass-type prefilter (see Fig. 2).

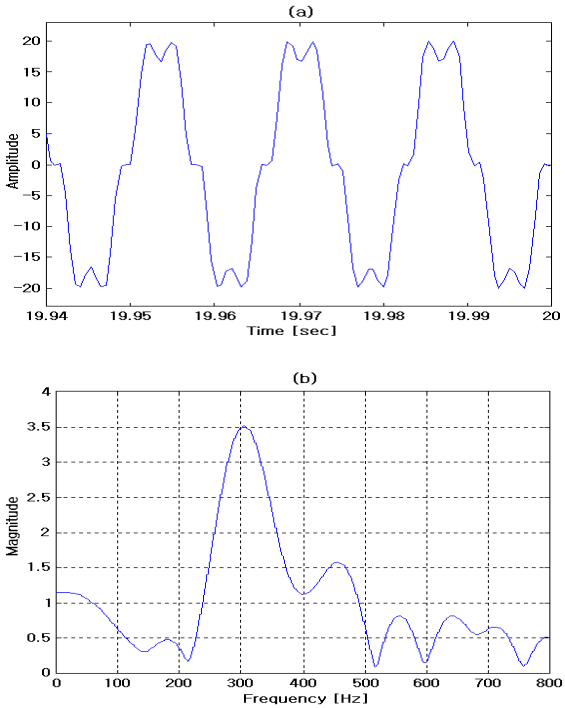

Fig. 7 Simulation results of the original reference signal generator at 20 seconds: (a) Output waveform, (b) Magnitude response of the entire filter

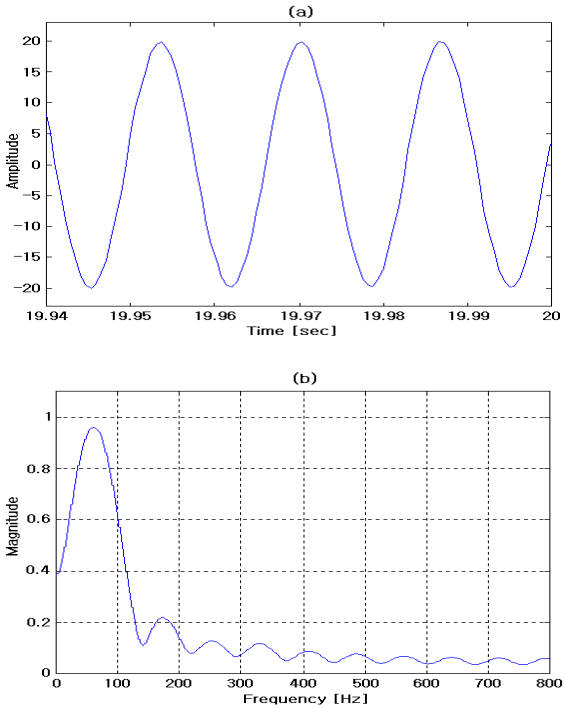

Fig. 8 Simulation results of the improved reference signal generator at 20 seconds: (a) Output signal waveform, (b) Magnitude response of the entire filter

Although the harmonic frequencies are attenuated through this prefilter, the cascaded adaptive predictive filter restores the correlating signal components—even the attenuated harmonics. Restoration of harmonics, however, takes longer

than restoration of the fundamental frequency (compare Figs. 6 (c) and 7 (b)), because the fundamental sinusoid has considerably higher amplitude. Eventually, all the harmonic components would be restored, if the predictive filter only had enough degrees of freedom available. This undesired phenomenon can be effectively prevented by using a *leaky* LMS algorithm instead of the basic LMS algorithm.

The graphs in Fig. 8 show the extracted fundamental component and the magnitude response of the entire filter when the input signal is passed through the improved reference signal generator.

The simulation was performed again for 20 seconds for the purpose of fair comparison. Here, the simulation results indicate that the level of output for the harmonics is

TABLE II
HARMONIC COMPONENTS OF TEST OUTPUT SIGNAL

Harmonic order	Amplitude [%]
Fundamental	100
5th	0.53
7th	0.245
11th	0.1
13th	0.075

extremely low as shown in Table II.

This result can also be distinguished in the magnitude response of the entire filter; now the gains of all harmonic frequencies are no more than 0.22. Consequently, the proposed adaptive predictive filter operates perfectly as a bandpass filter with an accurate compensation capability of a phase shift.

In order to verify the dynamic characteristic of the modified reference signal generator, an analysis of step input change was performed. Figure 9 shows the simulation results of the output signal when the input signal has a step increase of 20 % or 40% and a step decrease of 20 % or 40%. There are some transients at the instant of step change due to the delay of the peak detector. However, these transients exist only for one cycle of line frequency and then rapidly settle down.

VI. HARDWARE EXPERIMENT

The feasibility of hardware implementation for the proposed reference signal generator was evaluated by building and experimenting with a single-phase active power filter with a non-linear load composed of a diode rectifier with an RL load. Figure 10 shows the configuration of the experimental setup. The active power filter has a power rating of 1 kVA. It has an LRC passive filter to reduce the switching transients in the output current. The RL load has a variable resistance to simulate possible load variations. The system parameters of the hardware experiment setup are given in Table III. The proposed reference signal generator is implemented on the TMS320C31 DSP using C programming language. Moreover, all the algorithms composing the proposed reference signal generator were implemented using floating-point arithmetic. The current control of the active power filter is implemented with a dead-beat algorithm [9] on the DSP.

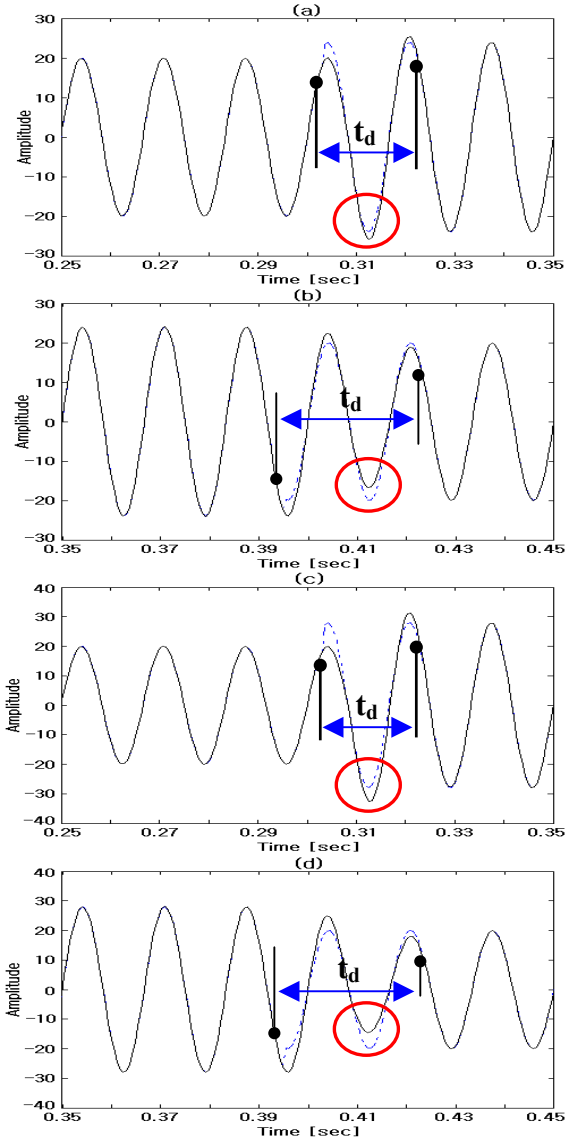

Fig. 9 Step-change response of the improved adaptive predictive filter:
(a) 20% step increase (b) 20% step decrease
(c) 40% step increase (d) 40% step decrease

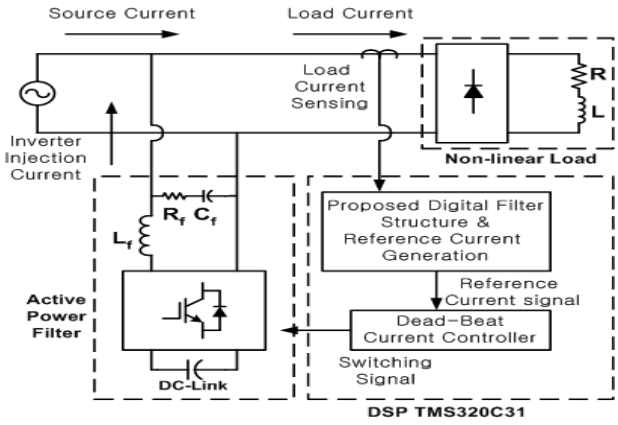

Fig. 10 Configuration of the experimental set-up

The dead-beat control, which is a method used to obtain a

dead-beat response, has been applied for the current control of active power filters since the early 1990's [3]. The dead-beat control requires knowledge of the input parameters, such as the line voltage, coupling reactor inductance, present inverter output current, and the reference current value. The control delay is an intrinsic disadvantage of this method. In order to reduce the harmful delay, this paper uses a scheme to compensate for the error of n-th and (n–1)-th points

TABLE III
HARMONIC COMPONENTS OF TEST OUTPUT SIGNAL

Source	
Input voltage	110 V, 60 Hz
Inverter	
Filter L_f	6 mH
Filter C_f	20 μF
Filter R_f	5 Ω
DC capacitor	2200 μF
RL load	
R (variable)	20 Ω → 16.6 Ω 16.6 Ω → 20 Ω
L	50 mH

simultaneously by means of predicting the error at n-th point with the output at (n – 1)-th point.

Experimental work is performed in accordance with two analysis conditions; when the load is in a steady state and in a transition state. Figure 11 shows the experimental result illustrating the operation of the proposed reference signal generator. Figures 11 (a), (b) and (c) show the load current, fundamental component, and harmonic components of the proposed reference signal generator. It is clear that the reference signal generator proposed can generate a satisfactory harmonic reference signal for the active power filter.

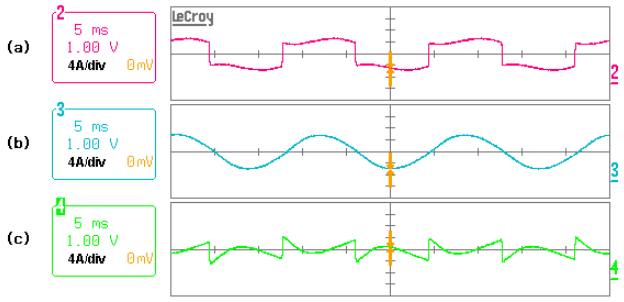

Fig. 11 Experimental results I with the improved reference signal generator: (4A/div) (a) Load current , (b) Fundamental current, (c) Harmonic reference current

Figure 12 shows the experimental result illustrating the operation of the active power filter using the proposed reference signal generator and the dead-beat controller. Figures 12 (a), (b) and (c) show the compensated current in the source, the compensating current from the active power filter, and the load current. The THD (total harmonic distortion) of compensated current is about 5.93%, while the THD of load current is 25.3%.

The active power filter using the proposed reference signal generator and the dead-beat controller can compensate the harmonics due to the non-linear load, although there exists some transients in the source current. These transients occurred at the instant of step rising in the load-side input current, because the step rising is too steep to make the control follow. The steepness of the load current can be mitigated in reducing the inductance of the dc reactor.

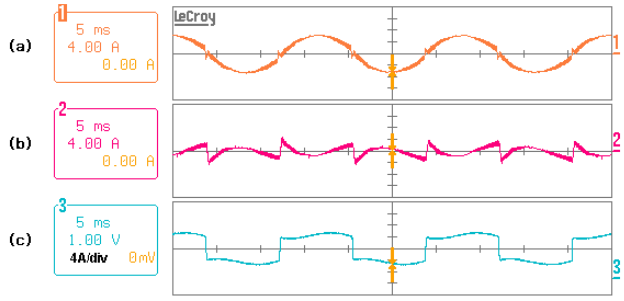

Fig. 12 Experimental results II with the improved reference signal generator: (a) Compensated current, (b) Compensating current, (c) Load current

In general, the load changes as time elapses. So, it is very important to check that the proposed reference signal generator operates in a stable manner with sudden load changes. Figure 13 shows the experimental result when the load has a step increase of 20 % and a step decrease of 20 %. Figure 13 (a) shows the compensated current in the source side and the fundamental component of the reference signal generator when the load has a 20 % step increase, while Fig. 13 (b) shows the compensated current in the source side and the fundamental component of the reference signal generator when the load has a 20 % step decrease. As expected, the proposed reference signal generator operates properly without severe transients at the instants of step load change.

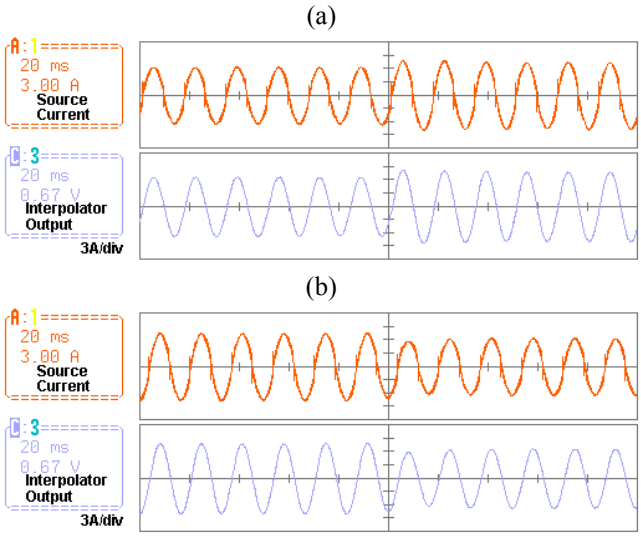

Fig. 13 Compensated current and fundamental component using the improved reference signal generator: (a) Step-increase of load, (b) Step-decrease of load

VII. CONCLUSION

This paper described an improved reference signal generator based on the adaptive predictive filter for the active power filter. The introduced reference signal generator has a modified adaptive predictive filter to eliminate the weight-drift phenomenon by introducing the leakage factor. The magnitude loss of the fundamental component due to the introduction of the leakage factor in the predictive adaptive filter is compensated with rescaling the output signal of the adaptive predictive filter.

The performance of the proposed reference signal generator was verified first through simulations with MATLAB. The application feasibility was evaluated by experimenting with a single-phase active power filter prototype based on the proposed reference generator, which was implemented using the TMS320C31 DSP. Both simulations and experimental results confirm that the proposed reference signal generator can be used successfully for active power filters.

REFERENCES

[1] L. Gyugy and E. C. Strycula, "Active ac power filter," in *Proc. IEEE IAS Annual Meeting*, 1976, pp. 529-535.

[2] H. Akagi. A. Nabae, and S. Atoh, "Control strategy of active power filter using multiple voltage source PWM converters," *IEEE Trans. on Industry Applications*, vol. 22, pp. 460-465, May/June 1986.

[3] S. Buso, L. Malesani, and P. Mattavelli, "Dead-beat current control for active filters," in *Proc. 24th Annual Conf. of the IEEE Industrial Electronics Society*, Aachen, Germany, 1998, vol. 3, pp. 1859-1864.

[4] H. Akagi, Y. Kanazawa, and A. Nabae, "Instantaneous reactive power compensators comprising switching devices without energy storage components," *IEEE Trans. on Industry Applications*, vol. 20, pp. 625-630, May/June 1984.

[5] S. Väliviita and S. J. Ovaska, "Delayless method to generate current reference for active filters," *IEEE Trans. on Industrial Electronics*, vol. 45, pp. 559-567, Aug. 1998.

[6] H. Akagi, Y. Kanazawa, and A. Nabae, "Generalized theory of the instantaneous reactive power in three-phase circuits," in *Proc. Int. Conf. Power Electronics*, Tokyo, Japan, 1983, pp. 1375-1386.

[7] M. El-Habrouk, M. K. Darwish, and P. Mehta, "Active power filters: A review," *IEE Proc. - Electric Power Applications*, vol. 147, pp. 403-413, Sept. 2000.

[8] V. H. Nascimento and A. H. Sayed, "Unbiased and stable leakage-based adaptive filters," *IEEE Trans. on Signal Processing*, vol. 47, pp. 3261-3276, Dec. 1999.

[9] K. Nishida, Y. Konishi, and M. Nakaoka, "Current control implementation with deadbeat algorithm for three-phase current-source active power filter," *IEE Proc. - Electric Power Applications*, vol. 149, pp. 275-282, July 2002.

”Sensorless” Control of 4-Quadrant-Rectifiers for Voltage Source Inverters (VSI)

Pawel Szczupak, Ralph Kennel
Wuppertal University
Germany
Email: kennel@ieee.org

***Abstract*— In this paper a sensorless control strategy for a voltage oriented controlled (VOC) three phase pulsewidth modulated (PWM) power supply rectifier is presented. This control method requires neither the measured AC-line voltages nor any accurate circuit parameters for estimation purposes. Furthermore there is no need for additional test signals. There are no additional hardware requirements with respect to the standard drive inverters available in the market which usually are not equipped with AC-side voltage sensors. This approach makes use of the slow varying AC-line voltage - the sample frequency of the inverter is at least ten times higher. The principle of the proposed method is explained, and its effectiveness is proved experimentally. The influence of the system parameter variations (e. g. line inductance) and disturbances in supply voltage on the control behavior is investigated.**

I. Introduction

In the last years voltage controlled pulsewidth modulation (PWM) rectifiers, providing almost unity power factor as well as sinusoidal AC input currents have been widely investigated with respect to harder restriction in the European market for the harmonic current contents. Therefore pulsewidth modulation converters are applied to applications that require less harmonic currents and/or energy recovery, e.g. in drive applications where the amount of regenerating energy demands to use 4-quadrant-operation The input line current is controlled by adjusting the AC side voltage of the bridge circuits. Unity power factor can be obtained by aligning the AC-line currents with the AC-supply voltage.

The conventional control technique for PWM converters measures the AC-line supply voltage and generates a rotating dq-reference frame in which all AC-quantities become DC-values [1],[2] in stationary state. This offers the well-known advantages of field or voltage oriented control for PWM rectifier and the two-phase dq-theory. The underlying PWM pattern is usually generated by a suboscillation method or space vector PWM method transforming the voltage reference values to pulsewidth modulated signals. Each pulse pattern is necessarily synchronized with control algorithm, the pulses themselves are not. So it is important to realize that there is not always access to each pulse data especially if the PWM unit is outside the controller. Therefore sensorless strategy relying on the exploration of the switching harmonics suffers under the lack of information about the instantaneous pulses. The aim was to develop an algorithm which gets rid of the pulse pattern information in each control cycle which focused the view to harmonics spectra lower then the switching frequency.

Generally drive converters are equipped with two sensors. The AC-side line currents sensors are needed for control and short circuit protection whereas the DC-link serves for over- and under-voltage protection and output voltage information. There is no direct access to the AC-side line voltage by sensors and therefore no direct voltage orientated control (DVOC) is possible using these converters. An alternative control strategy is the indirect voltage oriented control (IVOC), which is directly related to the indirect field oriented control. In drive application this control strategy is wide spread and known as a reliable solution. Nevertheless it requires the estimation of the grid voltage – if the norm of the voltage vector is not required, at least the angle of the grid voltage is needed.

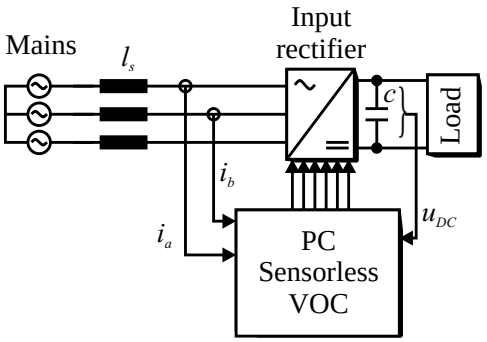

Fig. 1. 3-phase sensorless PWM input rectifier

This paper presents a sensorless control strategy for PWM rectifier and the estimation method of the gird voltage capable to reach unity power factor and insensitivity against parameter variations like inductance saturation interconnecting the grid voltage and output voltage of the converter. It shows also behavior of the proposed method, when there are disturbances of the supply voltage. The control method is applicable to PWM drive converters without hardware changes whether they use space vector modulation method or hysteresis based modulations.

II. Voltage Oriented Control

Space vector notation of PWM rectifier electrical circuit supports a clear understanding of the physical quantities an components and their behavior.

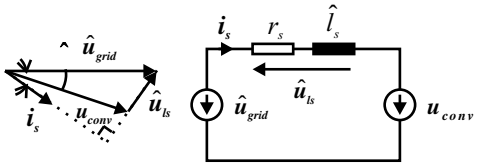

Fig. 2. Model of the PWM rectifier system

The line current vector $\boldsymbol{i_s}$ is controlled by the converter and is directly related to the voltage drop across the inductance $\hat{l}_s$.

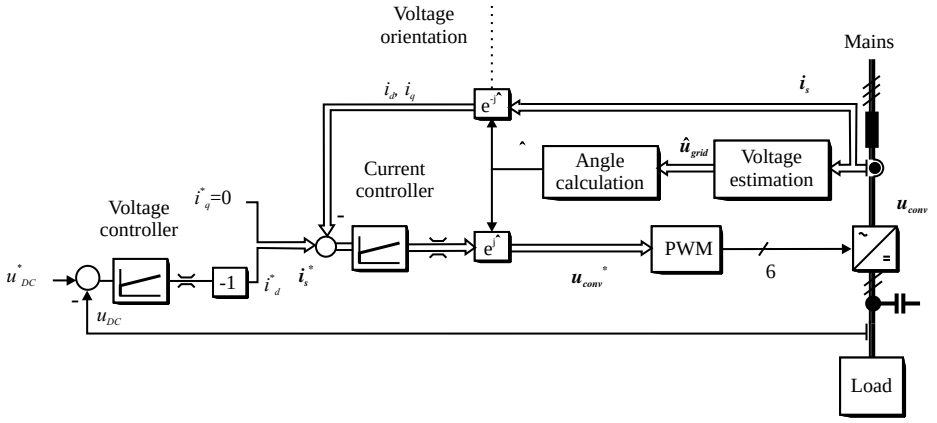

Fig. 3. Sensorless Voltage Oriented Control

The inductance is necessary to reduce the high harmonic switching content in the current caused by the switching of the rectifier and to decouple the supply voltage from the converter output voltage. The inductance voltage $\hat{\boldsymbol{u}}_{\boldsymbol{l_s}}$ is equal to the difference between the grid voltage $\hat{\boldsymbol{u}}_{\boldsymbol{grid}}$ and the converter voltage $\boldsymbol{u}^*_{\boldsymbol{conv}}$. All values are vectors in space vector notation [3]. Estimated values are marked with a hat $\hat{}$.

The control scheme is visualized in figure 3. Transformation in rotating dq voltage oriented reference frame is done using an estimated voltage angle. For high frequency analysis the resistive voltage drop can be neglected leading to a simplified model. Only the inductance restricts the high harmonic currents. The later explained sensorless method takes advantage from this fact due to less required calculations.

Using conventional voltage oriented control all quantities are referred to a synchronous reference frame aligned with the supply voltage. Therefore the control scheme is based on coordinate transformation between stationary $\alpha\beta$- and synchronous dq-reference system.

In the dq reference frame, the AC-line current vector is divided into rectangular components. The component i_q determines the reactive power whereas i_d determines the active power flow. If i_q is controlled to zero the minimum current for a given reactive power is ensured and the power factor is one.

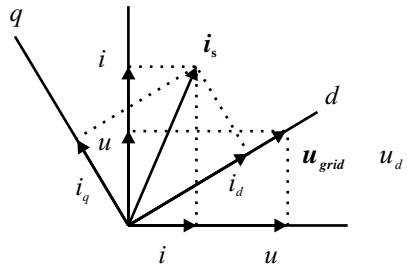

Fig. 4. Coordinate transformation from fixed $\alpha\beta$ to rotating dq reference frame

As in steady state the stator voltage can normally be considered sinusoidal, the voltage and flux orientation becomes equivalent except to $90°$ phase shift. This encouraged to consider the grid as a machine and apply the well-known principle of field orientation. This leads to the same simple and reliable principle as in revolving field machines. The equations for the PWM rectifier system in the dq reference frame are:

$$\begin{aligned} u_d &= l_s \frac{di_d}{dt} + u_{d,conv} - \omega_s \cdot l_s \cdot i_q \\ 0 &= l_s \frac{di_q}{dt} + u_{q,conv} + \omega_s \cdot l_s \cdot i_d \end{aligned} \tag{1}$$

Usually the line voltages must be measured for calculation of the voltage angle necessary for coordinate transformation. To reduce costs of the system, there is a possibility to estimate the line voltage. The estimated voltage is used to calculate a voltage angle. Coordinate transformation from fixed $\alpha\beta$ coordinates to rotating dq reference frame is done using the estimated voltage angle.

III. Grid Voltage Estimation by Phase Tracking

Based on the PWM rectifier system model, the grid voltage estimation is proposed to be a phase tracking method. The current i_s passing inductance $\hat{l}_s$ causing a voltage $\hat{\boldsymbol{u}}_{\boldsymbol{l_s}}$. Neglecting resistive voltage drop the voltage $\hat{\boldsymbol{u}}_{\boldsymbol{l_s}}$ can be calculated as:

$$\begin{aligned} \hat{u}_{l_s,\alpha} &= \hat{l} \frac{di_\alpha}{dt} \\ \hat{u}_{l_s,\beta} &= \hat{l} \frac{di_\beta}{dt} \end{aligned} \tag{2}$$

while estimated grid voltage $\hat{\boldsymbol{u}}_{\boldsymbol{grid}}$ is represented by equations:

$$\begin{aligned} \hat{u}_{grid,\alpha} &= \hat{u}_{l_s,\alpha} + u^*_{conv,\alpha} \\ \hat{u}_{grid,\beta} &= \hat{u}_{l_s,\beta} + u^*_{conv,\beta} \end{aligned} \tag{3}$$

If value of the inductance $\hat{l}_s$ is set correctly, the estimation error will be small during the following sample period (figure 5).

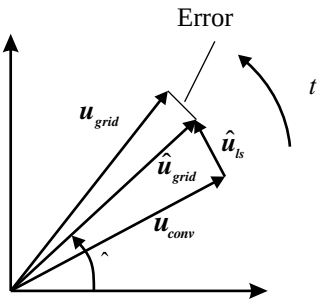

Fig. 5. Grid voltage estimation through phase tracking

As the currents depend on the voltage difference, any current variation results in voltages over the inductance; this voltage is considered when calculating the next sample period. This scheme tracks continuously the real voltage vector.

When the inductance value is estimated lower than the real inductance value, the system will still find and detect the voltage vector, but the dynamic response will decrease. This can be explained by the dynamic transfer function of the tracking method.

Equation 4 shows, that the dynamic response of the phase tracking estimation method decreases with increasing factor k, while k is the relation between the real and estimated inductance $l_s/\hat{l}_s$.

$$\hat{u}_{grid} = \frac{u_{grid}}{T_s k s + 1} \tag{4}$$

For the smallest possible factor $k = 1$ the fastest step response can be expected. Faster responses ($k < 1$) lead to instability of the estimation scheme.

IV. Experimental results

The system parameters used in the laboratory set-up are:

TABLE I
LABORATORY SET-UP PARAMETERS

Nominal line voltage	$230V_{rms}$
Nominal line current	$7A_{rms}$
Grid filter inductance l_s	$3.5mH$
Grid filter resistance r_s	$50m\Omega$
DC-Link capacitor C	$750\mu F$
Nominal DC-Link voltage U_{DC}	$750V$
Switching frequency f	$4kHz$

Figure 6 shows the measured δ and the estimated $\hat{\delta}$ voltage angles and an error (in radians) between measured and estimated angle. The shift between the estimation and measurement is caused by the estimated voltage filter and is constant during operation.

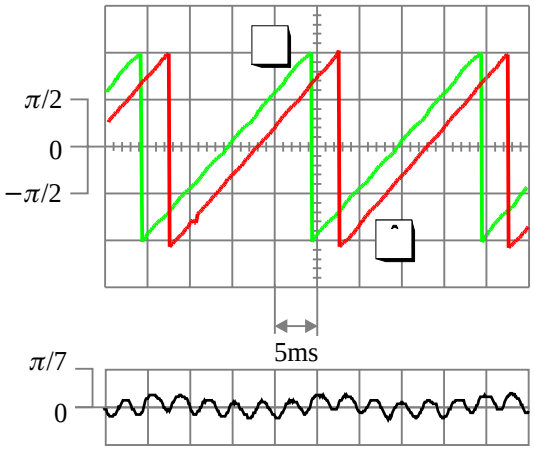

Fig. 6. Measured δ and estimated $\hat{\delta}$ angle, and error between them

A. Grid inductance value mismatch

Figure 7 shows the results while there is a parameter mismatch in the inductance l_s. Using greater grid inductance decreases the input current ripple (software parameters are unchanged).

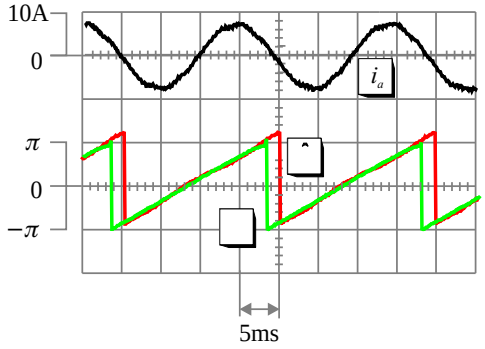

(a) $l_s = 3.5mH$

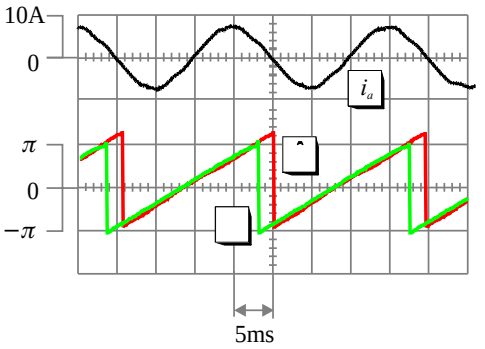

(b) $l_s = 8.5mH$

Fig. 7. Influence of the grid inductance on the sensorless control system

The voltage angle is estimated correctly even while there are wrong inductance parameters. As discussed before the estimated inductance only influences the dynamic behavior and not the steady state estimation.

B. Supply voltage distortions

The next tests show the behavior of the ”phase tracking” control scheme when there are disturbances in the grid voltage.

The investigations took place concerning the following grid voltage distortions:

1. Unbalanced grid voltage
2. Over-voltage
3. Under-voltage (voltage sags)

1) Unbalanced grid voltage: In this test a change in the amplitude of the grid voltage in one of the phases was made. The degree of grid voltage unbalance is defined as:

$$u = \frac{e_n}{e_p}, \tag{5}$$

where:

- e_n is the negative sequence grid voltage vector
- e_p is the positive sequence grid voltage vector

Usually in the grid the voltage unbalance should not exceed 3%. The tests presented in this paper were conducted with voltage unbalance of 2% and 6%.

Figure 8 shows the line currents [in stationary reference frame ($\alpha\beta$)], estimated $\hat{\delta}$ and measured δ grid voltage angle by the 2% unbalanced grid voltage. There is a low-pass filter of the estimated supply voltage, which leads to the offset between measured and estimated angle, but it is constant during operation.

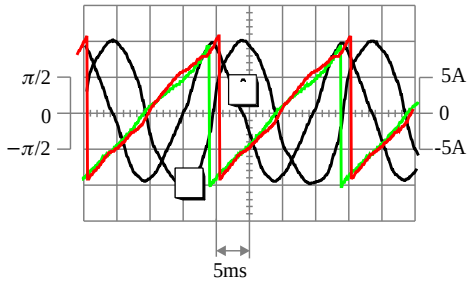

(a) Estimated angle is used

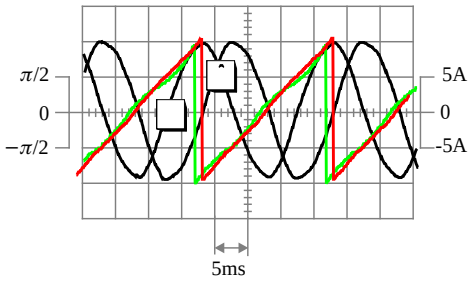

(b) Measured angle is used

Fig. 8. Line currents ($\alpha\beta$) and supply voltage vector angle by 2% unbalanced grid voltage

Figure 9 shows the same situation, but by 6% unbalanced grid voltage. It is shown, that there are more line currents higher harmonics when the measured grid voltage angle is used. Using the estimated angle lower harmonic content of the line currents can be provided.

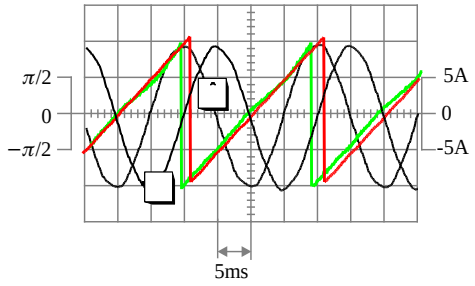

(a) Estimated angle is used

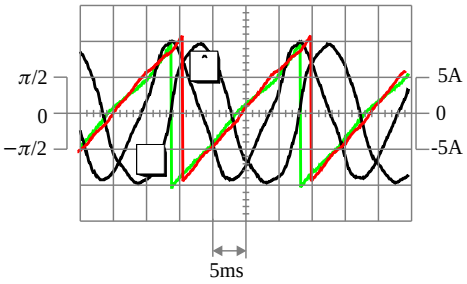

(b) Measured angle is used

Fig. 9. Line currents ($\alpha\beta$) and supply voltage vector angle by 6% unbalanced grid voltage

The grid voltage angle is estimated almost correctly in both cases. The difference between estimated and measured voltage angle is caused by the low-pass filter on the estimated supply voltage. The oscillations of the voltage angle lead to the slightly higher harmonics in the input current, but the operation of ”phase tracking” control works fine.

Note: the estimated angle in figure 8(b) and 9(b) is calculated parallel to the measured angle. The currents in figure 8 are sampled, that is why there is no switching frequency harmonic content seen.

2) Over-voltage: In the laboratory the over-voltage was simulated using an auto-transformer. It was possible to achieve about 10% higher supply voltage than nominal value. The tested voltage amplitude value was set to $250V_{rms}$. Using equation 6 the lowest possible DC-Link voltage can be calculated.

$$\begin{aligned} U_{DC} &\geq \frac{2\sqrt{2}}{m\sqrt{3}} \cdot u_{LL} + u_{l_s} \\ U_{DC} &\geq \frac{2\sqrt{2}}{m\sqrt{3}} \cdot u_{LL} + i_L X_L \end{aligned} \tag{6}$$

where:

a) U_{LL} is the line-line voltage (in the test $432.5V$)
b) u_{l_s} is the voltage drop on the input filter inductance
c) m is the modulation index (1 by sinusoidal PWM, 1.154 by Space Vector Modulation)

The proposed sensorless control of the PWM rectifier was working correctly and stable under over-voltage condition. Line currents could be controlled to flow in both directions (from the grid into the rectifier and from the rectifier into the grid).

Figure 10 presents the line currents and estimated and measured voltage angles. The harmonics content of current is high during the test. Current ripple can be reduced using

higher input filter inductance or higher DC-Link voltage. Care must be taken when increasing the filter inductance. Low inductance will lead to high current ripple. High value will give a low current ripple, but will reduce operation range of the rectifier. To control the input current the voltage drop over this inductance is used. But maximal value is limited by the DC-Link voltage and modulation strategy. Consequently, a high current (high power) through the inductance requires either a high DC-link voltage or a low inductance (low impedance).

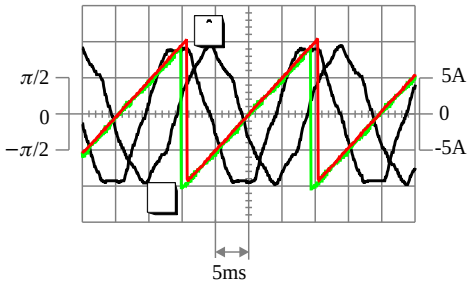

(a) Estimated and measured angles, line currents in $\alpha\beta$

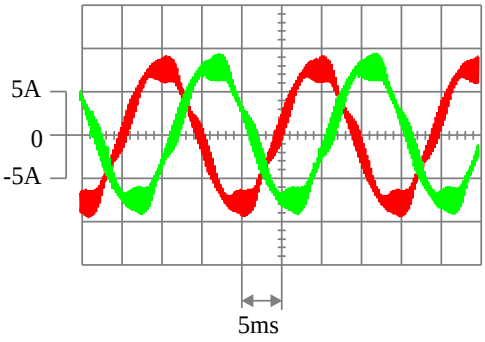

(b) i_a and i_b currents

Fig. 10. Line currents ($\alpha\beta$) and supply voltage vector angle by 10% over-voltage

3) Under-voltage (voltage sags): Voltage sags are the common disturbances in real applications. In the laboratory the under-voltage test was conducted. The supply voltage was reduced to 65% of nominal voltage. The estimated voltage angle was not distorted by the voltage sag and the system was working stable. It was possible to control the line currents in both directions (from the grid into the rectifier and from the rectifier into the grid). The DC-Link voltage was kept constant equal to the reference value of $750V$.

Results presented in figure 11 show, that the estimated angle is equal to the measured one. The currents are sinusoidal with low ripple due to the high DC-Link voltage (see section IV-B.2).

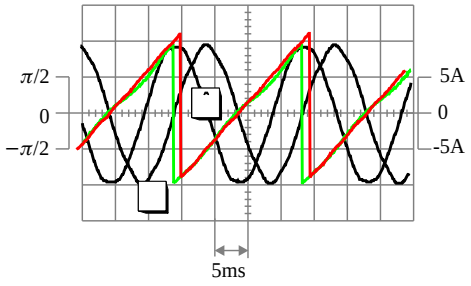

(a) Estimated and measured angles, line currents in $\alpha\beta$

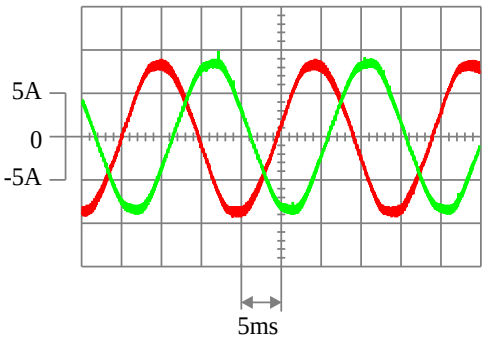

(b) i_a and i_b currents

Fig. 11. Line currents ($\alpha\beta$) and supply voltage vector angle by 65% under-voltage

V. Conclusion

In this paper a ”phase tracking” voltage estimation method is presented. The experimental tests show the advantages of the proposed phase tracking method. The influence of system parameter variations (grid inductance l_s value) on the phase tracking method is also tested. The proposed estimation method showed a good robustness against parameter variations. It proved to be simple and very cheap. The method was also tested in cases where there are distortions in the supply voltage. The results achieved show, that the sensorless controlled rectifier reacts in almost the same way to tested disturbances as standard PWM rectifier with sensors. There are cases where the sensorless control is superior to the one with sensors. Using the estimated grid voltage the current can be sinusoidal with lower harmonic content as by the conventional control method.

References

[1] M. P. Kazmierkowski, *Control Strategies for PWM Rectifier/Inverter-Fed Induction Motors*, Int. Conf. On Power Electr. and Motion Control - EPE-PEMC 2000 Kosice

[2] R. Kennel, A. Linder, *Predictive Control of Inverter Supplied Electrical Drives*, Conf. Record of PESC'00, Galway, Ireland, 2000

[3] J. Holtz, *The Dynamic Representation of AC Drive Systems by Complex Signal Flow Graphs*, Conf. Record of ISIE, Santiago de Chile, Chile, 1994, pp. 1-6

[4] T. Ohnuki, O. Miyashita, P. Lataire, G. Maggetto, *Control of a Three-Phase PWM Rectifier Using Estimated AC-Side and DC-Side Voltages*, IEEE Trans. on Power Elect., Vol. 14, No.2, March 99

[5] R. Kennel, M. Linke, P. Szczupak, *Parameter Independent Phase Tracking Method for Sensorless Control of PWM Rectifiers*, Conference on Power Electronics and Applications - EPE 2003 Toulouse, France

[6] M. Linke, R. Kennel, J. Holtz, *Sensorless speed and position control of synchronous machines using alternating carrier injection*, IEEE International Electrical Machines and Drives Conference IEMDC'03 Madison/Wi., USA, 1-4 June 2003

A Novel Voltage Controller on Dynamic Voltage Restorers by Use of Feed forward and State Feedback Scheme

HYOSUNG KIM
Department of Control Engineering
Cheonan National Technical College, Korea
hyoskim@cntc.ac.kr

SEUNG-KI SUL
School of Electrical Engineering & Computer Science
Seoul National University, Korea
sulsk@plaza.snu.ac.kr

Abstract - This paper discusses the control of the compensation voltages in dynamic voltage restorers (DVR). On analyzing the power circuit of a DVR system, control limitations and control targets are presented for the compensation voltage control. Based on the preceded power stage analysis, a novel controller for the compensation voltages in DVRs is proposed by feed forward and state feedback control scheme. This paper also discusses the time delay problems in the control system of DVRs. Digital control systems normally have control delay from the sampling period, the switching frequency of an inverter, and the sensor transmission time. The control delay increases the dimension of the system transfer function one grade higher, which makes the control system more unstable. This paper analyzes the relation among the control delay, closed loop damping factor, and the output filter parameters of DVR inverters. Based on the control system analysis, design guidelines are proposed for the output filter parameters and the inverter switching frequency of DVRs. The proposed theory is verified by an experimental DVR system with a full digital controller.

I. INTRODUCTION

Dynamic Voltage Restorers (DVR) are good candidates for compensating the voltage quality problems that come from voltage sags and swells. The control system for DVRs can be classified into two parts as shown in Fig. 1; first, determining the reference compensation voltages, second, regulating the output compensation voltages.

On determining the reference compensation voltages, whole situation of three phase voltages has to be considered. Typically d-q-o transformation has been widely used in determining the refernce compensation voltages [1][2]. A novel control algorithm has been proposed in determining the reference compensation voltage by use of PQR power theory [3].

The operation of DVRs is similar to that of active power filters (APF) in that both compensators must respond very fast on the request from abruptly changing reference signals. In case of current compensation in APFs, filter inductors and inverters are main components. The current in the filter inductor is controlled by switching the inverter in APFs. Three kinds of current control method have been compared in APFs; hysteresis control, ramp control, and deadbeat control. Hysteresis control method has best performances in APFs but has difficulty in implementing by digital controllers. In case of digital control applications, ramp control method showed better performance over the deadbeat control method [4].

In case of voltage compensation, output LC filters and inverters are main components. The voltage on the filter capacitor is controlled by switching the inverter in voltage compensation, where the output LC filters generate time delay and overshoot problems on the voltage. A deadbeat control method was adopted for uninterruptible power supplies (UPS), which was limited to sinusoidal voltage output [5][6]. To get fast voltage response, the capacitor current of an output LC filter has been sensed for a feedback controller in a ramp control method which also was limited to sinusoidal voltage output [7]. To control DVR systems, a cascade controller with outer voltage control loop and inner current control loop scheme has been proposed [8]. However, the cascade controller has low control dynamics since the control bandwidth of outer voltage control loop is limited by the inner current control loop. To overcome this limitation, a modified control method has been tried to feedback both current and voltage signal parallel, but its performance was not satisfactory [9].

Other critical issues on controlling the output compensating voltage are as follows; first, a microprocessor based digital control system has always time delay from the sampling and processing time, second, a PI regulator is not a proper measure when the reference is time-varying, and third, the transfer function of the inverter is quite not linear [10].

This paper analyzes the physical limitation of control bandwidth on DVR systems by the output LC filter. Based on the analysis, this paper proposes a novel controller for the compensation voltages on DVR systems which has maximum control bandwidth up to the output filter cutoff frequency that is the physical limitation. The proposed voltage controller consists of feedforward and state feedback control scheme, has good steady state and transient response. The proposed DVR system rides through the load voltages without oscillation nor overshoot, very fast within 0.5ms when sags or swells occur suddenly. Control gains for the proposed controller were determined with consideration of the control time delay, mainly the sampling time. This paper also presents critical switching frequency of DVR inverters which insures proper operation of DVR systems related with the cutoff frequency of output LC filters. Proposed controller is implemented by full digital controller equipped with TMS320VC33/150MHz processor to verify the theory.

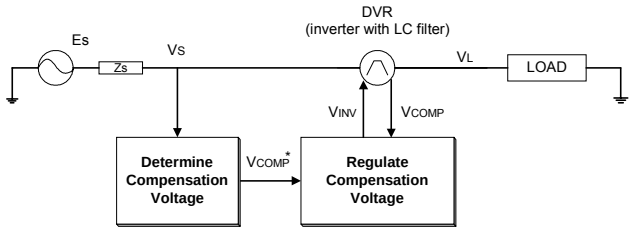

Fig. 1 Macro scope of a DVR control system.

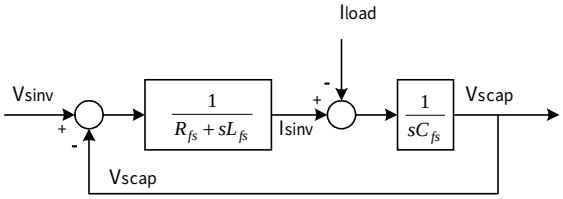

Fig. 2 Block diagram for a power stage of a DVR.

II. POWER STAGE AND CONTROL TARGET

A. Power Stage Analysis

Fig. 2 shows the block diagram for a power stage of a DVR system, where it is assumed that it consists of an inverter and output LC filters with some resistance in series. From the block diagram, the open loop transfer function can be described as (1).

$$\frac{V_{scap}}{V_{\text{sinv}}} = \frac{1}{s^2 L_f C_f + sR_f C_f + 1} = \frac{\omega_f^2}{s^2 + 2\xi_f \omega_f s + \omega_f^2}, \qquad (1)$$

here, L_f : filter inductance.

C_f : filter capacitance.

R_f : equivalent loss element..

$$\omega_f = \frac{1}{\sqrt{L_f C_f}},\ \xi_f = \frac{R_f}{2}\sqrt{\frac{C_f}{L_f}}.$$

When $\xi_f < 0.7$, the per unit overshoot of a step response can be calculated as (2).

$$\text{pu over shoot} = \frac{1}{2\xi_f \sqrt{1-\xi_f^2}}. \qquad (2)$$

The transfer function for a load current disturbance can be expressed as (3).

$$\frac{V_{scap}}{I_{load}} = -\frac{R_f + sL_f}{s^2 L_f C_f + sR_f C_f + 1}. \qquad (3)$$

B. Limitation of DVR Control System

A DVR control system should not only regulate the output compensation voltages according to reference voltages but also properly reject the disturbances from the load currents. Ideal design targets for the voltage regulator and the disturbance rejector may be (4) and (5) respectively.

$$\frac{V_{scap}}{V_{scap}^*} = 1. \qquad (4)$$

$$\frac{V_{scap}}{I_{load}} = 0. \qquad (5)$$

To accomplish the design target described by (4) at high frequency, the inverter output voltages has to be large enough to overcome the -40dB/dec attenuation of the output LC filter when the frequency range is $\omega > \omega_f$. For example the inverter output voltages must be 100 times larger than the reference voltages when the frequency is $\omega = 10\omega_f$, which needs prohibitively large size of inverter. Therefore, practically the control bandwidth of the compensation voltages of DVRs, ω_c , should be limited in $\omega_c \le \omega_f$.

C. Control Target in Analog Control System

When analog control systems are considered and the PWM inverter in DVRs is substituted by an ideal linear amplifier, the time delay in control systems between sensing the plant status and final actuating the plant can be neglected. In this case, a 2nd order system can be considered for the control target of DVR systems as (6).

$$\frac{V_{scap}}{V_{scap}^*} = \frac{\omega_c^2}{s^2 + 2\xi_c \omega_c s + \omega_c^2}. \qquad (6)$$

If the control bandwidth ω_c and the close-loop damping factor ξ_c can be selected properly, good control performance can be expected. Ideally, if proper control structure and gains are explored to select the control bandwidth and the damping factor as $\omega_c = \omega_f$ and $\xi_c = 1$ respectively, the DVR should have maximum performance within the physical limitation.

D. Control Target in Digital Control System

Time delay always occurs between the sensing of the plant status and the final actuating of the plant in discrete control systems because of the sampling time T_{samp}, digital signal processing time, the inverter switching period, the sensing time of a sensor itself, and etc. The open loop block diagram for a DVR system with the time delay can be figured out as Fig. 3.

The time delay element in Fig. 3 can be linearized as (7).

$$L[f(t-T_d)] \approx \frac{1}{1+sT_d} F(s). \qquad (7)$$

The open loop transfer function of a DVR system including the linearized time delay element can be expressed as (8).

$$\frac{V_{scap}}{V_{scap}^*} = \frac{1}{1+sT_d} \cdot \frac{1}{s^2 L_f C_f + sR_f C_f + 1} = \frac{1}{1+sT_d} \cdot \frac{\omega_f^2}{s^2 + 2\xi_f \omega_f s + \omega_f^2}. \qquad (8)$$

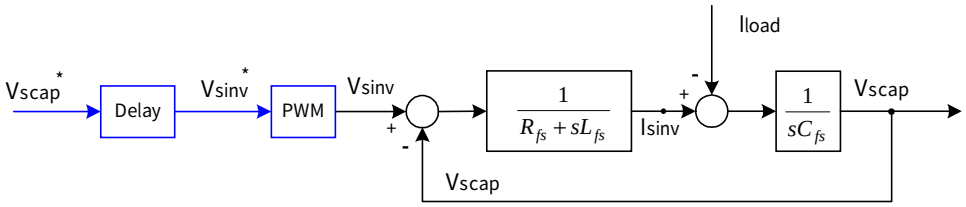

Fig. 3 Open loop block diagram for a DVR system included with time delay.

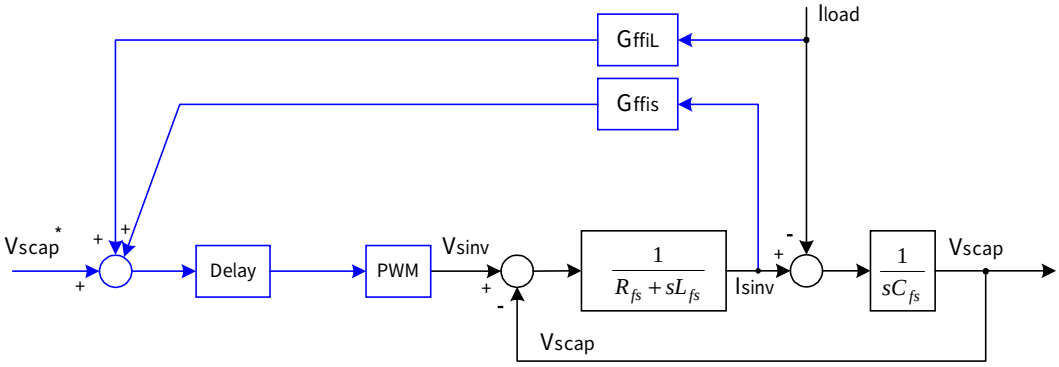

Fig. 4 Block diagram of proposed novel controller for DVR system included with time delay.

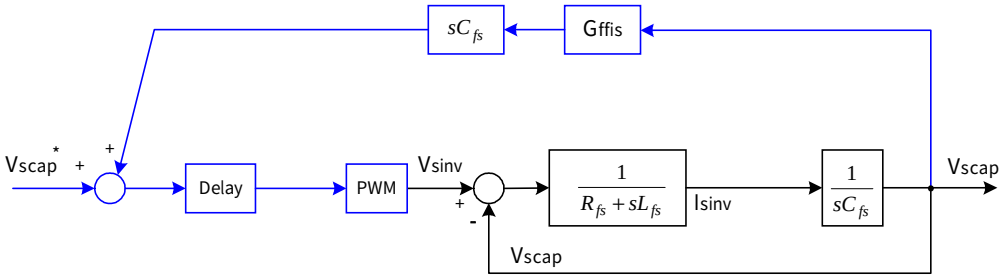

Fig. 5 Equivalent block diagram of the proposed voltage regulator.

As can see in (8) the transfer function for a DVR system including a time delay element becomes a 3rd order system that is combined with a 2nd order LC filter transfer function and a pole by the time delay element. It is important to notice that the physical limitation of voltage control loop on DVR systems is $\omega < \omega_f$. In other words, the control bandwidth ω_c may not be increased more than the filter resonant frequency ω_f by any controller. However, the closed loop damping factor ξ_c can be increased than the filter damping factor ξ_f by use of a proper controller.

III. CONTROLLLER DESIGN

A block diagram of the proposed control system with a feed forward and state feedback schemes is proposed as Fig. 4 for a DVR system included with a time delay element.

A. Voltage Regulation

When I_{load}=0, the transfer function of the voltage regulator becomes (9).

$$\frac{V_{scap}}{V_{scap}^{*}} = \frac{1}{(1+sT_d)} \cdot \frac{1}{(s^2 L_f C_f + sR_f C_f + 1) - sC_f G_{ffis}/(1+sT_d)} \quad (9)$$

If the time delay of the closed loop transfer function is set to equal to the time delay of the open loop transfer function, $T_c = T_d$, then the feed forward gain of the inverter current, G_{ffis}, can be determined as (10) to control the closed loop, and the damping factor can be determined as (11).

$$G_{ffis} = -(aR_f)(1+sT_d) = -aR_f - s(aR_fT_d), \quad (10)$$

$$\xi_c = (1+a)\frac{R_f}{2}\sqrt{\frac{C_f}{L_f}} = (1+a)\xi_f . \quad (11)$$

Thus the damping factor can in increased by adjusting factor "a".

B. Load Current Disturbance Rejection

When V_{scap}^{*}=0, the transfer function against the load current disturbance becomes (12).

$$\frac{V_{scap}}{I_{load}} = \frac{1}{(1+sT_d)} \cdot \frac{G_{ffiL} + G_{ffis} - (R_f + sL_f)(1+sT_d)}{(s^2L_fC_f + sR_fC_f + 1) - sC_fG_{ffis}/(1+sT_d)} . \quad (12)$$

The feed forward gain of the load current, G_{ffiL}, may be determined as (13) to completely reject the load current disturbance.

$$\begin{aligned} G_{ffiL} &= (R_f + sL_f)(1+sT_d) - G_{ffis} \\ &= s^2L_fT_d + s\left[(1+a)R_fT_d + L_f\right] + (1+a)R_f . \end{aligned} \quad (13)$$

It is very difficult to implement a 2nd order differentiation in a digital control system, but fortunately since $L_fT_d \approx 0$, (13) can be reasonably approximated to (14).

$$G_{ffiL} = s\left[(1+a)R_fT_d + L_f\right] + (1+a)R_f . \quad (14)$$

C. Time Delay in Control System

Fig. 5 shows an equivalent control block diagram of the proposed voltage regulator when the sensing point is moved from the inverter current to the output voltage. When only the damping factor is considered in (10) so that $G_{ffis} = -aR_f$, then G_{ffis} acts as a differential feed forward compensation for the output voltage as shown in Fig. 5. Here the equivalent differential feed forward gain for the output voltage is $sC_f \cdot G_{ffis} = -s(aR_fC_f)$. That is, the inverter current feed forward gain, G_{ffis}, attenuates the oscillation of the output voltages. Therefore abrupt change of the output voltages can be possible without an overshoot.

Besides, when no time delay element exists in the control system, the differential feed forward gain acts as a pure damping element against the voltage resonance. However, when a time delay is included into the control system, the differential feed forward gain does not always ensure damping against the voltage resonance. Simulations are used to investigate the relation between the closed loop damping factor and the differential feed forward gain with respect to the time delay.

TABLE I Simulation Condition

R_f	0.4 Ω
C_f	90 μF
L_f	400 μH
ξ_f	0.095
ω_f	2π(840Hz)
T_f	1.2ms

Here, filter resonance period $T_f = 1/f_{filter} = 2\pi/\omega_f$.

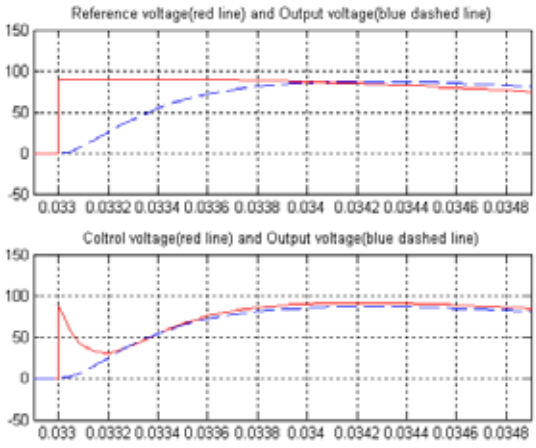

Fig. 6 Voltage response of an analog controlled DVR without time delay when ξ=1.0.

Simulation condition is shown in Table I. The filter resonance frequency is around $\omega_f = 2\pi\times840$Hz, that is, the filter resonance period is about T_f=1.2ms. The filter damping factor is around 0.095. Applying (11), the inverter feed forward gain should be G_{ffis}=-3.82Ω to get the closed loop damping factor as 1.0.

Fig. 6 shows the voltage response of an analog controlled DVR without time delay. Here the DVR inverter is assumed an ideal linear amplifier that has no time delay. The closed loop damping factor is set to 1.0. In the figure, the waveforms on the upper window display the reference compensation voltage (solid line) and the output compensation voltage (dashed line), and those on the lower window show the inverter control voltage (solid line) and the output compensation voltage (dashed line). At time t=0.033s, the reference compensation voltage is commanded suddenly. This kind of situation normally occurs in DVR systems. Although the steady state reference compensation voltage is 60Hz fundamental frequency and sinusoidal waveform, the voltage response can be regarded as a step response for a very short time interval.

As shown in Fig. 6, the inverter control voltage appears to be the same as the reference compensation voltage at first. However, the inverter control voltage drastically decreases

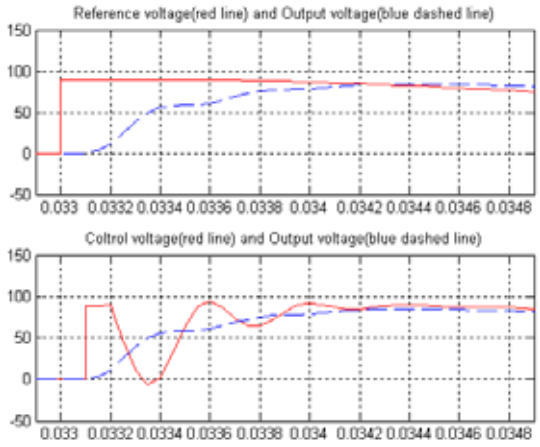

Fig. 7 Voltage response of a discrete controlled DVR with the sampling time of T_{samp} =T_f /12 when ξ=1.0.

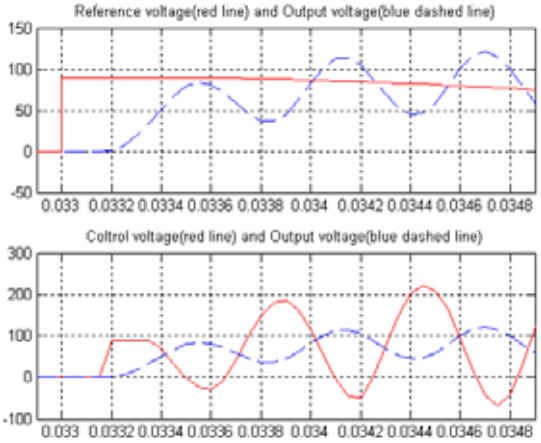

Fig. 8 Voltage response of a discrete controlled DVR with the sampling time of T_{samp} =T_f /6 when ξ=1.0.

according to the increase of the output compensation voltage in order to damp out the resonance of the output compensation voltage. This aspect occurs from the effect of the differential feed forward gain G_{ffis}. If the closed loop damping factor is set to smaller than 1.0, then this damping effect also decreases, resulting in an oscillation of the output compensation voltage. It is worth to mention that the maximum damping effect by the differential feed forward gain occurs around T_f /6 after the abrupt change of the reference compensation voltage regardless of the magnitude of the closed loop damping factor. As time passes, the inveter control voltage and the output compensation voltage smoothly converge to the reference compensation voltage.

The damping effect has to activate as possible as early stage according to the abrupt change of the reference compensation voltage. However, the activation of damping effect is always delayed by the inherent time delay in discrete control systems. For example, Fig. 7 and Fig. 8 show the voltage responses of the DVR system with the closed loop damping factor of 1.0 as like in Fig. 6, but different time delays are considered in a discrete control system.

In case of Fig. 7 a sampling time of T_{samp} =T_f /12=100μs was considered in the discrete control system to simulate the time delay effect. The first inverter control voltage appears T_f /12 after the abrupt change of the reference compensation voltage. Then the output compensation voltage starts to increase T_f /12 after the abrupt change of the reference compensation voltage. Besides, the differential feed forward controller spends one sampling time of T_f /12 from sensing the output compensation voltage to actuating the inverter voltage. This means that the output compensation voltage freely increases with the damping factor of 0.095 that is inherent damping factor of the output LC filter, during initial time interval of T_f /12. Moreover precise damping is not possible since the differential feed forward controller continuously delays by amount of T_f /12.

In case of Fig. 8 a sampling time of T_{samp} =T_f /6=200μs was considered in the discrete control system. Thus the output compensation voltage increases quite large amount during the initial time interval of T_f /6. In this case the delayed differential feed forward controller excites the oscillation of the output compensation voltage instead of damping it.

These simulation results show that in DVR systems there must be certain limitations on the closed loop damping factor when a sampling time exists in discrete control systems. Based on experience through simulations and experiments, a guideline to determine the closed loop damping factor in DVR systems with respect to the sampling time, T_{samp} , and the output LC filter resonance period, T_f , given by (15).

$$\xi_c^* \le 2^{-\frac{12T_{samp}}{T_f}} \tag{15}$$

D. Time Delay in Inverter

Inverter PWM switching may pose an additional time delay element in DVR systems. If the PWM switching frequency is high enough compared to the sampling time in discrete control systems, the voltage response by use of an ideal linear amplifier or a PWM inverter may make no difference in DVR systems except some switching frequency ripples at the output voltage. However, the switching frequency can not be increased infinitely because of the limitation of switching devices. This section discusses on the minimum inverter switching frequency, which is critical to guarantee the performance of DVR systems similar to the case of ideal linear amplifiers.

An inverter PWM switching may be an additional time delay element in DVR systems. The average delay time of a PWM inverter is half of the switching period. As shown in Fig. 6, the differential feed forward controller must output full damping effect within T_f /6 when a time delay is not considered. When only a sampling time T_{samp} except an inverter switching delay is considered in a discrete control system, the output of the maximum damping effect should be within T_f/6+T_{samp}. This means that the inverter has to generate the second actuating pulse within T_f /6+T_{samp} after the first

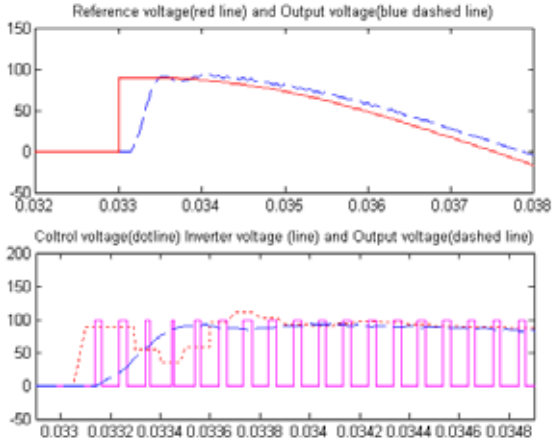

Fig. 9 Voltage response of a digital controlled DVR system with sampling time T_{samp} =T_f /12 when fsw=10kHz, ξ=0.5.

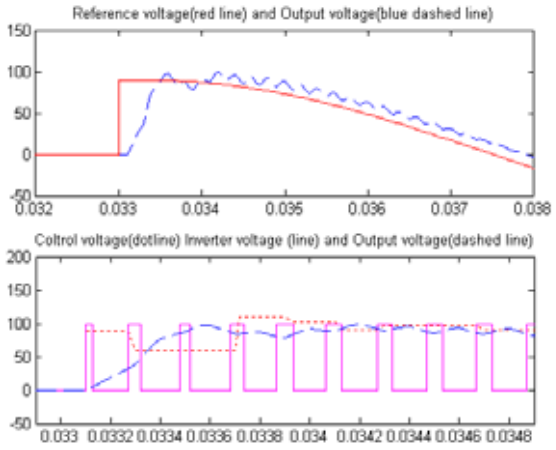

Fig. 10 Voltage response of a digital controlled DVR system with sampling time T_{samp} =T_f /12 when fsw=5kHz, ξ=0.5.

pulse to the output LC filter was generated. However, since the average time delay of the PWM switching is 0.5 times of the switching period, the inverter switching period must be shorter than (T_f /6+T_{samp})/1.5. Therefore, the design guideline for the minimum switching frequency of the PWM inverter for a sampling time T_{samp} of the discrete control system can be determined by (16).

$$f_{sw}^{*} \geq \frac{1.5}{T_f / 6 + T_{samp}} \tag{16}$$

For example, when a target damping factor is set to ξ_c=0.5, the sampling time should be T_{samp} <T_f /12 as determined by (15). Then the switching frequency of the PWM inverter has to be higher than 6/T_f Hz. That is, the switching frequency of the PWM inverter in the simulation condition has to be larger than 5 kHz.

Fig. 9 and Fig. 10 show the simulation results of the proposed DVR control system with the closed loop damping factor ξ_c=0.5 and the sampling time T_{samp}=100μs when the switching frequency was set to 10 kHz and 5 kHz respectively.

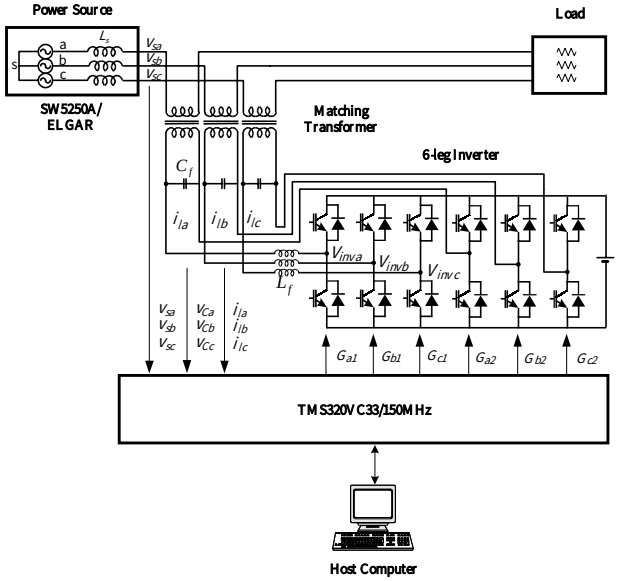

Fig. 11 Experimental DVR system with DSP control board.

Fig. 9 shows very stable and good dynamics of the output compensation voltage since the switching frequency was set to two times higher than the minimum switching frequency. The output compensation voltage is settled around 500μs. Although the ripples and the settling time are slightly increased, the output compensation voltage is stable and has good control dynamics even when the switching frequency was equal to the critical switching frequency in Fig. 10.

IV. EXPERIMENTAL RESULT

A. Experimental Setup

Experiments have been performed to verify the proposed control algorithm on a DVR system. Fig. 11 shows the experimental DVR system. The rated line voltage of the grid is 220Vrms/ 60Hz. 50% symmetrical voltage sags were generated by the power source, SW5250A/ELGAR. The fault was generated over 50 ms.

The experimental condition is on Table II. The DVR consists of a 6-leg inverter, three output LC filters, and three single-phase matching transformers. The 6-leg inverter has 12 IGBT switches and a dc power supply in the dc link. The switching frequency of the IGBT switches is 10 kHz.

TABLE II Experimental Condition

T_{samp}	100 μsec
f_{sw}	10 kHz
R_{Load}	40 Ω
R_f	0.4 Ω
C_f	80 μF
L_f	400 μH
ω_f	2π(890Hz)

B. Experimental Result

Fig. 12 and Fig. 13 show the experimental waveforms of the proposed DVR control system. The DVR compensates for the 50% voltage sags over 50ms. Since the control for the output compensation voltage is independent in each phase, only the a-phase voltage waveform was shown for convenience. The waveforms of the upper window of Fig. 12 show the reference compensation voltage v_{scap}^{*} and the actual output compensation voltage v_{scap} in relatively long time interval. The waveforms of the lower window of Fig. 12 show the zooming for the reference compensation voltage and the actual output compensation voltage at the instant of the abrupt change of the reference compensation voltage. No overshoot is observed in the output compensation voltage. The output compensation voltage decently converges to the reference compensation voltage within around 500μs.

The total time delay mainly comes from the sampling time of the digital controller, half of the inverter switching period, and the delay through the output LC filters. When the closed loop damping factor is set to unity, the output LC filter acts as two cascaded time delay components so that the transfer function of the voltage regulator becomes (17).

$$\frac{V_{scap}}{V_{scap}^{*}} = \frac{1}{(1+sT_{samp})} \cdot \frac{1}{(1+s/\omega_f)} \cdot \frac{1}{(1+s/\omega_f)} . \qquad (17)$$

Adding half of the inverter switching period to (17), the total time delay of the output compensation voltage v_{scap} from the reference compensation voltage v_{scap}^{*} can be calculated approximately as (18).

$$\begin{aligned} T_{delay} &= 0.5/f_{sw} + T_{samp} + 2/\omega_f \\ &\approx 50\mu s + 100\mu s + 358\mu s \\ &= 508\mu s \end{aligned} . \qquad (18)$$

Fig. 13 shows experimental waveforms for the source voltage V_{Src} (upper) and the load voltage V_{Load} (lower) of a digital controlled DVR system. Although 50% of voltage sag occurs in the source voltage, the DVR successfully rides through the load voltage with only small notch that has 0.5 ms of width.

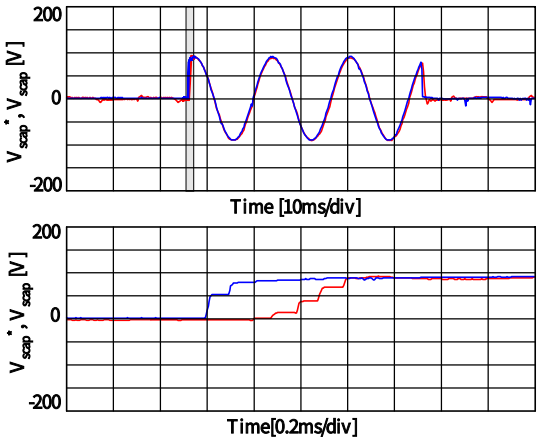

Fig. 12 Experimental voltage response of output compensation voltage v_{scap} to reference compensation voltage v_{scap}^{*} of a digital controlled DVR system with sampling time $T_{samp}=T_f/12$ when fsw=10kHz, ξ=0.5.

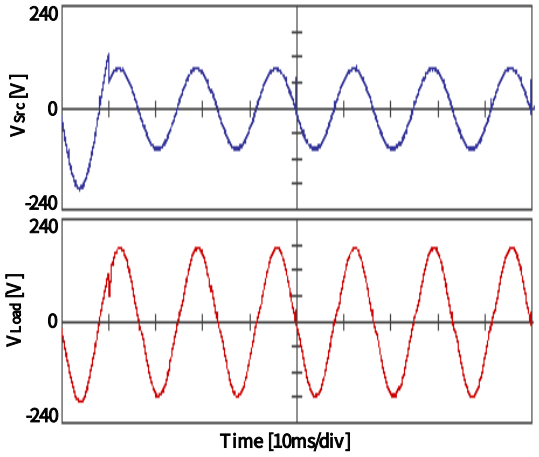

Fig. 13 Experimental waveforms for the source voltage V_{Src} (upper) and the load voltage V_{Load} (lower) of a digital controlled DVR system with sampling time $T_{samp}=T_f/12$ when fsw=10kHz, ξ=0.5.

V. Conclusion

This paper has proposed a novel control method for the compensation voltages in DVR systems. Through the discussion of the control targets for DVRs based on the analysis for the power stage of DVR systems, this paper proposed a novel controller structure for DVR systems by use of feed forward and state feedback control scheme. The control bandwidth of the proposed controller can be increased up to the filter resonance frequency, which is the physical limit of DVR systems. This paper presented some important design guidelines for the proposed DVR controller, with respect to the control delay and the filter resonance frequency. This paper also analyzed total time delay that is mainly resulted from the sampling time of the digital controller, the inverter switching, and the output LC filter.

The proposed theory has been verified by an experimental DVR system that shows very good performance as predicted by the analysis and simulations. Further study is going on to decrease the time delay of the control system in DVRs.

ACKNOWLEDGMENT

The authors wish to thank strategic project of EESRI (Electrical Engineering and Science Research Institute) for financial supports during the preparation of this paper.

REFERENCES

[1] G. Joos, "Three-Phase Static Series Voltage Regulator Control Algorithms for Dynamic Sag Compensation." *Proc. of the IEEE International Symposium on Industrial Electronics(ISIE)*, 1999, pp. 515-520.

[2] J. Nielson, F. Blaabjerg, N. Mohan, "Control Strategies for Dynamic Voltage Restorer Compensating Voltage Sags with Phase Jump," *Conf. Rec. IEEE-APEC Annu. Meeting*, 2001, pp. 1267-1273.

[3] S.J. Lee, S.K. Sul, H. Kim, and F. Blaabjerg, "The Novel Control Algorithm for Static Series Compensators by use of PQR Power Theory", *IEEE Trans. On Power Electronics*, vol.19, no.3, pp-, May, 2004 (in press).

[4] S.Buso, L.Malesani, P.Mattavelli, "Comparison of Current Control Techniques for Active Filter Applications," *IEEE Trans. Industrial Electronics*, vol. 45, no. 5, pp. 722-729, Oct. 1998.

[5] T. Kawabata, T. Miyashita, Y. Yamamoto, "Digital Control of Three-Phase PWM Inverter with LC Filter," *IEEE Trans. Power Electronics*, vol. 6, no. 1, pp. 62-72, Jan. 1991.

[6] O. Kueker, "Deadbeat Control of a Three-Phase Inverter with an Output LC Filter," *IEEE Trans. Power Electronics*, vol. 11, no. 1, pp. 16-23, Jan. 1996.

[7] M. Ryan, D. Lorenz, "A Synchronous-Frame Controller for a Single-Phase Sine Wave Inverter," *Conf. Rec. IEEE-APEC Ann. Meeting*, pp. 813-819, 1997.

[8] S. Lee Y. Chae, J. Cho, G. Choe, H. Mok, D. Jang, "A New Control Strategy for Instantaneous Voltage Compensator Using 3-Phase PWM Inverter," *Conf. Rec. IEEE-PESC*, 1998, pp. 248-254.

[9] M.Vilathgamuwa, A. Perera, S. Choi, "Performance Improvement of the Dynamic Voltage Restorer with Closed-Loop Load Voltage and Current-Mode Control," *IEEE Trans. Power Electronics*, vol. 17, no. 5, pp. 824-834, Sep. 2002.

[10] S.Fukuda, Y.Fukuwara, H.Kamiya, "An Adaptive Current Control Technique for Active Filters," *Conf. Rec. IEEE-PCC2002*, 2002, pp. 789-794.

New Concept for High Voltage – Modular Multilevel Converter
PESC 2004 Conference in Aachen, Germany

R. Marquardt, A. Lesnicar
Institute of Power Electronics and Control
Universität der Bundeswehr München, Germany
Email: rainer.marquardt@unibw-muenchen.de
Email: anton.lesnicar@unibw-muenchen.de

***Abstract* — Multi level voltage source converters are getting increased importance for applications in the high voltage range, for example network interties. This paper is focused on main aspects of industrial realization, scaling problems with increasing voltage level, modular construction and failure effects. The main converter topologies: diode-clamped, capacitor-clamped, cascade H-bridge and the new M²LC-type are analyzed and compared.**

A new universal plant, enabling back to back operation of various M²LC-converter systems up to 2MW real power flow is presented.

I. INTRODUCTION

The global trend to decentralized power generation and the deregulation of energy markets are increasing the importance of advanced power electronic systems. Several types of multilevel converters have been investigated for these new applications [1] …. [6].

High voltage/high power capability and low voltage distortion on the line side are basic requirements for this application field. In addition - regarding the industrial implementation of these converter system - a lot of other important aspects have to be taken into account:

A first goal is a strictly modular construction, in order to enable scaling to different power and voltage levels, using the same hardware. A second point is high availability, which calls for redundant operation capability after component failures. Failure management is a third point of very high importance. This includes avoidance of mechanical destruction due to high surge currents or arcing.

Known multilevel converter types and the new modular M²LC-type [7], [8] are investigated with respect to these requirements of industrial applications. Additionally, a universal prototype converter system for testing the new M²LC-types up to 9-level configurations is described.

II. MULTILEVEL CONVERTER FOR HIGH VOLTAGE APPLICATIONS

Four main topologies are known for multilevel converters:

- Diode-clamped type (NPC and up with DC-link capacitors [1], [2], [9]) (Fig. 1).
- Capacitor-clamped type (with flying capacitors and DC-link capacitors [3], [4]) (Fig. 2).
- Cascade H-Bridge type (with separate DC-sources, without common DC-link [5], [6]) (Fig. 3).
- Modular M²LC type (without separate DC-sources, with common DC-link, but without DC-link-capacitors). This new type enables direct and fast control of the DC-link voltage via the switching states of the submodules [7], [8] (Fig. 4).

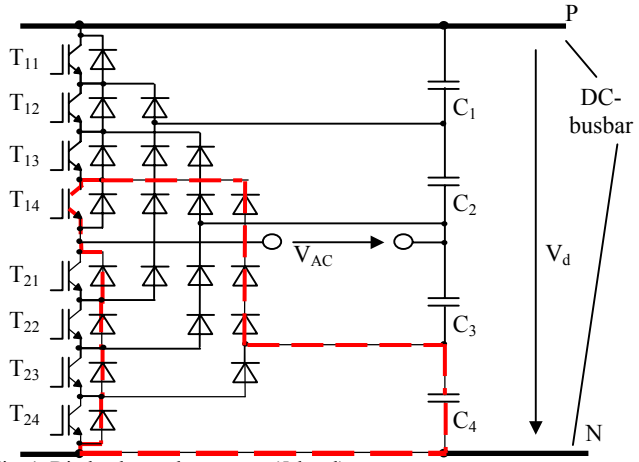

Fig. 1 Diode-clamped converter (5-level)

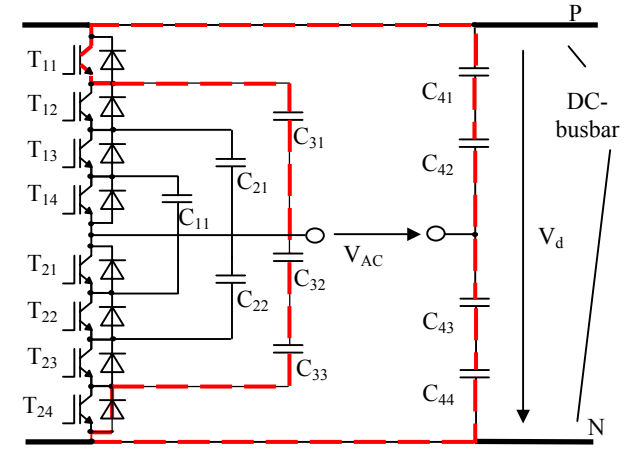

Fig. 2 Capacitor-clamped converter (5-level)

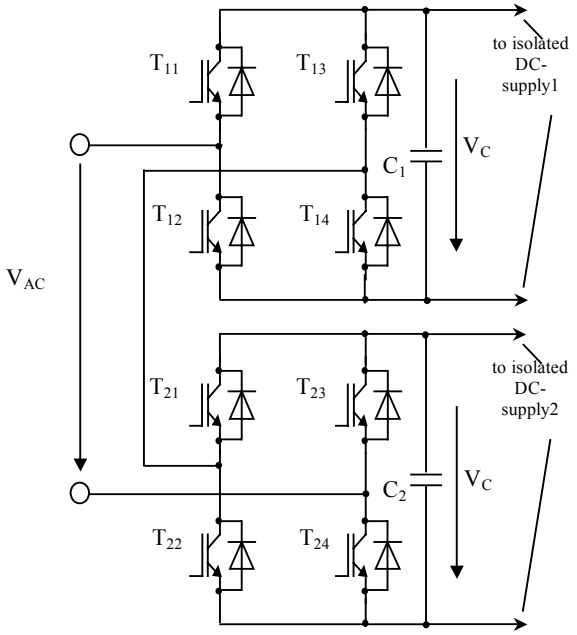

Fig. 3 Cascade H-Bridge converter (5-level)

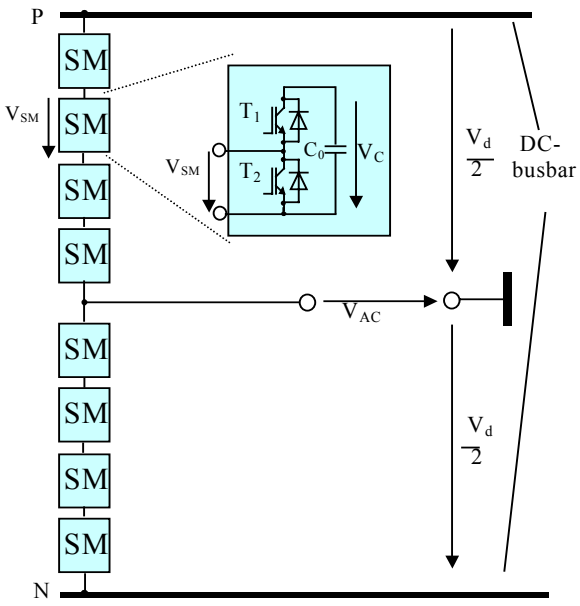

Fig. 4 **M**odular **M**ulti**l**evel **C**onverter M^2LC (5-level)

In this paper the focus will be on the main topics, which are important for industrial realization. Important points, concerning industrial implementation, are:

- Maximum surge current and mechanical destruction
- Stray inductance versus isolation requirements
- Modular construction and scaling effects
- Interface problems concerning isolation and EMC

A. Maximum surge current and mechanical destruction

The diode-clamped type (Fig.1) and the capacitor-clamped type (Fig.2) incorporate a central DC-link-busbar with directly connected DC-link-capacitors of high capacity. For the diode-clamped type these capacitors have to be split up into a series connection in order to form the voltage taps.

As well known, semiconductors failures and gating failures can lead to a "hard discharge" of DC-link-capacitors. In the high voltage range (V_d = 2kV … > 20kV) the resulting surge current (i_s) is not any more limited by ohmic resistances. On the contrary, with increasing V_d, the peak current ($\hat{I}_s$) approaches almost exactly the value without ohmic damping

$$\hat{I}_s = V_d \cdot \sqrt{\frac{C_d}{L_{ss}}} \qquad (1)$$

where (C_d) represents the total DC-capacitance installed at the DC-link and (L_{ss}) represents the total stray inductance of the short circuit loop including the DC-capacitors. Peak currents in the order of 200…300 kA and more lead to magnetic forces, which cause destruction of busbars and terminals. Long term experience from many industrial applications has proven that these values are very demanding for any mechanical construction. If the surge current leads to severe mechanical deformations or open circuit and/or arcing, the damage to the converter system and equipment in the neighborhood will be completely unacceptable. It can be shown from various long term experiences and theory that gate voltage monitoring and "short circuit proof" IGBTs cannot exclude the possibility of these catastrophic failures.

Both the diode-clamped type and the capacitor-clamped type suffer from this severe safety problem, when applied in the high voltage/high power range.

The use of IGCT-devices is slightly better with respect to this problem, because the generally applied chokes of the turn on snubber will increase the inductance (L_{ss}).

B. Stray inductance versus isolation requirements

The requirements for low stray inductance and reliable isolation are in severe contradiction when increasing the voltage level. As it is well known, the acceptable stray inductance is proportional to the switching overvoltage of the semiconductors and inversely proportional to their switching speed (di/dt).

The mechanical construction and physical layout of the multilevel converter has to assure a low magnetic field energy stored in the critical switching loops ("commutation loops"). Examples of "long" commutation loops are indicated in Fig. 1 and Fig. 2 by red dotted lines.

For a given current (i_C) that has to be switched this imposes the need to minimize the stray inductance (L_S) of the commutation loop. Since more than a decade in industry,

a flat "multilayer" busbar design with minimum isolation layer thickness, represents the standard construction for low stray inductance commutation loops. Using these constructions, the required number of terminals (for connecting the power devices) and the required air distances at the terminals will create most of the loop inductance. As a rule of thumb, each high voltage semiconductor with its terminals (IGBT or diode) will add at least 30nH and each power capacitors will add at least 50nH to the loop inductance. When increasing the number of voltage levels, the loop inductance will reach excessive values. Polarized snubbers will become necessary, adding to circuit complexity, power losses and cost.

C. *Modular construction and scaling effects*

Taking into account industrial production of the converter and service requirements, a strictly modular construction of the power circuit is an important advantage. Strictly spoken, this means that the power circuit should be solely composed from an arbitrary number of identical submodules and no additional central components.

The scaling to different voltage levels and power levels should be done by varying the number of submodules, only. Therefore, the same hardware with the same mechanical construction will be used for a wide range of applications.

Referring to the previous chapters A and B, further investigations have shown that the diode clamped-type and the capacitor clamped-type cannot meet these requirements. The mechanical construction has to be specially designed for a predefined number of voltage levels. In the best case, it could be downscaled to a reduced number of voltage levels, by replacing semiconductors and capacitors by short circuit parts or isolating parts.

In addition to these mechanical aspects, unwanted scaling effects of the electrical characteristics have to be taken into account: The stray inductance (L_S, see Fig.1 and 2) of the commutation loop increases with increasing number of voltage levels. The same applies to the surge current problem. The first point will force a derating of the nominal voltage and/or current per semiconductor. The second point will force an "improved" mechanical construction or an additional voltage derating.

On the other side, the topologies of Fig.3 and 4 present conditions, which enable significantly better solutions regarding modularity and scaling.

When implementing very high voltage converters (V_d>10kV), even the parasitic stray capacitances to earth can lead to unwanted scaling effects, because the dynamic voltage distribution of series connected devices may be influenced. Here, the topologies according to Fig.3 and 4 present the advantage that the local DC-capacitors are several orders of magnitude bigger than the parasitic capacitances to earth. Therefore, the voltage (V_C) will define the semiconductor voltages very well, even under transient conditions.

D. *Interface problems concerning isolation and EMC*

When increasing the number of voltage levels, all interfaces between the power circuit and the control side have to cope with the increased isolation- and EMC-requirements. Major EMC-problems are created by isolation transformers and their parasitic coupling capacitances (C_k). These transformers are generally used in order to supply gate drivers and transducers and will have (C_k) in the order of several tens of picofarads, if small in size and well designed.

When separate, isolated DC-Sources in the power circuit are needed for real power flow (Fig.3), these large transformers with high coupling capacitance (of several tens of nanofarads) must be taken into account. This leads to very high EMC-disturbing current peaks under dv/dt in the power circuit.

Regarding the M^{2}LC-type pilot plant, it was decided not to deteriorate the excellent characteristics of this concept. Therefore, each gate driver power supply is fed from the local DC-capacitor of each submodule. The gate driver- and transducer-signals are transmitted via optical fibre cable. Due to a special digital encoding with error correction, four gate signals, two transducer and fault signals can be transmitted per submodule via a common duplex fibre cable [10]. Therefore, no additional interfaces of the submodules are necessary - despite the two conventional cables at the AC-side.

III. SIMULATION RESULTS

For demonstrating the good performance of the M^{2}LC-topology, a 3-phase pulse-controlled inverter was simulated. For this purpose the simulation software SIMPLORER linked to MATLAB/SIMULINK was used. In the model, 3 inverter legs with 4 identical submodules per arm (Fig.4) are connected to a common DC-busbar. The capacitance (C_0) installed in each submodule has been calculated according to the equations in paper [7]. There is no additional central capacitive energy storage connected to the DC-busbar.

In practice difficulties occur when a common network intertie has to start without power from the utility from the de-energized condition to operation condition ("black start"). The new power converter topology enables a simple and safe black start. In the following, a possible process of charge per inverter arm is described.

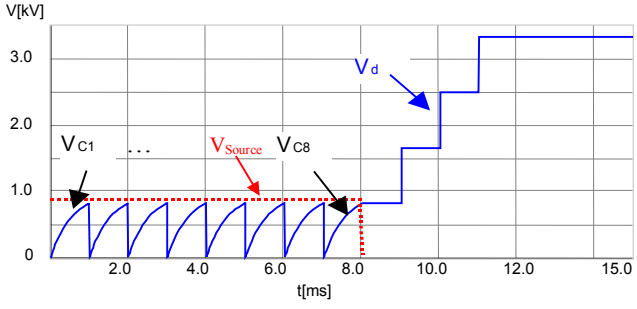

Fig. 5 Process of charge per inverter arm

In order to accomplish this procedure, only one auxiliary voltage source with a relatively low output voltage ($V_{Load} \approx V_C$) is necessary. The output terminals of the supply are connected to the DC-busbar of the M²LC. Per inverter leg a number of (2n-1) IGBTs T_2 (see Fig. 4) are turned on. The remaining IGBT T_2 and all remaining IGBTs T_1 in the inverter leg are kept off. When one capacitor per phase leg has reached the operation voltage, the next ones are selected by appropriate gating. In that way all capacitors in the arms are charged to the operation voltage (Fig. 5). Finally, the voltage source has to be disconnected by series diodes or mechanical switching.

For the purpose of inverter control, diverse approaches for sinusoidal pulse width modulation have been published [11], [12]. A suitable control scheme is described in former paper [8], for example. The desired voltage and current values per phase, the common-mode voltage as well as the DC-voltage are synthesized by controlling the voltages in each arm.

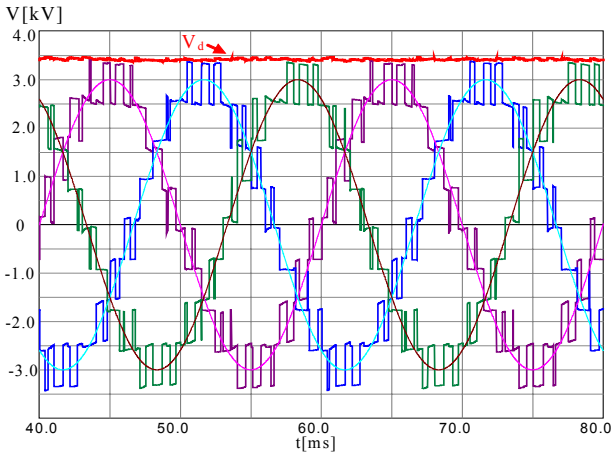

Fig. 6a Line-to-line voltages and DC-busbar voltage (5-level topology)

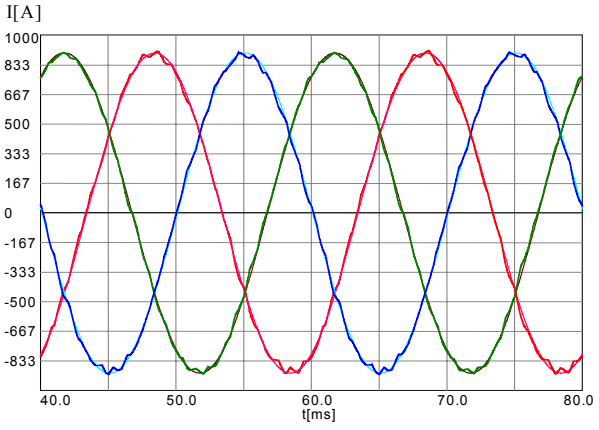

Fig. 6b Phase currents in the load

Fig. 6a illustrates both the controlled voltage on the DC-busbar and the line-to-line voltages. It can be seen that the voltages are synthesized on line without consideration of a predefined pulse pattern. The multilevel sinusoidal pulse width modulation is carried out with a pulse frequency of 1 kHz. The resulting switching rate of the power devices (IGBT) is about 300 Hz. In order to reduce the switching losses, the voltage balancing of the capacitors is applied solely when the control state is changing[8]. The setpoint values and the correspondent simulation results of the phase currents are illustrated in Fig. 6b. Neither the obtained current curves nor the voltage curves are remarkably influenced by the ripple content of the capacitor voltages in each arm (Fig. 6c).

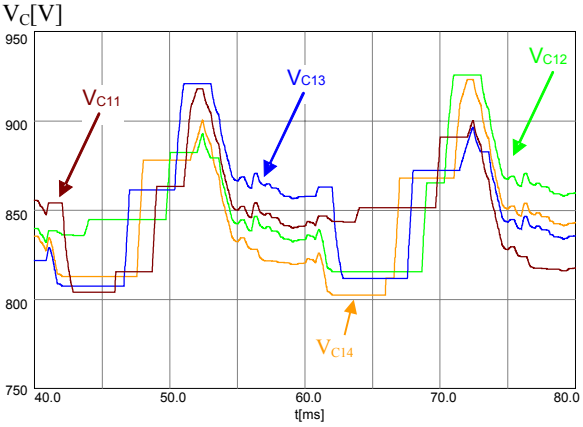

Fig. 6c Submodule voltages in an arm
(P_d = 2 MW; C_0 = 5.7 mF; V_d = 3400V; cosφ = 0.85)

IV. PROTOTYPE CONVERTER

To enable experimental tests and investigations under realistic conditions, using different control schemes, a prototype converter system was built in our laboratories. The converters are designed for real power transmission up to 2 megawatts per converter. Each converter cubicle contains 16 submodules, whereby one arm consists of a maximum of 8 identical submodules. Two converter systems can operate in back to back mode. By this means the real power flow is transmitted in circle, whereby the power supply has to compensate the power losses, only.

This pilot plant is designed for universal use in various configurations. It offers the possibility to realize two 9-level network interties, each composed of a DC-busbar with both 3-phase or 1-phase converters and inverters, respectively. Additionally, in this way asynchronous systems can be connected in back to back mode. Even AC/AC – direct converters can be realized and operated in back to back mode after reconfiguration of the pilot plant [10].

Two submodules are mounted per heat sink (Fig. 7). The construction of the submodules enables a variation of the capacity (C_0) per submodule in four equal steps. For this purpose Power-Chip-Capacitors (PCC) are used. The submodules are equipped with 1200V IGBTs. Via a common fibre-optical interface each submodule receives the correspondent switching commands and sends its capacitor voltage and error signal back to the central control unit. The power supply for the drive circuits and the data transfer are fed from the local capacitors. This autonomous supply is

able to operate in a wide voltage range (V_C = 100 … 850V). In consequence, the interface of a twin-submodule is composed solely of two conventional cables and one duplex fibre-optic cable. No additional connections or interfaces are necessary. Fig. 8 shows a completely 3-phase-M^{2}LC, as described in the former chapter.

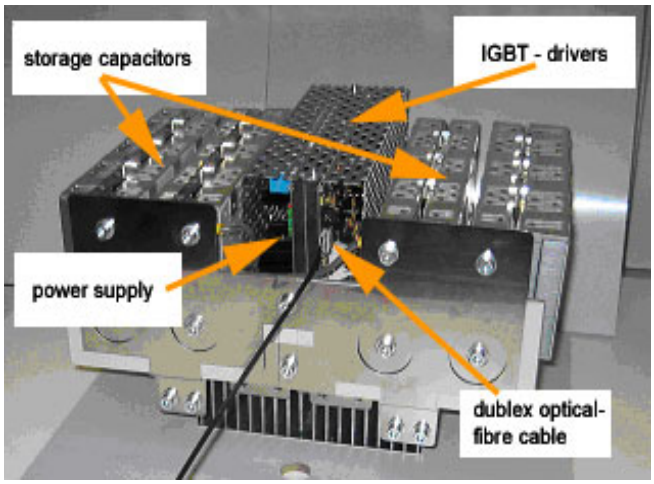

Fig. 7 Twin-submodule


Fig. 8 Complete 3-phase-M^{2}LC (5-level)

V. CONCLUSION

With regard to the construction and safety requirements the known multilevel converter topologies were investigated and compared. The complexity in design of the diode-clamped, as well as the capacitor-clamped types, increases considerably with the number of voltage-levels. In addition to this aspect, the central capacitive energy storage means a high potential hazard in a fault scenario. The H-bridge type is without the mentioned drawbacks, but for real power transmission it needs a high number of separate DC-supplies. As shown, the proposed M^{2}LC-topology is easily scalable to the desired high number of voltage steps. The modular construction simplifies failure management, maintenance and a consistent redundancy concept.

The presented universal pilot plant system will enable further extensive tests and investigation.

REFERENCES

[1] A. Nabae, I. Takahashi, and H. Akagi, “A new neutral-pint clamped PWM inverter,” IEEE Trans. Ind. Applicat., vol. IA-17, pp. 518-523, Sept./Oct. 1981.

[2] Xiaoming Yuan, Ivo Barbi, “A new diode clamping multilevel converter,” IEEE Trans. Ind. Applicat., vol. 15, pp. 495-501, March 1999.

[3] T. A. Meynard and H. Foch, “Multi-level choppers for high voltage applications,” Eur. Power Electron. Drives J., vol. 2, no. 1, p. 41, March 1992.

[4] C. Hochgraf, R. Lasseter, D. Divan, and T. A. Lipo, “Comparison of multilevel inverter for static var compensation,” in Conf. Rec. IEEE-IAS Annu. Meeting, Oct. 1994, pp. 921-928.

[5] F. Z. Peng and J. S. Lai, “Multilevel cascade voltage-source inverter with separate DC sources,” U.S. Patent 5 642 275, June 24, 1997.

[6] P. Hammond, “A new approach to enhance power quality for medium voltage ac drives,” IEEE Trans. Ind. Applicat., vol. 33, pp. 202-208, Jan./Feb. 1997.

[7] Rainer Marquardt, Anton Lesnicar, Jürgen Hildinger, “Modulares Stromrichterkonzept für Netzkupplungsanwendung bei hohen Spannungen”, ETG-Fachtagung, Bad Nauheim, Germany, 2002.

[8] R. Marquardt, A. Lesnicar, “A new modular voltage source inverter topology”, EPE’03, Toulouse, France, 2003.

[9] Xiaoming Yuan, Ivo Barbi, “Fundamentals of a new diode clamping multilevel inverter,” IEEE Trans. on Power Electron., vol. 15, no. 4, pp. 711-718, July 2000.

[10] M. Glinka, “Prototype of multilphase modular-multilevel-converter with 2MW power rating and 17-level-output-voltage,” PESC2004, Aachen, Germany, 2004.

[11] Nikola Celanovic, Dushan Boroyevich, “A fast space-vector modulation algorithm for multilevel three-phase converters,” IEEE Trans. Ind. Applicat. vol. 37, pp. 637-641, March/April 2001.

[12] Fei Wang, “Sine-triangle versus space-vector-modulation for three level PWM voltage-source inverters,” IEEE Trans. Ind. Applicat. vol. 38, pp. 500-506, March/April 2002.

Analysis and Improvement of Power Quality for A Fuel cell System based on Multilevel Converters

Yoon-Ho Kim Hyun-Wook Moon Soo-Hong Kim Eun-Jin Jeong
Dept. of Electrical Engineering, Chung-Ang University
221 Huksuk-dong, Dongjak-ku, Seoul, 156-756, Korea
Phone : +82-2-820-5290 Fax : +82-2-812-8417
E-mail : yhkim@cau.ac.kr

***Abstract*— The fuel cell system is one of very useful energy sources. The system has advantages as renewable and environmental sources. To obtain AC components from fuel cells it needs inverters. A multilevel converter is used as an inverter for a high power fuel cell system. Through harmonic analysis, it was shown that the harmonic components and THD increase while fundamental component decreases as voltage sag increases. To solve the voltage sag problems, three different approaches are investigated in this paper; installation of a boost converter at the fuel cell output, control of pulse widths, and use of ultracapacitors. The proposed three approaches are analyzed and compared using simulation results.**

I. INTRODUCTION

Fuel cell generation systems are expected to see increasing practical applications due to several advantages offered by them over conventional generation systems. These advantages include 1) low environmental pollution; 2) highly efficient power generation; 3) diversity of fuels (natural gas, LPG, methanol and naphtha); 4) reusability of exhaust heat; 5) modularity and 6) faster installation [1]. For the fuel cell generation systems to make an impact on future energy supply, they need to be utility interactive at medium to large power ratings in multi megawatt range [2]. The acceptance of large-scale fuel cell generation systems by power utilities is greatly influenced by the availability of high performance power conditioning system (PCS) in terms of efficiency, safety, reliability and cost [3]. Although fuel cell generation systems are to date not fully commercialized due to cost factor, progress towards this goal has been rather significant in recent years. In general, the function of a PCS in a fuel cell generation system is to convert the DC output power from the fuel cell to regulated AC power.

The multilevel inverter topology that seems to be gaining interest lately for high power application, is identified as an alternative for a fuel cell PCS [4]. The main feature of a multilevel inverter is its ability to reduce the voltage stress on each power device due to the utilization of multiple levels on the DC bus. This is especially important when a high DC side voltage is imposed by application. There are several types of multilevel inverters but the one considered in this paper is the H-bridge multilevel inverter. An important requirement of the multilevel inverter in applications involving real power transfer is DC sources that are isolated from one another thus revealing its suitability in fuel cell PCS applications due to the originally isolated DC voltages that are available from the fuel cell output. By considering this inverter topology, higher AC output voltage can be reached by employing either a small number of high-power fuel cell modules or a larger number of low-power fuel cell modules. In addition, other required fuel cell PCS inverter characteristics can also be fulfilled in terms of controllability of output voltage which depends on the proposed modulation strategy, availability for isolated operation, low output harmonics and high efficiency.

To solve the voltage sag problems, three approaches are introduced in this paper; installation of a boost converter at the fuel cell output, control of pulse widths, and use of ultracapacitors. The proposed three approaches are analyzed and compared using simulation results. The harmonic analysis results are described with different levels of inverters and voltage sag problems.

II. CASCADED H-BRIDGE MULTILEVEL INVERTER

Multilevel inverter structures have been developed to overcome shortcomings of solid-state switching device ratings so that they can be applied to high-voltage electrical systems. The multilevel voltage source inverters' unique structure allows them to reach high voltage with low harmonics without the use of transformers. This makes unique power electronics topologies suitable for flexible ac transmission systems and custom power applications [5], [6].

In multilevel inverters, there are two types; cascade and neutral point clamped (NPC). The H-bridge inverter is often used since it has advantages in switching control and non-requirement of additional diodes.

Fig. 2 shows the output voltage waveforms and switching patterns of the 7-level cascade inverter. Fig. 2(a) shows output waveforms of a stepped voltage and a fundamental component. Fig. 2(b) and fig. 2(c) show output voltages of converters. The number of output phase voltage levels m in a cascade inverter is defined by m=2s+1, where s is the number of inverters. Each separated dc source is connected to a single-phase full-bridge, or H-bridge, inverter.

Each inverter can generate three different voltage outputs, $+V_{dc}$, 0, and $-V_{dc}$ by connecting the dc source to the ac output with different combinations of the four switches, S_1, S_2, S_3, and S_4. To obtain $+V_{dc}$, switches S_1 and S_4 are turned on. Turning on switches S_2 and S_3 yields $-V_{dc}$. By turning on S_1 and S_2 or S_3 and S_4 or turning off all switches, the output voltage is zero [4]. As shown in fig. 2, the ac output of each of the different full-bridge inverter levels is connected in series such that the synthesized voltage waveform is the sum of the inverter

output. The output voltage is $v_{out} = v_1 + v_2 + v_3$.

The reason to have different switching patterns is for a power balance. When an H-bridge inverter cascades with two or more ones, if switching pattern has same duty cycle during a period at a specific switch, the power of fuel cells becomes unbalanced. Thus the switching patterns need to be designed for the power balance.

The factors that affect THD and harmonics of the output are the number of inverters in the implemented system and the duty cycle of the switching pulses.

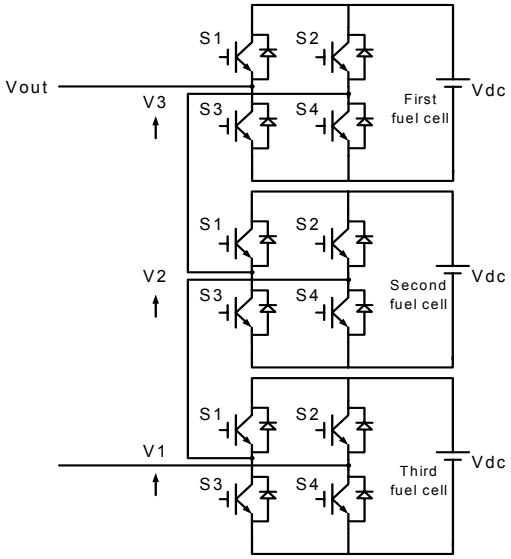

Fig. 1. A single-phase structure with a 7-level cascaded H-bridge inverter

III. HARMONIC ANALYSIS WITH DIFFERENT LEVELS OF MULTILEVEL INVERTERS AND A VOLTAGE SAG

The investigated fuel cell system has three independent fuel cells; each has 48V output and connected with multilevel cascade inverters. The system produces single phase output as shown in fig. 1. The final output has a 144V. Harmonic analysis is made when the level of cascade inverters varies and voltage sag of the fuel cell output is considered. The PSIM is used as a tool for simulation and analysis. Harmonics are analyzed when the levels of inverters varies from 3 to 9.

As shown in fig. 3, THD decreases when the number of levels increases.

IV. ANALYSIS WITH VOLTAGE SAGS

For the 7 level (3 H-Bridge inverters) system, harmonics analysis is made when the voltage sag of the fuel cell systems is assumed to vary from 0 to 40%. If the voltage sag exceeds 40% in fuel cells, it might cause damages in fuel cell systems. Thus it needs to keep the voltage sag not to exceed over 40% in fuel cell systems.

A. Voltage sag in first fuel cell

It is assumed that the first fuel cell has the voltage sag. Fig.

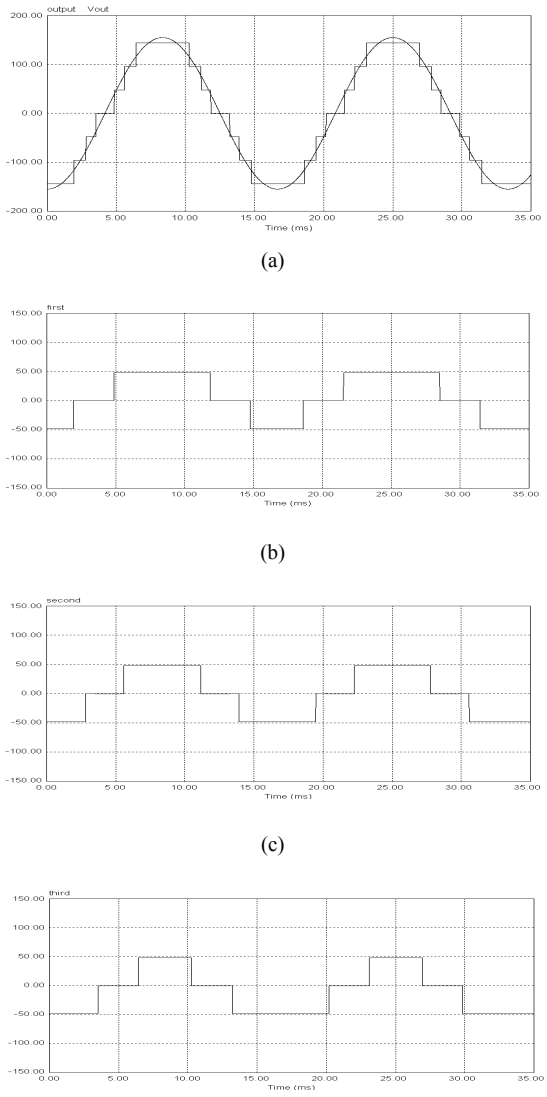

Fig.2. Waveforms and switching patterns of the 7-level cascade inverter.

(a) Final output (b) First converter output

(c) Second converter output (d) Third converter output

4. shows that THD increases as voltage sag increases.

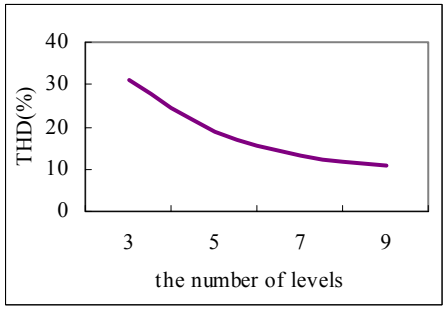

Fig. 3. THD with respect to the number of levels

B. *Voltage sag in second fuel cell*

Next, it is assumed that the second fuel cell has voltage sag. Fig. 5 shows that THD curve is U-shape as voltage sag increases.

However it can be seen that the THD with the second fuel cell voltage sag is lower than that with the first fuel cell voltage sag.

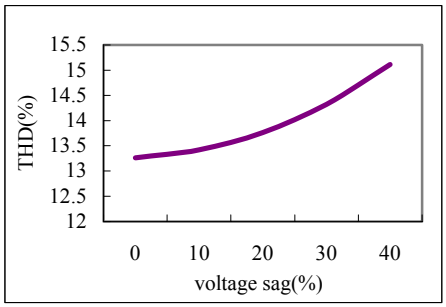

Fig. 4. THD with first fuel cell voltage sag

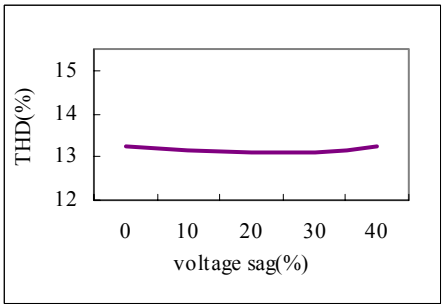

Fig. 5. THD with second fuel cell voltage sag

V. COMPENSATIONS OF VOLTAGE SAG

There are various approaches of the compensation for the voltage sag. Three different approaches are investigated in this paper: installation of a boost converter at the fuel cell output, control of pulse widths, and use of ultracapacitors. The proposed three approaches are analyzed and compared using simulation results.

A. *Installation of a boost converter*

Through harmonic analysis, it was shown that the harmonic components and THD increase while fundamental component decreases as voltage sag increases. To compensate the problems, a boost converter is installed at the fuel cell output. Instead of installing boost converters at all fuel cell output, only one boost converter is installed at one of the fuel cell output. A PI controller is designed to control boost converters. Fig. 6 shows the block diagram of the proposed fuel cell system. The system includes a boost converter, which is controlled by a PI controller to compensate the voltage sag.

Fig. 7 shows a boost converter. It is the conventional boost converter circuit.

Fig. 8 shows output waveforms when the first fuel cell has

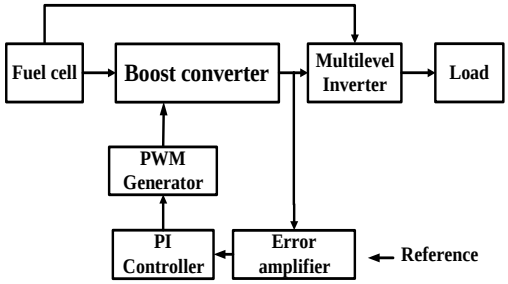

Fig. 6. Block diagram of the proposed fuel cell system with installation of a boost converter

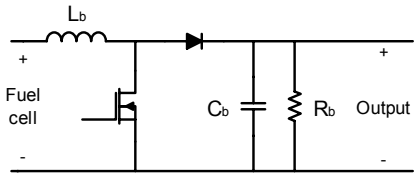

Fig. 7. A conventional boost converter

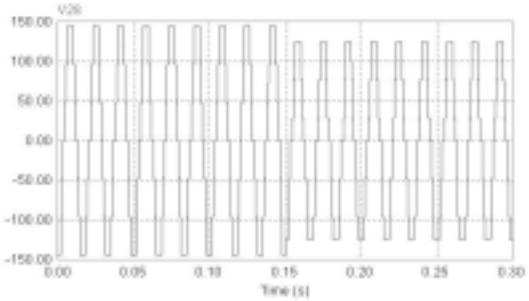

(a)

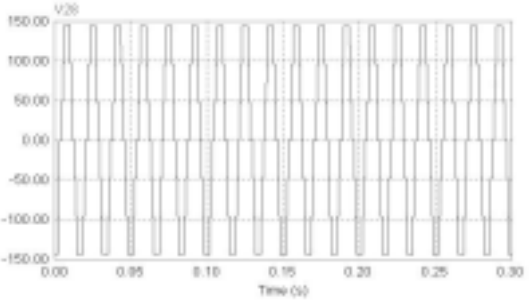

(b)

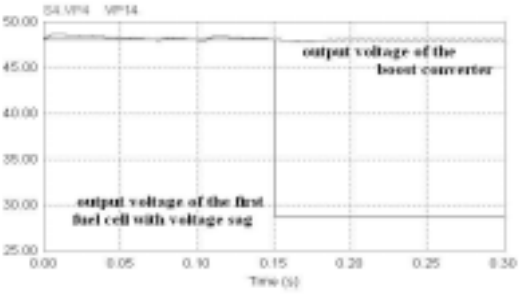

(c)

Fig. 8. (a) Non-compensated output voltage waveforms with voltage sag from 48V to 28.8V (40%)

(b) Compensated output voltage (c) Output voltage of the boost converter

40% voltage sag(from 48V to 28.8V) at t=0.15s. Fig. 8(a) shows that the fundamental component of the voltage decreases and THD increases. Fig. 8(b) shows that the fundamental component of the output voltage is compensated by installing a boost converter at the first fuel cell output. Fig. 8(c) shows that the boost converter output is that boosted to compensate the voltage sag using PI controllers.

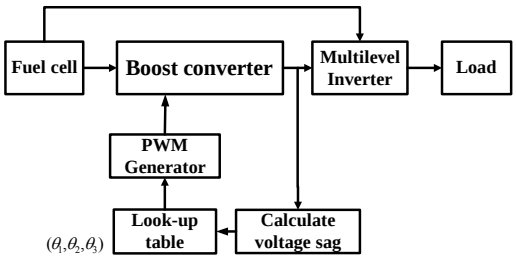

Fig. 9. Block diagram of the second proposed fuel cell system with control of pulse widths

B. Control of pulse widths

The proposed second approach for the compensation of voltage sag is to control pulse widths. Each H-bridge converter generates a step voltage by controlled duty width. If the voltage sag occurs at the first fuel cell in system, the system recalculates pulse widths at each converter. Rules of pulse width calculation at each converter are described as follows. 1) keep the fundamental voltage within the margin. 2) the output voltage has the minimum THD. Calculation of pulse widths is not simple. And it takes some time. Thus, it is better obtained data that are pre-calculated pulse widths with variation of the voltage sag. Fig. 9 shows the block diagram of the second proposed fuel cell system with control of pulse widths. If the voltage sag occurs, then sag information refers 'look-up table' which has values of pre-calculated pulse widths with respect to voltage sag. PWM generator produces new pulse patterns using 'look-up table'. Thus, although the system has the voltage sag, output voltage maintains the same fundamental voltage and has the minimum THD by control of pulse widths.

Fig. 10 shows output waveforms with the control of pulse widths when the first cell has the voltage sag. Fig. 10(a) shows output voltage of the first fuel cell. The time is divided into three intervals with respect to voltage sags. Voltage sag is 0% from 0s to 0.1s. From 0.1s to 0.2s, voltage sag is 40%, which is maximum voltage sag. After 0.2s, voltage sag is 20%. Fig. 10(b) shows a non-compensated output voltage of the system with voltage sags. The fundamental voltage decreases and THD increases with the voltage sag. Fig. 10(c) shows compensated output voltage by controlled pulse widths. When fuel cell experience the voltage sag, control of the pulse widths maintain the fundamental voltage and minimum THD.

Table 1 shows the difference between a non- compensated output voltage and compensated one. The fundamental voltage is set to be 138V (M.I. =0.9) with a margin. And θ_1, θ_2, θ_3 are calculated by rules in which the fundamental voltage maintains within the margin and an output voltage has the minimum THD. In case of a non-compensation, the fundamental voltage of output decreases as the voltage sag increases.

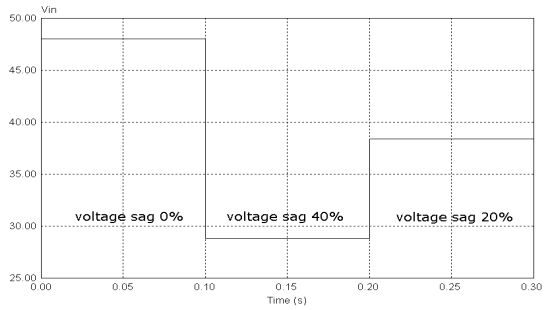

(a)

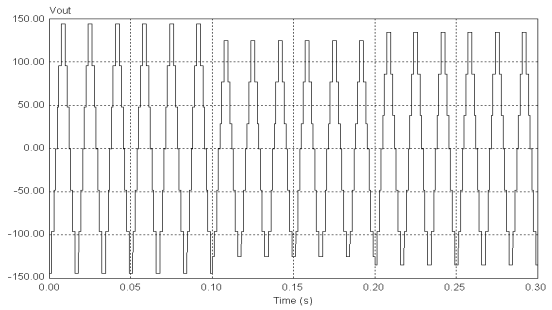

(b)

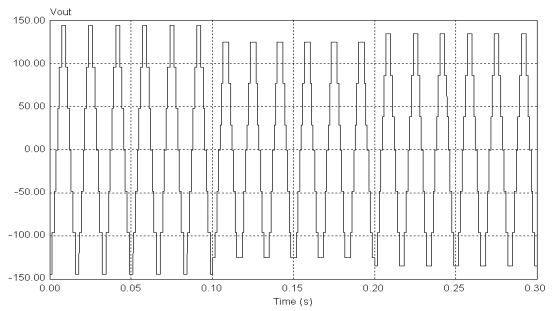

(c)

Fig. 10. (a) Output voltage of the first fuel cell according of the voltage sag

(b) Non-compensated output voltage waveforms

(c) Compensated output voltage waveforms

TABLE 1. THE DIFFERENCE BETWEEN NON-COMPENSATED OUTPUT VOLTAGE AND COMPENSATED ONE

	NON-COMPENSATED OUTPUT VOLTAGE			
VOLTAGE(SAG)	θ_1	θ_2	θ_3	V_1
48V(0%)	10.8°	33.3°	63.9°	138.001V
28.8V(40%)	10.8°	33.3°	63.9°	120.606V
38.4V(20%)	10.8°	33.3°	63.9°	129.303V

COMPENSATED OUTPUT VOLTAGE

VOLTAGE(SAG)	θ_1	θ_2	θ_3	V_1
48V(0%)	10.8°	33.3°	63.9°	138.001V
28.8V(40%)	9.9°	28.8°	48.6°	138.005V
38.4V(20%)	9.9°	32.4°	57.6°	138.011V

However, in case of compensation, the fundamental voltage maintains within the margin.

C. *Use of the ultracapacitors*

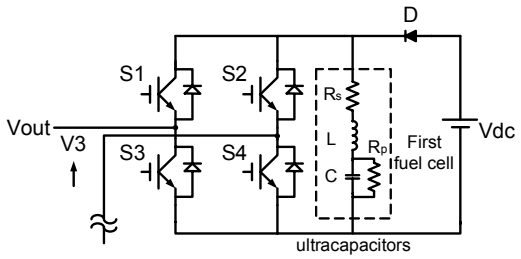

Fig. 11. One part of a 7-level cascaded H-bridge inverter with equivalent circuit of ultracapacitors

The proposed third approach for compensation voltage sag is to use ultracapacitors. If the voltage sag occurs at the first fuel cell in system, the voltage sag is compensated by the ultracapacitors.

Ultracapacitors are electrical energy storage devices, which offer high power density, extremely high cycling capability and mechanical robustness. Thus they are very useful storage device [7].

In fig. 11, ultracapacitors is modeled by the first-order circuit model. An ultracapacitor has 2.7V, C=1700F at NESSCAP [8]. For use ultracapacitors to compensate in this system, it consists of 17 ultracapacitors. Therefore, the rating voltage of ultracapacitors becomes 45.9V. The values of parameters are: R_s=0.7mΩ, R_p=300Ω, L=0.01mH, C=100F.

Diode D prevents a reverse current from ultracapacitors to fuel cells during voltage sag. With a reverse current into fuel cells, it can cause destruction of fuel cells.

Fig. 12 shows output waveforms when the first fuel cell has the voltage sag. Fig. 12(a) shows a non-compensated output voltage of the system with voltage sags. The fundamental voltage decreases and THD increases with the voltage sag. Fig. 12(b) shows compensated output voltage by use of ultracapacitors. When fuel cell experiences the voltage sag, the fundamental component of the output voltage remains constant without control of pulse. Fig. 12(c) shows that an output voltage of the first fuel cells and compensated output voltage of fuel cell system by ultracapacitors. When fuel cell system has a 40% voltage sag at 0.15s, compensated output voltage of fuel cell system decreases to 28.8V. However, as shown in the extended waveform in fig. 12(c), the voltage sag quickly recovers within 0.2ms by ultracapacitors. Therefore, although the system has a voltage, it is quickly compensated by use of ultracapacitors.

VI. CONCLUSIONS

The power quality for the fuel cell system is a very important issue. The fuel cell system has a voltage sag problems. When the multilevel inverter is used as an inverter for a high power fuel cell system, it is important to determine the number of levels of inverters. Harmonic analysis results can be used as an index in selecting number of levels of inverter. In this paper, harmonic analysis has been made with respect to number of level of inverters and voltage sag of the fuel cell output. Through harmonic analysis, it has been shown that the harmonic component decreases as voltage sag increases.

To solve the voltage sag problems, three approaches have been investigated. There are trade-offs among the proposed approaches. The approach using ultracapacitors has an advantage in that it requires no control of pulse patterns, but it requires an additional hardware. Thus the approach with control of the pulse widths can be efficiently used for the compensation the voltage sag problem of the fuel cell system.

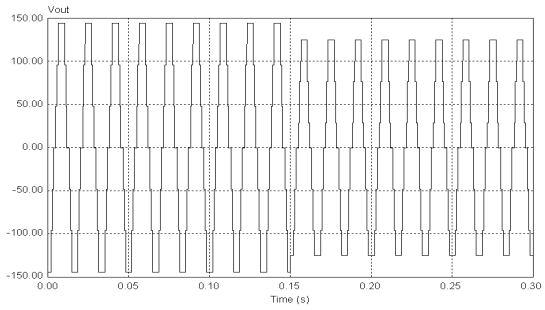

(a)

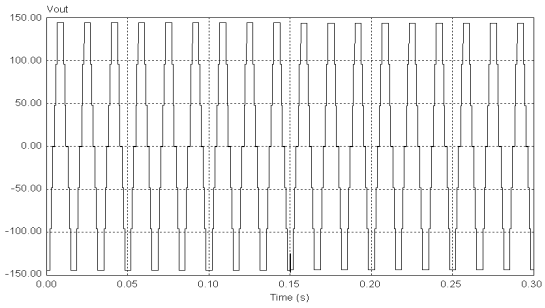

(b)

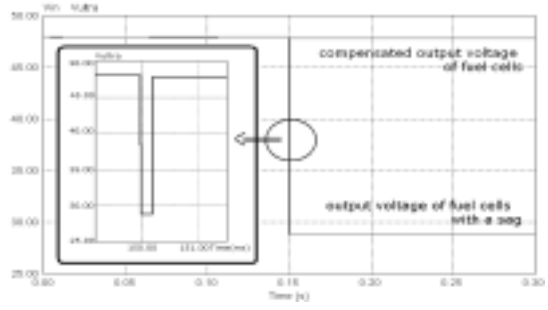

(c)

Fig. 12. (a) Non-compensated output voltage waveforms with voltage sag from 48V to 28.8V (40%)

(b) Compensated output voltage

(c) Output voltage of the first fuel cell and ultracapacitors

ACKNOWLEDGMENT

This work was financially supported by MOCIE through EIRC program

REFERENCES

[1] R. Anahara, S. Yokokawa and M. Sakurai, “Present status and future prospects for fuel cell power systems,” Proceedings of the IEEE, vol. 81, no. 3, pp. 399-408, 1993

[2] R. Naik, N. Mohan, M. Rogers and A. Bulawka, “A novel grid interface, optimized for utility-scale applications of photovoltaic, wind-electric and fuel-cell systems,” IEEE Transactions on Power Delivery, vol. 10, no. 4, pp. 1920-1926, 1995

[3] K. Tam and S. Rahman, “System performance improvement provided by a power conditioning subsystem for a central station photovoltaic-fuel cell power plant,” IEEE Transactions on Energy Conversion, vol. 3, no. 1, pp. 64-70, 1998

[4] Peng, F.Z., Tolbert, L.M. “Multilevel converters as a utility interface for renewable energy systems”, Power Engineering Society Summer Meeting, 2000. IEEE, Volume: 2, 2000

[5] L. Gyugi, “Dynamic Compensation of AC Transmission Lines by Solid-State Synchronous Voltage Sources,” IEEE Transactions on Power Delivery, vol. 9, no. 2, April 1994, pp. 904-911

[6] A. van Zyl, J. H. R. Enslin, R. Spee, “A New Unified Approach to Power Quality Management,” IEEE Transactions on Power Electronics, vol. 11, no. 5, Sept. 1996, pp. 691-697

[7] Linzen, D., Buller, S., Karden, E., De Doncker, R.W., "Analysis and evaluation of charge balancing circuits on performance, reliability and lifetime of supercapacitor systems", Industry Applications Conference, 2003. 38th IAS Annual Meeting. Conference Record of the, Volume: 3, 12-16 Oct. 2003, Pages: 1589 - 1595 vol.3

[8] Do Yang Jung, "Shield ultracapacitor strings from over voltage yet maintain efficiency: although active cell voltage-equalization circuitry adds complexity, it has greater energy efficiency than passive techniques. (Design Application)", Electronic Design, May 27, 2002, by Pages: 1 - 3

[9] M. Hsu, D. Nathanson, R. Goldstein, “Ultra-high Efficiency Fuel Cell/Gas Turbine System for Distributed Generation,” Proceedings of the American Power Conference, 1997, pp. 559-561

[10] Peng, F.Z., Tolbert, L.M. “Multilevel converters for large electric drives”, Applied Power Electronics Conference and Exposition, 1998. APEC '98. Conference Proceedings 1998., Thirteenth Annual , Volume: 2 , 15-19 Feb 1998

[11] Enjeti, P.N.; Montero-Hernandez, O.C , “A low cost approach to provide ride-through for critical loads”, Applied Power Electronics Conference and Exposition, 2001. APEC 2001. Sixteenth Annual IEEE, Volume: 2, 2001

Investigation of Practicable Bidirectional IGBT-Switches for Using in Matrix Converters

W. Hofmann
Chemnitz University of Technology
Chemnitz, Germany
e-mail: wilfried.hofmann@e-technik.tu-chemnitz.de

***Abstract* - Various types of bidirectional switches are examined simulatively and experimentally with regard to their commutation properties within a matrix converter arrangement. A newly developed IGBT with reverse blocking capability by means of which it is possible to set up bidirectional switches in an efficient way is dealt with in a more detailed way. Statements are made on the electric stress of the bidirectional switches within the commutation circuit and the losses arising. With the aid of the results obtained, the suitability of the respective bidirectional switches with regard to their application in the matrix converter is discussed. Finally, some ideas concerning the further improvement of the characteristics and properties of the bidirectional switches are touched upon.**

I. INTRODUCTION

Matrix converters are direct converters by means of which one can generate from multiphase alternating quantities of a given amplitude and frequency again multiphase alternating quantities with a variable amplitude and frequency. Conditioned by its principle, this type of converter is fully capable to inject the energy backwards and can be set up in a rather compact way because the intermediate circuit is not needed. Thanks to this fact, it offers a wide possible range of application. Fig.1 shows the principle structure of an ideal matrix converter.

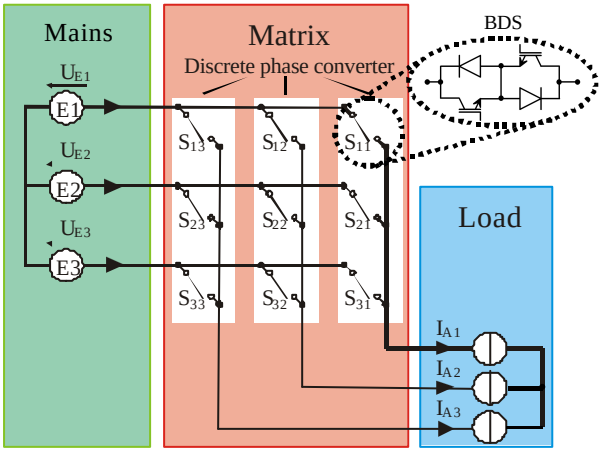

Fig. 1: Principle of matrix converter

In order to be able to reach a maximum of degrees of freedom of the control, bidirectional semiconductor switches must be used. These bidirectional switches must be able to inhibit a negative voltage and to conduct the current in a direction-selective way. New developments on the semiconductor market permit to construct these bidirectional switches (BDS) required in a more efficient way or to make available semiconductor switches being better suited for this special purpose of application. Since all the three discrete phase converters of the matrix converter have an identical structure, the following investigations will be made for one discrete phase converter only.

II. BIDIRECTIONAL SWITCHES IN COMMUTATION PROCESSES

Since there are no bidirectional switches available yet fulfilling the specific requirements in the matrix converter, the same have to be discretely set up out of conventional semiconductor switches. As far as the BDS are concerned, one distinguishes between two basic types, switches with four or with two basic states, as shown in Fig.2.

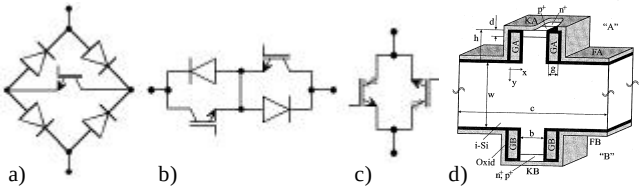

Fig. 2: Types of bidirectional switches: a) Diode-bridge BDS b) discrete BDS with two emitter-side connected IGBT's, c) BDS from two reverse blocking IGBT's , d) monolithic BDS (MBS)

Three basic components of bidirectional switches have been examined, see fig. 2:

1.) that forward direction is determined by the polarity of the collector-emitter voltage then the gate is active switched-on as shown for example in a).

2.) that forward direction is determined in each case by the active gate and the polarity of the commutation voltage as b) or c).

3.) that forward direction is determined by the polarity of the controlled gate and the polarity of the commutation voltage as d).

The BDS basic components to be examined were implemented as follows:

- The BDS of basic component 1, Fig. 2a consists of a diode bridge with integrated IGBT. This BDS variant is offered by the company IXYS, where the individual devices (semiconductor chips) had been put in a discrete package see IXYS, data sheet FIO-5012BD.

- The BDS of basic component 2, Fig. 2b and c. Here has been considered two possible variants of the basic component 2. The BDS of Fig. 2c consists of an inverse series circuit two unidirectional, emitter-sided combined IGBT's with antiparallel protecting diode. The mesial combination between the two series circuits from diode and IGBT is absolutely necessary since the diode bridges the opposite IGBT in reverse direction and carries off the stored charge of the serie diode during the shutdown. It is prevented that this is abandonend with reverse blocking voltage. If this cross connection is missing, it comes to a random distribution of the reverse voltage between diode and IGBT during the shutdown against negative voltage . The IGBT must include reverse voltage, that too to a high-powered avalanche and to the destruction of the semiconductor leads. This switch became from available semiconductor devices (two IGBT modules of Semikron), built up in discrete form. Semikron, data sheet SKM 100 GB 123 D.

As a representative of the first type, a discretely set-up bidirectional switch made of two IGBTs with antiparallel recovery diode which are not capable of reverse blocking and are connected by their emitters was examined. As the second representative of the switch type number one, an arrangement of two IGBTs in antiparallel connection and being capable of reverse blocking was studied [1], [2]. Fig.3 displays a schematic cross section of such a reverse blocking IGBT device. Cell structure as drawn will continue to the left, while the chip edge with the guard rings for junction termination is shown on the right. Geometry and thus mode of IGBT operation basically correspond to NPT IGBTs; this in particular means that – although the device is reverse blocking – voltage drop across the switch is limited to saturation voltage U_{CEsat} of the IGBT - there is no additional voltage drop U_F in any additional diode p – n junction.

To achieve this, the NPT-IGBT structure is complemented by the p^+ collector being folded up from the bottom to the top at the chip edge by means of isolation diffusion. This enables the IGBT's proprietary lower p^+ - n^- junction to block a reverse voltage - the collector being negative. Without this measure, the junction would break through at the chip edge due to lack of field stop, which is the reason why standard IGBTs must not be connected to significant reverse voltage.

A different approach is to combine a field stop IGBT [3] with a bridge of fast recovery diodes as depicted in Fig.4. Current through this kind of bidirectional switch passes two diodes and the IGBT. The latter being turned on, current flow is possible in both directions. This circuit , which has been integrated into a single, isolated component [4], thus belongs to the second group of bidirectional switches. Because this switch has only two states, step-commutation can not be used. It is either be employ it in a parallel circuit that takes over the load current, or use a commutation inductor that limits the current during the commutation. For further prospects see [8].

- BDS of basic component 3, Fig. 2d, can be taken as Monolithic Bidirectional switch (MBS) as own switch class.

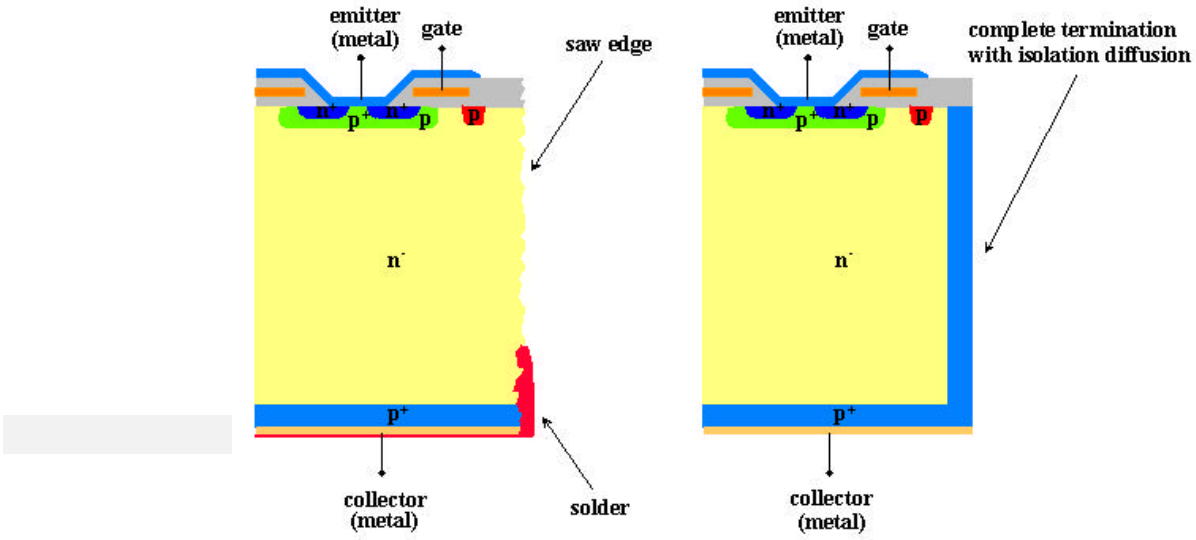

Fig. 3: Reverse blocking IGBT

That in [5], bidirectional switch being led to [6] and simulated characterizes to know-how of the simulation very well for the commitment in the matrix converter. In [7] the qualities special, resultant from the structure of the device set are demonstrated and explained his fixed operating conditions by means of results of numeric simulation circuits in detail. Also an aptitude test of the optimized MBS for his commitment in the matrix converter where the possibility of the direct switching operations is discussed through specific gate control methods is carried out. Unfortunately, such a device is not available at this time for test purposes yet.

With the help of the simulation system Simplorer®, the commutation properties and the electric loads occurring at the bidirectional switches are examined. In Fig. 4, the commutation circuit for positive load current being the basis for the simulations and $U_{N1} > U_{N2}$ are represented for the example of the discretely set-up bi-directional switch.

In accordance with the one-step commutation method, the current commutation of the load current between the two network phases is executed by one switching action which will lead directly to the commutation. A commutation on its part consists of two switching operations proceeding in the two BDS participating in the commutation.

In the state 0 (Fig. 4), the load current flows in phase N1 and through BDS1v. By the hard, active switching-off of BDS1v, the load current is forced to commutate to BDS2v. For this purpose, the BDS2v has, of course, to be switched on before switching off BDS1v. Now the load current flows in phase N2 and through BDS2v, consequently state 1 applies now. If BDS1v is switched actively on now, the load current naturally (because of $U_{N1}>U_{N2}$), and passively commutates back to N1. Thus, state 0 applies now again, the initial state has been reached again. By means of these two commutation operations and the two respective switching operations belonging to each of them, it is possible to examine all types of component stress occurring under the given general conditions. With the help of the simulation system Simplorer®, the commutation properties and the electric loads occurring at the bidirectional switches are examined. In the commutation circuit for positive load current being the basis for the simulations and $U_{N1} > U_{N2}$ are represented for the example of the discretely set-up bidirectional switch. In accordance with the one-step commutation method, the current commutation of the load current between the two network phases is executed by one switching action which will lead directly to the commutation. A commutation on its part consists of two switching operations proceeding in the two BDS participating in the commutation. In the state 0 (Fig. 4), the load current flows in phase N1 and through BDS1v. By the hard, active switching-off of BDS1v, the load current is forced to commutate to BDS2v. For this purpose, the BDS2v has, of course, to be switched on before switching off BDS1v. Now the load current flows in phase N2 and through BDS2v, consequently state 1 applies now. If BDS1v is switched actively on now, the load current naturally (because of $U_{N1}>U_{N2}$), and passively commutates back to N1. Thus, state 0 applies now again, the initial state has been reached again. By means of these two commutation operations and the two respective switching operations belonging to each of them, it is possible to examine all types of component stress occurring under the given general conditions.

Another commutation process is given with use of diode bridge BDS. It is noteworthy that this type of switch possesses only two switching states for which reason it is not possible to apply the commutation method used herein for this type of BDS. For this reason, a parallel circuit is required to use this component which carries the load current after the switching-off of the BDS until the switching-on of the following BDS, Fig. 4b. A second possibility is the application of commutation inductors limiting the circular current for the period during both BDSs are on. In both cases, additional components are required and additional losses will develop what will have a negative influence on the overall balance of the converter. The two possibilities are pictured in Fig. 4

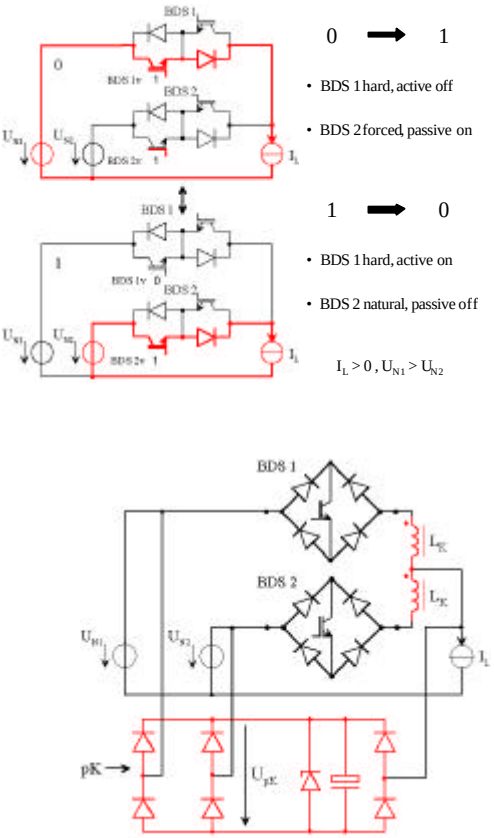

Fig. 4: Commutation circuits, a) by commutation control, b) with commutation helps

III. SIMULATION OF COMMUTATION

On basis of the two being led commutation circuits the switching behaviour and the switching-loads have been examined for all three BDS variants (Fig. 1 a-c) by means of simulation and experiment . The simulation tool Simplorer® was employed. Open and behaviour-based device models have been used and verified with the respective device parameters for dynamic modelling of the BDS. Unfortunately there were only few of the device parameters, necessary for the modelling, from data sheets, which formed the beginning of the simulation stage problematically. In order nevertheless to be able to carry out the necessary simulations, what succeeded in limited extent too was attempted to bring the needed parameters of the individual semiconductor devices into experience with the manufacturer. Kept on controlling through suitable measurements the semiconductors (for example by means of curve tracer) to be determined also important parameters so that finally the simulations could be carried out. Notes on the simulation circuit are Fig. 5 .

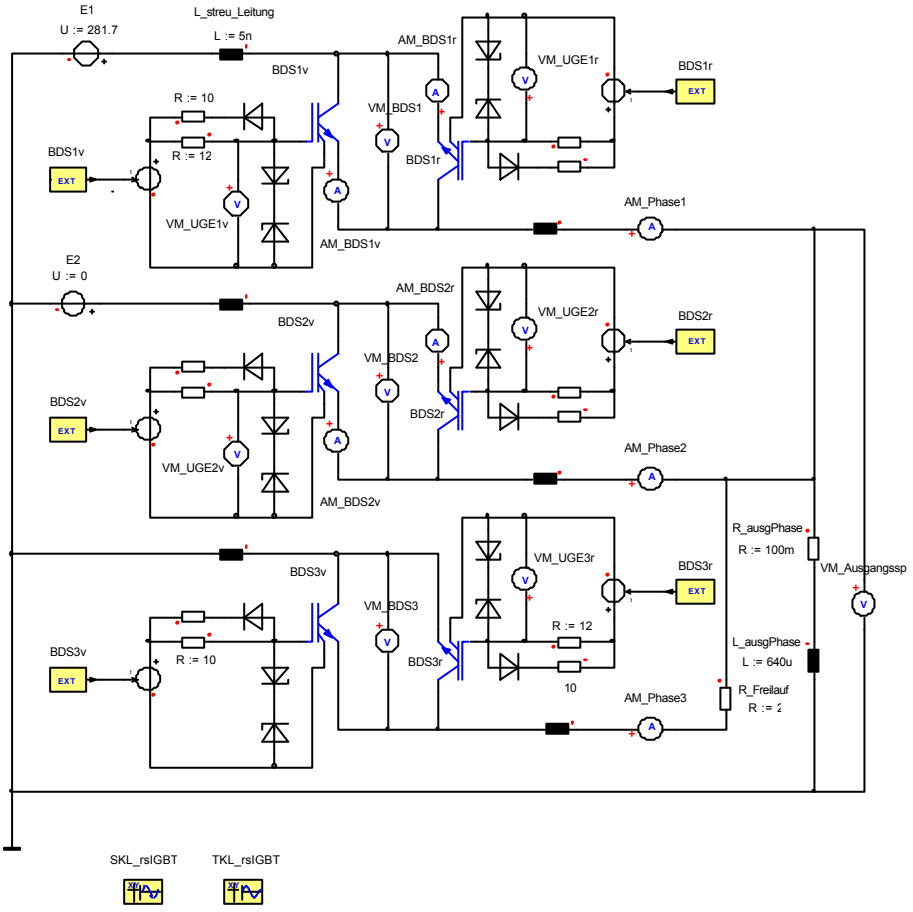

Fig. 5: Simulation circiut for reverse blocking IGBT's

K_IUIC	TKL_rsIGBT	transfer characteristic IGBT
K_DI	SKL_rsIGBT	saturation charactersitic IGBT
CGE	5n	gate-emitter capacity
CD	1.5n	gate-collector junction capacity
DU	15m	diffusion voltage of gate collector capacity CD
ECCG	2	auxilliary voltage for CD
R_TAIL	200	tail-resistance
C_TAIL	3n	tail capacity
LC	15n	collector-leakage inductivity
LE	15n	emitter- leakage inductivity

TABLE 1: parameter of RIGBT

In Fig.6 , the simulated curves of current and voltage for both commutation operations at the BDS being composed of two antiparallel IGBTs with reverse blocking capability are represented. In principle, the above-mentioned facts also apply to these switching operations, with the difference that the additional series diode can be cancelled with this BDS because of the reverse blocking capability. But during the natural switching-off of BDS2v, a recovery current develops also in this case, which comes from the intrinsic diode in the IGBT and increases the electrical load for the commutating BDS1v.

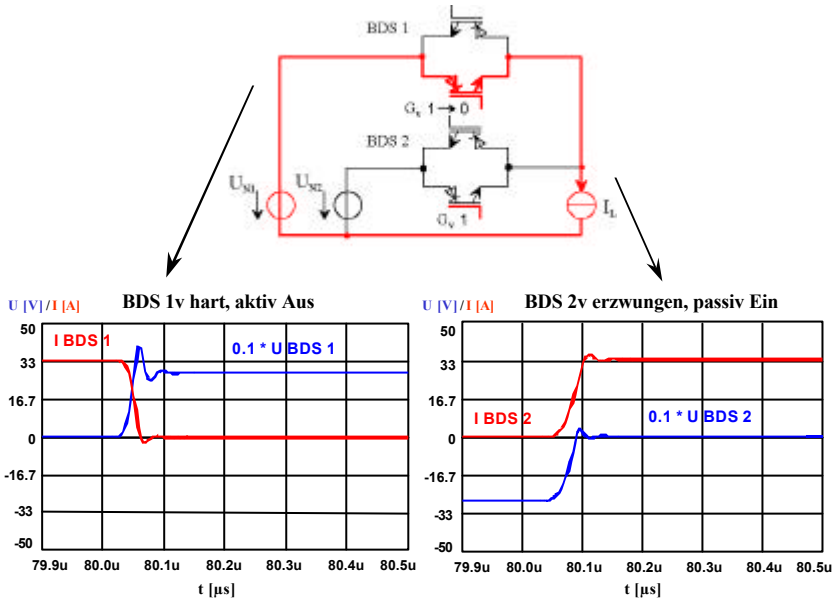

a)

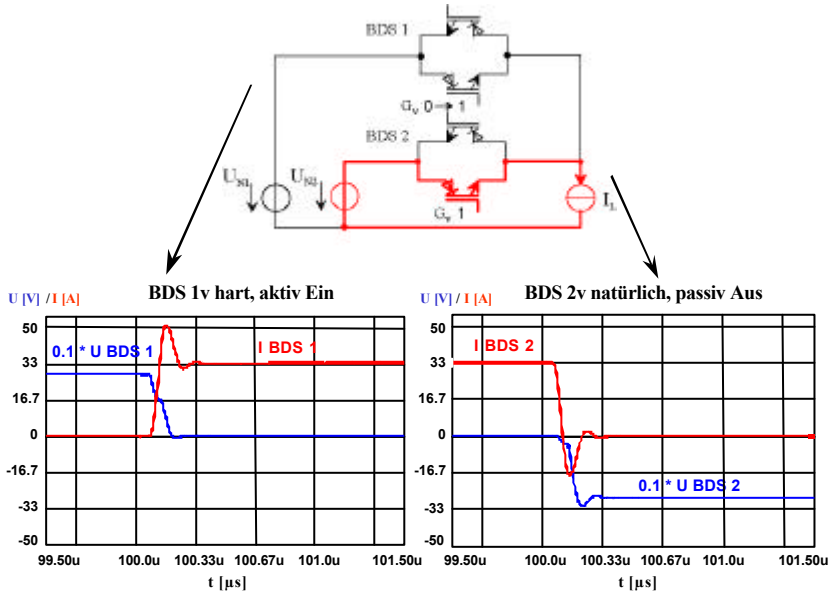

b)

Fig. 6: Simulation results of RIGBT's for different commutation processes,
a) hard active off and forced passive on, b) hard active on and natural passive off

IV. EXPERIMENTAL RESULTS

The measured curves of current and voltage for both commutation operations at the discretely set-up BDS are represented in Fig.7. In case of the hard switching-off, a switching overvoltage of about 350 V can be read off. This value of overvoltage is clearly higher compared with the value of the simulation results because the not ideal characteristics and properties of the commutation circuit in practical operation in contrast with the simulation where these characteristics and properties are ideal.

For this reason, a low-inductance structure of the commutation circuit has to be always aimed at if you want to reduce the voltage stress of the semiconductors. In case of the forced switching-on of BDS2v, the short-time increase of the flow voltage as a result of the delayed electrical conductance modulation is clearly to be seen as was to be expected. The recovery current being driven during the natural switching-off of BDS2v which is added to the load current and has to be taken over in addition by BDS1v is represented in the lower part of Fig.7. The really measured curves of current and voltage do on the whole meet those determined by means of simulation. Parasitic inductances and capacities within the commutation circuit do, however, cause higher switching overvoltages than in the simulation. In addition to that, these elements develop oscillating circuits which are excited by the fast switching operations which can be clearly seen in the measurements.

The measuring results for the BDS being composed of two IGBTs with reverse blocking capability are represented in Fig.8. Here you can see in a particularly distinct way the influence of the leakage inductances in the commutation circuit. Owing to the high current change speed of about 250 A/µs, a high voltage is induced at the leakage inductance during the hard switching-on which superimposes with the source voltage. Due to this fact, the voltage at the component even increases during this phase. The result of this effect is a high switching power loss during this switching operation. It is true that a relatively high power loss is being produced during the hard switching-on but the measured value is, caused by the structure of the commutation circuit, too high. In this case, the only help is a further reduction of the leakage inductance. In principle, the statements made in the preceding paragraph also apply to this type of BDS. With this BDS, the clearly to be recognized reverse-recovery current is driven by the intrinsic diode of the IGBT capable of reverse blocking.

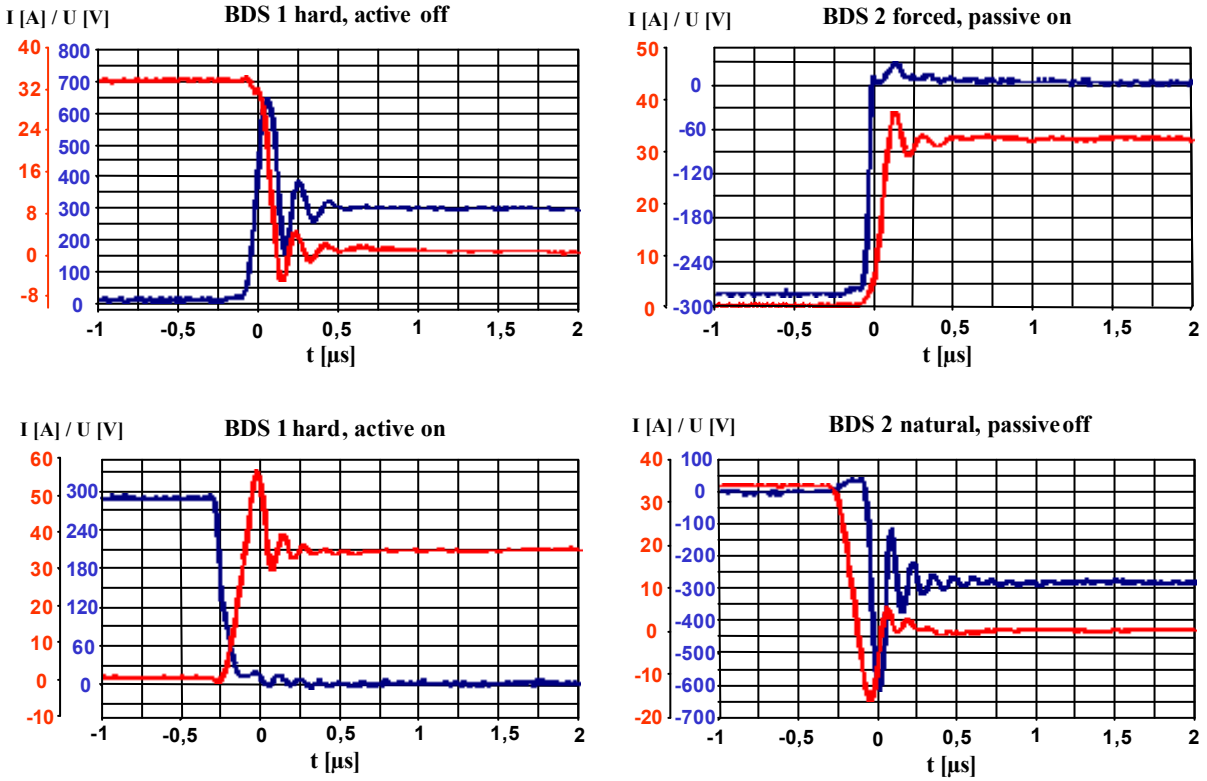

Fig.7: Measured switching behaviour of discrete BDS modules

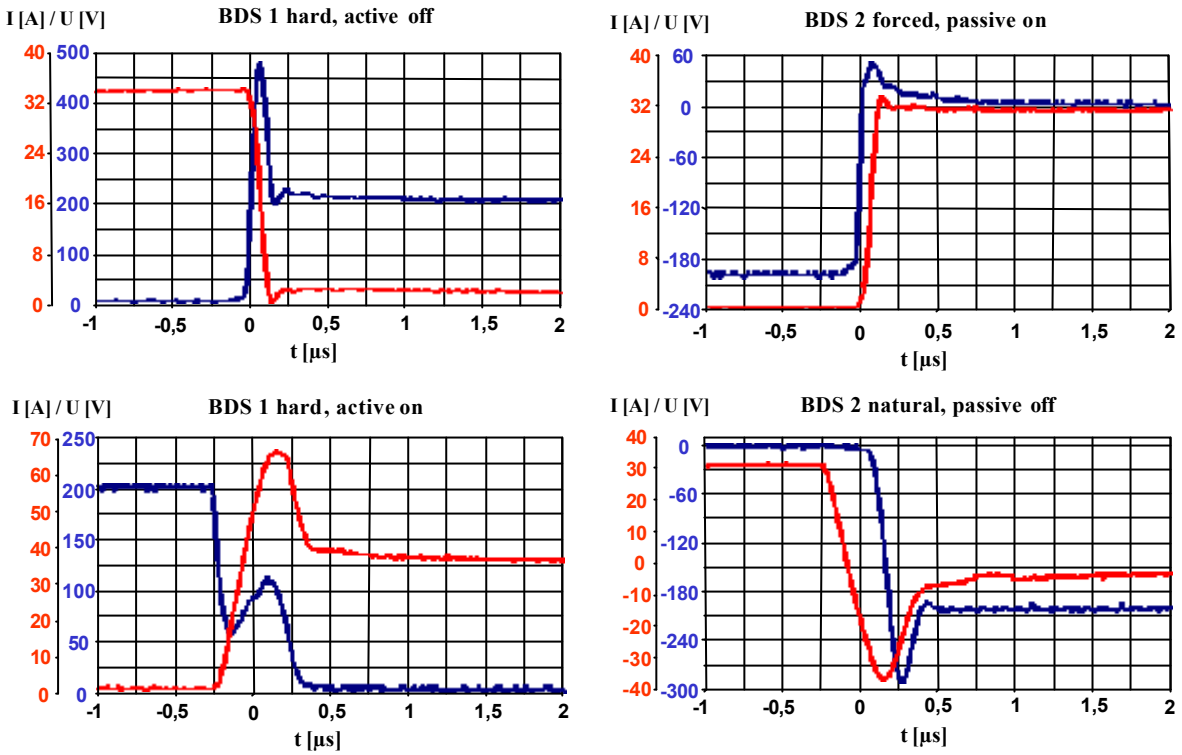

Fig.8: Measured switching behaviour of RIGBT during commutation

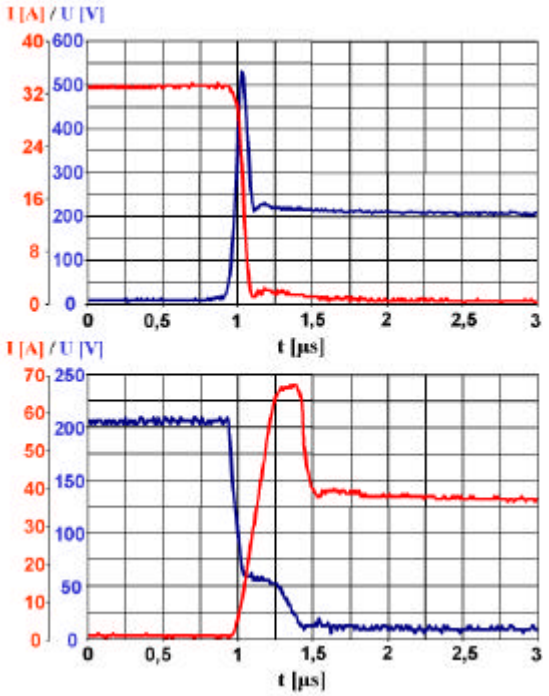

Fig.9: Measured switching behaviour of diode bridge IGBT,
a) BDS switches on, b) BDS switched off

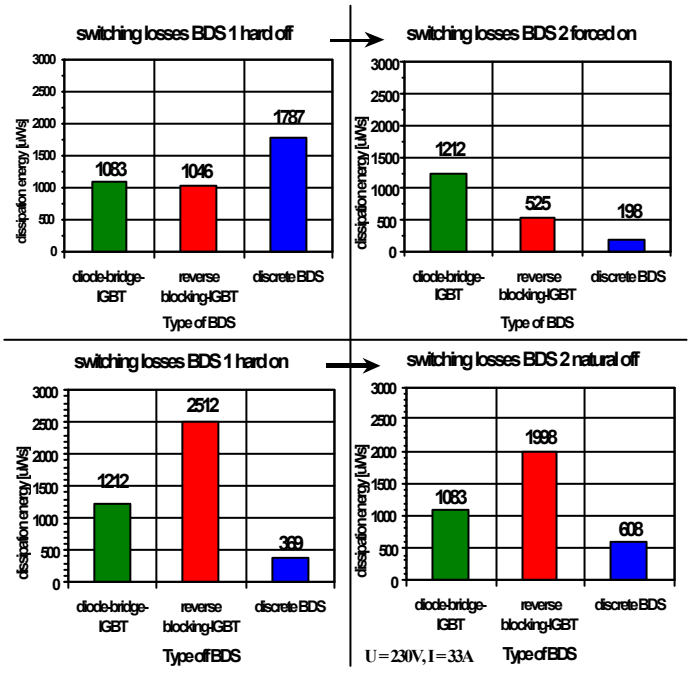

Fig. 10: Measured switching losses in comparison

Cu-package of supply	15 nH
Capacities (ESL)	20 nH
2 * IGBT L_{CE} + L_{pack}	80 nH
Wire (setup)	100 nH
Wire (measuring)	50 nH
Current transformer core (2x)	100 nH
Sum of leakage inductances	365 nH

TABLE 2: Leakage inductances of the test rig

In case of the diode-bridge IGBT only two different switching processes are available, see Fig. 9. We can note a very fast switch-off and a more lossy switch-on procedure. Furthermore the overvoltage caused by leakage inductances is remarkable. The determined leakage inductances of the test rig is listed in table 2. Summarizing the switching losses of diode-bridge IGBT we obtain the best results in comparison with the other kind of BDS. The dissipation energy has been calculated from the measured voltage and current curves and displayed in Fig.10.

In Fig. 11 the distribution of all losses arising in the respective bidirectional switch is represented under the already described general conditions. The diode-bridge IGBT has the highest forward losses since it exists from a series circuit of three devices, the switching losses are relatively small in relation to the forward losses. It has to be considered, that at this BDS the additional losses in the parallel circuit and/or in the commutation choke are included in the power dissipation balance. The discrete BDS causes smaller forward losses since only two devices are with the current path. The forced switch-on near precharged gate causes a little small switching losses, since the current increases through the BDS first then the reverse voltage has declined already far. During the hard switch-off higher losses can be well-founded by overvoltages induced at the leakage inductance. The switching losses occurring during the other switching operations are small under the considered conditions, with respect to the total losses of the device. At the BDS consisting of two RIGBT's the forward losses are the smallest, since only one devices is in the current path. The height of the losses during the passive switch-off is influenced by the reverse-recovery-current of the intrinsic diode contained in the IGBT. The power dissipation arising during this switching operation in the RIGBT is larger than those at the in discrete form built up BDS are. The cause is found in the slower switching of the intrinsic diode of the RIGBT's in the arrangement to the faster, optimized free-wheeling diode. Because the RIGBT in hard switch-on must load the reverse recovery current, also higher losses occur during this switching operation.

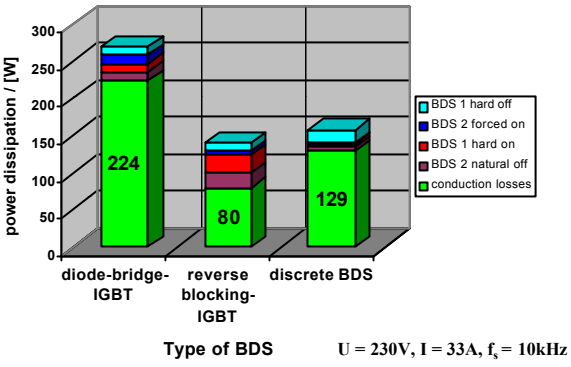

Fig. 11: Segmentation of power dissipation

About the examined BDS following can be summarized:

The diode bridge BDS has structural high forward losses and can be employed in the complete matrix converter only with additional hardware (which makes losses also again). The advantage of this structure is the most extremely robust commutation there even with serious mistakes as driver loss and loss of the mains voltage, always free-wheeling paths for the load current are available. The commitment of this BDS-model does not offer any further advantage which could compensate the high forward losses sufficiently for the here considered procedures for the step-wise current commutation otherwise. This BDS is better suitable for the commitment in modified device topologies (indirect matrix converters), as for example in the so-called converter Sparse Matrix proposed and described in [9] and [10].

For the BDS of type 2 during the hard on- and natural off the highest switching losses are measured. During the forced switch-on only small losses arise. Only the turning rate of the IGBT's can be changed by variation of the gate series resistor, onto the switch-off procedure the size of RG does not have almost any influence. The overvoltages induced at the leakage inductance during the fast switching require the IGBT', so that these overvoltages must be reduced by an inductance-poor construction. Furthermore from these overvoltages considerable part of the high-powered losses is caused.

The discrete BDS come off quite well. His switching losses are small due to his optimized free-wheeling diode and also the forward losses have an acceptable order of magnitude for a series circuit from diode and IGBT. The RIGBT achieves the best result with the total losses, in comparison with the two other BDS types, Since the intrinsic series diode switches relatively slowly and has a quite big storaged charge the switching losses are high, particularly at the second commutation procedure. An optimization of this diode forms itself due to the fact, that the diode is an elementary part of the IGBT's difficult, is, however, with regard to the improvement of the high-powered behaviour of this BDS inevitable. Also the relatively high forward voltage offers a good starting point for further optimization. At this

time the manufacturer of the RIGBT works on the optimization of the switching behaviour of this device.

Finally the total losses have been projected for the whole matrix converter dependent on the switching frequency . This came under the assumption that the $f_S >> f_{line}$- and that to occur the two possible commutation procedures are in each case 50 %, see calculation formula. The calculation base of the losses formed the measured power dissipation parts of the respective semiconductors. Those are the IGBT on- and switching-losses, forward losses, switching losses of the diodes and also their forward losses. Caused by the growth of the switching (frequency-dependent) losses, also the total losses increase proportionally.

The equation for determining the losses is:

$$P_{V\_BDS\_T} = \frac{f_S}{2}\left(E_{BDS\_hard\_off} + E_{BDS\_forced\_on}\right) + \frac{f_S}{2}\left(E_{BDS\_hard\_on} + E_{BDS\_natural\_Aus}\right) + P_{V\_BDS\_D} \quad (1)$$

$$P_{V\_MUR} = 3 \; P_{V\_BDS\_T} \quad (2)$$

where:

$P_{V\_BDS\_T}$ - total losses of a partial converter
f_S - switching frequency
$E_{BDS\_x\_x}$ - dissipation energy of IGBT and diode,
$P_{V\_BDS\_D}$ - forward losses of the BDS (IGBT + Diode)
P_{V_MUR} -total losses of matrix converter

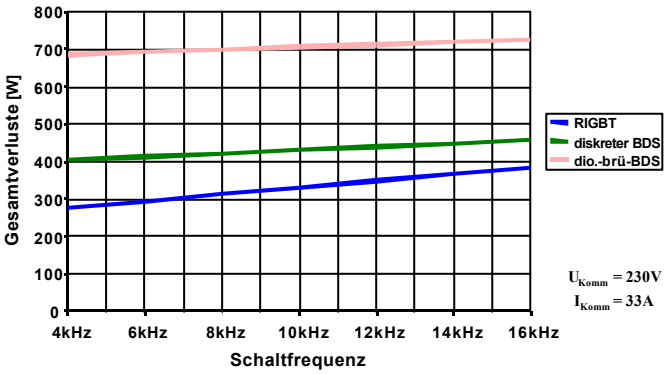

Fig. 12: Prospected losses of matrix converter

The RIGBT which has the least entire losses in the considered frequency range loses its loss-margin increasingly with increasing frequency. The basis is in the already mentioned, relatively bad dynamics of this BDS so that the part of the high-powered losses with increasing frequency rises disproportionately. It manages to correct the dynamics of this BDS, then this can be used also at higher switching frequencies effectively.

V. SUMMARY

The highest potential of development has the reverse blocking IGBT for using in matrix converters. The smallest conduction losses occur with these IGBTs. The intrinsic diode switches slower than the optimised diode in the discrete BDS. The conduction losses offer a good starting point for further optimisation. For future prospects an higher availability of new and optimised devices for use in MC will be given. In the future perhaps a monolithic bidirectional switch is also available.

REFERENCES

[1] Lindemann, A.: A New IGBT with Reverse Blocking Capability; EPE conference, Graz, 2001

[2] Advanced Technical Information: IGBT with Reverse Blocking Capability. IXYS Semiconductor GmbH, 2000

[3] Dewar, S., Linder, S., Arx, C. von, Mukhitinov, A., Debled, G.: Soft Punch Through – setting New Standards in 1200V IGBT; PCIM conference, Nürnberg, 2000

[4] Advanced Technical Information: Bidirectional Switch with IGBT and Fast Diode Bridge. IXYS Semiconductor GmbH, 2001

[5] F. Heinke, R. Sittig; The Monolithic Bidirectional Switch (MBS); Proceedings of ISPSD 2000, pp. 237-240

[6] F. Heinke, R. Sittig: Monolithic Bidirectional Switch Part I, Device Concept; Part II, Simulation of Device Characteristics; Solid State Electronics 44, August 2000, pp. 1387-1398

[7] F. Heinke: Monolithischer Bidirektionaler Schalter für Matrixumrichter; Dissertation am Institut für Elektrophysik der TU Braunschweig, 2002

[8] H. Kapels: IGBT- und Diodenstrukturen für moderne Schaltungskonzepte; Dissertation am Institut für elektrische Antriebe, Leistungselektronik und Bauelemente der Universität Bremen (IALB), 2002

[9] J. W. Kolar, M. Baumann, F. Schafmeister, H. Ertl: Novel Three-Phase AC-DC-AC Sparse Matrix Converter; Part I, published at the 17th IEEE Applied Power Electronics Conference, March 10-14, Dallas (TX), 2002

[10] F. Schafmeister, M. Baumann, J. W. Kolar: Analytically Closed Calculation of the Conduction and Switching Losses of Three-Phase AC-AC Sparse Matrix Converters; To be published at the 10th International Power Electronics and Motion Control Conference, Sept. 9-11, Cavtat & Dubrovnik, Croatia, 2000

A Modular IGBT Converter System for High frequency Induction Heating Applications

Sven H. Stier
University of Technology
Darmstadt
sstier@srt.tu-darmstadt.de

Peter Mutschler
University of Technology
Darmstadt
pmu@srt.tu-darmstadt.de

Abstract— **The requirements in induction heating cover a wide range of power and frequency. Different converter designs are used for different applications. To reduce costs, we propose a modular IGBT-based coverter system, where identical inverter-modules are combined to cover a wide range of power and frequency. To reduce switching losses the parallel connected IGBT modules are driven by a sequence control method [1].**

I. INTRODUCTION

In former times high frequency inverters were equipped with electrical tubes or MOS-FET switches. The tube-inverters needed much maintenance and the MOS-FET inverter were very expensive. Today fast IGBT switches are available. Compared to older IGBTs, the switching times, the switching-off tail current and the on-state voltages have improved. Now IGBTs become the first choice for resonantly operating high frequency inverters.

In many applications a galvanic insulation between the grid and the load is mandatory. Normally a high frequency transformer is used for this purpose. The main inductance of the transformer may become saturated, if the control imposes an offset to the voltage of the primary side. This control error must be avoided.

This paper discusses the influence of parasitics in the experimental set-up and switching characteristics of the IGBTs concerning the saturation of the HF-transformer. The simulations are done by the simulation tool Simplorer 6.0. For the validation of the results a 600 V, 80 kW, 400 kHz resonant inverter is constructed.

II. SERIES RESONANT VOLTAGE SOURCE INVERTER

The motivation to use the voltage source series resonant inverter is discussed in [2].

In high frequency applications, switching losses exceed the conduction losses clearly.

At hard switching applications turn-on losses dominate with MOS- controlled devices. To reduce these losses, zero voltage switching (ZVS) is introduced in high frequency applications. A switching frequency higher than the resonant frequency is employed for the series resonant voltage source inverter to operate in zero voltage switching mode. In this mode positive gate voltage is applied to the IGBT in the conduction period of its anti-parallel diode. After the current in the diode decreased to zero it commutates to the IGBT, which got positive gate voltage shortly before and the IGBT starts conducting at zero voltage, i.e. turn on with low losses.

In the series resonant inverter, the IGBTs are turned off at $i_C \approx 20\%$ of the peak value. In spite of this low turn-off current, the turn-off losses are still dominating.

In this project, the Eupec FF200R12KS4 [6] is used. This module is equipped with 1200 V, 200 A fastest thin transparent emitter NPT type chips. The overall losses at a peak current of 200 A and a switching frequency of 400 kHz are much higher than the module's case can dissipate, even with water cooled heat sink. Therefore, methods to reduce the losses further in one module have to be employed. There are two methods: Current derating and sequential control.

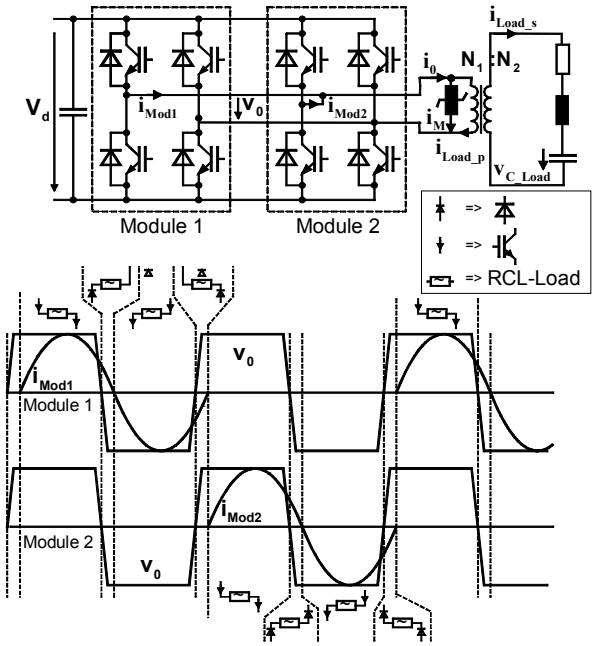

Fig. 1. Sequential gate pulsing with parallel connected inverter bridges

It was shown in [1] that the dominant turn-off losses of the IGBTs decay less than linearly with the current. Due to this, a simple current derating is far less efficient than a sequential gate pulsing.

As an example, Fig. 1 shows the principle of sequential gate pulsing with two modules.

In contrast to the method of current derating, with sequential gate pulsing there is an additional advantage concerning the power demand of the gate drivers.

The IGBT has a gate charge of 2.1 µC and a useable gate voltage range of –15V up to 15V [6]. The driving power demand is:

$$P = f \cdot Q \cdot \Delta V$$

For the method of current derating, the driver's frequency is 400kHz and the power **25.2 W** for each IGBT. With the method of sequential gate pulsing with four inverter bridges, the average driver's frequency is reduced to 100kHz and the driving power is only 25% i.e. **6.3 W.**

III. MODULAR CONCEPT WITH DISTRIBUTED OR CENTRAL CONTROL UNIT

One of the targets of this project is to develop a modular IGBT inverter system. The inverter bridges are designed to form a modular system. The signal transmission to the drivers is done by fibre optic links. The load current zero crossing signal i_{0_sign} and the load current maximum value $i_{0\_max\_sign}$ are transmitted by two current transducers (Fig. 2).
Concerning the control devices, either a distributed or a centralized approach may be considered. In [3], an approach of a distributed control system is presented. The advantage is the redundancy of control circuits and the easy parallel connection of the units. Inputs to the frequency control of one inverter bridge are phase angles between two voltages and the phase angles between the output current and voltage. The main difference however is the fact, that in [3] no sequential gate pulsing but current derating is involved.

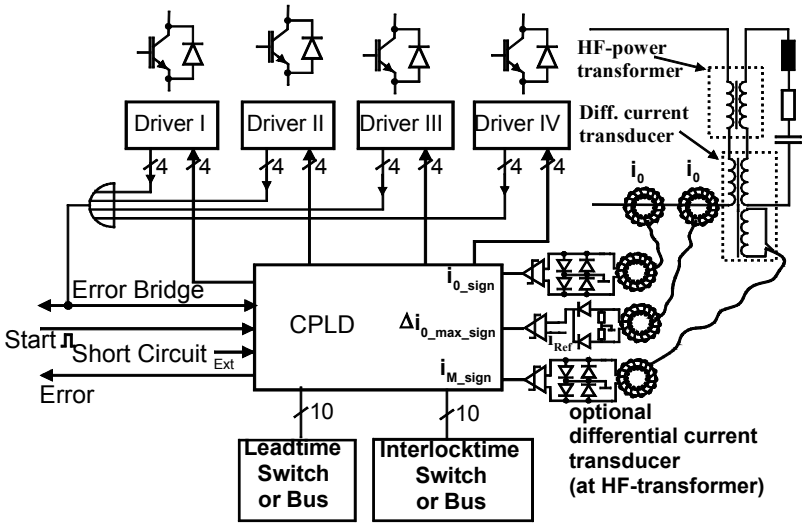

Fig. 2. General overview over the control circuit

With sequential gate pulsing, there would be a need of communication between the control units of the individual inverter bridges, in order to pass on the "token" for the next active cycle.
The current zero crossing signal i_{0_sign} is detected by a current transducer, consisting of two in series connected transformers and a comparator. The signal of the zero crossing of the load current must be transmitted very precisely with a jitter less than 10ns. To avoid such a high speed communication, a centralized hardware for the control scheme is employed here. The modularity concerning the control is implemented in the software, as our controller mainly consists of Complex Programmable Logic Devices (CPLDs), which may be programmed for different number of modules.
In our solution the zero crossing signal of the inverter output current i_0 is the only input for the frequency control unit. Fig. 2 gives an overview.

A. Implementation of the controller

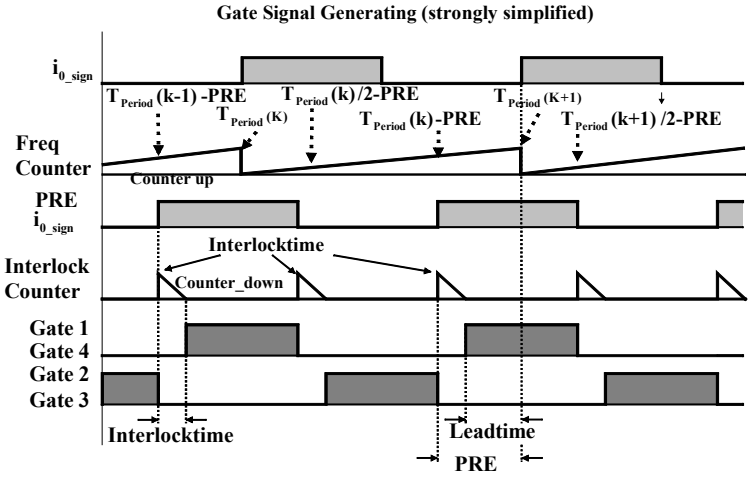

Fig. 3. Operation scheme of gate signal generation

The digital controller is implemented on a central CPLD control unit. User defined input parameters are interlock- and leadtime The parameter interlocktime affects the all switches off time. With the parameter leadtime the propagation delays for the gate signal are compensated.
These parameters can be adjusted by DIP switches or via a parallel bus. This two parameters strongly influences the IGBT losses (see chapter III *B*). The control circuit adapts itself to the resonance frequency of the load. This is necessary, because the load-inductance is not constant. Its value decreases with rising work piece temperature, especially around the curie temperature.
The inverter output current signal i_{0_sign} is the input value of the gate pulse generation controller (Fig. 3). An auxiliary signal PRE i_{0_sign} is generated. This signal is leading for the parameter PRE (= leadtime + interlocktime). The generation of this signal is done by a counter (here called frequency counter), that is reseted at any rising edge of the i_{0_sign} signal. The maximum count value gives the time of one period T. If the count value is T/2-PRE, the signal PRE_i_{0_sign} will be set to the low state and if the count value is T-PRE the signal is set to the high state. The gate pulses are deduced from the PRE i_{0_sign} signal considering the interlocktime. This is done by an other counter (interlock counter).

B. Influence of the control parameters lead- and interlocktime concerning the losses

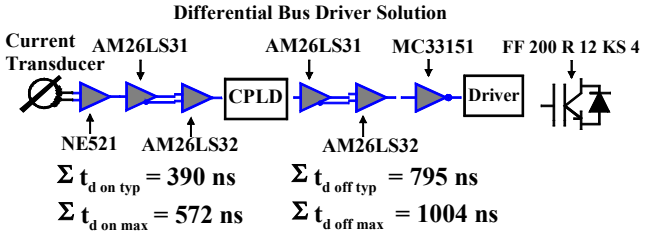

Fig. 4. Delays in the control circuit (cable and CPLD delays are neglected)

In Fig. 4 the data sheet specified time delays of the control circuit (with bus driver links, former communication link) are shown. From this time delay values the required adjustment of lead- and interlocktime can be deduced. A large part of the delay time is due to the driver and the IGBT. The data sheets values are valid for hard switching applications with the referenced gate resistance. In the set-up discussed here the external gate resistance is 0 Ω and the switched off current is almost a quarter of the data sheet referenced current. This illustrates the differences to the measured values in Fig. 6.

In Fig. 5 currents and voltages at IGBT T2 are shown for different settings of lead- and interlocktime. (Notation T1…T4; D1…D4 see Fig. 8).

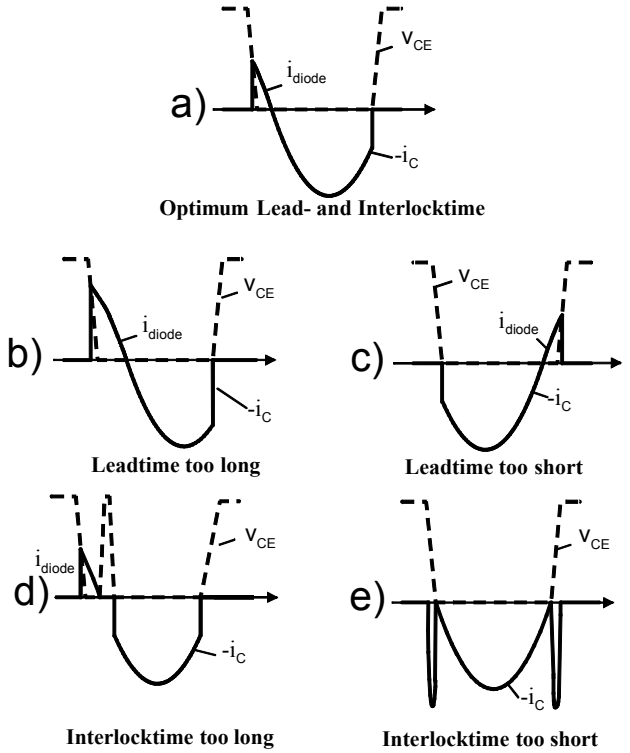

Fig. 5. Influence of the control parameters lead- and interlocktime

In Fig. 5a) lead- and interlocktime are optimised. The T1 collector current commutates to D2 shortly before the natural current zero crossing. The switch-off losses will be low, because of the low current at the switch-off time. Next, the current commutates to T2 that has already a positive gate signal. The switch on losses are minimized.

In Fig. 5b) the leadtime is too long. Turn-off is at a higher current; turn-off losses increase.

In Fig. 5c) the leadtime is too short. T1 turns off during the natural commutation. The current can not flow through T2 because its gate voltage is negative. The current will flow through D1 until T2 turns on. This is not a soft turn-on and so the turn-on losses will increase.

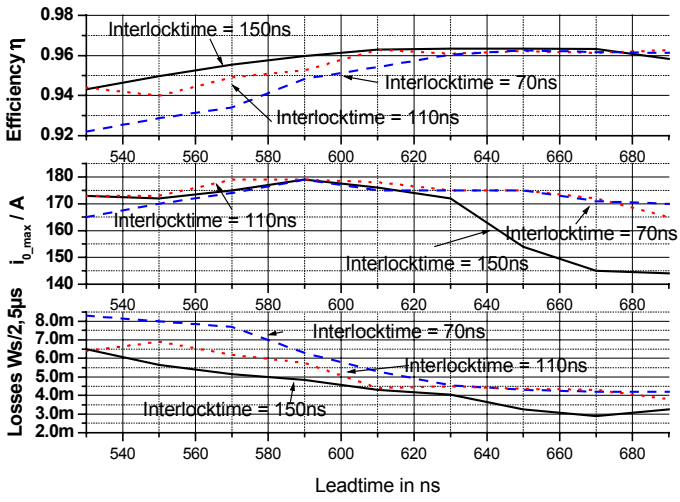

Fig. 6. Measurement of the efficiency, i_{0_max} and losses

In Fig. 5d) the interlocktime is too long. T1 turns off regular. D2 starts conducting, but the current falls to zero. The positive going current uses D1, as long as T2 has negative gate voltage. The losses in this case are high. The IGBT has to turn on and off in hard switching mode and additional switching occurs at D1.

In Fig. 5e) the interlocktime is too short. A high current peak will flow through T1 and T2 simultaneously. During this, the full DC link voltage V_d applies to both IGBTs. Such an operation has to be avoided, due to the very high losses.

Fig. 6 gives an overview over the losses under different interlock- and leadtime settings. All measurements are done with the same load resistance of 0.34 Ω. The output current control was disabled and output current may develop to its maximum value.

If the leadtime is much to short, the maximum output current and, in consequence, losses decrease. The turn-on will be a hard one and only a reduced voltage time area is applied to the load.

For a leadtime in the range of 560 – 600 ns the output currents achieve their maximum, but the turn-on is not at minimum losses. Between 600 – 650 ns leadtime has achieved its optimum in relation to losses and the maximum output current.

If the leadtime increases over 650 ns the output current can not come up to its maximum and the losses decrease because of the lower current.

If interlocktime is too low the losses increase especially at cooperation with a too low leadtime. At higher values of the leadtime the effect is less strong. The optimal tuning for leadtime is between 610 ns up to 650 ns and for interlocktime between 70ns and 110ns in this case. The efficiency of the inverter shows a maximum for leadtime values from 600 ns up to 670 ns. The efficiency is less sensitive to the parameter interlocktime. In the range of maximum efficiency, interlocktime may vary between 70 ns and 150 ns.

C. *Controlling the output power*

To control the output power, freewheeling cycles are inserted. Energy is fed to the load only during intervals where non zero DC link voltage is applied to the transformer. With zero voltage engaged, the resonant circuit can oscillate freely. In Cycle Control Mode, periods where energy is fed to the resonant circuit and periods where no energy is transferred are mixed to control the average output power. In [2] advantages and drawbacks of power control methods are discussed. The freewheeling paths are switched, when the peak value of the inverter side load current i_0 exceeds the reference value. To prevent a direct voltage component at the transformer, the freewheeling paths are switched by a flipflop alternatingly in the positive and negative inverter output voltage time areas. If the magnetization current controller and the output power controller are forcing freewheeling paths at the same time, the output power controller flipflop is not switching and stays in its previous state. Fig. 7 shows a simplified block diagram of the two control loops.

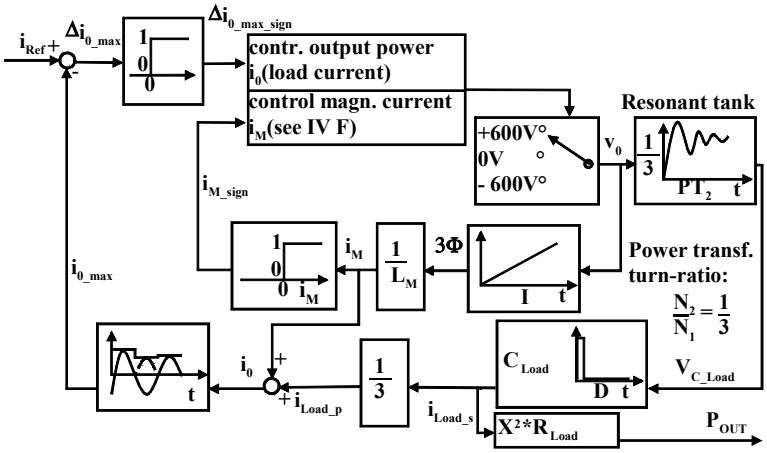

Fig. 7. Output current and HF-power transformer magnetization control circuit

D. *Short circuit detection and protection.*

Two kinds of short circuits are considered in the this application.

Short circuit in the IGBT bridges: The gate drivers include a v_{CE} monitoring option, that could be used for short circuit protection. In this application, the detection level for the v_{CE} monitoring has to be rather high, as a low saturation voltage will not be reached within a half-cycle (1,25µs).

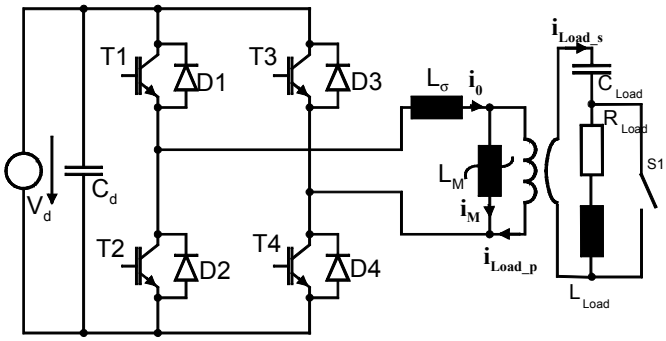

Fig. 8. A single bridge feeding the resonant load. A short circuit of the inductor coil is modeled by S1

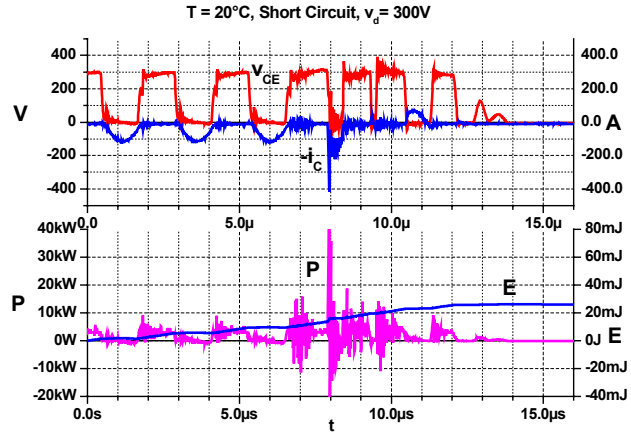

Fig. 9. Measured short circuit in the inductor during operation at reduced DC link voltage

Short circuit in the inductor coil: In industry applications, the load coil may be short circuited by melting particles of the work piece. The inductor coil or parts of it will be shorted partially or completely in this case (S1 in Fig. 8, completely shorted).

Under short circuit conditions, the resonance frequency will increase and the failure is detected by monitoring the time between zero crossings of the resonant current. To improve the starting behaviour an error will be detected, if the higher frequency occurs over 2 cycles (5 µs). The IGBTs are constructed to resist a short circuit up to 10 µs. The control circuit stops the gate pulses in the next period and reports an error.

At the left side of Fig. 9 the normal operation is shown. At t = 8 µs in the experimental set-up a short circuit is generated by closing a contactor (S1, which is likely to bounce). The frequency increases and the short circuit can be detected by the control unit.

IV. SATURATION EFFECTS AT THE HF-POWER-TRANSFORMER

A. *Mode of operation*

The transformer (Fig. 8) will saturate, if the voltage time areas applied to the primary winding do not add to zero.

Under ideal operating conditions the integral of the voltage is zero. Under real conditions, asymmetries may occur. The HF-power transformer is constructed to withstand 4 half-period voltage time areas with the same sign without getting saturated. See Fig. 10.

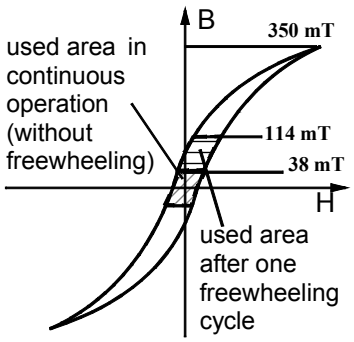

Fig. 10. Magnetic utilization of the HF-power transformer

If the switching behaviour is not the same for all IGBTs, there will be an unbalance in positive and negative voltage time area at the primary winding. Some reasons for different switching behaviour are:

- a temperature difference at the IGBT modules => different parameters
- differences in the driver circuit (tolerances of the gate resistance, different signal propagation times and so on)
- The control circuit operates with a clock frequency of 100 MHz => 10 ns time asymmetry is possible
- Different DC link voltages (the simulation with the parasitic elements shows a voltage swing of about 15 V). Normally the differences over a few periods should eliminate themselves, but this is not guaranteed.
- The current measurement shunt of the IGBT emitter- or collector current is normally mounted only on one IGBT. This causes an asymmetry.

B. Asymmetry in one IGBT-arm caused by measurement shunt

If there is a resistive asymmetry in only one arm of the inverter the voltage time areas at the current transducer and HF-power transformer do not add to zero. See Fig. 11. Consequently, the primary winding gets a direct current component. This current forces the transformers main inductance to saturate and so the inductance decreases.
If such an ohmic asymmetry occurs, the steady state current through the main inductance can be estimated with the equivalent network.

A simulation of this asymmetry with a shunt resistor of 2 mΩ shows a main inductance direct current of approximately 3 A, which is not critically.

C. Asymmetry in gate pulses duration

If an asymmetry in gate pulses duration occurs, the voltage time areas asymmetry will be much higher than in *B*. This error must be avoided. Fig. 12 shows a simulation with an asymmetry of 10 ns. The simulation is done under consideration of the saturation of the transformer and transducers. At a value of 13 A the value of the HF-power transformers main inductance starts to decrease. In the beginning of the simulation the main inductance oscillates with an amplitude of almost 4 A, at 8 ms the alternating part

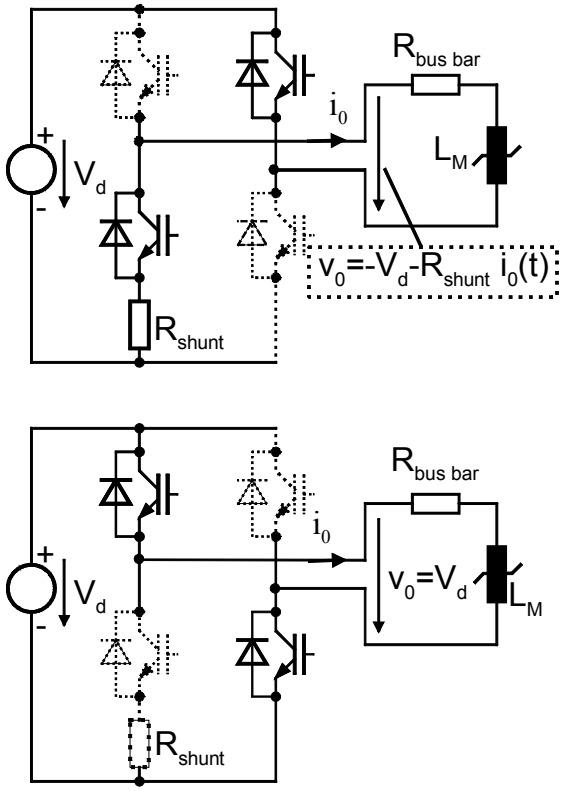

Fig. 11. Voltages at the HF-transformer (considering shunt resistors)
$R_{bus\ bar}$: ohmic resistance in the bus bar and symmetrical resistors at any module

of the amplitude is 14 A. The resolution of Fig. 12 is too low to see each single amplitude.

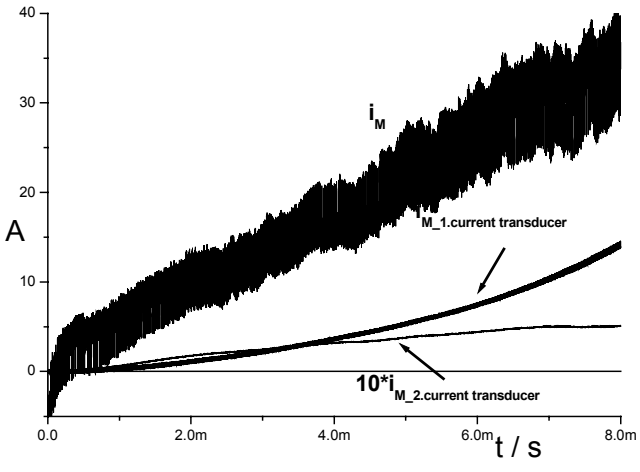

Fig. 12. Simulation of a gate pulse asymmetry of 10 ns

Of course a transformer is not able to transmit a direct current steadily, but if only low voltage time areas are applied, it is possible for a few ms. The current $i_{M\_2.transducer}$ describes the main inductance current of the 2. current transducer. It reaches values of 0.5 A and it starts to decrease at 7 ms. The resolution is too bad to see the alternating component of the measurement currents.

D. Asymmetries as a result of the power controlling by freewheeling paths

The power controlling is done by interleaving pulses and switching a freewheeling path. When T1 and T4 (T2 and T3) at Fig. 8 are conducting a voltage of 600 V (-600 V) is applied to the transformer's main inductance. During a freewheeling path (T2 and T4 are conducting) no voltage is applied. If in the next half-period the DC link voltage is applied to the primary winding, the current in the main inductance will rise. By this, the next zero crossing of the current will be delayed by a very short time interval (Fig. 13).

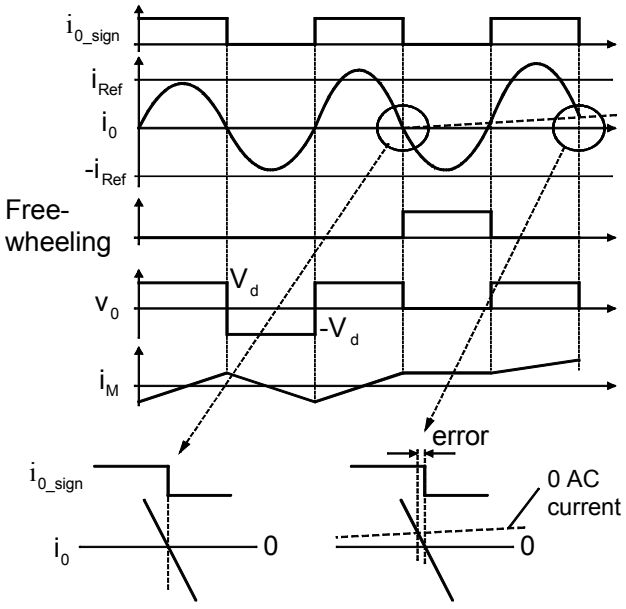

Fig. 13. Influence of the freewheeling path to the HF transformers main inductance current i_M

Depending on the control strategy the gate pulses will get an asymmetry too. In an earlier version of the control circuit the gate pulse was calculated by the duration of the previous half-cycle. In this case there was a positive feedback and the system was not stable (the instability occurs after several cycles). The first short time test set-up operates normal in the first periods. After 100 or more periods (depending on the adjusted reference value for the load current) the system failed sporadically.

One possibility to prevent the rising of the main inductance current is, to switch one freewheeling period at the upper and lower site shifted (flipflop) or to switch two freewheeling phases in series. The drawback of the last possibility is, that discretisation of the output power is very rough. The flipflop method seems to be more successful. Fig. 16 shows a simulation. The transformer has to withstand 2 full deviations of $\Delta\Phi$ before the main inductance decreases strongly as a consequence of the saturation.

E. Comparison to other transformer applications

In contrast to applications with lower frequencies, the high frequency application is critical concerning timing asymmetries. Even a small asymmetry adds up to a large voltage time area in a short time. A half-period at the normal operation frequency of 400 kHz is 1250 ns. The clock frequency of the digital control circuit is 100 MHz (higher frequencies seems to be possible, but they are not necessary). The resolution in this case is 10 ns. In relation to the IGBT on-time period it is almost 1%. If in this case an asymmetry occurs, there will be a rising $\Delta\Phi$ in any cycle of 2 µVs. The maximum flux density (before saturation) is approximately 350 mT, so there could be 588 times a digitalisation error before the transformer starts to saturate. If there is an asymmetry of 10ns in a 50 Hz transformer, the asymmetry is only 0.0001 % of one half-period. The asymmetric voltage in the direct current equivalent network is much less in this case.

F. Measuring saturation current and controlling the magnetization current

To avoid saturation a feedback control is proposed. The magnetization current in the transformer has to be measured and controlled.

Measuring the magnetization current by a differential current transducer

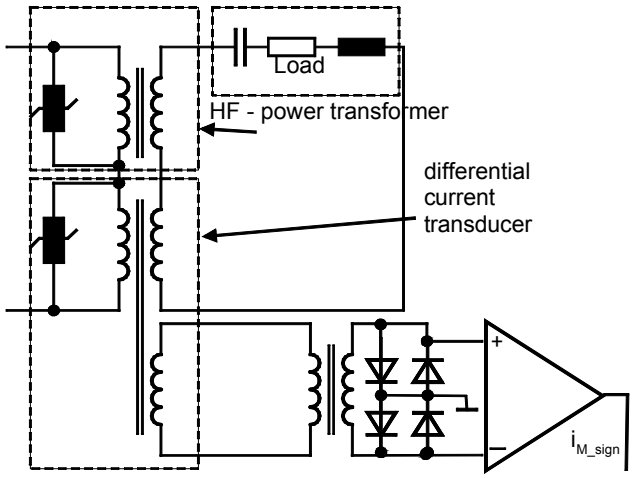

Fig. 14. Differential current transducer

The differential current transducer can be build very small, because the voltage time areas are low. The output signal can reach two values: differential current is positive (1) or negative (0). Over a normal operation cycle the value should be positive and negative. The losses are low and the

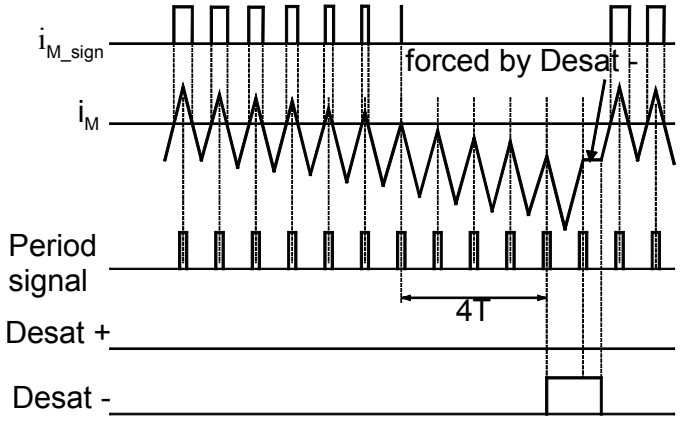

Fig. 15. Detection and compensation of a steady asymmetry

accuracy demands of the devices are low. See Fig. 14.
If in 4 cycles the signal i_{M_sign} has not changed, a suitable freewheeling path is switched. The i_0 current controller is active too (Fig. 15). A simulation with this detection method is shown in Fig. 16 under the assumption of high gate signal asymmetries. The effect of the output power control is shown in the cycles where i_M is constant at the lower part of the figure. The maximum value for i_M is up to 5 A (not critically).

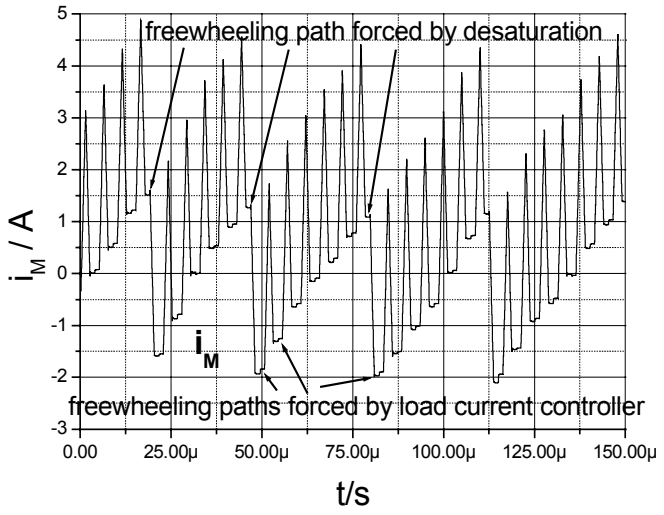

Fig. 16. Simulation of desaturation of the transformer main inductance by switching freewheeling paths. Detection method: differential current transducer

Measuring the magnetization current by analyzing the current signal i_{0_sign}

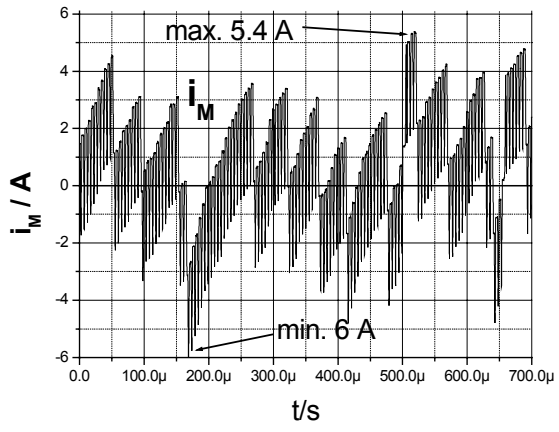

Fig. 17. Simulation of desaturation of the transformer main inductance by switching freewheeling paths. Detection method: analyzing $i_{M\ sign}$

The signal i_{0_sign} indicates the zero crossing of the inverter side alternating current. The resolution of this signal is 10 ns. The transformer saturation starts at a direct current of about 13 A. The amplitude of the alternating current is 200 A at normal operation. The duty cycle of the signal i_{0_sign} in Fig. 13 should be exactly 50%. If in four consecutive cycles the duty cycle is always greater or always less than 50%, then a suitable freewheeling path is switched.
Fig. 17 shows a simulation using this detection method. The deviation will be higher as in the previous discussed method.

V. MULTI INVERTER BRIDGES OPERATION

To share the losses, the inverter for continuous operation consists of 4 full bridges. It is possible to simulate and validate the commutation from one to the other module with two bridges. The hardware set-up has a possibility to operate with 4 modules, but only two are used. The modules can be placed at any of the 4 connectors (Fig. 18). The ac bus bar constitutes parasitic elements. (inductances and capacitors). Fig. 19 gives an overview of the simulated circuit.
Fig. 20 shows the simulation result. The du/dt at the load decreases because of the additional collector-emitter capacitances. This could effect the losses. Further measurements will give information about the influence to the losses.
The small gate voltage spikes of the non switched IGBT are due to the charge of the gate-collector capacitance. This capacitance is charged when the load voltage changes. The current flows through the gate resistor. The external resistance in the simulation is set to 0.5 Ω, but there is an internal gate resistance in the IGBT of 2.5 Ω. At a high du/dt of the collector-emitter voltage a displacement current is forced through the resistance, that generates a high internal gate-emitter voltage. V_{GE} (even the internal) must be forced to fall below the absolute value of 20 V to avoid a gate-emitter breakdown. One possibility to decrease the du/dt is to use an external snubber capacitor, connected to collector and emitter at any IGBT. [5] gives an impression of the effects. A switch-off loss reduction of 30% seems to be possible. Further measurements are required to decide, if additional du/dt limitation measures must be taken.

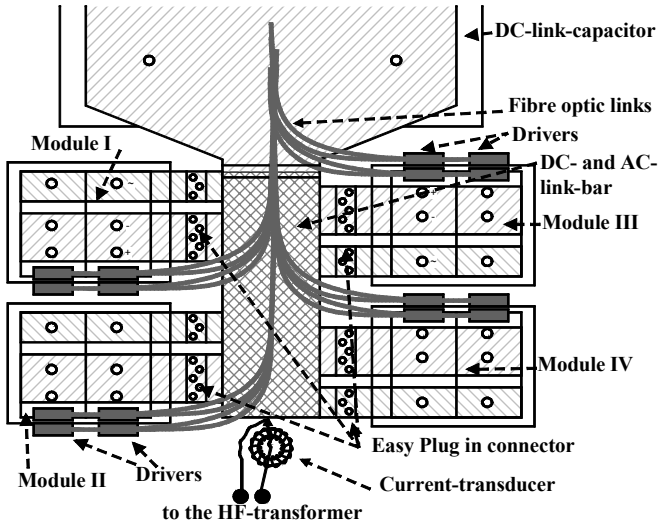

Fig. 18. Multi inverter bridges set-up

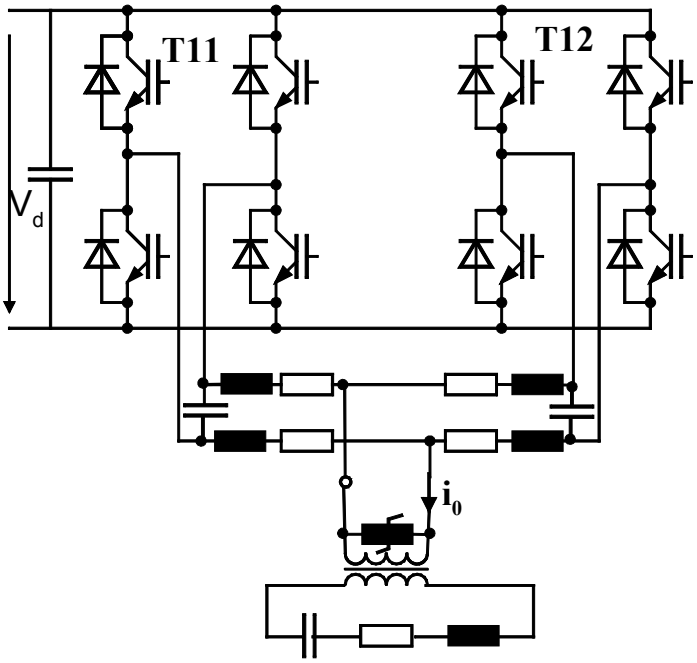

Fig. 19. Overview over the electrical set-up with parasitics (LCR in the ac bus bar)

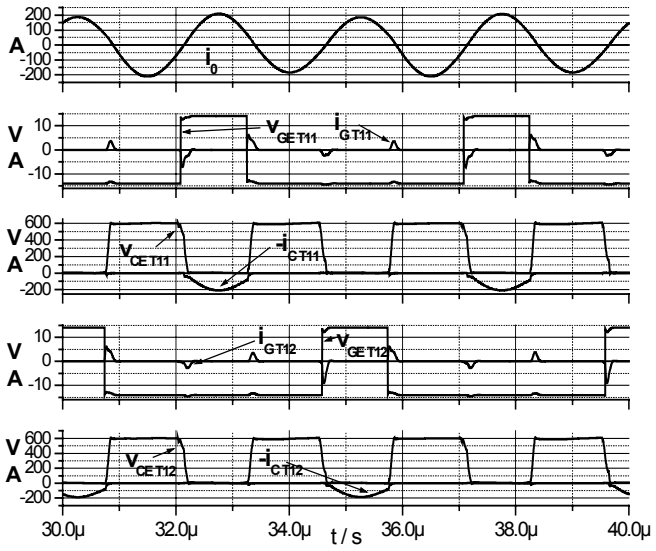

Fig. 20. Simulation of two paralleled bridges

VI. CONCLUSION:

The influence of the variation of the control parameters interlock- and leadtime was investigated by simulation and by experimental set-up. There is a time slot of 40 ns for the both parameters, where the losses will be almost equal. The efficiency shows a flat maximum, with a low sensitivity of the interlocktime. The resolution of the timing should be better than 20 ns. If a galvanic insulation transformer is used, it has to withstand 2 full voltage time areas of the inverter output voltage in minimum. The effects of an asymmetrical gate pulsing to the saturation of the HF-power transformer are great and can not be neglected. Controlling the transformers saturation by switching freewheeling paths seems to be mandatory. Multi inverter operation is simulated and the experimental set-up for multi inverter operation is under construction.

References

[1] T. Undeland, F. Kleveland, J. Langelid: ”Increase of Output Power from IGBTs in High Power High Frequency Resonant Load Inverters”, IEEE-IAS 2000 Rome

[2] H. Abo Zied, P. Mutschler: “A Modular IGBT Converter System for High frequency Induction Heating Applications”, PCIM 2002

[3] A. Schönknecht, R. W. De Doncker: “Distributed Control Scheme for Parallel Connected Soft-Switching High-Power High-Frequency Inverters”, PESC 2002

[4] H. Rüedi, P. Köhli: Application note AN-9701, version 1.0, CT-Concept Technologie AG

[5] M. Helsper, F. W. Fuchs : “Analysis and comparison of Planar- and Trench-IGBT-Modules under ZVS switching conditions”, PCIM 2002

[6] Eupec FF200R12KS4 Data sheet, revision: 3.0

Development a Heater using Induction Heating Based on a High Frequency Resonant Inverter

D.C. Shin, H.M. Kwon, Y.J. Kim
Hoseo University
Asan, Chungnam, Korea
dcdin@office.hoseo.ac.kr

H. D. Lee
Shinbo I. & C.
Anyang, Kyungkido, Korea
hdlee59@lycos.co.kr

K. H. Kim
Semyung University
Jecheon, Chungbuk, Korea
khkim@semyung.ac.kr

***Abstract*— This paper described the indirect induction heated boiler system and induction heated hot air producer using the voltage-fed series resonant high-frequency inverter which can operate in the frequency range from 20 [kHz] to 50 [kHz]. A specially designed induction heater, which is composed of laminated stainless assembly with many tiny holes and interconnected spot welding points between stainless plates, is inserted into the ceramic type vessel with external working coil. This working coil is connected to the resonant inverter. The heater is composed of two heating sections. The primary heating section produces low-pressure saturated steam and the secondary heating section generates heat distributed evaporating fluid from the turbulence fluid, which is flowing through the vessel. The operating performances of this unique appliance in next generation and its effectiveness are evaluated and discussed from the practical point of view.**

I. INTRODUCTION

Induction heating has been traditionally used to heat metal parts in applications such as soldering, brazing, hardening and melting of metals. The power from modern induction heating systems is so controllable, that is may be used to create ceramic components at temperatures in excess of 2400°C.

In brief, induction heating is a non-contact method of heating electrically conducting materials. It involves a source of alternating current (the induction heater), induction coil (often called the work coil) and the part to be heated (the work piece).

When an electrical current is made to alternate in a work coil, this produces an alternating magnetic field in and around the work coil. If an electrically conducting part is place within the magnetic field, a current will be developed in that part (the work coil may be considered as the primary winding of a transformer and work piece as a short-circuit secondary winding). [1][2]

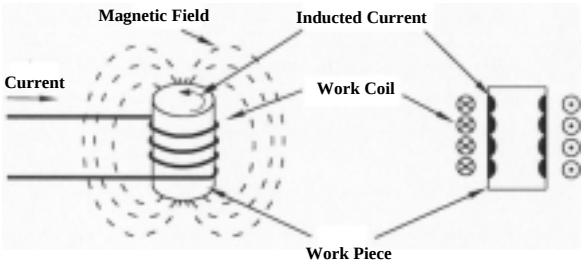

Fig. 1 Principle of Induction Heating

II. INDUCTION HEATING SYSTEM

A. Principle of Induction Heating

The theory behind induction heating systems is from the idea of a metal object being supplied with an alternating current. This creates a magnetic field, which in turn creates an induced current. This induced current heats the metal though its internal resistance. The density of the induced current is greatest at the surface and reduces as it penetrates the surface. This is known as the skin depth or penetration depth.

Heat transfer and electromagnetics are important to induction heating because the properties of heat-treated materials depend on temperature and magnetic field intensity. There are three modes of heat transfer, conduction, convection, and radiation. All three are present in conventional induction heating. According to Fourier's law, the rate of heat transfer in an object is proportional to the temperature difference.

Fourier's law is the basic law that describes heat transfer by conduction,

$$Q_{cond} = -\lambda \cdot grad(T) \qquad (1)$$

where, Q_{cond} = heat flux by conduction,
λ = thermal conductivity,
T = temperature.

Heat transfer by convection is carried from the heated object to the surrounding area by fluid, gas or air, and can be described by a well known Newton's Law. This method plays an important role in the cooling process.

$$Q_{cond} = \alpha(Ts - Ta) \qquad (2)$$

where,
Q_{cond} = heat flux density by convection, W/m^2,
α = convection surface heat transfer coefficient, $W/(m^2 \cdot ^\circ C)$,
Ts = surface temperature, ° C,
Ta = ambient temperature, ° C.

Heat radiation is the third mode of heat transfer. The effect

can be described by the amount of electromagnetic energy propagating due to a difference in temperature. Polished metal will radiate less heat than non-polished metal due to the emissivity of the metal. [3]

B. Structure of Induction Heating System

Fig 2. shows the structure of induction heating system. Inside of heating vessel in isolated pipeline the specially designed laminated metallic package, which can be heated by eddy current losses is inserted. Working coil, which is wrapped outside of pipeline, makes the eddy current. Electromagnetic induction heater can heat water or gases in pipeline very rapidly.

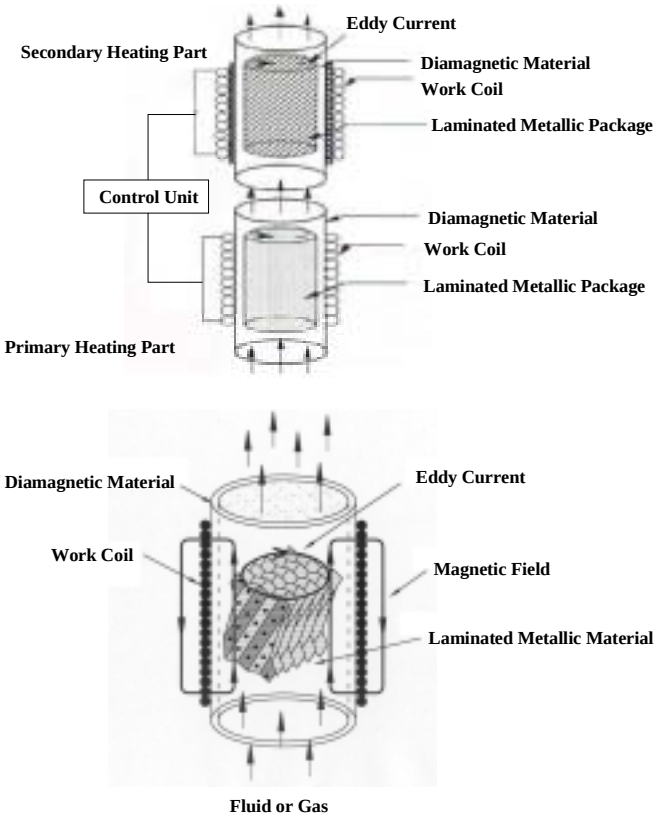

Fig. 2 Configuration of the Induction Heating System

Fig. 3 shows a laminated metallic package as heating material. This package is not composed of metallic wire but metallic plates. So in case of high temperature heating, the ability of electrical isolation, opening or shorting is superior. With this package one can obtain good temperature response of the outlet because the heat capability and the fluid resistance are small. So this appliance has many good characteristics.

Fig. 3 Induction heated metallic package

III. HIGH FREQUENCY RESONANT INVERTER

Fig 4. shows half bridge series loaded resonant inverter. It can be considered as an electrical circuit, which is composed of R and L that depends on the depth of isolated pipeline or the material of laminated metallic package. For the experiment a matching transformer is used between the working coil and the heated material. Capacitor C in Fig. 4 compensates inductance L. To choose a working frequency is very important in order to drive for high efficiency in series resonant circuit. By using series compensate capacitor C in R-L circuit we can construct R-L-C series resonant circuit as a load. If the load is not heated up to limitation, the circuit constants are scarcely changed, so that we can consider just as R-L circuit. The series load compensator C is used under the same condition as to compensate L in R-L load system. If the turn-on resistance of IGBT is greater than R in R-L load, the series resonant circuit is more effective. In other case the parallel resonant circuit is more effective. [4]

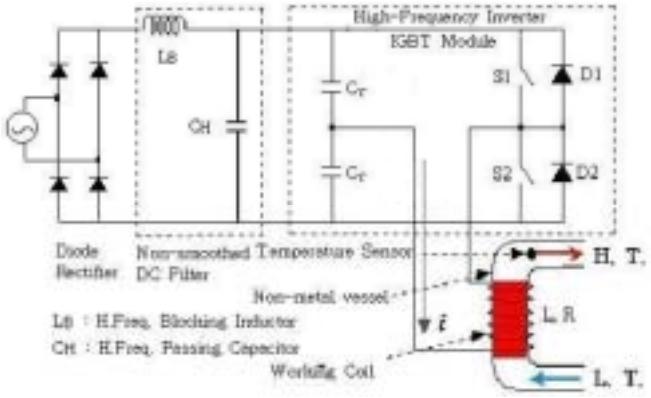

Fig. 4 Half-bridge resonant inverter

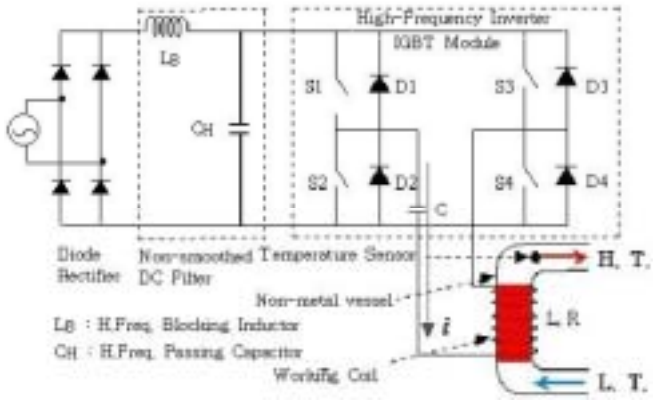

Fig. 5 Full bridge resonant inverter

In high-power switching circuit, the arm short of upper and lower part of IGBT generates penetration current. The penetration current is caused by Push-Full driving. Because of turn off delay at push-full driving, upper and lower part of IGBT will be on simultaneously. With this reason one gives a delay time between upper and lower part of IGBT's switching operation on purpose. Usually, IGBT needs 2 ~ 3[μs] and FET, which switching speed is faster than IGBT, needs 1 ~ 1.5[μs]. [5]

Table 1 shows switching conditions and inverter output voltages.

Table 1 Switching condition diagram

S1	S2	Controllability	Vo
on	on	impossible	-
on	off	possible	$V_{DC}/2$
off	on	possible	$-V_{DC}/2$
off	off	possible	$V_{DC}/2$ for $i_o<0$
			$-V_{DC}/2$ for $i_o<0$

When switch S1 and S2 are simultaneously turned on, DC input voltage source will be shorted. Thus switch S1 and S2 should be switched reciprocally. When S1 is turned on, voltage $V_{DC}/2$ is applied to the load and when S2 is turned on, voltage $-V_{DC}/2$ is applied to the load. Additionally, it is allowable that switch S1 and S2 are off at the same time. In this case, the load voltage is determined by the direction of load current. That means if i_o is greater than 0, D2 will be on and v_o is $-V_{DC}/2$. In other case, i_o is smaller than 0, D1 will be on and v_o is $V_{DC}/2$.

Fig. 5 shows high frequency full-bridge resonant inverter. The experimental circuit of single phase full-bridge inverter is made by two poles which can be independently switched. The construction of each pole is same as single half-bridge inverter. [6]-[8]

IV. Experimental Results

For the experiment, IGBT modules are used, which are made by FUJI 2MBI100L-120. The dielectric strength of this module is 1200[V], 100[A]. In the primary heating part several capacitors (capacity 0.1[μF]) are used. The inductance is adjusted in the range of 100[μH] to 200[μH].

As a resonant capacitor polypropylene type is used which has good frequency characteristics.

A diode rectifier with a non-smoothing LC filter is used, so that sinusoidal wave line current shaping in the utility-AC grid is to be easily performed without a complicated active PWM control. In this experiment, small capacity for the LC filter is used so that 120[Hz] ripple component can be accepted. In addition, to choose a filter power-factor control characteristic should be considered. In this experiment inductance in the range of several tens [μH] and capacitance of small range of some [μF] are used.

Fig. 6 shows voltage type serial resonant switching pulse pattern for half-bridge inverter. Switch S1 and S2 are reciprocally turned on and off. The phase difference between the S1 and S2 is 180°.

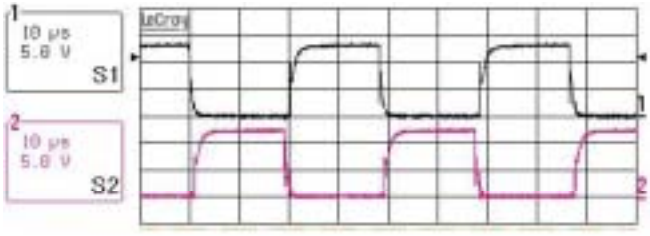

Fig. 6 Switching pattern of half bridge inverter

Fig. 7 shows waveforms of output voltage and current of half-bridge inverter.

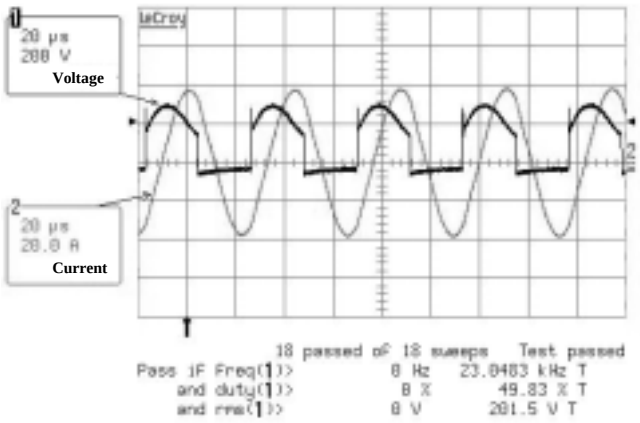

Fig. 7 Waveforms of output voltage and current of half bridge inverter

Fig. 8 shows switching pattern of full-bridge inverter. Switch S1 and S4 are simultaneously turned on and off. As well as S2 and S3 are simultaneously turned on and off. The phase difference between S1, S4 and S2, S3 is 180°.

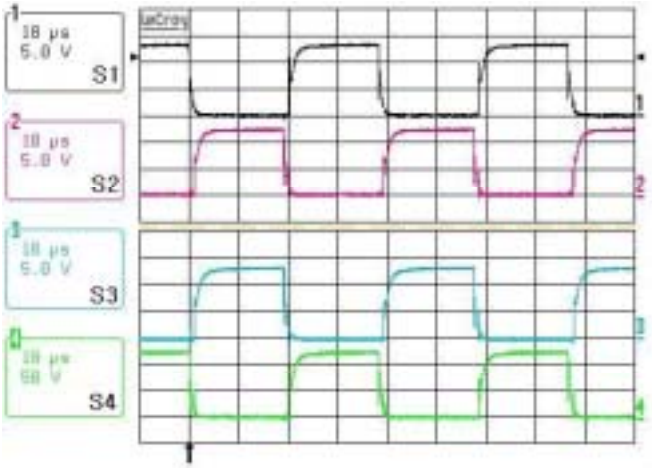

Fig. 8 Switching pattern of full bridge inverter

When the pole voltages are square waves and phase difference between two-pole voltages is 180°, the Fig. 9 shows waveforms of output voltage and current of single full-bridge inverter with inductor L as a load. At this moment, output voltage V(out) of the load becomes V(DC) square wave as shown in Fig. 7. When square voltage is applied to inductor L, load current I(out) increases while V(out)=V(DC) and it decreases while V(out)=-V(DC).

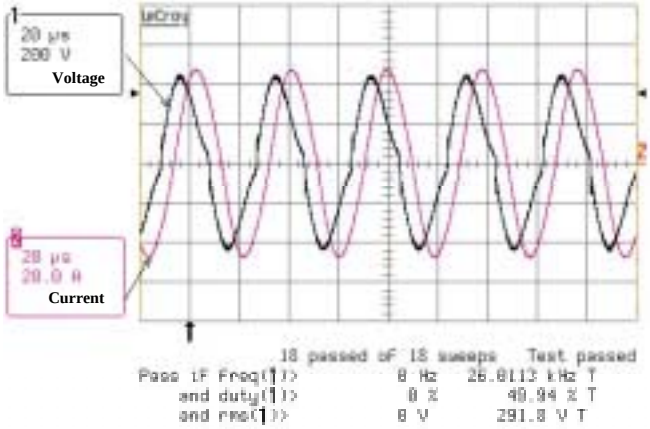

Fig. 9 Waveforms of output voltage and current of full bridge inverter

Table 2 Input and Output Characteristics of half- and full-bridge

Char. / Method	Input			Output (L-C)		
	[V]	[A]	[Hz]	[V]	[A]	[kHz]
Half-Bridge	220	6	60	200	12	23
Full-Bridge	200	20	60	290	40	26

Table 2 shows input and output characteristics of half- and full-bridge.

Fig. 10 shows structure of two-step superheating system, which consists of primary boiler system and secondary superheat generator. As shown in Fig. 10 the whole system is divided into two parts and connected in series. The primary heating part produces vapor, which is 100 [°C]. In the secondary heating part the vapor from the primary heating part is overheated to over 200[°C]. Fig. 11 shows experimental set up superheating system.

For the primary heating part and the secondary part are used full-bridge inverter and half-bridge inverter respectively.

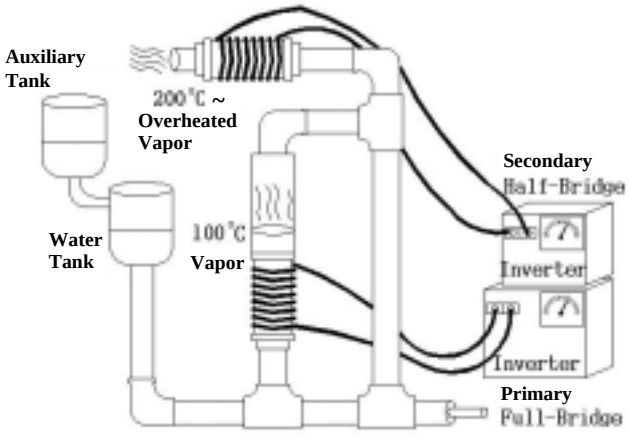

Fig. 10 Structure of proposed system

Fig. 11 Experimental setup superheated system

In primary boiler section, sufficient water supply is needed. In this experiment, a water tank with water level control system and auxiliary tank are mounted in order to supply sufficient water.

V. CONCLUSION

Fluid heating method using high-frequency inverter is one of the innovative methods of induction heating. This is proved in this paper by using sufficient thermal source. Fluid heating using induction heating is very stable and this process occurs not burning, so it makes no pollution and after all, the working environment is clean. In this experiment, input output voltage and current stability of each primary and secondary inverter superheat generator is proved.

Fluid heating method using induction heating is operated as follows. Working coil, which is wrapped outside of pipeline, makes the eddy current. Inside of heating vessel in isolated pipeline the specially designed laminated metallic package is inserted, which can be heated by eddy current losses.

The proposed electromagnetic induction heating system has high thermal exchange efficient and can control precisely the temperature. Also instantaneous heating is possible. This system is not a contact heating system, so that has high confidence. The deterioration of fluid is not occurred by scale. The whole heating system has compact size.

This induction heating method, when compared with conventional system, becomes more cost-effective, and has high-efficiency conversion, quick response and precise temperature control realization. Moreover, the field of exhaust gas cleaning system and exhaust corpuscle reducing system is researched by using resonant inverter.

In the future, studies such as controller for output control, material of packed heating element and protection circuit design are necessary. In addition, search for widely applicable fields on induction heating should be processed.

REFERENCES

[1] http://www.cih-group.co.uk/whatis.htm

[2] D. Y. Lee, D. H. Hyun, “A New Hybrid Control Scheme Using Active-Clamped Class-E Inverter with Induction Heating Jar for High Power Applications”, Journal of Power Electronics, vol. 2 No. 2, April 2002, pp. 104-111

[3] http://stuweb.ee.mtu.edu/~mtromble/induction/heat.html

[4] Y. J. Kim, D. C. Shin, "Soft-Switched PWM DC-DC Converter with Quasi Resonant-Poles and Parasitic Resonant Components of High-Voltage Transformer", The Transactions of The Korean Institute of Power Electronics, vol. 4, No. 4, Sept. 1999, pp. 384 395

[5] Y. Uchihori, Y. Kawamura, Y. J. Kim and M. Nakaoka, "New Induction Heated Fluid Energy Conversion Processing Appliance incorporating Auto tuning PID control based PWM Resonant IGBT Inveter with Sensorless Power Factor Correction", Proceedings of the IEEE power Electronics Specialist Conference, pp. 1191 1197, 1995, June.

[6] D. C. Shin, H. M. Kwon, K. H. Kim, Y. J. Kim, “A Study on the Development of Superheater Using High-frequency Resonant Inverter for Induction Heating”, The Transactions of The Korean Institute of Power Electronics, vol. 9, No. 2, April 2004, pp. 119 125

[7] Y. J. Kim, D. C. Shin, K. H. Kim, Y. Uchihori, Y. Kawamura, “Fluid Heating System using High-Frequency Inverter Based on Electromagnetic Indirect Induction Heating”, Proceedings of International Conference on Power Electronics, Oct. 2001, pp. 69 74

[8] H. M. Kwon, S. H. Kim, D. C. Shin, Y. J. Kim, “A Study on the Development of Induction Heating System for Using Full-Bridge High-Frequency Resonant Inverter”, Proceedings of Power Electronics Annual Conference, July 2003, pp. 19 22

Supply and Control of Piezoelectric Systems

Horst Grotstollen
University of Paderborn
D-33095 Paderborn, Germany
grotstollen@lea.upb.de

Abstract **- Piezoelectric actuators, motors and transformers are becoming more and more important. Without exception piezoelectric devices are fed by power electronic converters and at almost all applications they are operated in closed loop control. Considering the strong interdependence between actuator, power supply and control structure piezoelectric systems constitute typical mechatronic systems the components of which cannot be designed independently. Starting with typical applications the paper gives a survey on resonantly operated actuators, suitable power converters and adapted control schemes.**

I. INTRODUCTION

Piezoelectric actuators are becoming more and more attractive due to their high power density in particular when operated at high frequencies and when making use of resonant amplification in the mechanical part. But not only electromechanical energy conversion is possible: Piezoelectric transformers can be easily realized by implementing two pairs of electrodes on the same piece of piezoelectric ceramics. Up to now piezoelectric actuators have been realized with low power only (motors less than 100 W, transformers less than 40 W), but high efforts are made to increase power ratings.

In contrast with conventional electromagnetic actuators piezoelectric devices do not make use of magnetic fields and do not behave inductive. In fact their capacitive behaviour has to be considered when designing the power supply. Furthermore the control of piezoelectric systems becomes a demanding task when resonant operation is aspired. Finally it turns out that the choice of the control structure for a piezoelectric system depends strongly on the type of power converter. Consequently a resonant operated piezoelectric system proves to be a typical mechatronic system the parts of which cannot be developed independently of each other.

In the following a survey will be given on piezoelectric actuators, on adapted types of power converters and on control schemes which match the requirements of piezoelectric systems and the requirements being established by different applications. For general information on piezoelectric materials and devices see [1], [2].

II. Applications of resonant operated actuators

A. *Sonotrodes for ultrasonic machining*

Processing of materials can be accelerated and wear of the tool can be reduced when an ultrasonic oscillation is superimposed in quadratur to the cutting speed of the tool. For this purpose sonotrodes (ultrasonic power converters) are used consisting of a steel bar which is excited to structural resonance by a piezoelectric actuator, see Fig. 1. Normally resonance frequency is in the range of 20...30 kHz and reduction of cross-section is used to increase the amplitude of oscillation at the active surface.

The surface of the bar can be equipped with any machining tool like drill, knife, cutting chisel, dental elevator or bonding tool at production of chips. At other applications ultrasonic is applied to a liquid in which objects are cleaned or to a gas in which drops of liquid are spattered.

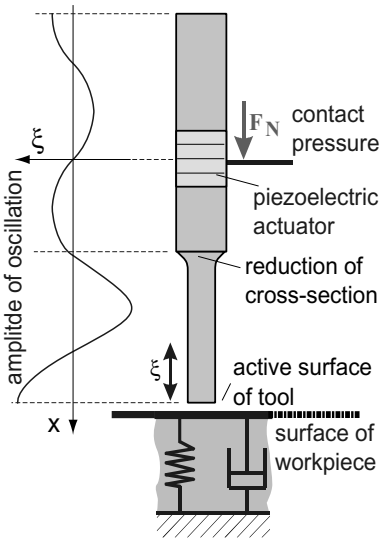

Fig. 1: Sonotrode

For excitation of sonotrodes small volumes of piezoelectric material is required. Sonotrodes therefore own good power factors (0.75 ... 0.9 at mechanical resonance).

B. *Piezoelectric transformers*

A piezoelectric transformer comes into being when a second actuator is introduced into the system as shown at Fig. 2a). Normally all the oscillating bar is from piezoelectric material (no steel) and different shapes are possible.

The transmission ratio of the transformer is determined by the design of the piezoelectric actuators. The system is operated at $\lambda = L$ as shown by the dotted lines of Fig. 2b). Excellent isolation of primary and secondary is achieved if the whole bar is made from ceramics.

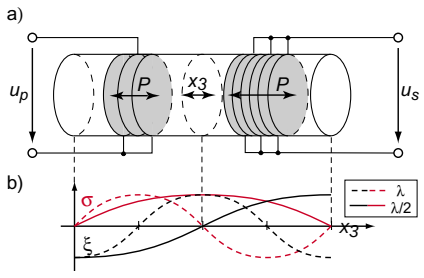

Fig. 2: Piezoelectric transformer
a) aggangement of actuators
b) distribution of strain and deviation

Piezoelectric transformers can also be designed by using ring-shaped ceramics which can oscillate in radial, axial or tangential direction. They offer small size and good efficiency and have been realized e.g. for 10 W for power supply of handys [3].

C. Ultrasonic travelling wave motors

At the well-known ultrasonic travelling wave motor a piezoelectric ring-shaped actuator system excites a travelling

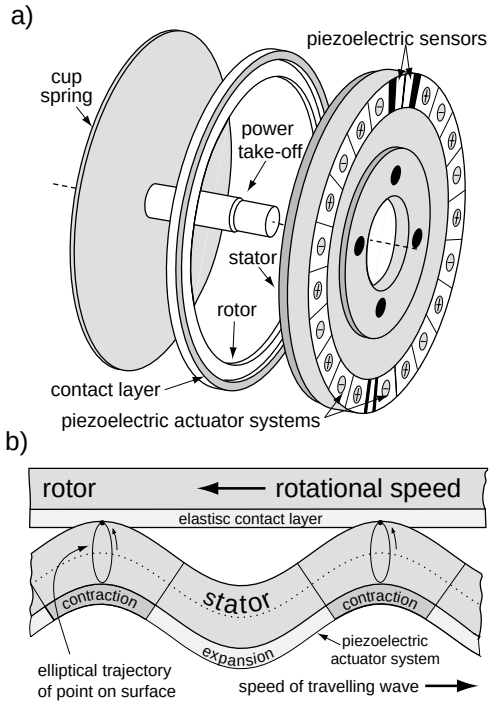

Fig. 3: Ultrasonic travelling wave motor
a) exploded view b) generation of travelling wave

bending wave at the circumference of a circular brass disc [4], see Fig. 3a). The actuator system consists of a piezoceramic ring which is divided into two actuator phases and two small sensor sections. By means of expanding and contracting zones each actuator phase generates a standing wave at 40...45 kHz which superimpose to a travelling wave, see Fig. 3b). The sensors are used to measure and to control the spacial amplitudes of the standing waves.

For power take-off a rotor-ring is pressed to the circumference of the stator-disk where the travelling wave causes a rotary movement of the rotor. Torque is generated in a difficult way by friction which causes a poor efficiency (less than 50 %). Since a great volume of piezo-ceramics is required to initiate the travelling wave power factors at mechanical resonance ω_{r1} are less than 0.1. Travelling wave motors with rated power up to 100 W generate high torque at low speed and are in use for autofocus in cameras and in cars for adjustment of head-rests and steering wheels [5].

IV. Modelling of piezoelectric actuators

For resonant operation of any mechanical structure its dimensions must be in the order or smaller of the wave length appearing at the operating frequency. In this case phenomenons of wave propagation inside the structure must be considered.

At sonotrodes and transformer the bar itself is oscillating, at motors only the disc is the oscillating structure.

A. Piezoelectric actuator with structural oscillation

Due to high frequencies the elasticity and mass of the ceramics and steel cannot be neglected; even more, these are essential for the resonant operation of the actuators which make use of structural oscillations.

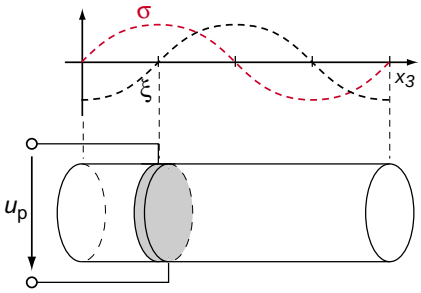

Fig. 4: Resonant operated sonotrode

The mechanism of structural oscillations is explained refering to the bar shown at Fig. 4 as used at a sonotrode, see Fig. 1. The bar is excited. and fixed at $x = L/4$ (therefore $\xi(L/4, t) = 0$) with a frequency for which $\lambda = L$ holds. At both surfaces of the bar no force and no strain are present $\sigma(0, t) = \sigma(L, t) = 0$. Due to these boundary conditions resonant operation is possible at an infinite number of discrete wave lengths being in accordance with

$$L/4 = (2k-1) \cdot \lambda_k/4 \qquad f_k = (2k-1) \cdot v_S/L \quad \text{where} \quad k = 1, 2, 3, \ldots \qquad (1)$$

Due to an infinite number of discrete wave lengths (characterized by order k) an infinite number of associated resonance frequencies f_k exists.

$$f_k = v_S/\lambda_k = (2k-1) \cdot v_S/L \qquad k = 1, 2, 3, \ldots \qquad (2)$$

For practical design some numbers are given: According to velocity of sound being 5,200 m/s for steel and 2,500 ... 4,600 m/s for piezoelectric ceramics wave length at a frequency of 20 kHz is 260 mm for steel and 125 ... 230 mm in piezoceramics.

For transfer of power to a load that is coupled to the bar's surface strain as well as deviation must be present at the positions of the actuator ($x = L/4$) and of the surface (e.g. at $\lambda = L$). These requirements can be fulfilled by a variation of frequency and wave length.

B. Equivalent circuits

Any mechanical system can be modelled by an electrical equivalent circuit. If the system is vibratory the model will be a resonant circuit which in case of piezoelectric actuators proves to be of the series connected type. If structural oscillations are to be modelled each resonant frequency has to be considered by an extra resonant circuit. This results in a parallel connection of an infinite number of series resonant circuits as shown at Fig. 5 the right section of which represents the mechanical part of the vibratory actuator.

The meaning of the variables and parameters is as follows: Inductance L_m, capacitance C_m and resistance R_m represent the inertial mass, stiffness and mechanical damping of the actuator, respectively.

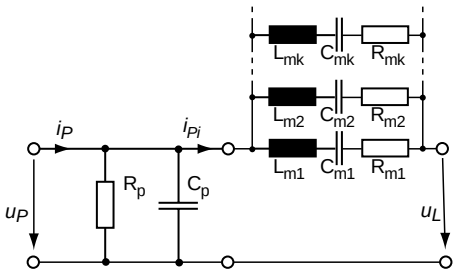

Fig. 5: Equivalent circuit of resonant operated actuator

In general voltages represent forces while currents represent speeds. Therefore the voltages at the inductances L_m, the capacitances C_m and the resistances R_m represent the forces accelerating the mass, stressing the elasticity and causing losses due to mechanical damping. The inner current i_{Pi} represents the speed of actuator and load while the output voltage u_L represents the external force f_L being applied to the surface of the actuator. If $f_L = 0$ the output of the circuit is shorted. .

At the left side of the equivalent circuit, see Fig. 5, the electric features of the actuator are modelled: The energy stored in the electric field and the dielectric losses of the ceramics are modelled by capacitance C_P and resistance R_P.

C. Equivalent circuit for resonant operation

For the discussion of suitable power converters and control schemes the model of piezoelectric actuator can be simplified as follows: First, resistance R_p can be neglected due to small and unimportant piezoelectric losses. Second, only one series resonant circuit of Fig. 5 needs to be considered as far as only one resonant mode is excited by application of sinusoidal voltage and/or current. Last not least, the load being applied to the actuator can be approximately modelled by a linear impedance which is connected to the output of the equivalent circuit. Equivalent inductance L_L, capacitance C_L and resistance R_L of the load can be combined with the accordant devices of the actuator L_m, C_m, R_m. Resulting parameters are

$$L_M = L_m + L_L \qquad C_M = \frac{C_m C_L}{C_m + C_L} \qquad R_M = R_m + R_L \quad (3)$$

Finally we get the equivalent circuit shown at Fig. 6a) which is reduced to the circuit of Fig. 6b) if the operation frequency matches the resonance frequency of the actuator.

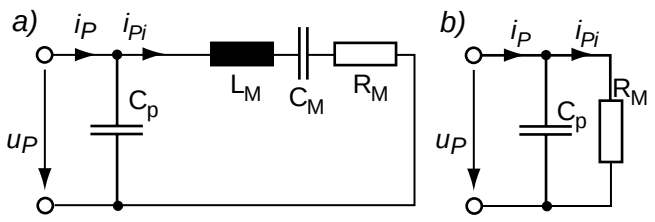

Fig. 6: Approximate equivalent circuits of loaded actuator
a) in surrounding of resonance frequency,
b) exactly at resonance frequency

IV. POWER CONVERTERS AND CONTROL

To transfer the net power to the mechanical output with minimum stress of the mechanical part piezoelectric actuators should be operated as close as possible to a resonance frequency. This means that one mode of oscillation (order k) has to be chosen; normally the lowest order ($k = 1$) is used. As a result fundamental frequency of the power converter is determined by the resonance frequency of the mechanical system. Furthermore sinusoidal input voltage and current have to be delivered by the converter and consequently equivalent circuits of Fig. 6a) can be used to model piezoelectric actuators for design of power converters and control schemes.

The frequency characteristic of the input admittance of this equivalent circuit is shown at Fig. 7. Due to three reactive devices two resonance frequencies are existing.

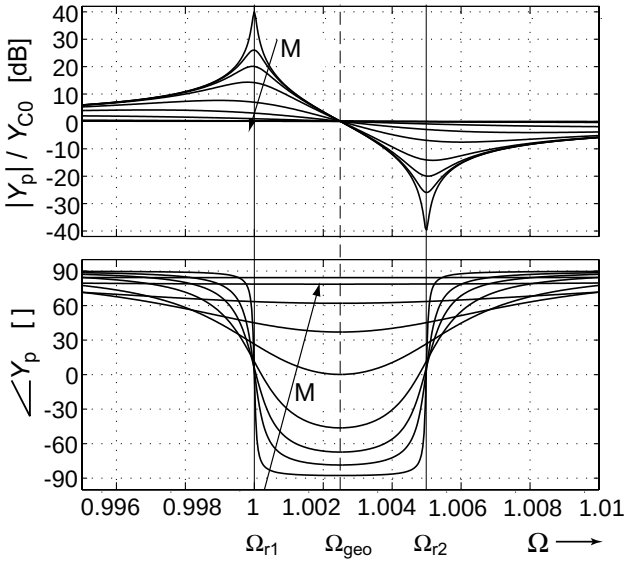

Fig. 7: Frequency characteristic of actuator systems input admittance (normalised frequency: $\Omega = \omega/\omega_{r1}$)
M = .001; .05; .01; .5; 1; 2; 5; 10 where $M = \omega_{r1} C_P R_M$

$$\omega_{r1} = \frac{1}{\sqrt{L_M C_M}} \qquad \omega_{r2} = \frac{1}{\sqrt{L_M \frac{C_M C_P}{C_M + C_P}}} . \quad (4)$$

Series resonance (ω_{r1}) is determined only by the mechanical part of the system. At this resonance input impedance of the equivalent circuit is low which means that low input voltage and high input current i_{Pi} are required to deliver the power demanded by resistor R_M representing load and losses.

Parallel resonance (ω_{r2}) depends additionally on the capacitance of the piezo-ceramics. In contrast with series resonance high input voltage and low input current are required. Note that ω_{r2} is always higher than ω_{r1}. With regard to high voltage levels required by piezoelectric actuators operation at series resonance is normally preferred.

In case the system is operated exactly at series resonance the input admittance of the actuator can be seen from Fig. 6b),

$$Y(j\omega = j\omega_{r1}) = R_M^{-1} + j\omega_{r1} C_P \qquad (5)$$

When the system is investigated in detail the ratio of the reactive and the active part $M = \omega_{r1} C_P R_M$ proves to be an important parameter by which two classes of systems can be distinguished [10]: Admittance ratio M indicates whether the input behaviour of the system is determined by the mechanical resonant part or by the piezoelectric capacity of the actuator.

If $M = \omega_{r1} C_P R_M < 1/2$ holds two frequencies exist at which the imaginary part of the input admittance disappears and $\angle G_{LC} = 0$ holds, see Fig. 7. As a result no reactive power is required by the actuator when operated at one of these frequencies. Condition $M < 1/2$ normally exists at sonotrodes where the actuator itself forms the oscillating structure.

In contrast at systems with $M = \omega_{r1} C_P R_M > 1/2$ the input admittance has a capacitive imaginary part at all frequencies. This is the case with ultrasonic travelling wave motors. At these motors a rather great volume of piezoceramics is required to excite oscillation of the stator disc and causes a great piezoelectric capacitance. Consequently these motors always have a high demand for reactive power.

V. POWER CONVERTERS AND CONTROL SCHEMES FOR piezoelectric ACTUATORS [10]

Power supplies for piezoelectric actuators normally are DC link converters, see Fig. 8.

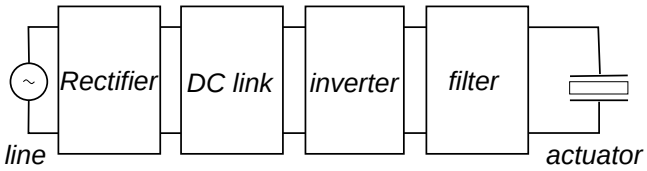

Fig. 8: Stages of DC link converter

Between the actuator and the inverter a filter with at least a series inductor must be inserted to decouple the capacitance of the actuator from the voltage source inverter.

For realisation of the inverter stage half bridge and full bridge as well as push-pull converter can be used, see Fig. 10. For the design of the filters and the operation of the inverter stage two basic possibilities are existing.

Furthermore attention must be paid to the low order harmonics of the fundamental frequency because these may excite unwanted oscillation modes which impair proper operation of the system.

Last not least in most cases the output must be separated from the input by a transformer. In many cases this device is inserted between the inverter and the piezoelectric actuator and therefore has to be designed in accordance with the transmitted apparent power.

As already mentioned two basic alternatives for the design of the filter exist which results in different features of the system.

A. PWM converters

As is generally known low order harmonics can be avoided by operating the inverter at high switching frequencies at which low current ripple can be achieved with small filter inductors [7]. By use of a suitable control structure in combination with PWM sinusoidal input current can be applied to the actuator causing voltage also to be sinusoidal.

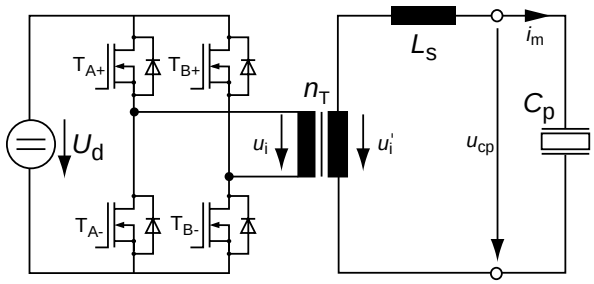

Fig. 10: Full bridge inverter with PWM filter inductor

The frequency characteristics resulting from the actuators capacitance and the small series inductor shows a resonance appearing at a frequency far beyond the operating frequency fs, see Fig. 11. Due to this fact parameter variations of the resonant circuit hardly influence the output voltage of the filter. Such variations can be caused by the actuator's capacitance which depends on temperature or by the load. In Fig. 11 also the frequency response can be seen (RC-approx.) which results from the simple equivalent circuit of Fig. 6b).

In case of PWM converters the whole apparent power of the actuator has to be delivered by the inverter and its DC link via the transformer. Due to this aspect PWM inverters are a good choice for sonotrodes which normally have low piezoelectric capacitance ($\omega_{r1} C_P R_m < 1/2$) and low reactive power consumption.

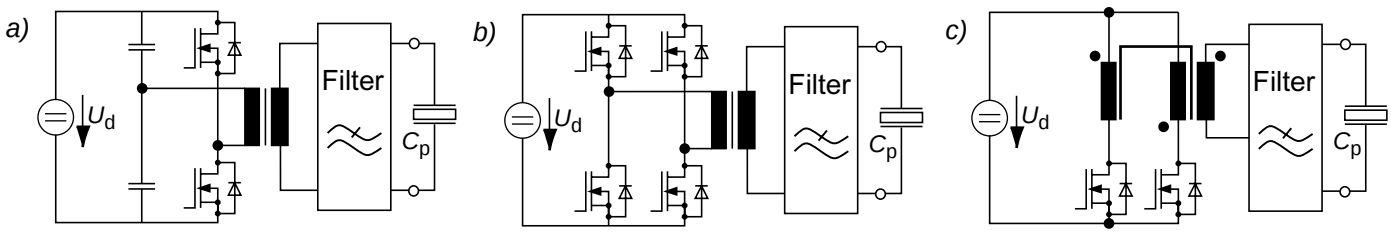

Fig. 9: Inverter topologies a) half bridge b) full bridge c) push-pull converter

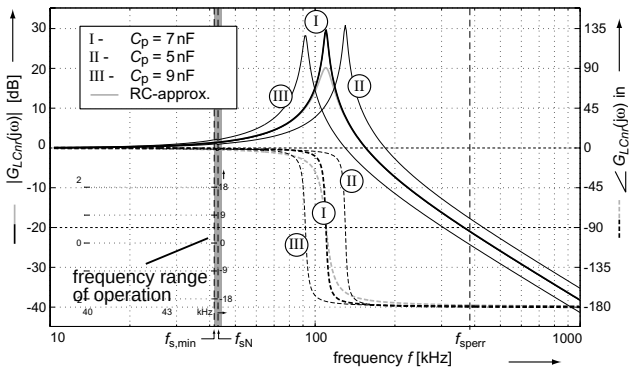

Fig. 11: Output voltage of PWM converter

As usual with PWM converters a cascaded control structure is used at which the current is controlled in an inner loop while the voltage of the actuator is controlled in the overlaid loop.

Fundamental frequency has to be set in a separate control loop. At sonotrodes with $\omega_{r1} C_P R_m < 1/2$ the phase shift between the actuator's voltage and current can be controlled to zero. By this measure operation close to resonance is achieved and transfer of reactive power is avoided.

B. Resonant converters

If the power supply shall be relieved from the high reactive power required by travelling wave motors or other piezoelectric systems with $\omega_{r1} C_P R_M > 1/2$ a compensating coil can be introduced into the circuit. This inductor has to be designed in such a manner that the actuator's capacitance is completed to a resonant circuit which is tuned to the resonant frequency at which the system is operated. Two types of resonant converters having different filter structures have proved to be suitable. They have the following advantages in common:

First, in principle inverter and transformer have to be designed for the active power only which results in low size and low losses of these devices. Second, with regard to the filter characteristic of the resonant circuits low harmonics of the inverter voltage are suppressed and must not be eliminated by use of PWM. Thus the switches of the power converter can be operated with the low fundamental frequency which leads to another reduction of inverter losses.

Considering the power converter and the piezoelectric actuator each containing a resonant systems having varying parameters it can be expected that design of the control is a demanding task. Additional problems arise at travelling wave motors at which coupling between the variables of the two phases exist which cannot be neglected [6].

Converter with low-pass characteristic (LC converter):

A series resonant converter characteristic results when the filter inductor of the PWM filter is replaced by a resonant inductor [6], [9]. Consequently the circuit is identical with that of the PWM inverter already shown at Fig. 10. Again this circuit has a second-order low-pass characteristic. But now the resonance peak is situated in the frequency range in which the inverter is operated. Consequently the operating point is strongly influenced by variations of the mechanical load R_m and the actuators capacitance which depends on temperature.

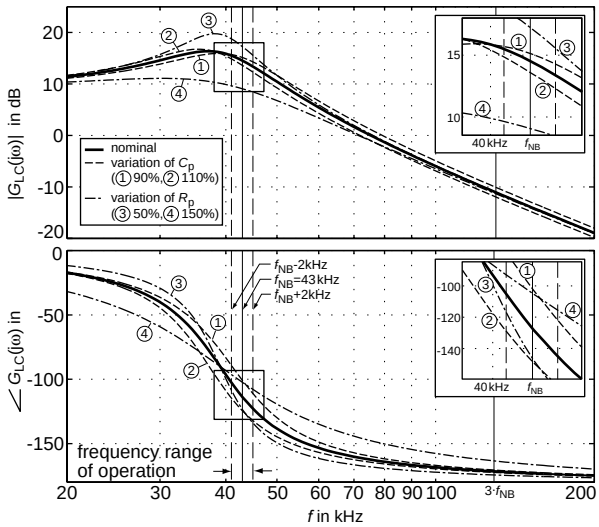

Fig. 12: Output voltage of LC resonant converter

As can be seen from the output voltage of a LC resonant converter (i.e. the input voltage of the actuator) depends strongly on frequency. Therefore voltage control can be performed by variation of frequency. By this measure the operating point is shifted on the frequency characteristic, see Fig. 12, which causes an increase or decrease of the filter's output voltage. Realisation of this control scheme is relatively simple but stable operation is only possible at one side of the resonant peak where the gradient has constant sign. Operation on the peak, where the reactive power is minimum, is not possible.

With regard to the great variation of frequency characteristic attention has to be played to avoid undue electrical or mechanical strain. To ensure safe operation the actuator's voltage is normally controlled in an underlaid control loop (which refers to the control loop at PWM converter).

A second possibility for controlling the output voltage of the LC converter is to vary the rectangular input voltage of the resonant filter. For this purpose either the DC link voltage or the width of rectangular half waves can be varied. With these control strategies frequency can be set independently from voltage amplitude which makes possible to operate the system in the peak of the resonant curve.

Converter with band-pass characteristic (LLCC converter):

Closed loop control of the actuator's voltage can be avoided by use of a filter with band-pass characteristic [8], [9]. At this circuit, see Fig. 13, the parallel inductance compensates the reactive power of the piezoelectric capacitance. The series resonant circuit is used to complete a voltage divider which is almost independent from frequency in the middle of its pass band. Since only few reactive power is delivered by the inverter devices of the series resonant circuit can be designed for low power only.

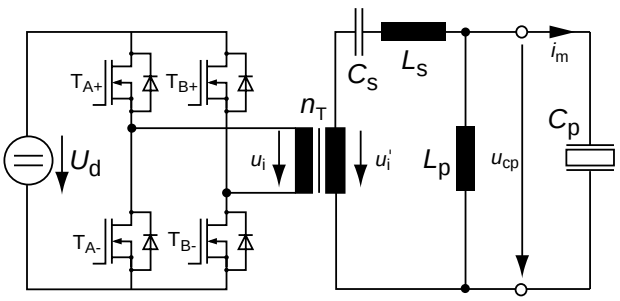

Fig. 13: Full bridge inverter with resonant LLCCfilter

The frequency characteristic of the converter's output voltage is shown at Fig. 14. To achieve symmetrical peaks as shown at the figure series and parallel resonant circuit must be tuned to the operating frequency ($L_P C_P = L_s C_s = \omega_{r1}^{-2}$). The band width depends on the ratio of the capacitances $\alpha = C_s/C_P$ which, for equal resonant frequencies, matches the ratio of characteristic impedances $\alpha = \sqrt{L_n/C_P}/\sqrt{L_s/C_s}$.

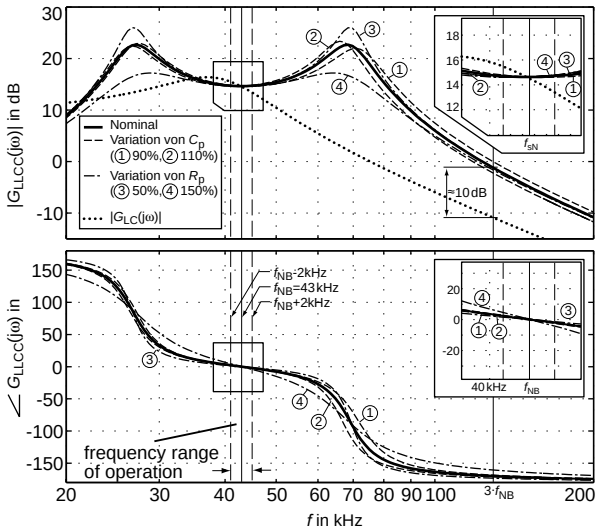

Fig. 14: Output voltage of LLCC resonant converter

The filter of LLCC converter is more complex than a that of LC converter. But it offers more simplicity with regard to control. In the middle of its bandwidth, where the converter is operated, amplitude of output voltage is almost independent of parameter variations. That is why open loop voltage control is possible and an underlaid voltage control is not required. As a consequence better dynamic response is achievable than with LC converter.

At last a possible disadvantage is mentioned. Due to the second resonant peak low order harmonics are not suppressed as well as with LC converter as can be seen from Fig. 15

III. CONCLUSION

At piezoelectric systems strong dependencies exist between all subsections. They therefore are typical mechatronic systems which demand for an integrated design of the mechanical and electrical subsystem as well as of the control under consideration of the requirements of the specific application.

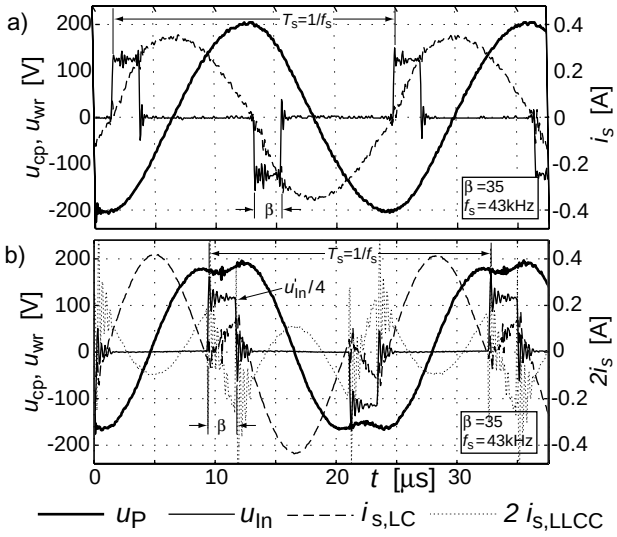

Fig. 15: Wave shapes at small voltage levels
a) LC converter, b) LLCC converter

IV. ACKNOWLEDGEMENT

The author acknowledges gratefully the support of the German Research Council (DFG) for financing research on the supply and control of piezoelectric motors. He also thanks Dr. Th. Schulte who delivered ideas and figures, [10].

REFERENCES

[1] Philips: Piezoelectric Ceramics - Properties and Applications. Philips Gloeilampenfabrieken, Eindhoven, Niederlande, 1991.

[2] Taylor, G. W. et al.: Piecoelectricity, Ferroelectricity and Related Phenomena. Vol. 4, Gordon and Breach Sciences Publishers, 1985.

[3] Navas, J. et al.: Miniaturised Battery Charger using Piezoelectric Transformers. 16th Annual IEEE Applied Power Electronics Conference (APEC 2001), Anaheim, California, USA, Vol.1, pp. 492-496.

[4] Sashida, T.; Kenjo, T.: An Introduction to Ultrasonic Motors. Clarendon Press, Oxford, 1993.

[5] Wallaschek. J.: Piezoelectric Ultrasonic Motors. Journal of Intelligent Materials and Structures (1995), Vol. 6, pp. 71-83.

[6] Maas, J.et al.: High Performance Speed Control for Inverter-fed Ultrasonic Motor Optimized by a Neural Network. 6th Int. Conf. on New Actuators. ACTUATOR'98, Bremen, 1998, pp. 260-263.

[7] Kauczor, C. et al.: Resonant Power Converter for Ultrasonic Piezoelectric Converter. ACTUATOR 2002, 8th International Conference on New Actuators, 10-12 June 2002, Bremen Germany, S. 485-488.

[8] Lin, F.J. et al.: An Ultrasonic Motor Drive Using LLCC Resonant Technique. Proc. of IEEE Power Electronics Specialists Conference (PESC'99), Vol. 2, 1999, pp. 947-952.

[9] Schulte, Th. et a.: PWM-Converter for Travelling Wave Type Ultrasonic Motors. ACTUATOR 2002, 8th International Conference on New Actuators, 10-12 June 2002, Bremen Germany, S. 442-445

[10] Schulte, Th.: Concepts for Power Supply and Control of Ultrasonic Travelling Wave Motors (in German). Dissertation, University of Paderborn, 2004.

Index